Molecular Dynamics Study of Clay-Polymer Interactions in the Treatment of Mature Fine Tailings

by

Wenyuan Sun

A thesis submitted in partial fulfillment of the requirements for the degree of

Doctor of Philosophy

Department of Mechanical Engineering
University of Alberta

Abstract

In this dissertation, all-atom molecular dynamics (MD) simulations were performed to study the mechanisms of clay-polymer interactions and the effects of solution chemistry in the treatment of mature fine tailings (MFT). The fine solids in MFT were mainly clay particles such as montmorillonite and kaolinite. Polymers with different properties were widely used to flocculate the clay particles.

Chitosan, polyacrylamide (PAM), and anionic polyacrylamide (APAM) as commonly used cationic, neutral, and anionic polymer flocculants were firstly introduced to the proximity of montmorillonite (Mt) surface. A monolayer coating of chitosan was observed to form quickly on the Mt surface, driven by coulombic attraction between the cationic polymer and anionic Mt surface. PAM and APAM did not show effective adsorption by themselves. However, when PAM or APAM was added after chitosan, their adsorption was facilitated by the pre-adsorbed chitosan. PAM could adsorb either directly on Mt or on chitosan, in the form of clusters or individual molecules. On the other hand, APAM only adsorbed on chitosan, forming a two-layer structure above the Mt surface. Adding chitosan simultaneously with PAM or APAM, instead of sequentially, did not change the characteristics of the adsorption. The synergetic adsorption of polymers was attributed to the interplay of electrostatic attraction between Mt and chitosan, hydrogen bonding between chitosan and PAM, as well as electrostatic attraction between chitosan and APAM.

In colloidal systems such as polymer-modulated MFT, the influence of ions on the solid-polymer interactions cannot be neglected, in particular the interaction between similarly charged polymer and solid. The adsorption of anionic polyacrylamide (APAM) on anionic Mt, in an aqueous solution containing monovalent or divalent salts was simulated to address the effects of

ions. Compared with monovalent salts (NaCl), the enhancement of APAM adsorption brought by divalent salts ($CaCl_2$) was significant, which could not be explained by the Poisson−Boltzmann theory alone. APAM coordinated to the solvated Ca^{2+} by displacing 1-2 water oxygens in the first coordination shell of Ca^{2+}. Ca^{2+} ions in the adsorbed Ca^{2+}−APAM complexes did not serve as bridges sandwiched between APAM and Mt; instead, the complexes carried a residual positive charge and were subsequently attracted to Mt. The number of adsorbed Ca^{2+}−APAM complexes changed with salinity in a nonmonotonic manner, due to the modulation of apparent charges of Mt and APAM by Ca^{2+}. Increasing adsorption of Ca^{2+}−APAM complexes also promoted APAM adsorption through direct hydrogen bonding with Mt.

Besides ions, the presence of asphaltene in MFT greatly influences the flocculation, through interacting with both the clay surfaces and the polymers. A model asphaltene, C5Pe, was simulated to study such effects. Potential of mean force (PMF) calculations demonstrated the interplay between enthalpy-driven adsorption of C5Pe on the hydrophilic alumina surface of kaolinite and entropy-driven adsorption on the hydrophobic siloxane surface of kaolinite. When added between different types of clay surfaces in water, participating in the hetero coagulation of clay particles, C5Pe tended to adsorb on the hydrophilic surface. In the adsorbed aggregate, the hydrophobic parts of C5Pe molecules stacked in a parallel manner, which aligned perpendicularly to the surface, while the hydrophilic part formed hydrogen bonds with the surface.

When APAM was added simultaneously with C5Pe to an adjacent Mt basal surface, the clustering of APAM molecules was suppressed by C5Pe and the adsorption of APAM was enhanced by the concurrent interaction of C5Pe with APAM and the Mt basal surface. In contrast, near a kaolinite edge surface, unadsorbed C5Pe in the bulk served as growth nucleus for APAM cluster, attracting APAM to the bulk solution and reducing their adsorption.

Together, the molecular insights derived from the simulation results in this dissertation complemented experimental investigations and can further help the polymer treatment of MFT.

Preface

Chapter 3 of this thesis has been published as Sun, W., Zeng, H., & Tang, T. (2020). Synergetic adsorption of polymers on montmorillonite: Insights from molecular dynamics simulations. *Applied Clay Science*, 193, 105654. I was responsible for designing and conducting simulations, data collection and analysis, as well as the manuscript composition and revising. Dr. T. Tang and Dr. H. Zeng were the supervisory authors who contributed to concept formation, proofreading, and revising the manuscript.

Chapter 4 of this thesis has been published as Sun, W., Zeng, H., & Tang, T. (2021). Enhanced Adsorption of Anionic Polymer on Montmorillonite by Divalent Cations and the Effect of Salinity. *The Journal of Physical Chemistry A*, 125(4), 1025-1035. I was responsible for conducting numerical simulations, data analysis, and writing the manuscript. Dr. T. Tang and Dr. H. Zeng were the supervisory authors who were involved in concept formation, results validation, and manuscript revision.

A version of Chapter 5 in this thesis is in preparation for publication as Sun, W., Zeng, H., & Tang, T. Molecular Dynamics Simulation of Model Asphaltenes between Surfaces with Different Polarity. I was responsible for designing and performing molecular simulations, analyzing the data, and manuscript drafting. Dr. T. Tang and Dr. H. Zeng were the supervisory authors who contributed to concept formation, results validation, and manuscript revision.

A version of Chapter 6 in this thesis is in preparation for publication as Sun, W., Zeng, H., & Tang, T. Interplay between Polycyclic Aromatic Hydrocarbons and Polymers in Their Adsorption on Clay-Water Interfaces. I was responsible for designing and performing molecular simulations, collecting and analyzing the data, as well as manuscript composition. Dr. T. Tang and Dr. H. Zeng were the supervisory authors who contributed to concept formation, results validation, and manuscript revision.

Chapter 1, 2 and 7 include the introduction, basic simulation methodology, summary, and future perspective of this project. The three chapters are originally written by Wenyuan Sun and have never been previously published.

Acknowledgements

First and foremost, sincere gratitude to my supervisor, Dr. Tian Tang. The wonderful experience I had in her group has made my PhD a fulfilling and delightful journey. I appreciate her unconditional support, valuable guidance, and ongoing encouragement. Her supervision style and scientific attitude have been and will remain be the role model for my career.

I would like to thank my co-supervisor, Dr. Hongbo Zeng, for his insightful ideas and generous support during my study and research. Studying in his group was a valuable opportunity and greatly broaden my view in science.

I gratefully acknowledge the computing resources and technical support from the Western Canada Research Grid (WestGrid), as well as the financial support from the Natural Sciences and Engineering Research Council of Canada (NSERC), Donald Lougheed Scholarship, and University of Alberta Doctoral Recruitment Scholarship.

Special thanks to my brilliant colleagues, Mr. Subhamoy Mahajan, Dr. Xiaoyu Sun, Dr. Sajjad Kaviani, and Mr. Zhen Yang for sharing knowledge and expertise with me.

Grateful thanks to my parents for their boundless love and indulgence, and to my lovely friends for making my life in Edmonton colorful.

Table of Contents

List of Tables

List of Figures

Chapter 1. Introduction

In bitumen exploiting process, water, sand, silt, and fine particles are usually brought together to the surface as a byproduct, which is known as tailings. A gel-like mature fine tailings (MFT) would form after the coarse fraction of these byproducts segregate quickly in the settling basin [1]. The fine particles in oil sands tailings settle very slowly, and it usually take 2-3 years for them to reach a concentration of about 30-40wt% [2]. Long-term storage structures are required, referred to as tailings ponds. The tailings ponds are settling basins that enable water separation, storage, and recycling [1]. In 2013, there were approximately 976 million cubic metres of fluid tailings stored within tailings ponds, covering the land of approximately 220 km^2 in Alberta [3]. Total volume of tailings will keep increasing due to the very slow consolidation of untreated MFT and the continuous bitumen production [4]. The environmental impacts brought by oil sands tailings cannot be neglected, e.g. chemicals leaching due to structure flaw [5] and toxic material seeping into groundwater [6]. Speeding the water and lands reclamation from tailings has become an urgent need. The government of Alberta released the tailing management framework (TMF) policy in 2015 [2] with the objective that all fluid tailings associated with a project are ready to reclaim within 10 years of the end of mine life of that project.

Slow consolidation and water recovery from the tailings ponds are mainly brought by the fine clay particles in MFT [3,7]. Solid particles with size equal to or less than 44 μm are considered as fines [3]. In MFT, about 4% of the clay particles larger than 44 μm, 46% between 6.5 μm and 44 μm, and 50% less than 6.5 μm [8]. These clay particles are usually entrained in slightly alkaline process water of which the pH is between 7.7- 8.8 [9]. A small amount of calcium, magnesium, chloride, and sulfate ions are also contained in the process water [10]. The clay particles are usually negatively charged in aqueous solutions [11], and the electrostatic repulsion between the particles makes them very stable in MFT.

Many methods have been used to address problems in MFT, especially fine clays treatment. Natural drying and sedimentation could help the coarse sands consolidate first. Physical treatment such as freeze-thaw cycles, filtration, centrifugation, electric treatment, or their combinations are used to help dewatering the tailings [12,13]. Chemical flocculants are also widely used to improve the flocculation and dewatering of MFT, and both inorganic salts and polymeric macromolecular additives have been applied as flocculants. Despite some successes, much remains to be done on the selection and synthesis of polymer flocculants for MFT. Firstly, the addition of some inorganic ions and ionic polymers would result in high ion strength in the recovered water, which is not economically and environmentally acceptable. Secondly, most commercial polymer flocculants are developed for other industries, e.g. mining and paper making, and cannot flocculate MFT in high efficiency [12]. In addition, bitumen in oil sands tailings could interact with the fine particles, affecting the performance of the added flocculants. It could also impede water release from the pores of clay aggregates, hindering the consolidation [14]. These existing challenges have motivated the study of clay-polymer interaction in this project.

1.1. Classification of Clay Minerals In MFT

Electron microscopic pictures of clay particles in MFT showed that they were mainly comprised of stacked clay mineral layers [15,16]. The clay minerals were mostly phyllosilicates with planer structure, in either 2:1 or 1:1 layer. The clay minerals in MFT that belonged to 2:1 class were mostly montmorillonite (Mt) [17,18], a type of smectite consisting of one alumina octahedral sheet sandwiched by two silica tetrahedral sheets, as shown in Figure 1.1a. Thus, the

2:1 structure was also referred to as TOT layer. The structure of Mt was similar to pyrophyllite, and yet with a layer charge arising from isomorphous atom substitution [19]. The isomorphous substitution was more likely to happen in the octahedral sheet than in the tetrahedral ones. For example, in Figure 1a, three aluminum atoms in the octahedral sheet of Mt were substituted by three magnesium atoms (only two are visible in the front view), giving rise to a permanent layer charge of -3. The negative charge was balanced by ions such as Na^+ and Ca^{2+} in the interlayer space, which could swell under water, making it possible to accommodate a wide range of guest molecules. Thus, Mt was widely adopted in many applications involving clay-polymer interactions, such as fabrication of nanocomposite [20] and waste removal [21].

Kaolinite (Kaol) was a representative 1:1 clay mineral layer in MFT [22,23], also referred to as the TO layer. As shown in Figure 1.1b, a common plane of oxygen atoms connected two sheets in a Kaol layer, one consisting of SiO_4 tetrahedra and the other consisting of AlO_6 octahedra. The chance for atom substitution in Kaol was small [24], and thus the charge density of Kaol basal surface was not comparable with Mt. Meanwhile, the edge surface could occupy as much as 50% of the total surface area of a Kaol particle, while the corresponding value was less than 5% for Mt [25]. The charge of the edge surface was pH dependent, which regulated the colloidal properties of clay minerals [26]. Taking Kaol as an example, when the solution pH is ~7, each edge surface was terminated by one $Al(OH_2)(OH)$ group and one $Si(OH)$ group, as showed in Figure 1.1b. The surface charge under this environment was zero. In acidic environment with $pH < 7$, hydroxyl of $Al(OH_2)(OH)$ groups tended to be protonated, resulting in an $Al(OH_2)(OH_2)$ group with a +1 charge. When $pH > 7$, the water bounded to Al atom deprotonated, generating an $Al(OH)_2$ group with charge of -1. When the environment became highly alkaline with $pH > 9$, the $Si(OH)$ group would also become deprotonated, turning into Si-O terminal, and the surface charge became -2 per unit [27].

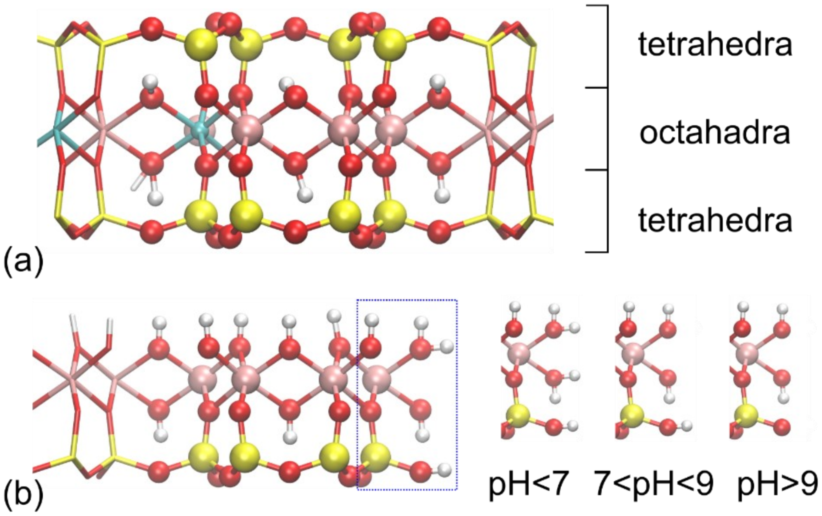

Figure 1.1. Molecular model of Mt (a) and Kaol (b). Model in (a) was extracted from a continuous Mt layer while model in (b) contains one edge surface (terminal on the right) of a Kaol layer. The protonation/deprotonation state of the edge surface varied with pH. A unit cell is marked in ball-and-stick format in (a) and (b). Color scheme for atoms: Si (yellow), Al (pink), Mg (cyan), O (red) and H (white).

Other clay minerals such as illite and chlorite also existed in MFT. They usually shared similar molecular structures with Mt or Kaol but varied in isomorphous substitution or interlayer materials. For example, illite belonged to 2:1 class, similar to the structure of Mt except that the isomorphous substitution usually took place in both the tetrahedral and the octahedral sheets [27,28]. Chlorite was also of 2:1 type, with hydroxide sheets intercalated in the interlayer spaces [15].

1.2. Features of Clay Mineral Surfaces

To modulate solid interactions in colloid systems such clay suspensions in MFT, it was of great importance to understand the surface properties of different clay minerals. In many theoretical models such as Gouy-Chapman relation and DLVO theory, the surfaces of fine solids were simplified into uniform spheres or planes [29]. However, the surface structures of real fine clays were more complex. As introduced in section 1.1, there were basically three types of clay surfaces in MFT, the siloxane basal surface, the alumina basal surface, and the pH dependent edge surface. The geometry, charge condition, and functional groups varied with the types of surfaces, which affected the surface properties such as the surface potential [30,31] and wettability [23,32], resulting in complex flocculation and dewatering behaviors.

The surface potential usually varied with the type of clay surface due to the different isomorphous substitution or protonation. Even within the same clay mineral layer, the surface potential could still display anisotropy, which challenged the fundamental understanding of the surface behaviors. Liu et al. [33] measured the average zeta potential of Kaol and Mt suspensions under different pH. The zeta potential of Kaol in 1mM KCl solution decreased from about 0 mV at pH 3 to about -30 mV at pH 10, while the zeta potential of Mt remained almost unchanged at different pH. Tournassat et al. [30] employed a two-dimensional Possion-Boltzman equation [34] to calculate the surface potential near two different edges of a Mt particle. The [010] edge surface became positive when the pH reduced to 5 while the [110] edge surface remained negative until the pH became less than 3.5, suggesting that the crystallographic orientation significantly affect the surface charge. Muscovite micas were differently cleaved by Zhao et al. [31] to study the surface potential of basal surface and edge surface of the 2:1 phyllosilicate. The forces were measured between a silica particle attached to the end of an atomic force microscopy (AFM) cantilever and two different crystallographic planes of mica in aqueous solutions. pH of the solution was varied. The long-range force for the basal plane remained repulsive despite of the change of pH (6-10) and fitted well with the DLVO theory. On the other hand, for the edge surface, the repulsive force decreased with pH, and reversed to be attractive when $pH < 6$. The measured force profile displayed a poor fitting with the classical DLVO theory.

The wettability of a clay surface was tightly related to its type. For the same type of surface, the wettability changed with the surface charges. Tunega et al. [23] investigated a water layer on the octahedral and tetrahedral basal surfaces of Kaol by ab initio molecular dynamics. The results showed that water molecules could form strong hydrogen bonds with all hydroxyl groups on the octahedral surface, via the proton of water and the oxygen of surface OH as well as the oxygen of water and the surface proton. While on the tetrahedral surface, water molecules have a slow rotation motion above the ditrigonal hole, forming and breaking weak hydrogen bonds with the basal oxygen atoms. The octahedral layer is therefore more hydrophilic than the tetrahedral layer. Zhang et al. [32] investigated the wettability of basal surface of Mt with different surface charges by molecular dynamics (MD) simulation. The different charged Mts were solvated by mixtures of decane and water. As the surface charge increased, the contact area between the basal surface and decane gradually decreased until becoming fully water wet. It was proposed that the increased surface charge attracted more counterions (Na^+ and Ca^{2+}) to distribute near the surface. The hydration of the counterions accumulated more water molecules in proximity to the surface, and thus increased the wettability. X-ray diffraction as well as water adsorption measurement by Saada et al. [35] showed that the surface of illite was overall more hydrophilic surface than Kaol, and Kaol had a higher affinity for asphaltene while illiite had a higher affinity for water.

1.3. Mechanisms for Clay-Polymer Interactions

The efficacy of many polymers with high molecular weight (HMW) in modulating the solids interactions has been widely demonstrated, either in clay mineral suspensions or MFT. The long polymer chains carried sufficient functional groups to simultaneously interact with multiple solid surfaces, so that the solids could be flocculated together, achieving desirable flocculation performances. The modulation could be driven by multiple mechanisms, independently or together, due to the variety of surface properties.

The solid interactions could be mediated by charged polymers through altering the electrostatic properties. In aqueous solutions, the negatively charged solids attracted the counter-ions and co-ions to distribute around the solid surface, forming the diffuse electric double layer (EDL) [29]. The aggregation of the similarly charged solids was hindered by the repulsive electric double layer forces. The addition of anionic HMW polymers served the same function of inorganic salts: to compress the thickness of EDL and thus suppress the EDL forces between solids. The solids were thus easier to approach each other and aggregated together. For example, Robert et al. [36] synthesized several nitrogen-containing polymers (PEIs (MW 600 g/mol), PDAMA (MW 5000 g/mol), AFPAAs (MW 5.0×10^4 g/mol), AFPMMA (MW 1.2×10^5 g/mol), AFPMMA-co-PS (MW 1.17×10^5 g/mol)) as switchable ionogens for Kaol and Mt treatment. The nitrogen-containing polymers could form ammonium bicarbonate salts with the addition of CO_2. The initial settling rate (ISR) was improved, and the supernatant turbidity was reduced when the polymers and CO_2 were added, which indicated that fine particles in the suspension started to aggregate. Meanwhile, zeta potential of the clays was increased, suggesting the suppression of EDL of Kaol/Mt particles by the ammonium bicarbonate salts, leading to less repulsion between the particles and initiation of aggregation and settling. The polymers were recycled after removing the CO_2 by injecting inert gas Ar into the extracted supernatant. Kaol particles were later added into the supernatant after recycling, and barely settled, which manifested that the polymers stayed in the aqueous phase of the supernatant during the whole process without binding to the clay particles.

In the regulation of electrostatic properties of the solids, charge neutralization or charge patching of the solids by cationic polymers were also commonly employed to promote the flocculation. The oppositely charged polymers reduced the surface charge of solids through adsorption, making the solids less repulsive to each other. Gumfekar et al. [37] compared the flocculation behavior of two cationic polymers: poly(TMAEMC) with a higher charge density and poly PCL_2ChMA with a lower charge density. For the same tailings, poly(TMAEMC) was found to lead to higher ISR, lower supernatant turbidity, and lower capillary suction time (CST). This stronger flocculation ability of poly(TMAEMC) was attributed to more significant charge neutralization caused by polymer adsorption. Similar conclusion was also drawn by Vajohinejad et al. [38], who tested the MFT flocculation behavior of copolymers AAm-co-DADMAC consisting of acrylamide and cationic poly (diallyldimethylammonium chloride). The charge density and average molecular weight (ranging from 9×10^4 g/mol ~ 1.4×10^6 g/mol) of the copolymer were controlled during polymer synthesis. The results showed better dewatering ability, represented by smaller CST and stronger specific resistance to filtration (SRF), with increasing charge density of the copolymer, while the molecular weight showed little influence. Better flocculation ability of polymers with high cationic charge density was also observed by other experimental work [39].

Besides modifying the surface charges and EDL thickness, HMW polymers were more often designed to bind onto the solid surfaces through certain chemical or physical bonds. The solids were thus flocculated together by the long polymer chain that they were binding to simultaneously. For example, Li et al. [40] measured the long-range electrostatic force and short-range adhesion force between a spherical model silica and tailing samples by AFM. The tailing samples were treated by negative charged HPAM (hydrolyzed polyacrylamide) of various dosage.

The electrostatic force remained repulsive irrespective of the dosage of HPAM, while an adhesion force of 0.4 mN/m was obtained when the HPAM was added at 15 and 30 ppm, along with an increase in ISR. Based on the results, it was proposed that HPAM promoted the flocculation mainly through the bridging effect through the hydrogen bonding between hydroxyl groups of HPAM and solid surfaces, rather than altering the electrostatic properties of the solids. Lu et al. [41] investigated the adsorption of neutral glycopolymers (PLAEMA, 2-lactobionamidoethyl methacry-lamide) onto mica sheets, which share similar structure as Kaol. The mica sheets were dipped into the polymer solution for 1h allowing for adsorption, and then rinsed to remove unattached polymers. Increased roughness of the mica surface characterised by AFM image proved that the polymers could attach to mica. Surface force apparatus (SFA) measurements showed adhesive force between two micas in the polymer solutions, which suggested that the polymers bridged the solids via hydrogen bonding between the hydroxyl groups from the pendent sugar residues of the glycopolymer and from the mica surface.

Entropic effects also played an important role in tuning the solid interactions by polymers. Zhang et al. [42] utilized the temperature-responsive wettability of poly(NIPAm) to enhance the dewatering of MFT. Working with a cationic polymer, it could flocculate the solids first. When the temperature was increased above a critical value, the polymer became hydrophobic and large flocs were formed. A two-step consolidation process, where the temperature was changed from 25°C to 50°C and back to 25°C, could further enhance the dewatering since in the second step (50°C-25°C) the hydrophobic interactions were absent, and the large flocs broke up allowing small flocs to fill the gaps. A theoretical model was developed to account for the hydrophilic/hydrophobic interactions between the particles in such a process [43]. The interaction between clay particles included four components, van der Waals force, electrostatic force, Lewis acid-base force, and lubrication force which became present when two particles approached each other squeezing out the fluid between them. The Lewis acid-base force was an extension of polar interactions. It considered the electron-acceptor-electron-donor interactions [44], and was used to capture the hydrophobic interactions between particles [43]. The model was implemented using the Lattice-Boltzmann method to simulate floc growth, and validated by the growth in particle number concentration in experiments [45]. Asakura and Oosawa modeled the phase separation of hard-sphere colloids caused by non-adsorbing polymers [46,47], and showed that two similar colloids particles attracted each other when immersed in a non-absorbing polymer solution. The attraction was attributed to the so-called "depletion effect". In particular, the mutually impenetrable particles were surrounded by a depletion zone inaccessible to the polymer coils. When the depletion zones of two particles overlapped, the polymers are expelled from the space between the particles, creating an effective osmotic pressure that pushes the particles together. Under this model, the pairwise interaction potential between two colloidal particles was written as: $U(r) = U_0(r) + U_{dep}(r)$, where $U_0(r)$ was the bare particle interaction potential, and the depletion potential $U_{dep}(r)$ was in the form of: $U_{dep}(r) = -P_{osmotic}V_{overlap}$, subjecting to $\sigma < r \leq \sigma + 2r_g$. Here σ was twice the particle diameter, r_g was the gyration radius of the polymer, $P_{osmotic}$ was the osmotic pressure that proportional to the number density of all polymers in a pure polymer solution, and $V_{overlap}$ was the volume of the overlapping depletion zones between particles.

When two solid surfaces approached each other closer than a few nanometers, additional short-range forces arise and dominated the separation and contraction of the surfaces, in particular, the solvation [50,51] and structural forces [41,52,53]. They were non-DLVO forces and much stronger than the DLVO forces (EDL and van der Waals forces) in highly constricted spaces.

Graber and Mingelgrin [50] performed a series of separation test of Na-Mt in different solutions. The results showed that the clays exhibited maximum separation in the solvent whose solubility was closest to that of the clays. Steric hindrance between the polymer brushes and mushrooms was frequently used to explain the decrease of MFT settling when the polymers were overdosed [41,52,53]. The maximum collision efficiency between particles was usually achieved when half of the particle surface was covered by flocculants [54].

Besides functioning via a single mechanism, HMW polymers commonly worked through multiple mechanisms to enhance the flocculation. Zhang et al. [42] performed a series of settling tests on MFT samples in a mixed solution of two polymers with different ratios, cationic AAm-st-DADMAC (MW 2.2 × 10^6 g/mol) and neutral NIPAm (MW 1.2 l× 10^6 g/mol) with hydroxyl groups. Pure poly (AAm-st-DADMAC) could absorb onto the solids via charge neutralization, but this only resulted in ISR less than 1 m/h at all dosage. ISR of MFT treated with pure NIPAm could reach 3 m/h via the bridging effect enabled by the hydroxyl groups. The best ISR result (3.5 m/h) was obtained at an optimum ratio of 30% AAm-st-DADMAC and 70% neutral NIPAm, which was supposed to be caused by the cooperative effect of hydrogen bonding and charge neutralization. Wang et al. [48] investigate the flocculation behaviors of Zetag (MW 12.7 × 10^6 g/mol) solution preconditioned by hot water bath and NaOH. Increasing temperature or pH of the polymer solution could enhance the hydrolysis of Zetag molecules, from which cationic choline ions were produced. The floc size obtained from focused beam reflectance measurement (FBRM) indicated that there were two stages of the floc growth, with significantly increased growth rate in the second stage. It was hypothesized that in the first stage the released cationic choline ions could attach to the solid surfaces causing charge neutralization and aggregation of some solids, whereas in the second stage the anionic polyacrylamide backbones bridged the choline coated solids or uncoated solids. Charge neutralization and initial coagulation in the first stage led to more efficient bridging and increased growth rate in the second stage. The two-step flocculation process was also investigated by Lu et al. [49] by sequentially adding two oppositely charged polymer flocculants, first anionic Magnafloc-1011 (MW 1.75×10^7 g/mol) and then cationic chitosan (MW $6 \sim 8 \times 10^4$ g/mol). Zeta potential of tailings particles changed from -38.6 mV to -39 mV after the addition of Magnafloc alone at 20 ppm but reached about 0 mV when 200 ppm of chitosan was added after Magnafloc. An adhesion force of 4 mN/m appeared between two micas in Magnafloc solution and became 31 mN/m when chitosan was added. The settling behavior, quantified by ISR, turbidity of supernatant and floc size, also reached the best when 200 ppm of chitosan was added after 20 ppm of Magnafloc. In these experiments, Magnafloc first bridged the particles to form flocs, and in the second stage chitosan bonded the negatively charged flocs or remaining particles, resulting in improved flocculation.

1.4. Effects of solution chemistry

1.4.1. pH of solution

The effects of pH on flocculation were multifold. By decreasing pH of the solution, the acid sites on the solid surfaces dissociated less, rendering reduced surface charge and enhanced hydrophobicity. Zhu et al. [55] pressurized CO_2 into industrial tailings to investigate how CO_2 affected the flocculation. Zeta potential of the particles increased from about -43 mV to -27 mV when pH value of the CO_2 treated solution decreased from about 8.5 to 5. The ISR and clarity of the supernatant also increased with the partial pressure of CO_2. Similar findings were also reported by others in MFT or clay suspension [56,57]. Gu et al. [58] measured the contact angle of water on Kaol particles at different pH. When the pH was greater than 3, the contact angles were less than 20°, while contact angles > 120° were obtained for pH < 3. The reduced surface charge consequently decreases the electrostatic repulsion between the fine solids. However, non-monotonic response of solids to pH was also reported. Menon and Wasan [59] observed a non-monotonic change in the zeta potential of Mt with pH. With increasing pH, the zeta potential first decreased from about -30 mV until a minimum of -70 mV was reached at pH 3.5-4.5. It then increased to a maximum of about -35 mV at pH 6-7, and finally stabilized at about -60 mV when pH was further increased. The non-monotonic change was attributed to the presence of two types of acid sites on the edge surface of Mt [60]: the strong acid site dissociated at pH ≈ 4.5, while the weak acid site dissociated at pH ≈ 9.

The pH-dependent charges on the edge surface could lead to different structures within the clay mineral aggregates. In acidic medium, since the edge surface would be positively charged and attracted a negatively charged basal surface, aggregates with a "card-house" structure would form by edge (+)/face (-) contact [61,62]. While in alkaline medium, the edge surface could be neutral or negatively charged. If the ionic strength of the solution was high enough to suppress the EDL repulsive forces between the particles, "card-pack" flocs would form by face (-)/face (-) contact due to the residual valence forces between the basal surfaces. Nasser and James [63] developed a sedimentation-consolidation mechanics model based on the work of Landman et al. [64]. Application of the model to Kaol suspension showed that at pH 2 and with a low electrolyte concentration, the particles were more likely to form "card-house" aggregates via edge/face interaction, resulting in a voluminous structure. When high ionic strength suppressed the EDL of the basal surfaces, face/face interaction was more favored, which led to tightly packed flake-like structures and the formation of denser gels.

Besides the dissociation of acid sites on clay surfaces, pH could also change the configuration and adsorption efficiency of ionic flocculants. Hasan and Fatehi [65] showed that the clarity and clay loss increased with pH when Kaol and bentonite suspensions were treated by cationic kraft lignin-AM-DMC (KAD) polymer. This was contradictory to the decreased zeta potential of the clays upon pH increase, which would have provided more stabilization for the suspension. The discrepancy resulted from the change of polymer adsorption efficiency with pH. The adsorption efficiency of cationic KAD polymer on Kaol was limited to 0.6 mg/g under pH 2 while increased to 2.3 mg/g when pH was larger than 7. Similar pH-dependent adsorption was found by Tekin et al. [66]. In their work, the adsorption efficiency of cationic PAM to Kaol samples was determined with the aid of UV-VIS spectrophotometer, which increased from about 15 mg/g to 75 mg/g as pH increased from 5.5 to 10.5.

1.4.2. Ions and salinity

The presence of electrolyte ions in MFT was inevitable, resulted from many production activities employing saline solutions [67,68]. Besides, inorganic salts were widely added to enhance the flocculation [69–71]. The presence of salt ions would greatly affect the solid interaction in the colloidal systems.

First and foremost, EDL at the solid-water interface would be suppressed by the ions, reducing the EDL forces between the solids. The ions could impact the EDLs of both solids and polymers, mediating the polymer adsorption and the resulted flocculation. Increasing the salinity could thus better suppress the EDL repulsion between the particles. The solids were easier to approach and adhere via other local forces such as van der Waals force and hydrogen bonding. Ji et al. [52] compared the settling behavior of oil sand tailings in fresh water and in saline solution, which were both treated by three kinds of polymers: anionic MF (Magnafloc 1011), nonionic PAM, and Al-PAM ($Al(OH)_3$-polyacrylamide). The ISR of fine solids and clarity of supernatant of MF treated tailings was significantly increased in saline solution compared with those in fresh water. Zeta potential of the clay particles in the supernatant increased from about -37 mV in fresh water to -15 mV in saline solution, leading to reduced electrostatic repulsion. Meanwhile, the hydrodynamics radii of MF, determined from dynamic light scattering (DLS), was much smaller in saline solution. This was because the EDL of the polymer was also suppressed, and the polymer became more coiled. The smaller radii made the adsorption layer of MF denser, enhancing the strength of solid-polymer-solid connection. Compared with the anionic MF, for the neutral PAM and Al-PAM, the increased salinity only suppressed the EDL of the fine solids, thus enhancement of flocculation in saline tailings was less significant. Zhang et al. [43] also investigated the effects of salinity on particle coagulation in their theoretical model based on extended DLVO theory. The EDL force was calculated from the model and found to decrease with increasing salt concentration. When the salinity (defined by Practical Salinity Scale [72]) was increased from 0 to 20, the settling velocity (vertical component of the particle's translational velocity) increased rapidly and reached a plateau of 0.16 mm/s at salinity of 2. The result was similar to the experiments [73] where the setting velocity of Kaol reached 0.137 mm/s when the chlorine level of sea water was increased to 2‰.

Besides the salinity, increasing ion valence could also suppress the EDL repulsive forces. The presence of divalent cations, e.g., Ca^{2+} and Mg^{2+}, had a significant effect on the counterion distribution closed to a negatively charged surface. Even with a small concentration of divalent cations in the bulk phase, the surface could have a very high local concentration [29], decreasing the surface charge and the surface potential. For example, Long et al. [74] showed that the addition of calcium or magnesium to aqueous solutions containing 5 ppm HPAM flocculants and 20 mM KCl significantly increased the adhesion force between a silica particle (sharing similar structure with the clay fines in MFT) and a silica wafer, measured by AFM. Settling test of MFT was also performed with same additives of polymers and ions, and the settling performance correlated well with the adhesion force. Similar finding was also reported by Sivasubramanian et al. [75].

In addition to suppress the EDL force, multi-valent ions could serve as bridges, connecting the polymer and solids through charge neutralization, further enhancing the polymer adsorption. Li et al. [40] found that the amount of Ca^{2+} and Mg^{2+} in process water decreased after the addition of HPAM. The above observations were attributed to the cation bridging (HPAM-Ca-clay) effect, where the calcium/magnesium ions simultaneously bound with the polymers and the solids to enhance the polymer adsorption on the solids. However, contrast with the case for monovalent ions that the increased salinity would promote the flocculation until reaching plateau, counter effects would come to play if the concentration of multi-valent ions was sufficiently high. Peng et al. [76] measured the height of supernatant of Kaol suspensions treated by APAM, with $CaCl_2$ in different concentrations (0, 0.0005 mol/dm^3, and 0.001 mol/dm^3). The height of supernatant decreased with $CaCl_2$ concentration, manifesting a negative correlation between the flocculation of Kaol particles and $CaCl_2$ concentration. The negative correlation was attributed to the precipitation of calcium hydroxyl on the surface of Kaol, blocking the hydroxyl groups on the surface to form H-bonds with the polymers and other surfaces. The polymer adsorption and solids coagulation were thus impeded. Charge reversal of the solids surface and polymers resulted from the excess adsorption of Ca^{2+} was proposed by Long et al. [74], to address the presence of optimum dosage of $CaCl_2$ in the treatment of MFT. The excessive adsorption of Ca^{2+} gradually compensated the negative charge of solids and polymers until reversed it, and thus the polymer adsorption increased first and then started decreasing with the salt dosage, mediated by the change of EDL forces. Similar phenomenon was also reported by Kaarmukhilnilavan et al. [77], who investigated the flocculation efficiency of avian egg-white on the Kaol suspensions. Quantities of Kaol in the supernatant were monitored in a standard jar-test apparatus as characteristics of flocculation. The flocculation displayed a nonmonotonic increase with dosage of $CaCl_2$. It was proposed that the Ca^{2+} gradually compensated the negative charge of Kaol by adsorbing on the basal plane, resulting in better flocculation, when dosage of $CaCl_2$ increased from 40 ppm to 100 ppm. When the dosage of $CaCl_2$ was higher than 100 ppm, negative Cl^- started binding with Ca^{2+}. The charge compensation was thus intervened by the Cl^-.

1.4.3. Effect of asphaltene

Unlike traditional crude oil, bitumen extracted from oil sands had abundant polymeric materials with high molecular weight. The heaviest components, known as asphaltenes, were soluble in liquid aromatics, e.g. toluene, and insoluble in n-alkanes [78]. Adsorption of asphaltene onto the fine particles, via hydrogen bonding between the hydroxyl groups on the solids and polar groups on the asphaltenes [79,80], was inevitable and impacted the flocculation process in oil sand tailings.

There have been conflicting reports on the effect of asphaltene on MFT stabilization and settling. Scott et al. [81] reported that tailings sludge containing asphaltene could settle with a higher efficiency than bare clays. They hypothesized that asphaltene molecules worked as a binding agent in the flocculation of solids. Jada et al. [57] observed that the zeta potential of asphaltene-coated Mt was less negative than the bare sample and independent of pH, which would enhance the clay flocculation. SEM images from Pourmohammadbagher [82] also showed that the floc size of asphaltene-coated Kaol and illite was bigger than the uncoated ones. Menon and Wasan [59] found that asphaltene adsorption changed the wettability of clay particles dramatically: the contact angle between Mt particle and water changed from 70° to 150° when asphaltene concentration changed from 0 to 0.4 g/L, suggesting a transformation from hydrophilic to hydrophobic.

On the other hand, many researchers reported that adsorbed asphaltene enhanced the stability of clays in aqueous solution. Majid et al. [83] found that the settling of clays increased linearly with bitumen removal. In the measurements of Liu et al. [33], at pH 8 the average zeta potential of asphaltene emulsion in KCl solution was about -80 mV while the corresponding value was about -30 mV for Kaol and Mt suspension. The more negative surface potential of the asphaltene could lead to stronger electrostatic repulsion and hence more stable suspension if they became adsorbed on the clay particles. Marlow et al. [84] showed that the zeta potential of illite particles increased from 0 to -40 mV when the bitumen content in the illite suspension increased from 0 to 5 wt%. And the settling rate of illite decreased quickly from 24 cm/min to 3 cm/min when the asphaltene adsorption density changed from 0 mg/g to 12 mg/g. Electrostatic repulsion between the asphaltene-coated particles were argued to be the dominant factor for the enhanced stability of the colloidal suspension. However, further increase of asphaltene contents had almost zero effect on the zeta potential. As well, the settling rate was about 2.5 cm/min when asphaltene adsorption density reached 24 mg/g. These were attributed to the steric hindrance between asphaltenes. Menon and Wasan [59] reported similar findings on Mt suspension, where the zeta potential of Mt changed from about -40 mV to -50 mV when the asphaltene concentration increased from 0 to 1 g/L and remained at -50 mV when asphaltene was further added.

Asphaltenes could also impact the function of polymer flocculants by interfering the polymer adsorption onto clay particles. Long [85] used single molecule force spectroscopy (SMFS) to investigate the adsorption of a HAPM molecule on clay and bitumen surfaces in process water. The desorption/adsorption forces of HPAM on mica and bitumen surfaces were about 100 pN and 40 pN respectively, which implies that asphaltene coated on the solid surface would undermine the adsorption of flocculants. Similar phenomenon was also found by Klein et al. [14], who studied the absorption of an anionic flocculants AF246 on alumina and bitumen surfaces with quartz crystal microbalance with dissipation monitoring (QCM-D), and observed a reluctant adsorption of the flocculants on bitumen. Li et al. [40] measured by AFM the long-range electrostatic repulsive force between asphaltene and an anionic HPAM flocculants, as well as the force between mica and HPAM, and found the former to be stronger than the latter. On the other hand, Klein et al. [14] explored the effect of bitumen content on the flocculation ability of an anionic flocculants AF246. The bitumen content in MFT was controlled by air flotation and blending. When the bitumen content was reduced from 0.45 wt% to 0.18 wt%, the ISR increased from about 2.5 m/h to 7 m/h, and the weight chord length in FBRM increased from 280 μm to 350 μm, suggesting an improvement in flocculation. However, by further reducing the bitumen content to 0.08 wt%, the ISR and FBRM chord length decreased to 1.3 m/h and 300 μm. Similar non-monotonic changes were also reported for the amounts of polymers that entered the settled clays, which first increased and then decreased with the reduction of bitumen.

1.5. Motivations and Objectives

Although there has been a lot of work on testing the performance of polymers as flocculant, little was done at the molecular level to directly reveal their mechanistic function. As such there still exist knowledge gaps. First of all, while it has been proposed based on experimental measurements that polymers could enhance clay flocculation by mechanisms such as cation exchange, charge neutralization and hydrogen bonding, stronger evidence at molecular level was greatly needed. In the experiments, multiple types of functional groups of a HMW polymer could mediate the flocculation differently, preventing accurate interpretation of the experimental results. Meanwhile, mixed types of clay mineral surfaces could be present simultaneously and interact differently with the polymers. The real-time "observation" of microscopic systems could well complement the experimental investigation, providing a comprehensive understanding of the function of polymer flocculants.

More specifically, some experiments have shown that two polymers working via different mechanisms could have a synergetic effect on MFT flocculation when they were both added. The mechanisms behind the synergies needed to be fully understood. The optimum dosage ratio and adding sequence of the polymers needed to be clarified, which would allow us to better design the flocculants as well as the process to promote clay flocculation.

The complex clay-clay interaction mediated by flocculants also led to debates in the literature on the role of solution environment such as pH and ions. For example, seemingly contradictory phenomena were reported regarding the influence of cations on the flocculation. Several hypotheses have been proposed such as cation-exchange, cation's blocking of the binding sites for polymer, suppression of EDL force, and the combination of multiple mechanisms. With atomistic resolution, the ambiguities as well as mechanistic insights on the effects of solution environment could be better addressed.

Another challenge was that reports about the effects of asphaltene on MFT treatment vary significantly among existing literature. The presence of asphaltene largely complicated the clay-

clay and clay-polymer interactions. The amphiphilic nature of asphaltene rendered its high affinities to multiple types of solid surfaces, altering the clay-clay interactions. Besides, the deprotonation/protonation and presence of heteroatoms of asphaltene could interfere with the clay-clay and clay-polymer interactions by mediating the long-range (electrostatic) and short-range (H-bonding) interactions. Since the amount of asphaltene in MFT cannot be neglected, the role of asphaltene on the interaction between clay and polymer needed to be investigated.

In this thesis, to fill the identified knowledge gaps, molecular dynamics (MD) simulation is employed to investigate the clay-polymer interactions as well as the effects of solution chemistry. With the observation of motions of atoms and molecules in microscopic systems, as well as the calculation of kinetic/thermodynamic properties and interacting forces, the following four objectives are aimed to be achieved: (1) reveal the flocculation mechanisms of three representative cationic, anionic, and neutral polymer flocculants, and provide quantitative analysis on the synergetic effects of polymers working via different mechanisms; (2) understand the effects of solution environment, in particular, the regulation of clay-polymer interactions by two common exchangeable cations (Na^+ and Ca^{2+}); (3) probe the interaction between asphaltene and different types of clay surfaces; (4) investigate the interplay between asphaltene and polymer flocculant in the mediation of clay-clay interactions.

1.6. Outline

Chapter 2 described the basic principle of MD simulations, including the interaction functions and equations of motion. Two important concepts in the analysis of MD simulations, radial distribution function and potential of mean force were reviewed. The umbrella sampling method as well as weighted histogram analysis method for the calculation of potential of mean force were described.

In Chapter 3, the functions of chitosan (cationic), PAM (neutral), APAM (anionic) on the flocculation of anionic Mt were revealed by MD simulations. Chitosan was added to aqueous systems, simultaneously or sequentially with PAM or APAM, to probe the synergy between two types of polymer flocculants, as well as the effects of adding sequence.

In Chapter 4, NaCl and $CaCl_2$ were added in aqueous systems containing anionic polyacrylamide (APAM) and anionic Mt. The effects of ion valence and salinity on the cation mediated clay-polymer interactions were revealed by varying the concentration of the monovalent and divalent salts in a series of MD simulations.

Chapter 5 presented the behaviors of monomer and aggregate of a model asphaltene between two solid surfaces with different surface groups, studied by MD simulations. The adopted solid surfaces were alumina and siloxane basal surfaces of Kaol. The driving mechanism of clay-asphaltene interactions were shown by the profiles of potential of mean force. Effects of solid surfaces, solvents, as well as asphaltene aggregation were discussed.

Chapter 6 studied the interplay between asphaltene and APAM in their adsorption on two types of clay surfaces, the hydrophobic basal surfaces of Mt and the hydrophilic edge surface of Kaol. Asphaltene, APAM, two types of solid surfaces were deprotonated to be consistent with the surface potentials reported in experimental works. The asphaltene-clay interaction mediated by APAM, as well as the APAM-clay interaction mediated by asphaltene were explored. The effects of asphaltene on the function of APAM as flocculants were identified.

Chapter 7 included the overall conclusion and future perspectives.

References

[1] Alberta Government, Alberta Oil Sands Industry Quarterly Update: Winter 2017, (2017) 1–16.

[2] A. Farkish, M. Fall, Rapid dewatering of oil sand mature fine tailings using super absorbent polymer (SAP), Miner. Eng. 50–51 (2013) 38–47. doi:10.1016/j.mineng.2013.06.002.

[3] Alberta Government, Coal and Mineral Development in Alberta 2017 Year in Review, 2017.

[4] Alberta Government, Lower Athabasca Region: Tailings Management Framework for the Mineable Athabasca Oil Sands, 2015. http://aep.alberta.ca/lands-forests/cumulative-effects/regional-planning/documents/LARP-TailingsMgtAthabascaOilsands-Mar2015.pdf.

[5] Price, Matt. "11 million litres a day: the tar sands' leaking legacy." (2008).

[6] Natural Resources Defense Council, Alberta's tailings ponds, (2017) 1–8.

[7] C. Wang, D. Harbottle, Q. Liu, Z. Xu, Current state of fine mineral tailings treatment: A critical review on theory and practice, Miner. Eng. 58 (2014) 113–131. doi:10.1016/j.mineng.2014.01.018.

[8] A. Alamgir, D. Harbottle, J. Masliyah, Z. Xu, Al-PAM assisted filtration system for abatement of mature fine tailings, Chem. Eng. Sci. 80 (2012) 91–99. doi:10.1016/j.ces.2012.06.010.

[9] E.W. Allen, Process water treatment in Canada's oil sands industry: I. Target pollutants and treatment objectives, J. Environ. Eng. Sci. 7 (2008) 123–138. doi:10.1139/S07-038.

[10] H.A.W. Kaminsky, T.H. Etsell, D.G. Ivey, O.E. Omotoso, Characterization of clay minerals in froth, middlings and tailings streams produced by hot water extraction of Athabasca oil sands, (2014) 1–29.

[11] R.K. Schofield, H.R. Samson, Flocculation of kaolinite due to the attraction of oppositely

charged crystal faces, Discuss. Faraday Soc. 18 (1954) 135–145. doi:10.1039/DF9541800135.

[12] D.R.L. Vedoy, J.B.P. Soares, Water-soluble polymers for oil sands tailing treatment: A Review, Can. J. Chem. Eng. 93 (2015) 888–904. doi:10.1002/cjce.22129.

[13] R. Hogg, Flocculation and dewatering, Int. J. Miner. Process. 58 (2000) 223–236. doi:10.1016/S0301-7516(99)00023-X.

[14] C. Klein, D. Harbottle, L. Alagha, Z. Xu, Impact of fugitive bitumen on polymer-based flocculation of mature fine tailings, Can. J. Chem. Eng. 91 (2013) 1427–1432. doi:10.1002/cjce.21863.

[15] R.I. Barnhisel, P.M. Bertsch, Minerals in Soil Environments, Soil Science Society of America, Madison, WI, USA, 1989. doi:10.2136/sssabookser1.2ed.

[16] X. Kang, Z. Xia, R. Chen, H. Sun, W. Yang, Effects of inorganic ions, organic polymers, and fly ashes on the sedimentation characteristics of kaolinite suspensions, Appl. Clay Sci. 181 (2019) 105220. doi:10.1016/j.clay.2019.105220.

[17] H.A.W. Kaminsky, T.H. Etsell, D.G. Ivey, O. Omotoso, Distribution of clay minerals in the process streams produced by the extraction of bitumen from athabasca oil sands, Can. J. Chem. Eng. 87 (2009) 85–93. doi:10.1002/cjce.20133.

[18] R.J. Chalaturnyk, J.D. Scott, B. Özüm, Management of oil sands tailings, Pet. Sci. Technol. 20 (2002) 1025–1046. doi:10.1081/LFT-120003695.

[19] V. Stubičan, R. Roy, Isomorphous substitution and infra-red spectra of the layer lattice silicates, Am. Mineral. J. Earth Planet. Mater. 46 (1961) 32–51.

[20] F. Altaf, R. Batool, R. Gill, Z.U. Rehman, H. Majeed, A. Ahmad, M. Shafiq, D. Dastan, G. Abbas, K. Jacob, Synthesis and electrochemical investigations of ABPBI grafted

montmorillonite based polymer electrolyte membranes for PEMFC applications, Renew. Energy. 164 (2021) 709–728. doi:10.1016/J.RENENE.2020.09.104.

[21] S.B. Mishra, t-Y. tsai, S.S. Hwang, A.K. Mishra, Melt processing of polypropylene-grafted-maleic anhydride/chitosan polymer blend functionalized with montmorillonite for the removal of lead ions from aqueous solutions, (n.d.). doi:10.1038/s41598-019-57079-2.

[22] G.W. Brindley, B.G. Editors, C. Structures, Reviews, (1981) 1981.

[23] D. Tunega, M.H. Gerzabek, H. Lischka, Ab Initio Molecular Dynamics Study of a Monomolecular Water Layer on Octahedral and Tetrahedral Kaolinite Surfaces, J. Phys. Chem. B. 108 (2004) 5930–5936. doi:10.1021/jp037121g.

[24] M.D.A. Bolland, A.M. Posner, J.P. Quirk, Surface charge on kaolinites in aqueous suspension, Soil Res. 14 (1976) 197–216.

[25] P. V. Brady, R.T. Cygan, K.L. Nagy, Molecular controls on kaolinite surface charge, J. Colloid Interface Sci. 183 (1996) 356–364. doi:10.1006/jcis.1996.0557.

[26] F. Bergaya, B.K.G. Theng, G. Lagaly, Handbook of Clay Science, Elsevier Ltd, Amsterdam, 2006. doi:10.1016/S1572-4352(05)01002-0.

[27] B.K.G. Theng, Formation and Properties of Clay-Polymer Complexes, Vol. 4, Elsevier, 2012. doi:10.1016/B978-0-444-53354-8.00014-1.

[28] Y. Hao, L. Yuan, P. Li, W. Zhao, D. Li, D. Lu, Molecular Simulations of Methane Adsorption Behavior in Illite Nanopores Considering Basal and Edge Surfaces, Energy and Fuels. 32 (2018). doi:10.1021/acs.energyfuels.8b00070.

[29] J.N. Israelachvili, Intermolecular and Surface Forces, third ed., Elsevier Inc., 2011. doi:10.1016/C2011-0-05119-0.

[30] C. Tournassat, J.A. Davis, C. Chiaberge, S. Grangeon, I.C. Bourg, Modeling the acid-base

properties of montmorillonite edge surfaces, Environ. Sci. Technol. 50 (2016) 13436–13445. doi:10.1021/acs.est.6b04677.

[31] H. Zhao, S. Bhattacharjee, R. Chow, D. Wallace, J.H. Masliyah, Z. Xu, Probing surface charge potentials of clay basal planes and edges by direct force measurements, Langmuir. 24 (2008) 12899–12910. doi:10.1021/la802112h.

[32] L. Zhang, X. Lu, X. Liu, K. Yang, H. Zhou, Surface Wettability of Basal Surfaces of Clay Minerals: Insights from Molecular Dynamics Simulation, Energy and Fuels. 30 (2016) 149–160. doi:10.1021/acs.energyfuels.5b02142.

[33] J. Liu, Z. Zhou, Z. Xu, J. Masliyah, Bitumen-clay interactions in aqueous media studied by zeta potential distribution measurement, J. Colloid Interface Sci. 252 (2002) 409–418. doi:10.1006/jcis.2002.8471.

[34] I.C. Bourg, G. Sposito, A.C.M. Bourg, Modeling the acid-base surface chemistry of montmorillonite, J. Colloid Interface Sci. 312 (2007) 297–310. doi:10.1016/j.jcis.2007.03.062.

[35] A. Saada, B. Siffert, E. Papirer, Comparison of the Hydropholicity/Hydrophobicity of Illites and Kaolinites, J. Colloid Interface Sci. 174 (1995) 185–190.

[36] T. Robert, S.M. Mercer, T.J. Clark, B.E. Mariampillai, P. Champagne, M.F. Cunningham, P.G. Jessop, Nitrogen-containing polymers as potent ionogens for aqueous solutions of switchable ionic strength: application to separation of organic liquids and clay particles from water, Green Chem. 14 (2012) 3053. doi:10.1039/c2gc36074h.

[37] S.P. Gumfekar, T.R. Rooney, R.A. Hutchinson, J.B.P. Soares, Dewatering Oil Sands Tailings with Degradable Polymer Flocculants, ACS Appl. Mater. Interfaces. 9 (2017) 36290–36300. doi:10.1021/acsami.7b10302.

[38] V. Vajihinejad, R. Guillermo, J.B.P. Soares, Dewatering Oil Sands Mature Fine Tailings (MFTs) with Poly(acrylamide-co-diallyldimethylammonium chloride): Effect of Average Molecular Weight and Copolymer Composition, Ind. Eng. Chem. Res. 56 (2017) 1256–1266. doi:10.1021/acs.iecr.6b04348.

[39] L. Pennetta de Oliveira, S.P. Gumfekar, F. Lopes Motta, J.B.P. Soares, Dewatering of Oil Sands Tailings with Novel Chitosan-Based Flocculants, Energy & Fuels. (2018) acs.energyfuels.7b03634. doi:10.1021/acs.energyfuels.7b03634.

[40] H. Li, J. Long, Z. Xu, J.H. Masliyah, Synergetic role of polymer flocculant in low-temperature bitumen extraction and tailings treatment, Energy and Fuels. 19 (2005) 936–943. doi:10.1021/ef049744e.

[41] H. Lu, L. Xiang, X. Cui, J. Liu, Y. Wang, R. Narain, H. Zeng, Molecular Weight Dependence of Synthetic Glycopolymers on Flocculation and Dewatering of Fine Particles, Langmuir. 32 (2016) 11615–11622. doi:10.1021/acs.langmuir.6b03072.

[42] D. Zhang, T. Thundat, R. Narain, Flocculation and dewatering of mature fine tailings using temperature-responsive cationic polymers, Langmuir. 33 (2017) 5900–5909. doi:10.1021/acs.langmuir.7b01160.

[43] J.F. Zhang, Q.H. Zhang, J.P.Y. Maa, Coagulation processes of kaolinite and montmorillonite in calm, saline water, Estuar. Coast. Shelf Sci. 202 (2018) 18–29. doi:10.1016/j.ecss.2017.12.002.

[44] C.J. van Oss, Development and applications of the interfacial tension between water and organic or biological surfaces, Colloids Surfaces B Biointerfaces. 54 (2007) 2–9. doi:10.1016/j.colsurfb.2006.05.024.

[45] W.H. McAnally, Aggregation and deposition of estuarial fine sediment, Engineer research

and development center vicksburg ms coastal and hydraulicslab, 2000. doi:No. ERDC/CHL-TR-00-8.

[46] S. Asakura, F. Oosawa, On interaction between two bodies immersed in a solution of macromolecules, J. Chem. Phys. 22 (1954) 1255–1256. doi:10.1063/1.1740347.

[47] S. Asakura, F. Oosawa, Interaction between particles suspended in solutions of macromolecules, J. Polym. Sci. 33 (1958) 183–192. doi:10.1002/pol.1958.1203312618.

[48] C. Wang, C. Han, Z. Lin, J. Masliyah, Q. Liu, Z. Xu, Role of Preconditioning Cationic Zetag Flocculant in Enhancing Mature Fine Tailings Flocculation, Energy and Fuels. 30 (2016) 5223–5231. doi:10.1021/acs.energyfuels.6b00108.

[49] Q. Lu, B. Yan, L. Xie, J. Huang, Y. Liu, H. Zeng, A two-step flocculation process on oil sands tailings treatment using oppositely charged polymer flocculants, Sci. Total Environ. 565 (2016) 369–375. doi:10.1016/j.scitotenv.2016.04.192.

[50] E.R. Graber, U. Mingelgrin, Clay Swelling and Regular Solution Theory, Environ. Sci. Technol. 28 (1994) 2360–2365. doi:10.1021/es00062a021.

[51] D.M.C. MacEwan, Adsorption by montmorillonite, and its relation to surface adsorption, Nature. (1948) 439–440. doi:10.1038/162680a0.

[52] Y. Ji, Q. Lu, Q. Liu, H. Zeng, Effect of solution salinity on settling of mineral tailings by polymer flocculants, Colloids Surfaces A Physicochem. Eng. Asp. 430 (2013) 29–38. doi:10.1016/j.colsurfa.2013.04.006.

[53] Y. Zhu, X. Tan, Q. Liu, Dual polymer flocculants for mature fine tailings dewatering, Can. J. Chem. Eng. 95 (2017) 3–10. doi:10.1002/cjce.22628.

[54] L. Besra, D.K. Sengupta, S.K. Roy, P. Ay, Polymer adsorption: Its correlation with flocculation and dewatering of kaolin suspension in the presence and absence of surfactants,

Int. J. Miner. Process. 66 (2002) 183–202. doi:10.1016/S0301-7516(02)00064-9.

[55] R. Zhu, Q. Liu, Z. Xu, J.H. Masliyah, A. Khan, Role of dissolving carbon dioxide in densification of oil sands tailings, Energy and Fuels. 25 (2011) 2049–2057. doi:10.1021/ef200203f.

[56] A. Sworska, J.S. Laskowski, G. Cymerman, Flocculation of the Syncrude fine tailings Part I. Effect of pH, polymer dosage and Mg^{2+} and Ca^{2+} cations, Int. J. Miner. Process. 60 (2000) 143–152. doi:10.1016/S0301-7516(00)00012-0.

[57] A. Jada, H. Debih, M. Khodja, Montmorillonite surface properties modifications by asphaltenes adsorption, J. Pet. Sci. Eng. 52 (2006) 305–316. doi:10.1016/j.petrol.2006.03.016.

[58] G. Gu, Z. Zhou, Z. Xu, J.H. Masliyah, Role of fine kaolinite clay in toluene-diluted bitumen / water emulsion, 215 (2003) 141–153.

[59] E.S.P.B. V, V.B. Menon, D.T. Wasan, Particle-fluid interactions with application to solidstabilized emulsions, 19 (1986) 89–105.

[60] G.A.P. James, Robert O., Characterization of aqueous colloids by their electrical double-layer and intrinsic surface chemical properties., Springer US, Boston, MA, 1982.

[61] H. Vali, L. Bachmann, Ultrastructure and flow behavior of colloidal smectite dispersions, J. Colloid Interface Sci. 126 (1988) 278–291. doi:10.1016/0021-9797(88)90122-1.

[62] H. Van Olphen, Introduction to Clay Colloid Chemistry, Interscience, New York, 1963.

[63] M.S. Nasser, A.E. James, Numerical simulation of the continuous thickening of flocculated kaolinite suspensions, Int. J. Miner. Process. 84 (2007) 144–156. doi:10.1016/j.minpro.2007.05.005.

[64] K.A. Landman, L.R. White, Solid/liquid separation of flocculated suspensions, Adv.

Colloid Interface Sci. 51 (1994) 175–246. doi:10.1016/0001-8686(94)80036-7.

[65] A. Hasan, P. Fatehi, Separation and Purification Technology Cationic kraft lignin-acrylamide as a flocculant for clay suspensions : 1 . Molecular weight effect, 207 (2018) 213–221. doi:10.1016/j.seppur.2018.06.047.

[66] N. Tekin, Ö. Demirbaş, M. Alkan, Adsorption of cationic polyacrylamide onto kaolinite, Microporous Mesoporous Mater. 85 (2005) 340–350. doi:10.1016/j.micromeso.2005.07.004.

[67] H. Huang, H. Zhang, D. Han, Ferrocene addition for suppression of hydrogen sulfide formation during thermal recovery of oil sand bitumen, Energy. 230 (2021) 120744. doi:10.1016/J.ENERGY.2021.120744.

[68] G. Yang, T. Chen, J. Zhao, D. Yu, F. Liu, D. Wang, M. Fan, W. Chen, J. Zhang, H. Yang, J. Wang, Desorption Mechanism of Asphaltenes in the Presence of Electrolyte and the Extended Derjaguin-Landau-Verwey-Overbeek Theory, Energy and Fuels. 29 (2015) 4272–4280. doi:10.1021/acs.energyfuels.5b00866.

[69] A. Govedarica, E.J. Molina Bacca, M. Trifkovic, Structural investigation of tailings flocculation and consolidation via quantitative 3D dual fluorescence/reflectance confocal microscopy, J. Colloid Interface Sci. 571 (2020) 194–204. doi:10.1016/J.JCIS.2020.02.098.

[70] M.H. Gorakhki, C.A. Bareither, Salinity effects on sedimentation behavior of kaolin, bentonite, and soda ash mine tailings, Appl. Clay Sci. 114 (2015) 593–602. doi:10.1016/j.clay.2015.07.018.

[71] D.M. Grewer, R.F. Young, R.M. Whittal, P.M. Fedorak, Naphthenic acids and other acid-extractables in water samples from Alberta: What is being measured?, Sci. Total Environ. 408 (2010) 5997–6010. doi:10.1016/j.scitotenv.2010.08.013.

[72] R.G.P. Andedward, L.Y.N. Lewis, The Practical Salinity Scale 1978 : Fitting the Data, (1980).

[73] U.G. WHITEHOUSE, L.M. JEFFREY, J.D. DEBBRECHT, Differential Settling Tendencies of Clay Minerals in Saline Waters, Pergamon Press, 2013. doi:10.1016/B978-0-08-009235-5.50006-1.

[74] J. Long, H. Li, Z. Xu, J.H. Masliyah, Role of colloidal interactions in oil sand tailings treatment, AIChE J. 52 (2006) 371–383. doi:10.1002/aic.10603.

[75] R. Sivasubramanian, G. hao Chen, H.R. Mackey, The effectiveness of divalent cation addition for highly saline activated sludge cultures: Influence of monovalent/divalent ratio and specific cations, Chemosphere. 274 (2021) 129864. doi:10.1016/J.CHEMOSPHERE.2021.129864.

[76] F.F. Peng, P. Di, Effect of multivalent salts-calcium and aluminum on the flocculation of kaolin suspension with anionic polyacrylamide, J. Colloid Interface Sci. 164 (1994) 229–237. doi:10.1006/jcis.1994.1161.

[77] R.S. Kaarmukhilnilavan, A. Selvam, J.W.C. Wong, K. Murugesan, Ca^{2+} dependent flocculation efficiency of avian egg protein revealed unique surface specific interaction with kaolin particles: A new perception in bioflocculant research, Colloids Surfaces A Physicochem. Eng. Asp. 603 (2020) 125177. doi:10.1016/J.COLSURFA.2020.125177.

[78] A. Okada, A. Usuki, The chemistry of polymer-clay hybrids, Mater. Sci. Eng. C. 3 (1995) 109–115. doi:10.1016/0928-4931(95)00110-7.

[79] T.S.L. Maravilha, A. Middea, L.S. Spinelli, E.F. Lucas, Reduction of asphaltenes adsorbed on kaolinite by polymers based on cardanol, Brazilian J. Chem. Eng. 38 (2021) 155–163. doi:10.1007/s43153-020-00082-2.

[80] S.T. Dubey, M.H. Waxman, Asphaltene adsorption and desorption from mineral surfaces, SPE Reserv. Eng. (Society Pet. Eng. 6 (1991) 389–395. doi:10.2118/18462-PA.

[81] J. Don Scott, M.B. Dusseault, W. David Carrier, Behaviour of the clay/bitumen/water sludge system from oil sands extraction plants, Appl. Clay Sci. 1 (1985) 207–218. doi:10.1016/0169-1317(85)90574-5.

[82] A. Pourmohammadbagher, J.M. Shaw, Probing the Impact of Asphaltene Contamination on Kaolinite and Illite Clay Behaviors in Water and Organic Solvents: A Calorimetric Study, Energy and Fuels. 30 (2016) 6561–6569. doi:10.1021/acs.energyfuels.6b00646.

[83] A. Majid, B.D. Sparks, J.A. Ripmeester, Characterization of solvent-insoluble organic matter isolated from Alberta oil sands, Fuel. 70 (1991) 78–83. doi:10.1016/0016-2361(91)90098-U.

[84] B.J. Marlow, G.C. Sresty, R.D. Hughes, O.P. Mahajan, Colloidal stabilization of clays by asphaltenes in hydrocarbon media, Colloids and Surfaces. 24 (1987) 283–297. doi:10.1016/0166-6622(87)80235-4.

[85] J. Long, Z. Xu, J.H. Masliyah, Adhesion of single polyelectrolyte molecules on silica, mica, and bitumen surfaces, Langmuir. 22 (2006) 1652–1659. doi:10.1021/la052757f.

Chapter 2. Simulation Methodology

2.1. Ensemble Average and Time average

Molecular dynamics (MD) is a methodology that provides solutions to N-body problems in a system by solving Newton's equations of motion [1]. In microscopic world, the behaviors of a particle are ultimately determined by quantum mechanics, and the situation can be complicated due to the ill-defined existence of the particle, e.g., it can exist in many states simultaneously. However, a great number of the behaviors of a particle in its many states can be understood with classical terms, and thus a system consisting of particles can be simplified into a classical N-body system [1]. The task of MD is to find the numerical solutions to N-body problems at microscopic scale, empowered by the digital computers.

The ability of MD to observe every particle in the system has distinguished itself from many other forms of computation. The microscopic system consisting of moving particles can be connected to macroscopic thermodynamic properties via statistical mechanics. Ensemble is a concept in statistical mechanics, which is a set of replicas of the same system in different microscopic states but with identical macroscopic or thermodynamic state [2]. Natural MD simulations by directly integrating Newton's equations of motion correspond to microcanonical ensemble (NVE), whose thermodynamic state is characterized by particle number (N), system volume (V) and total energy (E). When constant temperature is also required, the MD equilibrium corresponds to canonical ensemble (NVT); and likewise, the isobaric-isothermal ensemble (NPT) is for fixed temperature and pressure.

Statistical mechanics usually deals with ensemble average that can be compared with the macroscopic property observed in experiments. An ensemble average is taken over the replicas of the system, for instance, in the canonical ensemble:

$$\langle A \rangle_{ensemble} = \frac{\iint A e^{-\frac{H}{k_B T}} d\boldsymbol{p}_1 \ldots d\boldsymbol{p}_N d\boldsymbol{r}_1 \ldots d\boldsymbol{r}_N}{\iint e^{-\frac{H}{k_B T}} d\boldsymbol{p}_1 \ldots d\boldsymbol{p}_N d\boldsymbol{r}_1 \ldots d\boldsymbol{r}_N} \tag{2.1}$$

where H is the Hamiltonian energy, $\boldsymbol{p}$ is momentum of an atom, $\boldsymbol{r}$ is the location of an atom, $k_B T$ is the thermal energy, and A is the targeted quality. The integral in the ensemble average is extremely difficult to calculate due to the difficulty to capture all the possible states over the entire phase space. In an MD simulation, time average is performed:

$$\langle A \rangle_{time} = \lim_{\tau \to \infty} \frac{1}{\tau} \int_{t=0}^{\tau} A(t) dt \approx \frac{1}{M} \sum_{t=1}^{M} A \tag{2.2}$$

where τ is the simulated time, M is the number of time steps, and $A(t)$ is the instantaneous value of A. The time average is easier to obtain in MD simulations, but ensemble average is the one needed for comparison with experiments. The connection of the two averages is resolved by the ergodic hypothesis [3], the most fundamental axiom of MD, in which the time average is considered an approximation of ensemble average if the MD is run long enough so that the system effectively explores all possible states. Thus, MD simulations should be run for a sufficient long time to ensure successful sampling.

2.2. Interaction Functions

The microscopic systems in MD simulations consist of spherical particles interacting with each other, and the resolution of the particles represents atoms in all-atom MD simulations. Pairwise potentials are typically assumed between two atoms, which should be able to capture the repulsion when the atoms are at a close range and attraction when they are separated at a moderate distance [1]. For example, in the Lennard-Jones potential expressed as:

$$u_{LJ}(r_{ij}) = 4\epsilon_{ij}\left(\left(\frac{\sigma_{ij}}{r_{ij}}\right)^{12} - \left(\frac{\sigma_{ij}}{r_{ij}}\right)^{6}\right) \tag{2.3}$$

r_{ij} is the distance between the ith and jth atoms, ϵ_{ij} is the depth of the potential well governing the strength of the interaction between the two atoms, and σ_{ij} is a length scale representing the distance at which the potential is zero. The interaction is thus repulsive at close range and attractive when the separation increases. When dealing with charged particles, coulombic interaction between two atoms should be included, which is in the form of:

$$u_{coul}(r_{ij}) = \frac{q_i q_j}{4\pi\varepsilon_0\varepsilon_r r_{ij}} \tag{2.4}$$

where q represents the atomic charge, ε_0 and ε_r are respectively the permittivity of vacuum and dielectric constant of the medium. The Lennard-Jones and coulombic potentials are called non-bonded potentials, as they are used to describe interactions between atoms that are not connected by covalent bonds. It is worth mentioning that other forms of functions can also be employed to describe these non-bonded interactions.

Besides the non-bonded interactions, bonded interactions are also required to describe the conformation of covalent bonds between atoms [4]. They are not exclusively pair potentials, but also many-body potentials. Potentials for bond length, bond angle, and dihedral angle define 2-body, 3-body, and 4-body interactions, respectively. Example forms in modeling the bond length [5], bond angle [5], and dihedral angle [6] are:

$$u_b(r_{ij}) = \frac{1}{2}k_{ij}^{b}(r_{ij} - r_{ij}^{0})^2 \tag{2.5}$$

where k_{ij}^{b} is the harmonic force constant for bond stretching and r_{ij}^{0} is the equilibrium bond length.

$$u_a\left(\theta_{ijk}\right) = \frac{1}{2} k_{ijk}^{\theta}\left(\theta_{ijk} - \theta_{ijk}^{0}\right)^2 \tag{2.6}$$

where k_{ijk}^{θ} is the harmonic force constant for bond angle, θ_{ijk} is the angle formed by the ith, jth and kth atoms, and θ_{ijk}^{0} is the equilibrium angle.

$$u_d(\varphi_{ijkl}) = k_{\varphi}[(1 + \cos(\delta_n)(m_n\varphi_n)] \tag{2.7}$$

Where k_{φ} is the force constant, δ_n is the phase shift, m_n is the multiplicity of the dihedral angle and φ_n is the dihedral angle formed between the plane formed by the ith, jth, kth atoms and the plane formed by the jth, kth, and lth atoms.

In classical MD, the total potential energy is the sum of all the non-bonded and bonded interactions, i.e.

$$U = \sum_{pairs\ i,j} u_{LJ}\left(r_{ij}\right) + \sum_{pairs\ i,j} u_{coul}\left(r_{ij}\right) + \sum_{pairs\ i,j} u_b\left(r_{ij}\right) + \sum_{angles\ i,j,k} u_a\left(\theta_{ijk}\right) + \sum_{diehedrals\ i,j,k,l} u_d\left(\varphi_{ijkl}\right) \tag{2.8}$$

The expression for U here is one example for the potential function of a system. In MD simulations, the information of potential functions is provided by the so-called "force field". For example, CLAYFF force field [7] is employed in this thesis to describe the interactions between atoms in the clay minerals. In the development of the CLAYFF force field, except for the hydroxyls, all the atoms in the clay minerals are treated as ions in aqueous solution, and thus only the parameters for non-bonded interactions are fitted. As a result, the potential energy modeled in CLAYFF force field is comprised of Lennard-Jones and coulomb interactions for all atoms, and bond stretching terms only for hydroxyls.

2.3. Equations of Motion

In typical MD, given the potential function U, the force on the ith atom can be calculated by [8]:

$$F = -\nabla_{\boldsymbol{r}_i} U \tag{2.9}$$

where $\boldsymbol{r}_i$ is the position vector of the *i*th atom. The equations of motion [8] are:

$$m_i \frac{d^2 r_i}{dt^2} = \boldsymbol{F}_i \qquad \boldsymbol{v}_i = \frac{d\boldsymbol{r}_i}{dt} \qquad \boldsymbol{a}_i = \frac{d\boldsymbol{v}_i}{dt} \tag{2.10}$$

The motion of all particles can be obtained after the integration of the Newtonian equations of motions. In this project, the MD simulations were mainly integrated by the leap-frog algorithm [9]. A simple expression is given below without the consideration of temperature and pressure coupling:

$$\boldsymbol{v}_i\left(t + \frac{1}{2}\Delta t\right) = \boldsymbol{v}_i\left(t - \frac{1}{2}\Delta t\right) + \frac{\boldsymbol{F}_i(t)}{m_i}\Delta t \tag{2.11}$$

$$\boldsymbol{r}_i(t + \Delta t) = \boldsymbol{r}_i(t) + \boldsymbol{v}_i\left(t + \frac{1}{2}\Delta t\right) \cdot \Delta t \tag{2.12}$$

The position and velocities are updated based on the force calculated at time *t*, position at time *t*, and velocity at time $t - \frac{1}{2}\Delta t$. The starting points in each time step for the velocity and position are $\frac{1}{2}\Delta t$ behind each other, similar to leaping frogs, thus the name.

2.4. Radial Distribution Function

Equilibrium properties of a system can be obtained from the pair correlation function or radial distribution function (RDF), such as structure and pressure. The pair correlation function describes the probability of finding a pair of atoms separated by a distance of *r* within a medium. Suppose the bulk number density is *ρ*, and the total number of particles is *N*. In the canonical ensemble, the pair correlation function is expressed as [10]:

$$g(r_1, r_2) = \frac{N(N-1)\int e^{-\frac{U(r)}{k_B T}} d\boldsymbol{r}_3 \ldots d\boldsymbol{r}_N}{\rho^2 \int e^{-\frac{U(r)}{k_B T}} d\boldsymbol{r}_1 \ldots d\boldsymbol{r}_N} \tag{2.13}$$

where the integral in the dominator is the configurational partition function, and the one in the numerator excludes $\boldsymbol{r}_1$ and $\boldsymbol{r}_2$. In an isotropic and homogeneous system, the equation reduces to summation over all atom pairs [1]:

$$g(\boldsymbol{r}) = \frac{V}{N^2}\sum_{i=1}\sum_{j=i}\delta\left(\boldsymbol{r} - \boldsymbol{r}_{ij}\right) \tag{2.14}$$

RDF gives the information of local organization around any given atoms. The delta function gives a zero when $\boldsymbol{r} \neq \boldsymbol{r}_{ij}$. In the practical calculation with a computer program, the delta function is usually replaced by a function over a small but finite range of separations, all pairs within this range will counted towards the summation.

2.5. Potential of Mean Force

The free energy difference between different states is important in understanding the driving force in MD simulations. The free energy difference between two states can be calculated by gradually modifying the initial state to the final state [11]. A more general way is to create the profile of free energy change along a predefined “reaction coordinate”. Reaction coordinate is a continuous parameter which provides a distinction between two thermodynamics states. It could be one or more dimensional, and often refers to geometric variables such as separation distance between two molecules, torsion of a residue, etc. [12].

In a canonical ensemble, the Helmholtz free energy F is expressed as

$$F = -k_B T \cdot \ln(Z_{\mathrm{can}}) \tag{2.15}$$

where Z_{can} is the configurational partition function in the form of:

$$Z_{\mathrm{can}} = \int e^{-\frac{U(r)}{k_B T}}\, d\boldsymbol{r} \tag{2.16}$$

where U is potential energy of the system, k_B is Boltzmann constant, and T is absolute temperature. As discussed in section 2.1, the integral over the entire phase space to obtain the partition function is not practical. Hence the free energy needs to be calculated otherwise. Defining a reaction coordinate as x, the probability distribution of the system along x is [13]:

$$P(x) = \frac{\int \delta(x - x(\boldsymbol{r})) e^{-\frac{U(\boldsymbol{r})}{k_B T}} d\boldsymbol{r}}{\int e^{-\frac{U(\boldsymbol{r})}{k_B T}} d\boldsymbol{r}} \tag{2.17}$$

where the delta function $\delta\big(x - x(\boldsymbol{r})\big)$ returns zero when $x \neq x(\boldsymbol{r})$. Analogous to Equations (2.15) and (2.16), a potential $W(x)$ can be obtained from $P(x)$ via:

$$W(x) = -k_B T \ln P\,(x) \tag{2.18}$$

$W(x)$ is the so-called "potential of mean force (PMF)", i.e., it is a potential whose negative gradient is a mean force when the reaction coordinate is at x.

As seen from Equation (2.7), when sampling over the configurational space, the probability for finding the states with high potential energy is low. The system prefers to stay in the states with low potential energy. Therefore, $W(x)$ tends to be separated by high potential energy peaks (energy barriers) into multiple parts. If the energy barrier is sufficiently high, the sampling process can be restricted to certain regions of the reaction coordinate. Configurations in other regions are thus inaccessible, resulting in poor sampling.

2.5.1. Umbrella Sampling

The umbrella sampling method is introduced to resolve the poor sampling problem caused by standard sampling, developed by Torrie and Valleau [14]. An additional biasing potential is applied to overcome the effect of energy barrier. Efficient sampling by a series of windows along the reaction coordinate is thus guaranteed. The effect of the biasing potential that connects multiple separated regions in the phase space gives rise to the name of umbrella sampling.

Suppose *s* simulations for the system are subjected to the biasing potential $U_{b,i}(\boldsymbol{r})$, where *i* is the simulation number ($i = 1,2,3......s$), and $U_{b,i}(\boldsymbol{r})$ depends on $\boldsymbol{r}$ through *x*. The potential energy $U_i(\boldsymbol{r})$ of a biased system in one simulation is given as:

$$U_i(\boldsymbol{r}) = U_0(\boldsymbol{r}) + U_{b,i}(\boldsymbol{r}) \tag{2.19}$$

where $U_0(\boldsymbol{r})$ is the potential energy of the unbiased system. Split the path along *x* from the initial state to the final state into *j* windows in each simulation, x_j is the value of the reaction coordinate *x* at the center of the *j* th window. The probability density for the *j*th window in the *i*th simulation is:

$$P_{ij} = \frac{\int \delta(x-x_j) e^{-\frac{U_i(r)}{k_BT}} d\boldsymbol{r}}{\int e^{-\frac{U_i(r)}{k_BT}} d\boldsymbol{r}} = \frac{\int \delta(x-x_j) e^{-\frac{U_0+U_{b,i}(r)}{k_BT}} d\boldsymbol{r}}{\int e^{-\frac{U_i(r)}{k_BT}} d\boldsymbol{r}} \tag{2.20}$$

Because the biasing potential $U_{b,i}(\boldsymbol{r})$ depends only on *x*, the equation can be further written as:

$$P_{ij} = \frac{e^{-\frac{U_{b,i}(x_j)}{k_BT}} \int \delta(x-x_j) e^{-\frac{U_0}{k_BT}} d\boldsymbol{r}}{\int e^{-\frac{U_i(r)}{k_BT}} d\boldsymbol{r}} = \frac{e^{-\frac{U_{b,i}(x_j)}{k_BT}} P_j^0 Z_0}{\int e^{-\frac{U_i(r)}{k_BT}} d\boldsymbol{r}} = \frac{Z_0}{Z_i} e^{-\frac{U_{b,i}(x_j)}{k_BT}} P_j^0 \tag{2.21}$$

$$Z_0 = \int e^{-\frac{U_0(r)}{k_BT}} d\boldsymbol{r} \tag{2.22}$$

$$Z_i = \int e^{-\frac{U_i(r)}{k_BT}} d\boldsymbol{r} \tag{2.23}$$

where Z_0 gives the configurational partition function for canonical ensemble; Z_i is the configurational partition function for the *i*th simulation of the biased system. Substituting Equation (2.21) into Equation (2.15) yields

$$F_0 - F_i = k_BT\, ln \frac{Z_i}{Z_0} = k_BT\, ln \left[\frac{P_j^0}{P_{ij}} e^{-\frac{U_{b,i}(x_j)}{k_BT}}\right] = W_{ij} - W_j^0 - U_{b,i}(x_j) \tag{2.24}$$

where F_0 is the free energy of the unbiased system, F_i is free energy of the biased system in the *i*th simulation, W_j^0 is the PMF of the unbiased system in *j*th window and W_{ij} is the PMF in the *j*th window of the *i*th simulation. Defining $f_i = \frac{Z_0}{Z_i}$, Equation (2.24) can be written as [13]:

$$\Delta F_i = k_B T \ln f^{-1} = k_B T \ln \frac{\int e^{-\frac{U_i(r)}{k_B T}} dr}{\int e^{-\frac{U_0(r)}{k_B T}} dr} = k_B T \ln \frac{\int e^{-\frac{U_0}{k_B T}} \cdot e^{-\frac{U_{b,i}(r)}{k_B T}} dr}{\int e^{-\frac{U_0(r)}{k_B T}} dr} = k_B T \ln \left\langle e^{-\frac{U_{b,i}(r)}{k_B T}} \right\rangle \qquad (2.25)$$

Figure 2.1 provides an illustration of umbrella sampling. The solid curve in the upper part is the unbiased free energy. The path of reaction coordination is divided into several windows. The probability distribution for one window in one simulation is represented by one histogram in the bottom figure.

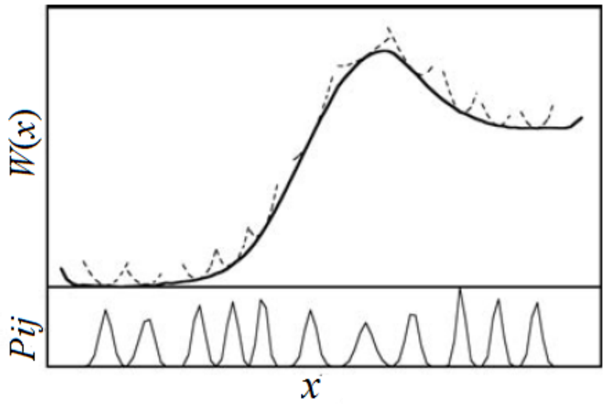

Figure 2.1. Global free energy (solid curve) and the contributions for some of the windows. At the bottom, the biased distribution of P_{ij} is obtained by using umbrella sampling, adapted from Kastner. J [15].

2.5.2. Weighted Histogram Analysis Method

The weighted histogram analysis method (WHAM) [12] was developed to calculate the PMF from the sampled results. An optimized weighting factor is assigned to each of the simulation so that the statistical error is minimized when estimating the unbiased distribution from the sampled data. The advantage of WHAM compared with other methods is that it utilizes all the information from umbrella sampling simulation which reduces the statistical errors. The WHAM method requires enough overlaps in the probability distribution along the reaction coordinate to ensure the accuracy.

Equation (2.21) indicates that theoretically P_j^0 calculated from P_{ij} should be the same for all biasing potential $U_{b,i}$ in each simulation. However, statistical errors will affect the practical calculations. The variance of P_j^0 is thus needed to be minimized by increasing the number of simulations. Introducing

$$\Omega_{ij} = P_{ij}\frac{Z_i}{Z_0}e^{\frac{U_{b,i}(x_j)}{k_BT}} \tag{2.26}$$

which gives the unbiased probability of the *j*th window calculated from the *i*th simulation. The average of Ω_{ij} from all the *s* simulations should give a more realistic unbiased probability distribution P_j^0. Thus,

$$P_j^0 = \left\langle P_{ij}\frac{Z_i}{Z_0}e^{\frac{U_{b,i}(x_j)}{k_BT}} \right\rangle = \langle \Omega_{ij} \rangle \tag{2.27}$$

To calculate P_j^0 from Ω_{ij} statistically,

$$P_j^0 = \sum_{i=1}^{s} w_i\,\Omega_{ij} \tag{2.28}$$

where w_i is the weighting factor for each simulation, and $\sum_{i=1}^{s} w_i = 1$. The variance of P_j^0 can be minimized through the determination of w_i, which is shown in Appendix A. In the end, P_j^0 is expressed as:

$$P_j^0 = \frac{\sum_{i=1}^{s} n_{ij}}{\sum_{i=1}^{s} N_i e^{-\frac{U_{b,i}(x_j)}{k_BT}} e^{-\frac{\Delta F_i}{k_BT}}} \tag{2.29}$$

where n_{ij} is the number of counts in the *j*th windows of the *i*th simulation, and N_i is the total number of counts for the *i*th simulation in the sampling process. To perform this calculation, an arbitrary initial value of f_i or ΔF_i is usually assumed and used to calculate P_j^0. The value of the calculated P_j^0 is used to obtain another value for f_i and these iterations continue until self-consistency is reached.

References

[1] D.C. Rapaport, The art of molecular dynamics simulation, Cambridge university press, 2004.

[2] R.C. Tolman, The principles of statistical mechanics, Courier Corporation, 1979.

[3] C.R. de Oliveira, T. Werlang, Ergodic hypothesis in classical statistical mechanics, Rev. Bras. Ensino Física. 189–201 (2007).

[4] M. Karplus, G.A. Petsko, Molecular dynamics simulations in biology, 1990.

[5] W.L. Jorgensen, D.S. Maxwell, J. Tirado-Rives, Development and testing of the OPLS all-atom force field on conformational energetics and properties of organic liquids, J. Am. Chem. Soc. 118 (1996) 11225–11236.

[6] C. Oostenbrink, A. Villa, A.E. Mark, W.F. Van Gunsteren, A biomolecular force field based on the free enthalpy of hydration and solvation: The GROMOS force-field parameter sets 53A5 and 53A6, J. Comput. Chem. 25 (2004) 1656–1676.

[7] R.T. Cygan, J.J. Liang, A.G. Kalinichev, Molecular models of hydroxide, oxyhydroxide, and clay phases and the development of a general force field, J. Phys. Chem. B. 108 (2004) 1255–1266.

[8] J.P. Ryckaert, G. Ciccotti, H.J.C. Berendsen, Numerical integration of the cartesian equations of motion of a system with constraints: molecular dynamics of n-alkanes, J. Comput. Phys. 23 (1977) 327–341.

[9] R.. Hockney, S.. Goel, J.. Eastwood, Quiet high-resolution computer models of a plasma, J.

Comput. Phys. 14 (1974) 148–158.

[10] R. Schneider, A.R. Sharma, A. Rai, Introduction to Molecular Dynamics, in: 2008: pp. 3–40.

[11] X. Kong, C.L. Brooks, λ-dynamics: A new approach to free energy calculations, J. Chem. Phys. 105 (1996) 2414–2423.

[12] Kumar, S., Rosenberg, J. M., Bouzida, D., Swendsen, R. H., Kollman, P. A., 1992. The Weighted Histogram Analysis Method for Free-Energy Calculations on Biomolecules. I. The Method. Journal of computational chemistry, 13(8), 1011-1021.

[13] S. Bagai, C. Sun, T. Tang, Potential of Mean Force of Polyethylenimine-Mediated DNA Attraction, (2012).

[14] G.M.Torrie, J.P.Valleau, Nonphysical sampling distributions in Monte Carlo free-energy estimation: Umbrella sampling, J. Comput. Phys. 23 (1977) 187–199.

[15] Johannes K, Umbrella sampling, Wiley Interdisciplinary Reviews: Computational Molecular Science 1.6 (2011): 932-942.

Chapter 3. Synergetic Adsorption of Polymers on Montmorillonite: Insights from Molecular Dynamics Simulations

3.1. Introduction

Removing fine particles and recycling water from industrial wastewater especially tailings have become an urgent need in the past decades [1]. After the coarse fraction of tailings segregated, a gel-like dispersion could form with very slow rate of consolidation [2], which made the removal of fine particles very difficult. As a result, the tailings required long-term storage structures causing huge wasteland [3]. The slow dewatering of industrial tailings, continuous exploitation of natural resources, and growing industrial manufacturing led to global shortage of clean water and lands [3,4]. Consequently, environmental impacts brought by the fine particles have been gaining more attention in recent years [4,5].

The fine particles in mineral tailings are mainly clay minerals such as kaolinite, illite, and montmorillonite (Mt) [1,6,7]. It was found that basal surfaces of the clay minerals often carried permanent negative charges, while the protonation of hydroxyl groups made the charge on the edge surfaces pH-dependent [8–10]. The negative charges were reported to be balanced by interlayer exchangeable cations, e.g., Na^+, K^+, Ca^{2+} [11]. Distributions of counter-ions and co-ions around the solid surface lead to the formation of the diffuse electric double layer (EDL) [12] which contributes to the stability of fine clay minerals.

To reduce the stability of these mineral tailings, many chemical treatments were introduced towards solid-liquid separation via flocculation [13–18]. Natural or synthetic polymers and inorganic salts are considered as major types of flocculants. Many natural polymers such as chitosan were shown to flocculate fine particles by adsorbing on the solid surface through electrostatic attraction [19–21]. For example, Lu et al. [20] reported that the zeta potential of particles in the supernatants of mature fine tailings (MFT, concentrated dispersion of fine clay minerals generated from water-based mining of oil sands) gradually increased from -38.6 mV to +30.2 mV when treated with increasing dosage of chitosan. Before reaching an optimum dosage (zeta potential = 0 mV), as more chitosan was added, more particles were flocculated and settled downwards, represented by the increasing initial settling rate (ISR) and decreasing turbidity of the supernatant. On the other hand, hydrogen bonding (H-bonding) was also demonstrated to facilitate the adsorption of polymers, such as neutral polyacrylamide (PAM) [22] as well as its anionic derivatives Magnafloc (MF) [22], Zetag [23] and poly (N-isopropyl acrylamide) [24]. These polymers have been extensively used for solid-water separation since they are effective, inexpensive and have low toxicity. For instance, Li et al. [25] observed an increase in ISR when tailing samples were treated by anionic HPAM (hydrolyzed PAM). It was proposed that H-bonding between the hydroxyl groups of HPAM and clay mineral surfaces could induce bridging interactions between the clay mineral particles, thus enhancing the phase separation.

Interestingly, instead of using a single type of polymers as flocculant, recent experimental studies reported enhanced flocculation performance when two types of polymers were applied. For example, in the work of Lu et al. [20] the ISR reached as high as 10.26 m/h (meters per hour) when the MFT were treated by MF at its optimum dosage, but the clarity of the supernatant had no improvement compared with the untreated one. On the other hand, chitosan could render a high clarity of the release supernatant, with turbidity of 15 NTU (nephelometric turbidity unit, an indication of the relative clarity of water), but the highest ISR was only 1 m/h. Both high ISR (7.7 m/h) and clear supernatant (turbidity of 71 NTU) were achieved by treating the MFT first by MF and then by chitosan. Similar phenomena were also reported by other researchers [24].

Despite the observations from experiments, very limited theoretical work has been conducted to investigate the mechanisms behind the solid-liquid separation, and as such there were discrepancies between explanations proposed for the same observations [11]. While the adsorption of a single type of polymers onto clay mineral layers was examined by theoretical simulations [26–30], there has been no theoretical studies on the possible synergy between multiple types of polymer flocculants in the vicinity of clay mineral surfaces. The effects of polymer charges, adding sequence, and how the synergy is tied to the flocculation capability are among the most interesting but unaddressed questions in the field.

To fill this gap, in the present work a series of molecular dynamics (MD) simulations were performed to reveal the synergetic behaviors of two types of polymer flocculants when they were added to the vicinity of a clay mineral surface. The clay mineral was represented by Mt with negative charges. Three polymers were simulated: chitosan (cationic), PAM (neutral) and APAM (anionic). Chitosan was added with either PAM or APAM to study potential synergetic effects. For comparison, simulations were also conducted on systems containing a single type of polymers. As well, the effect of adding sequence was addressed by adding the two types of polymers in different manners: simultaneously and sequentially.

3.2. Simulation methods

3.2.1. Molecular models

Mt belongs to the 2:1 mineral class, with a central sheet of octahedrally coordinated Al atoms, sandwiched between two sheets consisting of SiO_4 tetrahedra [31]. The unit cell of Mt used in this work was based on the structure available in the American Mineralogist Crystal Structure Database [32], and their atomic coordinates were derived by [31]. The unit cell parameters were *a*

= 5.18 Å, b = 8.95 Å, c = 15 Å, and $\alpha = \beta = \gamma = 90°$, where a, b and c were lattice constants in the three directions respectively, and α, β and γ were the angles between the lattice sides. Hydrogen atoms were manually added to oxygen atoms in the octahedral sheet. A neutral 2×2×1 supercell was then built by closely stacking the unit cells. Three Al atoms in octahedral sheet were isomorphically substituted by Mg, resulting in a negative layer charge of -0.75e. The negative layer charge was neutralized by sodium ions in the system, yielding a unit cell formula of $Na_{0.75}Si_8(Al_{3.25}Mg_{0.75})O_{20}(OH)_4$. Molecular structure of the Na-Mt clay mineral corresponded to the measured compositions by X-ray diffraction (XRD) [33] and was widely adopted in previous theoretical investigations [34–37]. The supercell was subsequently expanded to a 16×10×1 supercell (Figure 3.1a) to accommodate the polymers.

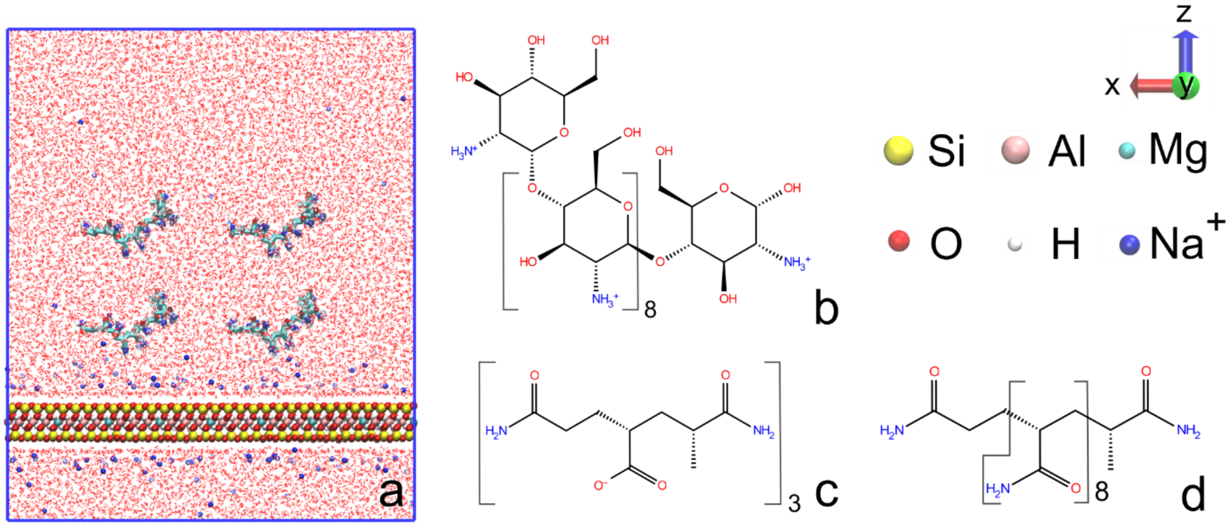

Figure 3.1. Initial configuration of system Mt-PAM (a), chitosan (b), MF 1011 (c), and PAM (d). In (a), the Mt supercell is represented by ball and stick. PAM is in licorice representation. Water as solvent is in line representation.

Chitosan, PAM, and APAM were all modeled based on compounds in the PubChem database [38]. The pH condition in the simulated systems was set to be slightly alkaline (7.5-8). Such a pH was typical in the treatment of process water as a result of adding alkaline reagents such as sodium hydroxide [39], and was consistent with previous experimental works [40]. Dissociation constant for the amino groups in chitosan was demonstrated to vary with the molecular weight and degree of deacetylation of chitosan [41]. For chitosan with molecular weight less than1000 kDa and deacetylation degree of ~80%-100%, the dissociation constant was 6.3-7.8 [41]. Under the slightly alkaline pH, 2%-67% of amino groups of chitosan would become protonated. The cationic nature of chitosan in alkaline tailings was also measured in the work of Lu et al. [20], where the negative zeta-potential of tailings became positive when treated by a certain dosage of chitosan (60-80 kDa) under a pH of 8.6-8.9 [20]. In this work, a 10-mer chitosan ($C_{60}H_{112}N_{10}O_{41}$, MW 1638 g/mol, Figure 3.1b) was built with all amino groups protonated, to mimic the local interactions between cationic polymer segments of chitosan and the surfaces of solid particles. The APAM model adopted was a sodium salt of hydrolyzed PAM. APAM ionomers with 9 units ($C_{27}H_{44}N_6O_{12}$, MW 641 g/mol, Figure 3.1c) was simulated with a charge density of 33% based on the structure proposed in a previous experimental report [20]. A neutral 10-mer PAM ($C_{30}H_{52}N_{10}O_{10}$, MW 712 g/mol, Figure 3.1d) was used, corresponding to the same pH condition [42,43].

3.2.2. Systems simulated

A total of nine systems (see Table 3.1) were simulated to study the adsorption of polymers on the surface of Mt. System Mt-H_2O, with neutralizing sodium ions but without any polymers, was first simulated to allow water and ions to equilibrate around the basal surface of Mt. Three systems, namely Mt-CT, Mt-PAM, and Mt-APAM, were simulated next to probe the adsorption of single types of polymers on Mt. These simulations also allowed for comparison with systems that involve two types of polymers. In each of these three systems, twelve molecules of chitosan, PAM or APAM were introduced into the equilibrated aqueous solution above the Mt, forming a

3×2×2 array as shown in Figure 3.1a. The number of sodium ions was adjusted accordingly in each system to maintain charge neutrality.

The following two simulations, Mt-(CT-PAM) and Mt-(CT-APAM), were performed where chitosan and PAM (in system Mt-(CT-PAM)) or chitosan and APAM (in system Mt-(CT-APAM)) were added simultaneously above the clay mineral surface. The polymers were also added in the form of a 3×2×2 array as shown in Figure 3.1a, with one type of polymers forming the 3×1×2 array on the left and the other on the right. Lastly, to study the effect of adding sequence, twelve APAM molecules were placed above the Mt previously coated by chitosan, which resulted from the Mt-CT simulation. This formed the initial configuration for system (Mt-CT)-APAM. System (Mt-CT)-PAM was constructed in the same manner, with APAM replaced by PAM. One additional system, (Mt-PAM)-CT, was simulated by using the configuration of system Mt-PAM at 100 ns and adding twelve chitosan molecules, in the form of a 3×2×2 array, above the Mt surface pre-coated by PAM.

Table 3.1. Details of Simulated Systems

system name	polymers	number of Na^+	simulated time
Mt-H_2O	0	120	2.5 ns
Mt-CT	chitosan (3×2×2)	0	7 ns
Mt-PAM	PAM (3×2×2)	120	110 ns
Mt-MF	MF (3×2×2)	156	50 ns
Mt-(CT-PAM)	chitosan (3×1×2) + PAM (3×1×2)	60	80 ns
Mt-(CT-MF)	chitosan (3×1×2) + MF (3×1×2)	78	80 ns
(Mt-CT)-MF	Mt-CT + MF (3×2×2)	0 → 36	80 ns
(Mt-CT)-PAM	Mt-CT + PAM (3×2×2)	0 → 0	80 ns

system name	polymers	number of Na^+	simulated time
(Mt-PAM)-CT	Mt-PAM + chitosan (3×2×2)	120 → 0	80 ns

3.2.3. Simulation details

The force field parameters for Mt were adopted from the CLAYFF force field [44,45]. CLAYFF was designed for clay mineral models and has a good compatibility with organic force fields. The partial charges of all the atoms remained the same as in CLAYFF, however the potentials for van der Waals were converted into forms compatible with GROMOS96 53A6 [46]. Validation of the force field parameters is given in Appendix B (Section B1). Force field parameters for chitosan, PAM and APAM were first obtained from the GlycoBioChem PRODRG server [47] by submitting the initial atomic coordinates and invoking the GROMOS96 force field parameter set 53A6. The partial atomic charges were then manually adjusted based on the density functional theory (DFT) calculation from Gaussian 16 [48]. More details about the calculation of partial atomic charges of the three types of polymers are given in the Appendix B (Section B2).

All MD simulations were carried out using GROMACS [49–51] with periodic boundary conditions applied in all directions. As such, the polymers were essentially located between two basal surfaces of Mt. Water and sodium ions were first introduced and equilibrated for 2.5 ns in NPT ensemble. Then, polymers were solvated into the equilibrated Mt-H_2O system with the number of sodium ions adjusted accordingly. Each system was subjected to a geometrical optimization followed by NPT equilibration. Due to the different nature and strength of interactions between the polymers and Mt, different systems required different time to reach equilibrium (see Table 3.1, more details in Appendix B Section B3).

The temperature was controlled at 300 K by Nose-Hoover thermostat [52,53], and pressure was controlled at 1 bar by Parrinello–Rahman barostat [54]. Leap-frog algorithm [55] was used for the integration of equations of motion, with a time step of 1 fs. The bonds within all molecules were constrained by LINC algorithm [56] except those in H_2O which were constrained by SETTLE [57]. Long-range electrostatic interactions were handled by particle mesh Ewald (PME) method [58].

3.3. Results and discussion

3.3.1. Adsorption of a single type of polymers

The final configurations of systems Mt-CT, Mt-PAM, and Mt-APAM are displayed in Figure 3.2. In Figure 3.2a, the adsorbed chitosan molecules formed a stable monolayer coating on each Mt surface. In Figure 3.2b, only the chitosan molecules adsorbed on the upper surface are shown, which adhered to the surface in a dispersed manner. Detailed examination of the adsorption sites revealed a close correlation with the locations of the isomorphic substitutions (see more details in Appendix B, section B3). Interestingly, Willemsen et al. [59] reported an anticorrelation between the adsorption sites of phthalate esters with locations of isomorphic substitutions, which was caused by the hydrophobic nature of phthalate esters and the resulting preference of adhering to uncharged patches. Different from chitosan, PAM molecules as shown in Figures 3.2c and d tended to form clusters among themselves. All the APAM molecules remained dispersed in bulk water without adsorbing to the clay mineral surfaces, as shown in Figures 3.2e and f.

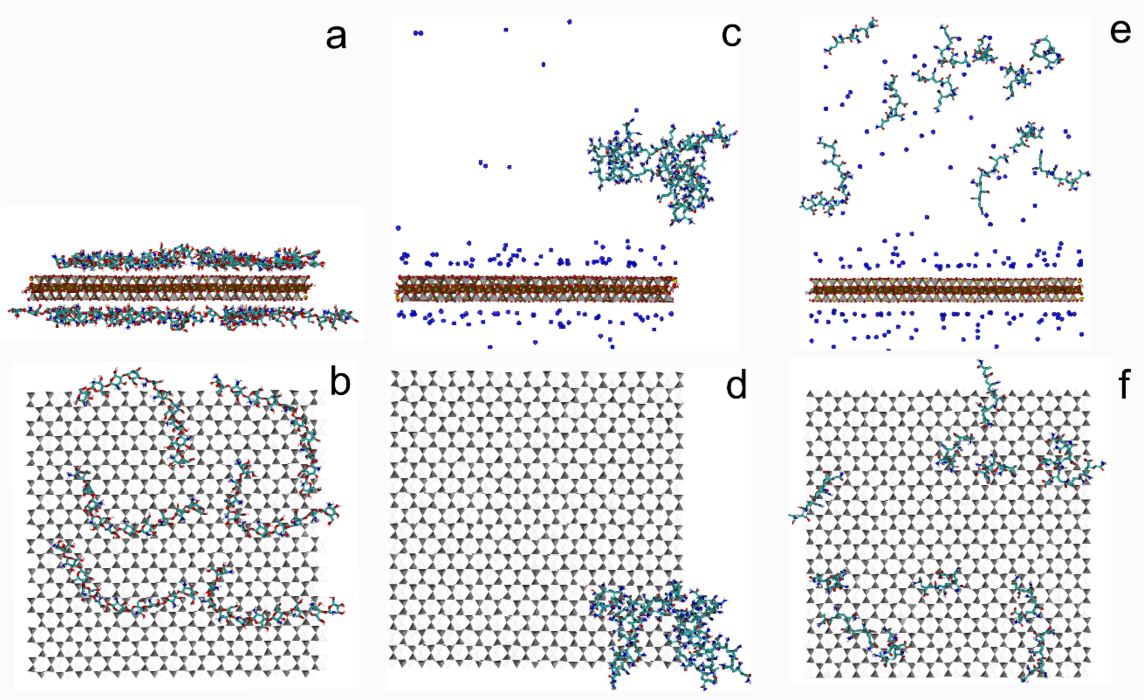

Figure 3.2. Snapshots of the final configuration of systems Mt-CT (a, b), Mt-PAM (c, d), and Mt-MF (e, f). Side view (a, c, e) and top view (b, d, f) are shown for each system. In top view, the alumina octahedron in Mt is not displayed, and water as well as ions are removed for clarity.

The vertical distances (*D*), as a function of time, between the center of geometry (COG) of Mt and the COG of one representative polymer molecules in each of the three systems are shown in Figure 3.3. The results for the other polymer molecules in each system are shown in Appendix B (Section B3), which shared similar characteristics. All chitosan molecules moved towards Mt quickly, with a fast decay in *D* in the first 2 ns, and then stayed on the surfaces without detaching again. The adsorption of chitosan was driven by the strong electrostatic attraction between the positively charged chitosan and the negatively charged Mt. Meanwhile, the electrostatic repulsion among the chitosan molecules caused them to adsorb separately on the surface and form a monolayer coating. Consistent with the snapshots shown in Figures 3.2e and f, APAM molecules were dispersed in the bulk without adsorption, and the value of *D* was above 2 nm for most of the simulation time. The electrostatic repulsions between the negatively charged APAM and Mt as well as among APAM molecules kept them apart from approaching each other. The adsorption of PAM molecules was much slower and weaker, as *D* was below 1 nm at ~10 ns for the first time and increased again. Throughout the simulation, *D* underwent large fluctuations, corresponding to frequent exchange between adsorbed and desorbed states. Such unstable adsorption was driven by the H-bonds between amides of PAM and bridging O in the basal surfaces of Mt. In addition, PAM could adsorb on Mt in the form of either a single molecule or an aggregate. More details on determining the aggregation state of PAM molecules are given in Appendix B (Section B3). For example, the representative PAM molecule shown in Figure 3.3 was adsorbed as a single molecule (square symbols) at around 10 ns, 25 ns, and 60 ns, whereas between 90 ns and 105 ns it was adsorbed as a molecule in an aggregate ("×" symbols).

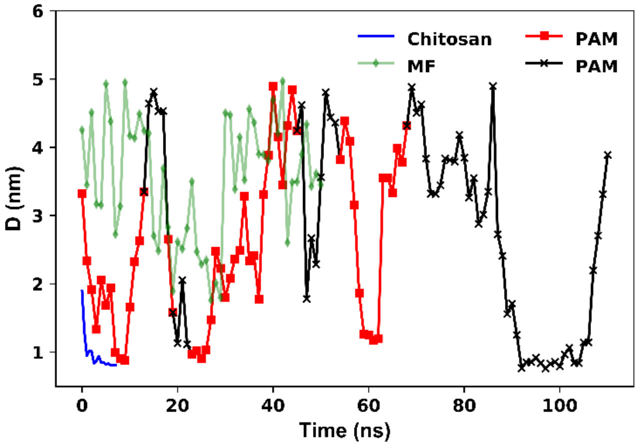

Figure 3.3. Vertical distances (*D*) between COG of Mt and COG of one representative chitosan molecule in system Mt-CT, one representative MF molecule in Mt-MF, and one representative PAM molecule in Mt-PAM, plotted against simulation time. For the representative PAM molecule in Mt-PAM, the "×" symbol corresponds to it being aggregated with other PAM molecules while the square symbol corresponds to it being in an un-aggregated state.

Quantitative analysis on H-bonding provided further assessment on the characteristics of PAM adsorption. The total numbers of H-bonds between PAM and Mt (n_{H}) was calculated and then normalized with respect to the number of donor/acceptor pairs available (N_0, more details in Appendix B, section B4). This ratio, $p = \frac{n_{\mathrm{H}}}{N_0}$, represented the percentage of available donor/acceptor pairs that actually contributed to H-bonding. The same calculation was done for the H-bonding between PAM molecules, and both results are shown in Figure 3.4. In the first 8 ns, *p* between PAM and Mt remained zero while the number among PAM molecules quickly increased, corresponding to the clustering of PAM molecules in the bulk solution. The value of *p* among PAM molecules fluctuated steadily between 7% and 16% for the rest of the simulation time, indicating the stability of the formed aggregates. Meanwhile, participating percentage of donor/acceptor pairs between PAM and Mt remained less then 2%, and frequently reduced to zero, suggesting reversible adsorption/desorption of the PAM molecules. The increases of *p* between PAM and Mt from 50 to 80 ns, and from 90 to 110 ns, were caused by PAM adsorption in either individual or aggregated forms, and examples are shown in the snapshots in Figure 3.4.

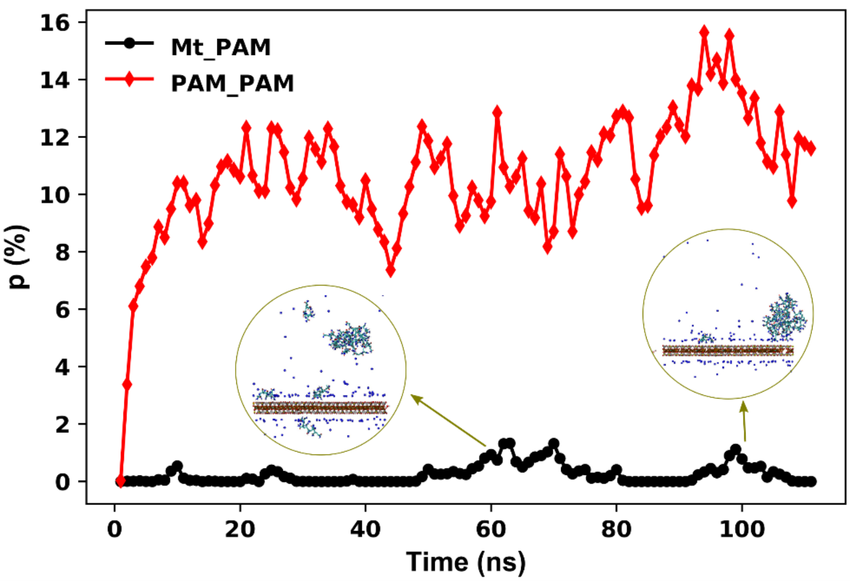

Figure 3.4. Percentage of available donor/acceptor pairs that contributed to H-bonding, among PAM molecules as well as between PAM and Mt in system Mt-PAM.

3.3.2. Adsorption of simultaneously added polymers

The configurations of systems Mt-(CT-PAM) and Mt-(CT-APAM) at different time are shown in Figure 3.5. Consider first system Mt-(CT-PAM) in Figures 3.5a-d. At $t = 3$ ns (Figure 3.5b), all the chitosan molecules became adsorbed on Mt while the PAM molecules were still in the bulk. Because chitosan molecules were initially placed on the right side of the simulation box, the adsorption occurred on the right side as well. That is, the chitosan molecules found the shortest path to form contact with Mt. As the simulation continued, the chitosan molecules started spreading over the entire Mt surface, forming a thin monolayer similar to what was seen in Figure 3.2a. Meanwhile, several PAM molecules started adhering to the adsorbed chitosan while some of them also adsorbed directly on Mt surrounded by chitosan molecules, as illustrated in Figure 3.5c. At the end of the simulation (Figure 3.5d), all the polymers were adsorbed, and the PAM molecules conformed much better to the surface than in Figure 3.2b where a bulky PAM cluster adhered to the surface with significant exposure to the solvent. Clearly, the presence of chitosan greatly enhanced the adsorption of PAM.

The behaviors in system Mt-(CT-APAM) as depicted in Figures 3.5e-h were similar to those in system Mt-(CT-PAM): the process also began by attachment and subsequent spreading of chitosan, followed by the adsorption of APAM via chitosan, and all the polymer molecules were adsorbed at the end. The enhancement of APAM adsorption was significant, considering that in Figure 3.2c all APAM molecules were dispersed in the bulk with no adsorption at all. Compared with system Mt-(CT-PAM), there were a few differences in system Mt-(CT-APAM). First of all, in the initial stage of the simulation some chitosan could be "captured" by the negatively charged

APAM in the bulk (see Figure 3.5f at $t = 3$ ns) and their adsorption to Mt was delayed (not until $t = 30$ ns in Figure 3.5g where the clustered chitosan and APAM adsorbed together). On the contrary, for system Mt-(CT-PAM), there was little interaction between the positively charged chitosan and neutral PAM before surface adsorption of chitosan. Secondly, while PAM molecules could adsorb on Mt via two modes (directly and indirectly through chitosan bridges), all APAM adsorption occurred via binding with chitosan.

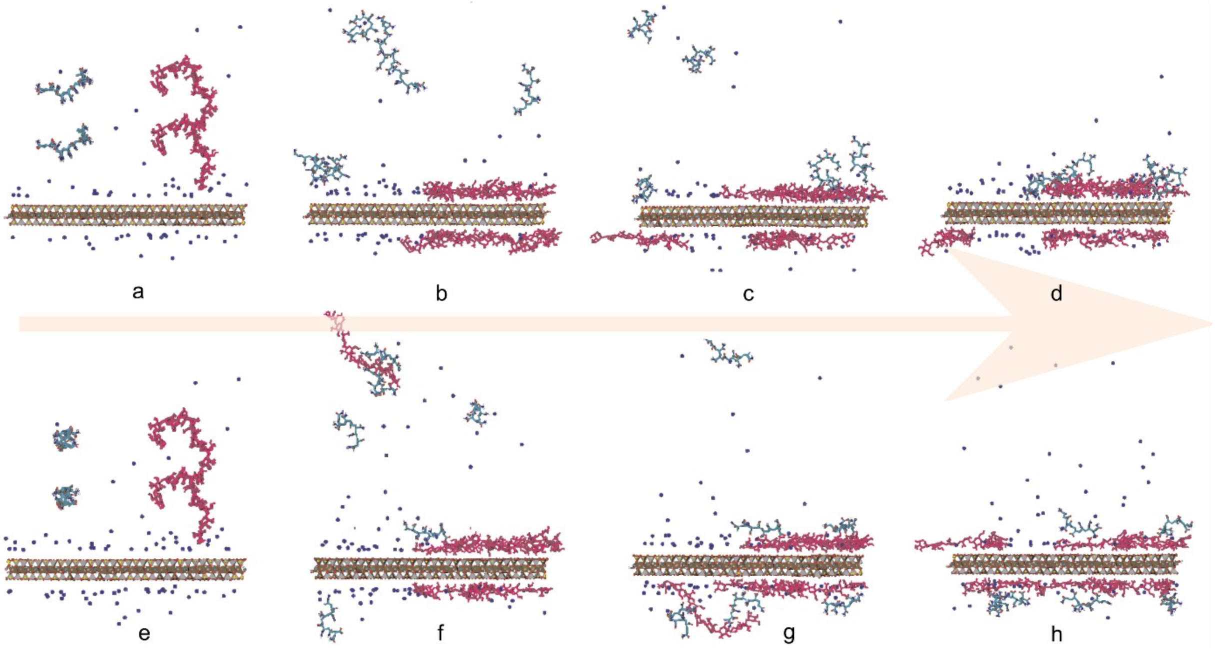

Figure 3.5. Snapshots of system Mt-(CT-PAM) at t = (a) 0 ns, (b) 3 ns, (c) 31 ns and (d) 80 ns; and of system Mt-(CT-MF) at t = (e) 0 ns, (f) 10 ns, (g) 40 ns and (h) 80 ns. At $t = 0$ ns, chitosan molecules are on the right while PAM and MF molecules are on the left. Water is removed for clarity.

The different modes of adsorption could be further confirmed by the vertical distances (D) between the COG of polymer molecules and COG of Mt, as plotted in Figure 3.6, against simulation time. Results are only shown for one chitosan (labeled as CT_1), two PAM molecules (labeled as PAM_1, PAM_2) in Mt-(CT-PAM), and one APAM molecule (labeled as APAM_1) in Mt-(CT-APAM), while the rest are given in the Appendix B (Section B3). Chitosan in both systems displayed the same trend as CT_1: *D* reduced to about 0.5 nm after 2 ns and remained constant, corresponding to fast, direct and stable adsorption. All APAM in Mt-(CT-APAM) also exhibited the same mode of adsorption, as *D* reduced to 1.5 nm at ~25 ns in Figure 3.6 and was stable afterwards. This larger steady-state value of *D*, compared to chitosan (0.5 nm), suggests that APAM adsorbed on top of the chitosan monolayer and could not move closer to Mt. The fast movement and stable coating of chitosan on Mt were due to the strong electrostatic attraction between positively charged chitosan and negatively charged Mt. Such attraction also existed between chitosan and negative APAM, while APAM and Mt were mutually repulsive. These interactions determined the mode of adsorption in Mt-(CT-APAM), where chitosan molecules were sandwiched between Mt and APAM serving as bridges.

PAM in system Mt-(CT-PAM) displayed two modes of adsorption. The first was represented by PAM_1, for which *D* maintained a value of ~0.5 nm after 25 ns, representing a stable adsorption directly on the surface of Mt. Contrary to PAM_1, PAM_2 displayed a more dynamic motion. At ~20 ns, it approached Mt with *D* staying at ~1.5 nm for about 10 ns. During this time, PAM_2 adsorbed to Mt via a chitosan bridge, similar to APAM molecules in Mt-(CT-APAM). Afterwards *D* increased rapidly corresponding to departure of PAM_2 from Mt. It adhered to Mt again after 45 ns with *D* fluctuating between 0.5 nm and 1.5 nm. Such fluctuation represented the switch between the two adsorption modes: directly on Mt and adsorption via chitosan.

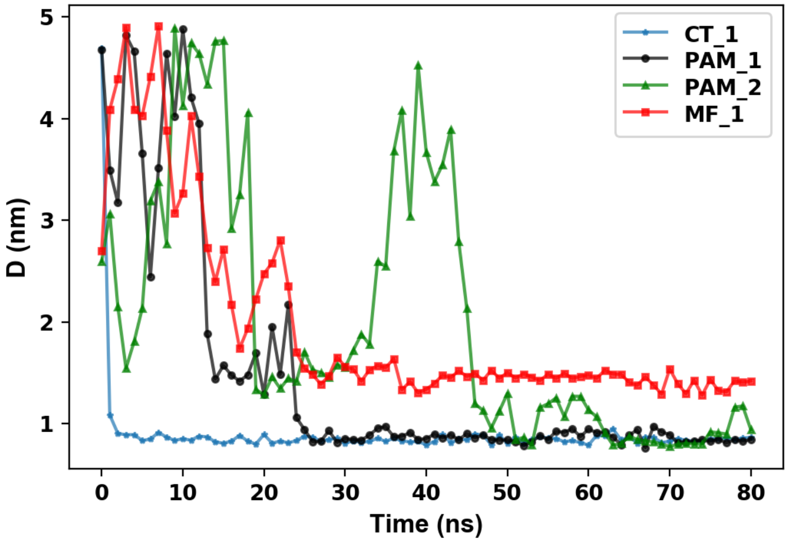

Figure 3.6. Vertical distances (*D*) between COG of Mt and COG of representative polymer molecules, plotted against simulation time.

Overall charge neutral PAM molecules interacted with chitosan via the formation of H-bonds between the hydroxyl groups of chitosan and amides of PAM. The ability of PAM to form H-bonds with chitosan as well as with Mt led to both direct adsorption and indirect adsorption via chitosan bridges. Similar to Figure 3.4, the percentages of available donor/acceptor pairs that contributed to H-bonding, *p*, were calculated for system Mt-(CT-PAM) and shown in Figure 3.7. From 0 to 10 ns, *p* value was highest among PAM molecules, slightly above zero between chitosan and PAM, and zero between PAM and Mt. Therefore, similar to system Mt-PAM, during the initial stage clustering of PAM was favored and no immediate adsorption onto Mt was observed. Meanwhile, PAM started interaction with the adsorbed chitosan layer. From 10 to 25 ns, *p* among PAM molecules reduced to one half of the original value while *p* between PAM and chitosan increased. H-bonds between PAM and Mt also began to form. The results suggested conversion of some PAM-PAM H-bonds to PAM-chitosan and PAM-Mt H-bonds. PAM aggregates previously formed in the bulk broke into smaller ones to facilitate the adsorption. From 25 to 80 ns, the value of *p* among PAM first increased and then decreased, indicating the reversibility of PAM aggregation. The value of *p* between PAM and chitosan fluctuated at a lower level than the curve between PAM and Mt which increased significantly, suggesting that direct adsorption was more favorable compared to indirect adsorption via chitosan bridges.

Comparing the data in the last 20 ns of Figure 3.4 and Figure 3.7, there was a 50% reduction in the *p* value among PAM molecules, from ~12% in Figure 3.4 to ~6% in Figure 3.7. Meanwhile, there was a 20-fold increase in *p* between PAM and Mt, from ~0.2% in Figure 3.4 to ~4% in Figure 3.7. Chitosan not only served as bridges for the indirect adsorption of PAM, but also suppressed the aggregation of PAM molecules and greatly promoted the direct adsorption of PAM on Mt. As PAM molecules were brought closer to Mt via the chitosan bridges, their short-ranged attractions with Mt were enabled, which drove them to continue moving towards Mt until direct H-bonding was established.

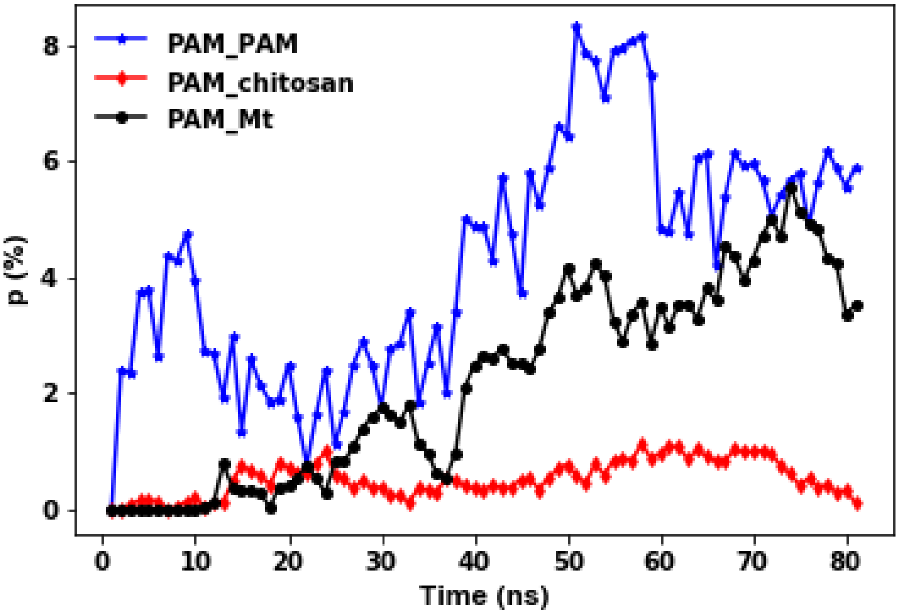

Figure 3.7. Percentage of available donor/acceptor pairs that contributed to H-bonding, among PAM molecules, between PAM and chitosan, and between PAM and Mt in system Mt-(CT-PAM).

3.3.3. Adsorption of sequentially added polymers

The configurations of systems (Mt-CT)-PAM and (Mt-PAM)-CT at different time are shown in Figure 3.8. Consider system (Mt-CT)-PAM as shown in Figures 3.8a-d, the adsorption showed no difference compared with system Mt-(CT-PAM) shown in Figures 3.5a-d. Since chitosan moved much faster towards Mt than PAM, adding chitosan first or adding them simultaneously did not affect the adsorption. Similar observations were found for system (Mt-CT)-APAM (more details in Appendix B, Section B3).

What is more interesting is system (Mt-PAM)-CT where chitosan molecules were added to Mt-PAM with an adsorbed PAM cluster on Mt. Even though in this case PAM adsorption had already occurred before the introduction of chitosan, the stronger long-range electrostatic attraction between chitosan and Mt still drove the formation of a chitosan monolayer on Mt at the end of the simulation (Figure 3.8h), which was similar to systems (Mt-CT)-PAM and Mt-(CT-PAM). During this process, however, the PAM aggregate was never "released" from the surface into the bulk. Instead, chitosan maintained their interactions with PAM while forming intimate contact with Mt (see Figures 3.8f and g). Consequently, the PAM aggregate was anchored to the vicinity of the Mt, gradually allowed chitosan to insert between PAM and Mt, and finally adsorbed on the formed chitosan monolayer. PAM initially adsorbed as individual molecules (Figure 3.8e) remained adsorbed directly and were not disrupted by chitosan.

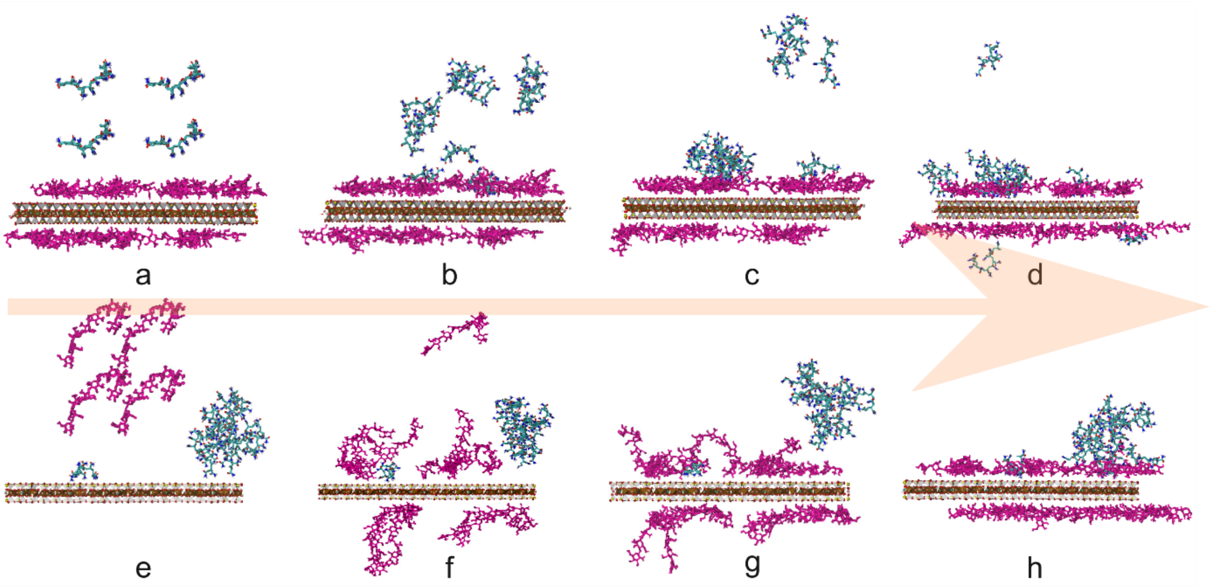

Figure 3.8. Snapshots of system (Mt-CT)-PAM at *t* = (a) 0 ns, (b) 3 ns, (c) 20 ns, and (d) 80 ns; and of system (Mt-PAM)-CT at *t* = (e) 0 ns, (f) 0.2 ns, (g) 0.6 ns, and (h) 80 ns. The 3×2×2 arrays of molecules above Mt in (a) and (e) correspond to PAM and chitosan, respectively. Water is removed for clarity.

3.3.4. Implications

As discussed in Section 3.1, chitosan molecules adsorbed quickly and formed a monolayer coating on Mt. Though the two clay mineral surfaces could not be brought together by chitosan due to the application of periodic boundary conditions, the ability of chitosan to bridge two bare clay mineral surfaces were proved in other contexts such as fabrication of nanocomposites [60,61]. In industrial tailings, a clay mineral particle coated by chitosan could have neutral or even reversed zeta potential [20,62]. As such, it could attract another bare clay mineral surface, flocculating them together. However, if both particles were coated by chitosan and possessed positive surface charges, the electrostatic repulsion between them would hinder their aggregation and limit the growth of flocs, as illustrated in Figure 3.9a. As a result, it can be hypothesized that the flocs will settle slowly due to their small size. Since the adsorption of chitosan is highly stable, clay mineral particles captured in the flocs are less likely to be released back to the supernatant, resulting in high clarity. This result is consistent with the experimental observation that the ISR of chitosan or other cationic polymers treated wastewater/tailings showed a low ISR but high clarity of supernatant [20,24].

PAM molecules by themselves could adsorb on Mt, but the adsorption tended to be in the form of an aggregate and was not stable. It could then be inferred that in macroscopic systems, PAM alone might induce multi-layer adsorption with reversible desorption. Two clay mineral particles with adsorbed PAM can further aggregate since the neutral PAM does not introduce repulsion between them while allowing for H-bonding among the adsorbed PAM molecules. This interaction mechanism can lead to large flocs that settle quickly in clay mineral dispersion, consistent with experimental observation [24,63]. On the other hand, the unstable adsorption can allow a large amount of clay minerals to be released back to the bulk solution, as illustrated in Figure 3.9b. Consequently, the clarity of clay mineral dispersion is expected to be low, which was observed by various experiments [20,64].

In experiments, when two types of flocculants were added simultaneously, the floc size displayed a two-stage growth [23] which was consistent with the two-step adsorption as shown in the system Mt-(CT-PAM). Regardless of the adding sequence, our simulations showed that the cationic polymers formed the most intimate adsorption on the clay mineral followed by the neutral polymers. The cationic coating stabilized the adsorption of neutral flocculants, while the outer layer of neutral polymers promoted the local attractive forces such as H-bonding, bridging them together to form larger aggregates, as illustrated in Figure 3.9c. Compared with the application of a single type of flocculants, such synergetic effect is expected to not only increase the ISR by forming larger clay mineral aggregates but also enhance the clarity of the supernatant by reducing the number of bare clay mineral particles in it. The result is consistent with previous reports where the addition of two types of polymers showed both high ISR and clarity [20,24]. The synergetic effect was also present when cationic and anionic flocculants were added, as our simulations showed a similar two-stage adsorption process for chitosan and APAM. The bonding strength between chitosan and APAM was in fact larger than that between chitosan and PAM. Although if two particles both possessed an outer APAM layer they would repel, in macroscopic systems it is possible to have multi-layer adsorption in the form of CT-APAM-CT, CT-APAM-CT-APAM, etc., which would allow particles with opposite apparent surface charges to aggregate. To the best of our knowledge, this is the first theoretical work that investigated the adsorption of polymer flocculants from molecular level and accounted for the different flocculation behaviors. The results provided molecular evidence that applying polymers with different charge properties would promote the flocculation and the applying sequences had limited influence. Our findings may also be of value to other applications, such as capture and storage of organic resources, as well as the design of clay polymer nanocomposite.

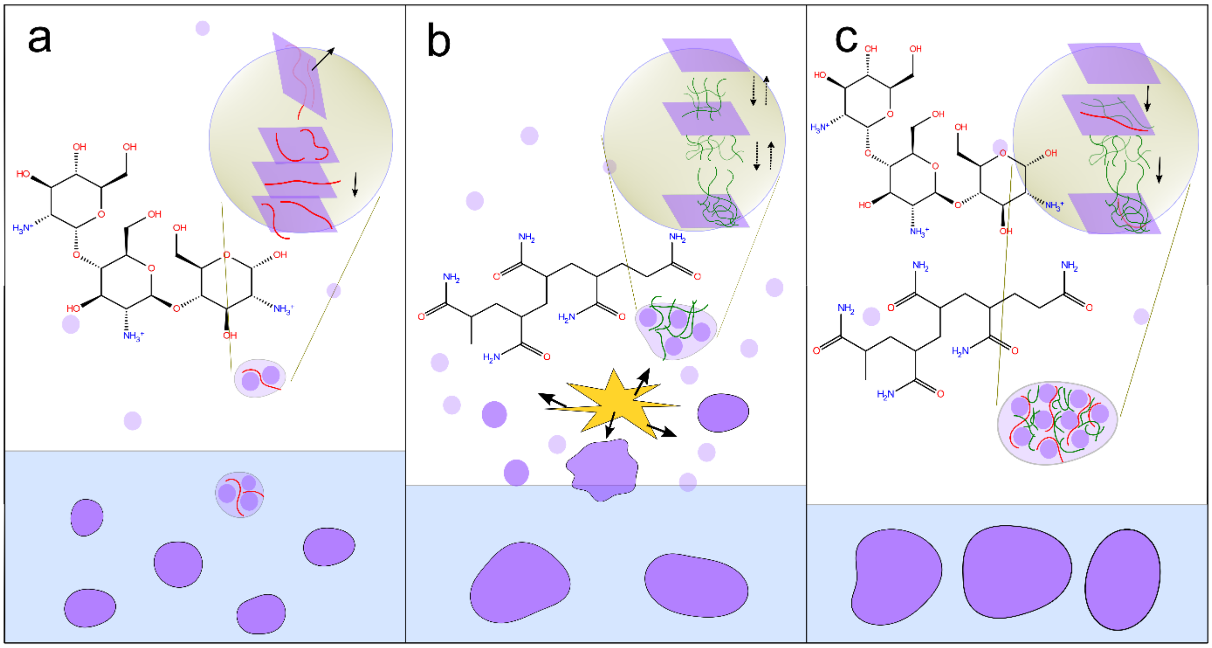

Figure 3.9. Proposed mechanism for the macroscopic flocculation of Mt by the addition of chitosan (a), PAM (b), chitosan and PAM (c). Plates represent the clay mineral particles; chitosan and PAM are represented by strings. Refer to Figure 3.1 for detailed molecular structures.

3.3.5. Limitations

In the present work, the basal surface of Mt was chosen as a representative clay mineral surface, while actual clay particles also contain edge surfaces and interlayers. When it comes to polymer flocculation, the likelihood of adsorption of polymer flocculants in the interlayers is expected to be low. This is because the interlayer spacing is on the order of nanometers [65], which is difficult to accommodate polymer flocculants whose molecular mass is usually in the range of 10^6-10^7 g/mol [14,66]. The relative importance of basal and edge surfaces is an interesting but complex problem. For example, characterization results from XRD and SAXS showed preferential interactions of polymers with basal surface [59,67], with edge surface [68], or comparable affinities to both surfaces [69]. The distinct results were likely caused by the different charges and terminating groups on the basal and edge surfaces, different polymer properties, as well as different solution chemistries (e.g., pH, ions). Since the focus of this study was to investigate the synergy of polymer adsorption arising from interactions such as electrostatics and hydrogen bonding, the use of a single-layer basal surface served the purpose. The mechanism discovered in this work should also be applicable to an edge surface if its interactions with the polymer flocculants were governed by the same types of intermolecular forces, although confirmation of this hypothesis would require additional investigations.

In addition to Mt, other types of clay minerals also exist in industrial tailings [11], for example, kaolinite and illite. Kaolinite is a 1:1 type planar phyllosilicate with one tetrahedral siloxane sheet and one octahedral alumina sheet [9]. Under the same pH (= 8) condition as considered in this work, it tends to have a neutral basal surface as atom substitutions are less likely to happen. However, its edge surface can carry negative charges as the physically bonded water would get deprotonated under the pH of 8 [9]. Thus, adsorption of cationic chitosan on kaolinite is expected to occur but mostly on the edge surface. PAM and APAM may display more adsorption on kaolinite than on Mt because of the exposed hydroxyl groups on the alumina basal and edge surfaces of kaolinite, which promote hydrogen bonding. The synergetic effect demonstrated in this work is expected to be present for kaolinite, since all three types of polymers are expected to adsorb on it and the interactions driving adsorption are similar. Illite is a dioctahedral mica-like mineral [11] which has similar molecular structure with Mt. Its basal surface carries permanent negative charges due to atom substitutions while the charges on the edge surface are pH dependent. Therefore, the synergetic polymer adsorption observed for Mt is expected to be similar for illite. Slight difference might come from the fact that atom substitution in Mt usually occurs only in the octahedral sheet while it can occur in both tetrahedral and octahedral sheets in illite [11,70]. Because of this, the charge density on the basal surface of illite can be higher which may lead to enhanced adsorption of cationic chitosan.

Due to the size limitation in MD simulations, it was not possible to reproduce the bulk concentration of polymer molecules in experiments. In fact, typical bulk concentrations used in experiments [20,71] would correspond to at most one polymer molecule in the simulation cell, which would not have allowed us to investigate the interactions among the polymer molecules, a key aspect of this work. On the other hand, because this work focused on polymer adsorption, the higher concentration used mimicked the fact that the concentration of the polymers near the clay surface should be much higher than that in the bulk solution. Different loadings of polymers can affect polymer adsorption. As some of the experimental works suggested [20,24], there could be an optimal dosage of polymers for which the extent of flocculation was maximized. The mechanism behind the observations is unclear and is a very interesting question to address in the future.

Furthermore, the ions included in the simulation systems were monovalent (Na^+). Multiple types of ions can exist in waste-water, such as Na^+, Ca^{2+}, Mg^{2+}, Cl^-, HCO_3^-, SO_4^{2-}, NH_4^+ [39]. There was evidence that divalent ions, such as Ca^{2+}, could form more stable bridges between clay mineral and anionic polymers which enhanced their adsorption [25]. In fact, in our simulations APAM by themselves did not exhibit any adsorption, which appeared contradictory to earlier experimental studies where APAM and other anionic polymers showed flocculating abilities. The presence of divalent ions in the experiments [20,25] could be a reason for the discrepancy; another contributing factor could be the hydroxyl groups on the edge surfaces of Mt and basal/edge surfaces of kaolinite [72] in the experiments. It is worth mentioning that some ions could also compete with polymers in the adsorption and even formed surface complexes on Mt [73] that hindered polymer adsorption. Effect of different ions are being investigated and will be reported elsewhere.

Finally, the sizes of clay mineral particles (~1 μm) and polymers (molar mass $10^{6\sim7}$ g/mol) in practical settling [1] are much larger than the molecular models studied here. As with any molecular simulations, the length and time scales of our simulations are limited by the state-of-the-art computing capabilities. On the other hand, the atomistic simulations revealed the intermolecular interactions that give rise to synergetic adsorption, which could not be obtained with lab-scale resolution. The good agreement found here between mechanistic insights from simulations and synergetic flocculation observed in experiments supports the complementarity of the two approaches, which have great potential for other advanced studies in clay science.

3.4. Conclusion

Molecular dynamics simulations revealed different characteristics for the adsorptions of cationic (chitosan), neutral (PAM), and anionic (APAM) polymers on the negatively charged basal surface of montmorillonite. When a single type of polymers was added, chitosan showed fast and stable monolayer adsorption, driven by electrostatic attraction; PAM displayed weak adsorption driven by hydrogen bonding, mainly in an aggregated form; and APAM showed no adsorption. When chitosan was added to PAM or APAM, their adsorption was significantly enhanced. Chitosan not only served as bridges between PAM (or APAM) and montmorillonite, but also promoted direct adsorption of PAM on montmorillonite. The findings correlated well with the synergetic effect observed in flocculation experiments and have direct implications on the selection of flocculants as well as the design of flocculation procedure.

References

[1] C. Wang, D. Harbottle, Q. Liu, Z. Xu, Current state of fine mineral tailings treatment: A critical review on theory and practice, Miner. Eng. 58 (2014) 113–131. doi:10.1016/j.mineng.2014.01.018.

[2] N.N. Bakhshi, R.G. Gillies, P. Khare, Treatment of Tar Sands Tailings with Fly Ash, Environ. Sci. Technol. 9 (1975) 363–364. doi:10.1021/es60102a013.

[3] A.H. Watson, P.G. Corser, E.E. Garces Pardo, T.E. Lopez Christian, J. Vandekeybus, A comparison of alternative tailings disposal methods—the promises and realities, in: Proc. First Int. Semin. Reduct. Risk Manag. Tailings Mine Waste, Australian Centre for Geomechanics, 2010: pp. 499–514.

[4] L. Moreno, I. Neretnieks, Long-term environmental impact of tailings deposits,

Hydrometallurgy. 83 (2006) 176–183. doi:10.1016/j.hydromet.2006.03.052.

[5] A.T. Kaniki, K. Tumba, Management of mineral processing tailings and metallurgical slags of the Congolese copperbelt: Environmental stakes and perspectives, J. Clean. Prod. 210 (2019) 1406–1413. doi:10.1016/j.jclepro.2018.11.131.

[6] O.E. Omotoso, R.J. Mikula, High surface areas caused by smectitic interstratification of kaolinite and illite in Athabasca oil sands, Appl. Clay Sci. 25 (2004) 37–47. doi:10.1016/j.clay.2003.08.002.

[7] M.H. Gorakhki, C.A. Bareither, Salinity effects on sedimentation behavior of kaolin, bentonite, and soda ash mine tailings, Appl. Clay Sci. 114 (2015) 593–602. doi:10.1016/j.clay.2015.07.018.

[8] I.C. Bourg, G. Sposito, A.C.M. Bourg, Modeling the acid-base surface chemistry of montmorillonite, J. Colloid Interface Sci. 312 (2007) 297–310. doi:10.1016/j.jcis.2007.03.062.

[9] T.R. Zeitler, J.A. Greathouse, R.T. Cygan, J.T. Fredrich, G.R. Jerauld, Molecular Dynamics Simulation of Resin Adsorption at Kaolinite Edge Sites: Effect of Surface Deprotonation on Interfacial Structure, J. Phys. Chem. C. 121 (2017) 22787–22796. doi:10.1021/acs.jpcc.7b06688.

[10] J. Chen, F. Min, L. Liu, C. Cai, Systematic exploration of the interactions between Fe-doped kaolinite and coal based on DFT calculations, Fuel. 266 (2020) 117082. doi:10.1016/j.fuel.2020.117082.

[11] B.K.G. Theng, Formation and Properties of Clay-Polymer Complexes, Vol. 4, Elsevier, 2012. doi:10.1016/B978-0-444-53354-8.00014-1.

[12] J.N. Israelachvili, Intermolecular and Surface Forces, third ed., Elsevier Inc., 2011.

doi:10.1016/C2011-0-05119-0.

[13] T. Nasim, A. Pal, A. Bandyopadhyay, Flocculation of aqueous kaolin suspension using a biodegradable flocculant system of poly (vinyl alcohol)-Acacia nilotica gum blends, Appl. Clay Sci. 152 (2018) 83–92. doi:10.1016/j.clay.2017.10.035.

[14] A. Alamgir, D. Harbottle, J. Masliyah, Z. Xu, Al-PAM assisted filtration system for abatement of mature fine tailings, Chem. Eng. Sci. 80 (2012) 91–99. doi:10.1016/j.ces.2012.06.010.

[15] T. Robert, S.M. Mercer, T.J. Clark, B.E. Mariampillai, P. Champagne, M.F. Cunningham, P.G. Jessop, Nitrogen-containing polymers as potent ionogens for aqueous solutions of switchable ionic strength: application to separation of organic liquids and clay particles from water, Green Chem. 14 (2012) 3053. doi:10.1039/c2gc36074h.

[16] J. Long, H. Li, Z. Xu, J.H. Masliyah, Role of colloidal interactions in oil sand tailings treatment, AIChE J. 52 (2006) 371–383. doi:10.1002/aic.10603.

[17] S.M.R. Shaikh, M.S. Nasser, M. Magzoub, A. Benamor, I.A. Hussein, M.H. El-Naas, H. Qiblawey, Effect of electrolytes on electrokinetics and flocculation behavior of bentonite-polyacrylamide dispersions, Appl. Clay Sci. 158 (2018) 46–54. doi:10.1016/j.clay.2018.03.017.

[18] X. Kang, Z. Xia, R. Chen, H. Sun, W. Yang, Effects of inorganic ions, organic polymers, and fly ashes on the sedimentation characteristics of kaolinite suspensions, Appl. Clay Sci. 181 (2019) 105220. doi:10.1016/j.clay.2019.105220.

[19] Z. Yang, Y. Shang, Y. Lu, Y. Chen, X. Huang, A. Chen, Y. Jiang, W. Gu, X. Qian, H. Yang, R. Cheng, Flocculation properties of biodegradable amphoteric chitosan-based flocculants, Chem. Eng. J. 172 (2011) 287–295. doi:10.1016/j.cej.2011.05.106.

[20] Q. Lu, B. Yan, L. Xie, J. Huang, Y. Liu, H. Zeng, A two-step flocculation process on oil sands tailings treatment using oppositely charged polymer flocculants, Sci. Total Environ. 565 (2016) 369–375. doi:10.1016/j.scitotenv.2016.04.192.

[21] O. Molatlhegi, L. Alagha, Adsorption characteristics of chitosan grafted copolymer on kaolin, Appl. Clay Sci. 150 (2017) 342–353. doi:10.1016/j.clay.2017.09.032.

[22] Y. Ji, Q. Lu, Q. Liu, H. Zeng, Effect of solution salinity on settling of mineral tailings by polymer flocculants, Colloids Surfaces A Physicochem. Eng. Asp. 430 (2013) 29–38. doi:10.1016/j.colsurfa.2013.04.006.

[23] C. Wang, C. Han, Z. Lin, J. Masliyah, Q. Liu, Z. Xu, Role of Preconditioning Cationic Zetag Flocculant in Enhancing Mature Fine Tailings Flocculation, Energy and Fuels. 30 (2016) 5223–5231. doi:10.1021/acs.energyfuels.6b00108.

[24] D. Zhang, T. Thundat, R. Narain, Flocculation and dewatering of mature fine tailings using temperature-responsive cationic polymers, Langmuir. 33 (2017) 5900–5909. doi:10.1021/acs.langmuir.7b01160.

[25] H. Li, J. Long, Z. Xu, J.H. Masliyah, Synergetic role of polymer flocculant in low-temperature bitumen extraction and tailings treatment, Energy and Fuels. 19 (2005) 936–943. doi:10.1021/ef049744e.

[26] R.T. Cygan, J.A. Greathouse, H. Heinz, A.G. Kalinichev, Molecular models and simulations of layered materials, J. Mater. Chem. 19 (2009) 2470. doi:10.1039/b819076c.

[27] F. Azevedo Rios Silva, M.J. Araújo Sales, M. Ghoul, L. Chebil, G. Duarte Ramos Matos, E.R. Maia, Molecular dynamics simulations of montmorillonite reinforcing amylose plasticized by Brazilian Cerrado oils: Polymer-clay nanocomposite, MRS Commun. 8 (2018) 266–274. doi:10.1557/mrc.2018.41.

[28] Q. Wei, Y. Wang, S. Wang, Y. Zhang, X. Chen, Investigating the properties and interaction mechanism of nano-silica in polyvinyl alcohol/polyacrylamide blends at an atomic level, J. Mech. Behav. Biomed. Mater. 75 (2017) 529–537. doi:10.1016/j.jmbbm.2017.08.027.

[29] H. Cheng, S. Zhang, Q. Liu, X. Li, R.L. Frost, The molecular structure of kaolinite-potassium acetate intercalation complexes: A combined experimental and molecular dynamic simulation study, Appl. Clay Sci. 116–117 (2015) 273–280. doi:10.1016/j.clay.2015.04.008.

[30] B. Ren, F. Min, L. Liu, J. Chen, C. Liu, K. Lv, Adsorption of different PAM structural units on kaolinite (0 0 1) surface: Density functional theory study, Appl. Surf. Sci. 504 (2020). doi:10.1016/j.apsusc.2019.144324.

[31] A. Viani, A.F. Gualtieri, G. Artioli, The nature of disorder in montmorillonite by simulation of X-ray powder patterns, Am. Mineral. 87 (2002) 966–975.

[32] R.T. Downs, M. Hall-Wallace, The American Mineralogist crystal structure database, Am. Mineral. 88 (2003) 247–250. doi:https://doi.org/.

[33] G.W. Brown, G., Brindley, Crystal structures of clay minerals and their Xray identification, J. Mineral. Soc. (1980) 305-356. doi:10.1016/j.jenvman.2011.05.031.

[34] P. Simonnin, V. Marry, B. Noetinger, C. Nieto-Draghi, B. Rotenberg, Mineral- and Ion-Specific Effects at Clay-Water Interfaces: Structure, Diffusion, and Hydrodynamics, J. Phys. Chem. C. 122 (2018) 18484–18492. doi:10.1021/acs.jpcc.8b04259.

[35] Q.H. Zeng, A.B. Yu, G.Q. Lu, R.K. Standish, Molecular Dynamics Simulation of Organic-Inorganic Nanocomposites: Layering Behavior and Interlayer Structure of Organoclays, Chem. Mater. 15 (2003) 4732–4738. doi:10.1021/cm0342952.

[36] Y.-W. Hsiao, M. Hedström, Swelling Pressure in Systems with Na-Montmorillonite and

Neutral Surfaces: A Molecular Dynamics Study, J. Phys. Chem. C. 121 (2017) 26414–26423. doi:10.1021/acs.jpcc.7b09496.

[37] M. Hedström, O. Karnland, Donnan equilibrium in Na-montmorillonite from a molecular dynamics perspective, Geochim. Cosmochim. Acta. 77 (2012) 266–274. doi:10.1016/J.GCA.2011.11.007.

[38] S. Kim, J. Chen, T. Cheng, A. Gindulyte, J. He, S. He, Q. Li, B.A. Shoemaker, P.A. Thiessen, B. Yu, L. Zaslavsky, J. Zhang, E.E. Bolton, PubChem 2019 update: Improved access to chemical data, Nucleic Acids Res. 47 (2019) D1102–D1109. doi:10.1093/nar/gky1033.

[39] E.W. Allen, Process water treatment in Canada's oil sands industry: I. Target pollutants and treatment objectives, J. Environ. Eng. Sci. 7 (2008) 123–138. doi:10.1139/S07-038.

[40] D. Fernandes, W. Conway, X. Wang, R. Burns, G. Lawrance, M. Maeder, G. Puxty, Protonation constants and thermodynamic properties of amines for post combustion capture of CO 2, J. Chem. Thermodyn. 51 (2012) 97–102. doi:10.1016/j.jct.2012.02.031.

[41] Q.Z. Wang, X.G. Chen, N. Liu, S.X. Wang, C.S. Liu, X.H. Meng, C.G. Liu, Protonation constants of chitosan with different molecular weight and degree of deacetylation, Carbohydr. Polym. 65 (2006) 194–201. doi:10.1016/j.carbpol.2006.01.001.

[42] H. Grant, P. Mctigue, D. Ward, The basicities of aliphatic amides, Aust. J. Chem. 36 (2010) 2211. doi:10.1071/ch9832211.

[43] G. Fraenkel, C. Franconi, Protonation of Amides, J. Am. Chem. Soc. 82 (1960) 4478–4483. doi:10.1021/ja01502a010.

[44] R.T. Cygan, J.J. Liang, A.G. Kalinichev, Molecular models of hydroxide, oxyhydroxide, and clay phases and the development of a general force field, J. Phys. Chem. B. 108 (2004) 1255–1266. doi:10.1021/jp0363287.

[45] M. Pouvreau, J.A. Greathouse, R.T. Cygan, A.G. Kalinichev, Structure of Hydrated Gibbsite and Brucite Edge Surfaces: DFT Results and Further Development of the ClayFF Classical Force Field with Metal-O-H Angle Bending Terms, J. Phys. Chem. C. 121 (2017) 14757–14771. doi:10.1021/acs.jpcc.7b05362.

[46] C. Oostenbrink, A. Villa, A.E. Mark, W.F. Van Gunsteren, A biomolecular force field based on the free enthalpy of hydration and solvation: The GROMOS force-field parameter sets 53A5 and 53A6, J. Comput. Chem. 25 (2004) 1656–1676. doi:10.1002/jcc.20090.

[47] A.W. Schüttelkopf, D.M.F. Van Aalten, PRODRG: A tool for high-throughput crystallography of protein-ligand complexes, Acta Crystallogr. Sect. D Biol. Crystallogr. 60 (2004) 1355–1363. doi:10.1107/S0907444904011679.

[48] D.J. Frisch, M. J., Trucks, G. W., Schlegel, H. B., Scuseria, G. E., Robb, M. A., Cheeseman, J. R., Scalmani, G., Barone, V., Petersson, G. A., Nakatsuji, H., Li, X., Caricato, M., Marenich, A. V., Bloino, J., Janesko, B. G., Gomperts, R., Mennucci, B., Hratch, Gaussian 16 Revision B. 01., Wallingford CT. (2016).

[49] H.J.C.J.C. Berendsen, D. van der Spoel, R. van Drunen, GROMACS: A message-passing parallel molecular dynamics implementation, Comput. Phys. Commun. 91 (1995) 43–56. doi:10.1016/0010-4655(95)00042-E.

[50] S. Pronk, S. Páll, R. Schulz, P. Larsson, P. Bjelkmar, R. Apostolov, M.R. Shirts, J.C. Smith, P.M. Kasson, D. Van Der Spoel, B. Hess, E. Lindahl, GROMACS 4.5: a high-throughput and highly parallel open source molecular simulation toolkit, Bioinformatics. 29 (2013) 845–854. doi:10.1093/bioinformatics/btt055.

[51] E. Abraham, M. J., Murtola, T., Schulz, R., Páll, S., Smith, J. C., Hess, B., Lindahl, M.J. Abraham, T. Murtola, R. Schulz, S. Páll, J.C. Smith, B. Hess, E. Lindah, Gromacs: High

performance molecular simulations through multi-level parallelism from laptops to supercomputers, SoftwareX. 1–2 (2015) 19–25. doi:10.1016/j.softx.2015.06.001.

[52] S. Nosé, A molecular dynamics method for simulations in the canonical ensemble, Mol. Phys. 52 (1984) 255–268. doi:10.1080/00268978400101201.

[53] W.G. Hoover, Canonical dynamics: Equilibrium phase-space distributions, Phys. Rev. A. 31 (1985) 1695–1697. doi:10.1103/PhysRevA.31.1695.

[54] M. Parrinello, A. Rahman, Polymorphic transitions in single crystals: A new molecular dynamics method, J. Appl. Phys. 52 (1981) 7182–7190. doi:10.1063/1.328693.

[55] R.. Hockney, S.. Goel, J.. Eastwood, Quiet high-resolution computer models of a plasma, J. Comput. Phys. 14 (1974) 148–158. doi:10.1016/0021-9991(74)90010-2.

[56] B. Hess, H. Bekker, H.J.C. Berendsen, J.G.E.M. Fraaije, LINCS: A linear constraint solver for molecular simulations, J. Comp. Chem. 18 (1997) 1463–1472.

[57] S. Miyamoto, P.A. Kollman, Settle: An analytical version of the SHAKE and RATTLE algorithm for rigid water models, J. Comput. Chem. 13 (1992) 952–962. doi:10.1002/jcc.540130805.

[58] T. Darden, D. York, L. Pedersen, Particle mesh Ewald: An N_log(N) method for Ewald sums in large systems, J. Chem. Phys. 98 (1993) 10089–10092.

[59] J.A.R. Willemsen, S.C.B. Myneni, I.C. Bourg, Molecular Dynamics Simulations of the Adsorption of Phthalate Esters on Smectite Clay Surfaces, J. Phys. Chem. C. 123 (2019) 13624–13636. doi:10.1021/acs.jpcc.9b01864.

[60] Y. Wang, J. Wohlert, M. Bergenstråhle-Wohlert, Y. Tu, H. Ågren, Molecular mechanisms for the adhesion of chitin and chitosan to montmorillonite clay, RSC Adv. 5 (2015) 54580–54588. doi:10.1039/c5ra06424d.

[61] F. Razmimanesh, S. Amjad-Iranagh, H. Modarress, Molecular dynamics simulation study of chitosan and gemcitabine as a drug delivery system, J. Mol. Model. 21 (2015). doi:10.1007/s00894-015-2705-2.

[62] Y. Zvulunov, Z. Ben-Barak-Zelas, A. Fishman, A. Radian, A self-regenerating clay-polymer-bacteria composite for formaldehyde removal from water, Chem. Eng. J. 374 (2019) 1275–1285. doi:10.1016/j.cej.2019.06.017.

[63] X.W. Wang, X. Feng, Z. Xu, J.H. Masliyah, Polymer aids for settling and filtration of oil sands tailings, Can. J. Chem. Eng. 88 (2010) 403–410. doi:10.1002/cjce.20283.

[64] Y. Liu, C. Lv, J. Ding, P. Qian, X. Zhang, Y. Yu, S. Ye, Y. Chen, The use of the organic-inorganic hybrid polymer Al(OH)3-polyacrylamide to flocculate particles in the cyanide tailing suspensions, Miner. Eng. 89 (2016) 108–117. doi:10.1016/j.mineng.2016.01.018.

[65] J.L. Suter, P. V. Coveney, R.L. Anderson, H.C. Greenwell, S. Cliffe, Rule based design of clay-swelling inhibitors, Energy Environ. Sci. 4 (2011) 4572–4586. doi:10.1039/c1ee01280k.

[66] H. Lu, Y. Wang, L. Li, Y. Kotsuchibashi, R. Narain, H. Zeng, Temperature- and pH-Responsive Benzoboroxole-Based Polymers for Flocculation and Enhanced Dewatering of Fine Particle Suspensions, ACS Appl. Mater. Interfaces. 7 (2015) 27176–27187. doi:10.1021/acsami.5b09874.

[67] P. Li, M.A. Khan, M. Xia, W. Lei, S. Zhu, F. Wang, Efficient preparation and molecular dynamic (MD) simulations of Gemini surfactant modified layered montmorillonite to potentially remove emerging organic contaminants from wastewater, Ceram. Int. 45 (2019) 10782–10791. doi:10.1016/j.ceramint.2019.02.152.

[68] K. Song, G. Sandí, Characterization of montmorillonite surfaces after modification by

organosilane, Clays Clay Miner. 49 (2001) 119–125. doi:10.1346/CCMN.2001.0490202.

[69] G. Ngnie, D. Baitan, G.K. Dedzo, C. Detellier, Sedimentation of fine particles of kaolinite and polymer-coated kaolinite in cyclohexane: Implications for fines removal from extracted bitumen in non-aqueous processes, Fuel. 234 (2018) 218–224. doi:10.1016/j.fuel.2018.07.032.

[70] Y. Hao, L. Yuan, P. Li, W. Zhao, D. Li, D. Lu, Molecular Simulations of Methane Adsorption Behavior in Illite Nanopores Considering Basal and Edge Surfaces, Energy and Fuels. 32 (2018). doi:10.1021/acs.energyfuels.8b00070.

[71] A.K. Nittala, S.P. Gumfekar, J.B.P. Soares, Multifunctional CO 2 -switchable polymers for the flocculation of oil sands tailings, J. Appl. Polym. Sci. 136 (2019) 1–9. doi:10.1002/app.47578.

[72] D.L. Bish, Rietveld refinement of the kaolinite structure at 1.5 K, Clays Clay Miner. 41 (1993) 738–744. doi:10.1346/CCMN.1993.0410613.

[73] I.C. Bourg, G. Sposito, Molecular dynamics simulations of the electrical double layer on smectite surfaces contacting concentrated mixed electrolyte (NaCl-CaCl2) solutions, J. Colloid Interface Sci. 360 (2011) 701–715. doi:10.1016/j.jcis.2011.04.063.

Chapter 4. Enhanced Adsorption of Anionic Polymer on Montmorillonite by Divalent Cations and the Effect of Salinity

4.1. Introduction

Polymer adsorption at solid-liquid interfaces is ubiquitous in many industrial applications. For example, the adsorption of supramolecular complexes composed of polymers (e.g., poly(diallyldimethylammonium chloride), PDADMAC) on keratinic substrate (hair) is of great interest in the design of conditioner cosmetic formulations [1]. Intercalation of polymer chains (e.g., chitosan) into clay mineral layers in aqueous environment is a widely used method in the fabrication of nanocomposites [2]. In many industrially produced waters, polymeric wastes such as polymeric dyes can be collected via their adsorption onto synthesized adsorbents[3,4], and likewise waste suspensions of fine solids can be treated by polymer flocculants (e.g., polyacrylamide) [5].

In particular, interaction between solid particles in colloidal systems may be modulated by controlled polymer adsorption onto the solid particles. For example, water-soluble cellulose polymers were widely used to regulate the interactions between drug particles in pharmaceutical formulations, promoting their stabilities. Drug particles such as ibuprofen became well dispersed in the suspension due to the steric effect produced by the adsorbed polymer layers [6]. Thickness as well as the composition of the adsorbed layer were among the most important factors affecting the strength of the steric interaction. On the other hand, polymers could also promote aggregation of solid particles and solid-liquid phase separation in many colloidal systems [7,8]. Via adsorption, the polymers could provide hydrogen bonding (H-bonding) sites or charge patches on the surfaces of solid particles, enabling inter-particle attraction. Understanding the behaviors of polymer molecules as they adsorb on solid surfaces is thus of great importance to modulating the properties of colloidal dispersions.

In an aqueous medium, interaction between polymer molecules and solid particles is largely affected by the solution chemistry [9,10]. Certain polymers and solids can become charged from the dissociation and ionization of functional groups into the solution. The charge properties (e.g., charge density, charge distribution or pattern) are sensitive to the constituents of the solution, such as salt ions. The effects of salt ions on solid-polymer interactions have been extensively investigated because of the wide existence of salts in many systems such as cosmetics, wastewater, and drugs [11,12]. Ions have been shown to markedly improve polymer adsorption, especially when the polymer and the solid are like-charged. For example, Ji et al. [13] compared the settling rate of negatively charged solid particles in saline water and freshwater, both treated by Magnafloc 1011 (MF, an anionic copolymer of polyacrylamide and sodium acrylate). The settling relied on MF adsorbing on the fine particles and subsequently bridging them into larger aggregates/flocs. It was shown that the solids settled faster in saline water. The observation was attributed to the compressed electrical double layer caused by high salinity, which led to enhanced polymer adsorption and suppressed electrostatic repulsion among the particles. Zeta potential measurements confirmed such a hypothesis, which showed a less negative surface charge on the solid particles in saline water than in freshwater.

The valence of ions has been shown to have a pronounced effect on the adsorption of polymers on like-charged surfaces in aqueous media[14–19]. Deng et al. [14] studied the impact of cations (Na^+, K^+, Mg^{2+}, Ca^{2+}) on the adsorption of anionic polyacrylamide (APAM) on anionic smectite, using Fourier transform infrared spectroscopy (FTIR) and X-ray diffraction. By comparing the IR-band positions among the APAM-smectite complexes containing different cations, it was deduced that APAM bound more strongly to smectites in solutions containing divalent cations (Mg^{2+}, Ca^{2+}) than those containing monovalent cations (Na^{+}, K^{+}). The adsorption of APAM was believed to be mainly driven by the ion-dipole interactions, which was stronger between the divalent cations and the carbonyl dipole of APAM. Vermöhlen et al. [15] observed a higher adsorption isotherm of polyelectrolytes (polyacrylic acid, polymethacrylic acid, and humic acid) onto oxide surfaces (gibbsite, goethite, and alumina) in 0.0033 M $CaCl_2$ solution, compared with 0.01 M NaCl solution. It was proposed that divalent cations served as bridges between the negatively charged polyelectrolytes and adsorbent, in addition to suppressing the electrostatic repulsion between them. Similar observation was made by Braganca et al. [16], who prepared nanocomposites from montmorillonite (Mt) and styrene-acrylic latex in an aqueous medium, both possessing negative charges. When varying the cation valence, better adhesion between Mt and styrene-acrylic latex was found in the presence of Ca^{2+} than Na^{+}, which was attributed to the formation of Ca^{2+} bridges. However, an opposite observation was reported by Ait-Akbour et al. [17], who measured the adsorption isotherm of PCP (negatively charged polycarboxylate poly(ethylene glycol) ester) in the interlayer space of Mt containing different cations. Mg^{2+}, Ca^{2+} and Na^{+} were considered, and the systems were referred to as Mg-Mt, Ca-Mt, and Na-Mt respectively. Decreased PCP adsorption was found in the interlayer space of Mg-Mt and Ca-Mt compared with Na-Mt. It was postulated that cations were coordinated to water molecules in their solvation. PCP adsorbed to the Mt interlayers via the cations, by displacing the water molecules in the coordination shell of the cations. The displacement of water was argued to be more difficult for Ca^{2+}/Mg^{2+}, based on their more negative solvation energy (-553.6 kJ mol^{-1}/-454.8 kJ mol^{-1}) than Na^{+} (-261.9 kJ mol^{-1}). Other roles of the valence were also proposed. For instance, Santos et al. [18] and Wang et al. [19] performed theoretic calculations that predicted multi-valent cations to promote the adsorption of anionic polyelectrolyte on a like-charged planar surface. They proposed that the enhancement was due to the stronger electrostatic correlation effects brought by the multivalent cations, which could cause the planar surface to be reversely charged.

The effects of multivalent ions on polymer adsorption are also tied to the salinity of the solution. The adsorption isotherm of polyelectrolytes on oxide sufaces in Vermöhlen et al. [15] increased with $CaCl_2$ concentration. This result was explained by the stronger screening of the negative charges on both the solid surfaces and the polymers at higher salt concentration. However, a contradictory conclusion was drawn by Peng et al. [9], who measured the height of clear supernatant of kaolinite suspensions treated by APAM, with 0 mol/dm^3, 0.0005 mol/dm^3, and 0.001 mol/dm^3 of $CaCl_2$. The hydroxyl groups on the surface of kaolinite particles could enable APAM adsorption through H-bonding, followed by the settling of kaolinite particles bridged by the polymer chains. The height of clear supernatant in the suspension would thus increase with solid settling. It was reported that the height of clear supernatant decreased with $CaCl_2$ concentration, suggesting less APAM adsorption at higher salinity. The authors held the view that the presence of Ca^{2+} triggered precipitation of calcium hydroxyl on the active sites of kaolinite, preventing the formation of H-bonds between kaolinite and APAM.

In summary, while the adsorption of anionic polymers on like-charged solid surfaces was generally shown to be promoted by salts, various mechanisms have been proposed from different experimental observations, some seemingly conflicting. Ambiguities on the effect of valence and its interplay with salinity are better addressed if a molecular-level picture can be painted providing direct visualization of the interactions between polymers and solid surfaces. Motivated by this, molecular dynamics (MD) simulation has been employed in this work to study the adsorption of a representative polyanion on an anionic model surface. The objectives were two-fold: to reveal the role of the valence of ions, by simulating both NaCl and $CaCl_2$ solutions; and to address the effect of salinity, by applying a series of different salt concentrations.

4.2. Simulation methods

4.2.1. Models & Systems

APAM was chosen as the representative polyanion, which has been popularly used to enhance solid particle aggregation in colloidal suspensions [9,13,20,21]. The simulated APAM model had a molecular weight (MW) of 641 g/mol ($C_{27}H_{44}N_6O_{12}$, Figure 4.1a), with every third amide group substituted by a carboxylate group, resulting in a charge of -3. All carboxylate groups of APAM were deprotonated to represent a neutral to slightly alkaline pH condition[22,23], which is typical in polymer-clay systems [24]. The solid surface was represented by a negatively charged molecular model of Mt, a common clay mineral [12,25–27]. Mt is an aluminosilicate usually referred to as 2:1 or TOT layer: it is composed of a central sheet with octahedrally coordinated Al atoms, sandwiched between two other sheets with tetrahedrally coordinated Si atoms [28]. A 2 × 2 × 1 supercell was first developed by closely stacking the neutral unit cells in three dimensions, followed by isomorphically substituting three random Al atoms with Mg. The substitution of +3 charged Al atoms by +2 charged Mg atoms in the central octahedral sheet resulted in a local charge deficiency, and the net charge of this supercell became -3. Then the 2 × 2 × 1 cell with a permanent layer charge was expanded to a 16 × 10 × 1 supercell, as shown in Figure 4.1b, carrying a negative charge of -120.

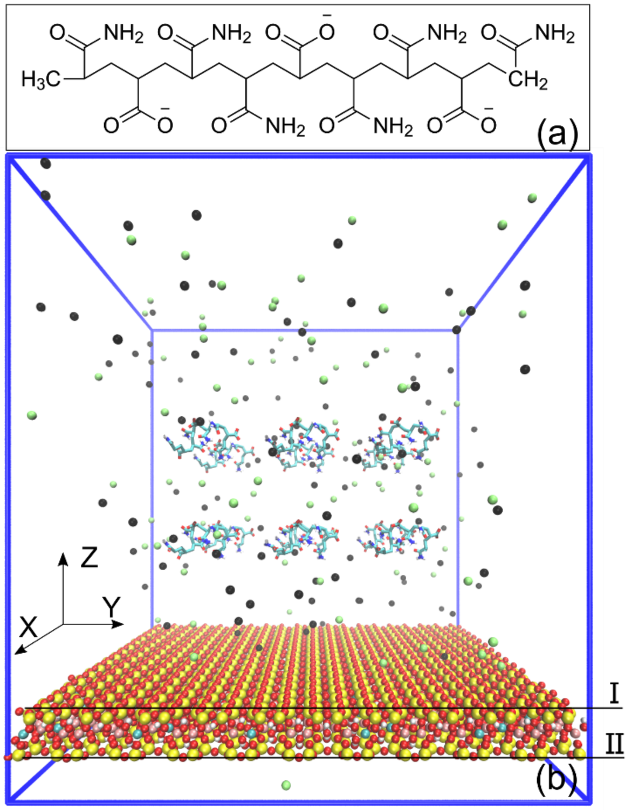

Figure 4.1. (a) Molecular structure of APAM and (b) initial configuration of system Ca-0.1. In (b), Mt is represented by balls, and two basal surfaces are marked by I and II respectively. Color scheme for atoms in Mt: Si (yellow), Al (pink), Mg (cyan), O (red), and H (white). APAM is represented by licorice with C (green) and N (blue). The solvent, water, is removed for clarity, whereas ions are shown as Ca^{2+} (black) and Cl^- (lime).

To investigate the adsorption of APAM on Mt in presence of salts, a series of 7 simulations, divided into two sets, were performed (Table 4.1). The first set investigated the effect of valence of cations, where 0.5 M NaCl was solvated into system Na-0.5 in addition to the Na^+ used to neutralize the negative charges of Mt, and similarly 0.5 M $CaCl_2$ was introduced in system Ca-0.5 in addition to the neutralizing Ca^{2+}. Systems containing only the neutralizing ions were simulated for comparison, namely systems Na-0 and Ca-0. The second set of simulations were run to study APAM adsorption in divalent salt solutions with different concentrations. Three additional systems were simulated, Ca-0.05, Ca-0.1 and Ca-0.3, corresponding to $CaCl_2$ concentration of 0.05 M, 0.1

M and 0.3 M. In each simulation, the supercell of Mt was placed at the bottom of a simulation box with dimension of 8.30 × 8.95 × 10.0 nm^3. A total of 12 APAM molecules were then introduced above the Mt surface in a 2 × 3 × 2 array, followed by solvation of the system with water and an appropriate amount of salt (Table 4.1). The initial configuration for Mt and APAM was the same for all systems and is represented by Figure 4.1b.

Table 4.1. Simulated Systems

system name	neutralizing ions	additional salt
Na-0	156 Na^+	0
Ca-0	78 Ca^{2+}	0
Na-0.5	156 Na^+	0.5 M NaCl
Ca-0.5	78 Ca^{2+}	0.5 M $CaCl_2$
Ca-0.3	78 Ca^{2+}	0.3 M $CaCl_2$
Ca-0.1	78 Ca^{2+}	0.1 M $CaCl_2$
Ca-0.05	78 Ca^{2+}	0.05 M $CaCl_2$

4.2.2. Simulation details

The force field parameters for Mt and APAM have been developed and validated in our previous work[29]. Briefly, the molecular topology of APAM was created by submitting its molecular structure to the GlycoBioChem PRODRG server [30]. Because PRODRG is compatible with GROMOS96 53A6 force field [31], the parameters for intra- and inter-molecular potentials were automatically generated. To confirm the accuracy of the partial atomic charges, geometrical optimization was performed using density functional theory (DFT) at B3LYP/6-31+G (d) level in

Gaussian 16 [32], followed by charge calculation using the CHelpG method [33]. Manual adjustment of partial atomic charges was then made to the topology file. More details on the topology of APAM were given in Appendix C, section C1.1. SPC water model was adopted for the solvent and the ions were represented by GROMOS96 53A6 force field. Parameters for Mt were adopted from the CLAYFF force field [34,35] with all partial atomic charges unaltered.

The MD simulations were carried out in the GROMACS package[36–38] under NPT ensemble (isotropic pressure coupling) for 80 ns. Due to the application of periodic boundary conditions, the atoms in the simulation box were effectively moving between two charged Mt surfaces: plane I in Figure 4.1b and plane II in the periodic image above. Therefore, unless otherwise specified any reference to Mt surface hereafter includes the consideration of both planes I and II. Before the NPT run, each system was minimized by the steepest descent method so as to limit the maximum force to 1000.0 kJ/(mol·nm), followed by equilibration in NVT ensemble for 100 ps. Nose-Hoover thermostat[39,40] and Parrinello–Rahman barostat[41] were employed to control the temperature and pressure at 300 K and 1 bar respectively. Equations of motions were integrated using the Leap-frog algorithm[42], with a time step of 1 fs. Constraints were applied to all the bonds using the LINC algorithm[43], except those in water which were constrained using the SETTLE algorithm. Cut-off distances for van der Waals and electrostatic interactions were both set to be 1.0 nm. PME method was used to calculate the long-range electrostatic interactions[44].

4.3. Results and Discussion

4.3.1. Effect of cation valence on APAM adsorption

Systems Na-0, Na-0.5, Ca-0, Ca-0.5 in the first set of simulations were used to study the role of valence in the adsorption of APAM on Mt. Snapshots of the final configurations for these systems are shown in the Appendix C, section S1.2. The density profiles (number per unit volume) of carbonyl oxygens (CO) near the Mt surface are shown in Figure 4.1a, plotted against *Z* coordinate, defined as the vertical distance measured upwards from the basal plane I of Mt (see Figure 4.1b). The profiles of other key atoms of APAM (amide N and carboxylate oxygen COO^-) are showed in Appendix C, Section C1.3, which correlated well with the density profile of CO.

Examination of the minimum distance between CO atoms and Mt surface demonstrated that CO became adsorbed at $Z \leq 0.43$ nm from the Mt surface (refer to Appendix C, section C2.4 for more discussion on this criterion). Consider first the cases of monovalent ions, systems Na-0 and Na-0.5. The number density of CO remained ~0 when $Z < 0.5$ nm. The result shows that when there were no extra salts added and the aqueous environment contained only neutralizing monovalent ions (Na^+), it was difficult for the anionic polymer to approach Mt. In system Na-0.5 where 0.5 M NaCl was added besides the neutralizing Na^+, density of CO remained higher than that in system Na-0 near the Mt surface ($Z < 3.8$ nm). However, the values were still ~0 for $Z \leq 0.43$ nm, suggesting that it was still difficult for the polymer molecules to form stable adsorption on the surface in system Na-0.5.

Ions distributions, in terms of number density, near the Mt-water interface are shown in Figure 4.2b. The plot against full range of *Z* ($Z = 0\text{-}10$ nm) is shown in Appendix C, section C1.3. Because of the periodic boundary condition, increase in *Z* corresponds to departure from plane I and approach to plane II in the periodic image above. Since planes I and II have the same surface properties, the distributions were found to be symmetric about $Z = 4.7$ nm (thickness of the Mt model was ~0.6 nm), and the number densities were constant between $Z = 3.7$ and 5.7 nm representing the bulk solution (see Figure C3). Thus, in Figure 4.2b, only the results for $Z < 3$ nm are shown.

The formation of electric double layer (EDL) was observed from the density profiles of counterions and co-ions[45]. Taking system Na-0.5 as an example, Na^+ displayed a pronounced peak at $Z = 0.4$ nm where the density of Cl^- was still 0. The region with $Z = 0\text{-}0.4$ nm can therefore be identified as the "stern layer" according to the EDL theory[46]. After $Z = 0.4$ nm, the density of co-ions (Cl^-) began to grow while the density of counterions (Na^+) decreased until both converged to the bulk value at $Z = 1.39$ nm (refer to Appendix C section C2.1 for more details). The region where $Z = 0.4\text{-}1.39$ nm can be identified as the "diffuse layer". Stern layer and diffuse layer were divided by the outer Helmholtz plane (OHP), which corresponded to $Z = 0.4$ nm in this case. The outer location of the diffuse layer, 1.39 nm here, is a measure of the thickness of the EDL, at which the surface charge of Mt became neutralized (the cumulative charges for each system are shown in Appendix C, section C1.4). The locations for the OHP and outer boundary of the EDL are marked in Figure 4.2b for all the systems. As shown in the figure, the thickness of the EDL in system Na-0.5 (1.39 nm) was smaller than that in system Na-0 (2.49 nm), consistent with the prediction from the Poisson-Boltzmann (PB) theory where the "decay length" reduces as salinity is increased.

In contrast to systems Na-0 and Na-0.5 where stable adsorption was absent, adsorption was observed when the neutralizing ions were replaced by Ca^{2+}, even without adding extra salts. As shown in Figure 4.2a, in system Ca-0, CO atoms started accumulating before $Z = 0.43$ nm, indicating that they became adsorbed. In Figure 4.2b the counterions (Ca^{2+}) converged to the bulk density at $Z = 1.90$ nm in system Ca-0, faster than the counterions in system Na-0. Similarly, ion densities in system Ca-0.5 converged to their bulk values at a shorter distance ($Z = 1.35$ nm) than that in system Na-0.5. To conclude, the EDL was suppressed by replacing monovalent ions with divalent ions ($Na^+ \rightarrow Ca^{2+}$); meanwhile adsorption of CO atoms on the surface was observed.

The number of adsorbed CO atoms was calculated by integrating the density profile in Figure 4.2a from both Mt surfaces to the distance of 0.43 nm from them. The results are summarized in Table 4.2, along with the thickness of EDL determined from Figure 4.2b and the Debye length predicted by PB theory. The number of adsorbed CO atoms followed the order of Na-0 = Na-0.5 < Ca-0.5 < Ca-0. The thickness of the EDL and the predicted Debye length followed the same sequence of Na-0 > Ca-0 > Na-0.5 > Ca-0.5. Interestingly, significantly enhanced adsorption was observed from Na-0.5 to Ca-0 evidenced by the much larger amounts of adsorbed CO in Ca-0, while the thickness of EDL was larger in system Ca-0. In addition, less adsorption was found in Ca-0.5 than in Ca-0 although the EDL was ~57% thinner in Ca-0.5. It can thus be inferred that besides suppressing the EDL, divalent Ca^{2+} played other roles in the adsorption of APAM on Mt.

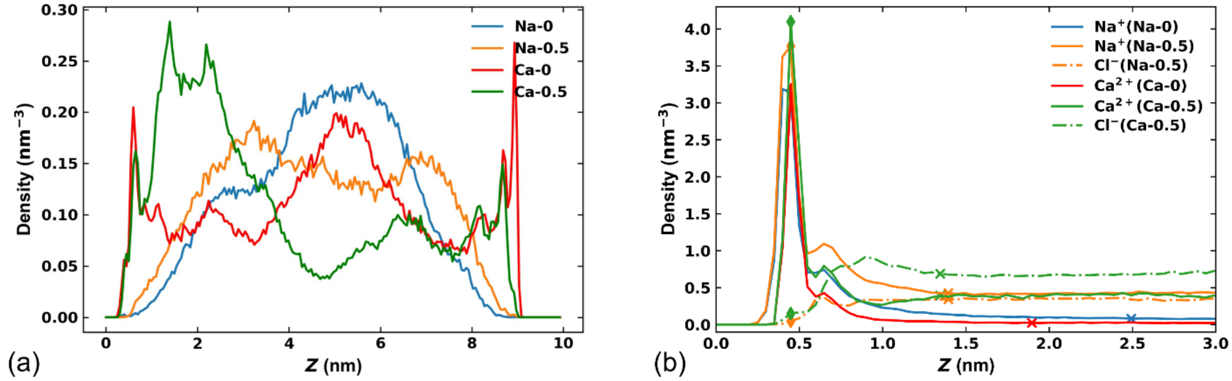

Figure 4.2 (a) Density profiles of carbonyl oxygens along *Z* axis, averaged over the last 20 ns of the simulations. (b) Density profile of counterions ions and co-ions along the *Z* axis, averaged over the last 20 ns of the simulations. For each system, the location of OHP is marked with diamond symbol, and the location where the EDL ends is marked with '×' symbol.

Table 4.2. Summary of number of adsorbed CO atoms, EDL thickness, and decay length predicted by PB theory

system	No. adsorbed CO atoms in last 20 ns	thickness of EDL [a] (nm)	Debye length [b] (nm)
Na-0	0.02	2.49	0.73
Na-0.5	0.02	1.39	0.37
Ca-0	2.16	1.90	0.51
Ca-0.5	0.37	1.35	0.22

a. The calculation of EDL thickness for all systems are shown in Appendix C, section C2.1. b. Predicted by PB theory, a measure of the EDL thickness. The Debye length κ^{-1} was calculated from $\kappa^{-1} = \left(\frac{\varepsilon_0 \varepsilon k_B T}{\sum C_i e^2 z_i^2}\right)^{\frac{1}{2}}$, where ε_0 is the permittivity of vacuum, ε is dielectric constant (78.4 for water), k_B is the Boltzmann constant, T is the temperature (300 K), C_i is the number density of i^{th} ion, z_i is the valence of i^{th} ions, and e is the elementary charge. The number of counterions (Na^+/Ca^{2+}) and co-ions (Cl^-) in each system are shown in Appendix C, section C2.2.

4.3.2. Coordination to divalent ions

To further probe the role of Ca^{2+}, radial distribution functions (RDFs) of APAM carbonyl oxygen (CO), carboxylate oxygen (COO^-), and water oxygen (Ow) around Ca^{2+} in system Ca-0.5 are shown in Figure 4.3a. The first peak in the RDF of water was at ~0.25 nm (see enlarged inset in Figure 4.3a), indicating the solvation of Ca^{2+} ions [47]. Meanwhile, the first peak in the RDF of carbonyl oxygen was located at ~0.24 nm, suggesting that APAM formed a stable complex around Ca^{2+} at a distance similar to water.

To better understand the interactions of water and APAM with Ca^{2+}, system Ca-0.5 was examined in more detail by tracking two representative Ca^{2+} ions in the EDL, marked as Ca^{2+}_1 and Ca^{2+}_2. Based on 2000 snapshots uniformly sampled from the last 20 ns of the simulation, the number of water oxygens within 0.25 nm of Ca^{2+}_1, denoted by N, was calculated and plotted in Figure 4.3b (left panel, green segments) as a function of time. The histogram for N is shown in the same figure (right panel, green bars). As shown in the histogram, N was nearly normally distributed, and 92% of the data were in the interval of N = 4-7. Besides, all the atoms within 0.25 nm of Ca^{2+}_1 were found to be water oxygens after analyzing the atom types (refer to Appendix C, section C2.3 for calculation details). This indicates the formation of a hydration shell around Ca^{2+}_1 by 4-7 water oxygens at the distance of 0.25 nm. Ca^{2+} ions and water oxygens are known to form coordinate covalent bonds[48]. The center Ca^{2+} and the surrounding water oxygens constituted a coordination complex. The coordinate bond length (0.25 nm) suggested by the first peak in the RDF of water around Ca^{2+}, as well as the number of water oxygens per Ca^{2+} in the first coordination shell (4-7), are in good agreement with previous reports[48].

While the atoms within 0.25 nm of Ca^{2+}_1 were entirely water oxygens, atoms within 0.25 nm of Ca^{2+}_2 included two types, water oxygens and APAM CO. N vs. time for Ca^{2+}_2 is shown as red dots in the left panel of Figure 4.3b and the corresponding histogram is shown in the right panel as red bars. Here, 93% of the data fell into the range of 3-6, suggesting that Ca^{2+}_2 was coordinated to 3-6 water oxygens for most of the time. This range was lower than the number of water oxygens coordinated to Ca^{2+}_1. The '×' symbol in Figure 4.3b (left panel) represents the number of CO within 0.25 nm of Ca^{2+}_2, which fluctuated between 1-2. It can thus be deduced that in the first coordination shell of Ca^{2+}_2, 1-2 water oxygens were displaced by CO, while the same number of total oxygens were maintained as in the first coordination shell of Ca^{2+}_1. The close proximity between CO and Ca^{2+}_2 led to the formation of a Ca^{2+}-APAM complex.

While CO formed stable complex with Ca^{2+}, the number of COO^- oxygens that coordinated to Ca^{2+} was collected in Appendix C, section C1.6. Table C2 showed that the binding of COO^- to Ca^{2+} was much less prominent than CO, which was also consistent with the weaker peak intensity of the COO^- RDF around Ca^{2+} shown in Figure 4.3a. The number of CO that coordinated to Na^+ is also shown in Table C2, where the binding of CO to Na^+ was much less favored compared with Ca^{2+}, suggesting that the replacement of water by APAM in the first coordination shell of Na^+ was much weaker."

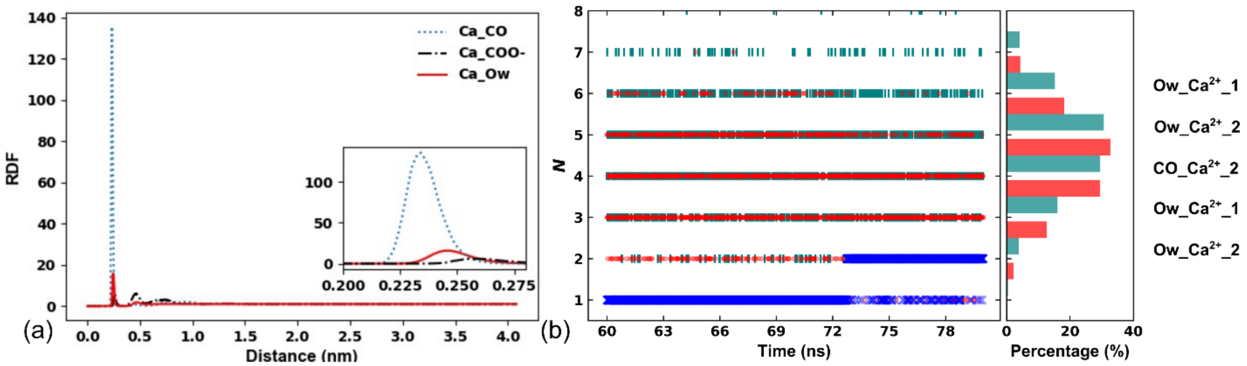

Figure 4.3. (a) RDFs of carbonyl oxygens of APAM (Ca_CO), carboxyl oxygens of APAM (Ca_COO$^-$), and water oxygens (Ca_Ow) around Ca^{2+} in system Ca-0.5. (b) Number (*N*) of water oxygens within 0.25 nm of Ca^{2+}_1 (left panel, green segments, one data every 1 ps) and statistical histograms for *N* (right panel, green bars). Corresponding data for Ca^{2+}_2 is shown as red dots for *N* vs. time and red bars in the histogram. Blue '×' in the left panel represents the carbonyl oxygens of APAM within 0.25 nm of Ca^{2+}_2. All data points were sampled from the last 20 ns simulation of system Ca-0.5.

To explore whether the coordination of APAM to Ca^{2+} was related to its adsorption on Mt, a three-dimensional (3-D) map was created to show the locations of adsorbed APAM CO that were simultaneously coordinated to at least one Ca^{2+} ions. Such a map is shown in Figure 4.4a for system Ca-0.5, based on data from the last 20 ns of the simulation (corresponding maps for systems Ca-0, 0.05, 0.1, 0.3 are given in Appendix C, Section C1.4). To generate this map, a Ca^{2+} ion and a CO atom were said to be coordinated if this CO atom was within 0.24 nm of the Ca^{2+} ion (location of first peak in the RDF of CO around Ca^{2+} in Figure 4.3a), suggesting the formation of a Ca^{2+}-APAM complex. All CO atoms that were both adsorbed (refer to Appendix C, Section C2.4 for more discussion on this criterion) to Mt and coordinated to Ca^{2+}, i.e., those adsorbed from Ca^{2+}-APAM complexes, were mapped onto Figure 4.4a, with their *X*, *Y* coordinates as defined in Figure 4.1b, as well as their distance *D* to the nearest Mt surface (plane I or the periodic image of plane II). The Ca^{2+} ions in those adsorbed Ca^{2+}-APAM complexes were also mapped onto Figure 4.4a in the same way.

In Figure 4.4a, the Ca^{2+} ions stayed at an average distance of 0.42 nm from Mt, around the OHP (see Figure 4.2b). The CO atoms were located at a closer distance (average around 0.35 nm) within the stern layer of Mt. Therefore, unlike what was hypothesized in some literature [49], the Ca^{2+} ions did not serve as bridges sandwiched between APAM and Mt. Instead, our results showed that the Ca^{2+}-APAM complexes, which resulted from the coordination of carbonyl groups to solvated Ca^{2+}, carried residual positive charges and were subsequently attracted to Mt. Figure 4.4b shows an image of a Ca^{2+}-APAM complex near the OHP of the Mt surface. As shown in the enlarged area, there were five water oxygens and one APAM CO in the first coordination shell of the Ca^{2+} ion; the CO and Ca^{2+} were at similar distances from Mt in this image. The ability of Ca^{2+} to form a coordination complex with APAM and the lack of such ability by Na^+ was the main reason for the significant improvement in adsorption from the Na^+ systems to the Ca^{2+} systems as seen in Table 4.2.

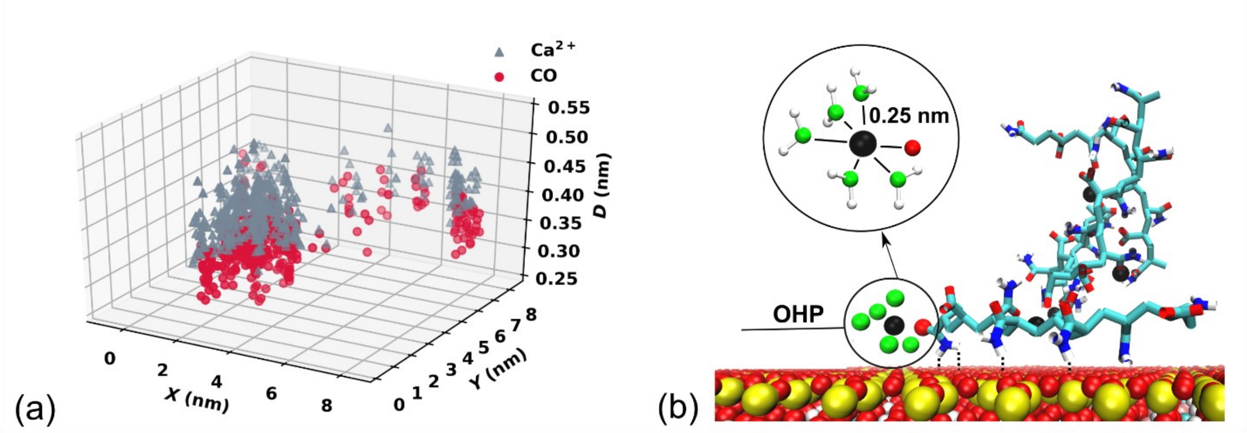

Figure 4.4. (a) 3-D map of CO and Ca^{2+} in Ca^{2+}-APAM complexes adsorbed on Mt, data from the last 20 ns of the simulation for system Ca-0.5. (b) Snapshot extracted from system Ca-0.1 at 65 ns. Green spheres represent water oxygen, while the other atoms are in the same color scheme as in Figure 4.1b.

4.3.3. Non-monotonic influence of salinity on the adsorption of Ca^{2+}-APAM complexes

One interesting observation from Table 4.2 was that APAM adsorption appeared to be reduced as the concentration of $CaCl_2$ increased from 0 to 0.5 M. To further investigate the effect of salinity, additional simulations were performed with $CaCl_2$ concentrations of 0.05 M, 0.1 M and 0.3 M. Snapshots of final configurations of these systems are shown in Appendix C, Section C1.1. Figure 4.5a shows the average number of Ca^{2+}-APAM complexes adsorbed on the Mt surface (N_{cpl}). N_{cpl} was determined in the same way as described in section 3.2, by counting the number of adsorbed APAM CO that were simultaneously coordinated to at least one Ca^{2+} ions. N_{cpl} was ~0.9 in system Ca-0, where the number of Ca^{2+} was just enough to neutralize the system. When the concentrations of $CaCl_2$ increased to 0.05 M and 0.1 M, N_{cpl} increased to 1 and 2, respectively. However, the increasing trend of N_{cpl} reversed when the concentration of $CaCl_2$ reached 0.3 M ($N_{\mathrm{cpl}} = 0.6$) and continued decreasing to $N_{\mathrm{cpl}} = 0.2$ at $CaCl_2$ concentration of 0.5 M, both lower than the value in system Ca-0.

To understand the non-monotonic trend of N_{cpl} with salinity, the cumulative charges around Mt were calculated and displayed in Figure 4.5b (results for full range of Z are given in Appendix C, Section C1.3). In system Ca-0, because of the distribution of counterions and APAM molecules in the EDL, the Mt surface charge was gradually compensated until the cumulative charge approached zero in the bulk solution. However, when additional $CaCl_2$ was added, the PB theory failed, and the charge of Mt was overcompensated. This phenomenon can be attributed to the "ion-correlation" effect, in which ions are no longer treated as point charges but have finite volume. It was shown that when electrostatic correlation was considered among ions with finite volume, free energy minimization of the system would lead to a surface charge reversal, and the "ion-correlation" effect was more prominent for multivalent ions than monovalent ions [50–52].

The average number of Ca^{2+} ions coordinated to each APAM molecule (including both adsorbed and unadsorbed ones) is plotted in the inset of Figure 4.5b (calculation details are in Appendix C, Section C2.5). As shown in Figure 4.4a, for the adsorbed Ca^{2+}-APAM complexes, the Ca^{2+} and CO were mostly within or around the OHP ($Z = 0.4$ nm) of Mt. In system Ca-0, the cumulative charge was negative around the OHP. The average number of Ca^{2+} coordinated to each APAM molecule was ~0.83, less than the Ca^{2+} needed to neutralize each APAM molecule (1.5 since each APAM carried a charge of -3). As a result, on average the electrostatic interaction between Ca^{2+}-APAM complexes and Mt was repulsive, which hindered their adsorption. In system Ca-0.05, the cumulative charge was also negative at OHP and became close to 0 after $Z = 0.65$ nm. The average number of Ca^{2+} coordinated to each APAM was around 1.33, indicating that the Ca^{2+}-APAM complexes were close to charge neutrality and their repulsion with Mt diminished. The cumulative charge around Mt in system Ca-0.1 was similar to that in Ca-0.05, negative at OHP and close to neutral after $Z = 0.65$ nm. The average number of Ca^{2+} coordinated to APAM was 1.65, thus the Ca^{2+}-APAM complexes carried a residual positive charge and were attracted by the long-range electrostatic interaction to the OHP. However, when the ion concentration further increased, i.e., represented by systems Ca-0.3 and Ca-0.5, the cumulative charge around Mt was positive after the OHP. Meanwhile, the average numbers of Ca^{2+} coordinated to each APAM were more than 1.5, resulting in residual positive charges. Hence there was a long-range electrostatic repulsion between the Ca^{2+}-APAM complexes and the OHP preventing the accumulation of the complexes in the EDL. To conclude, the adsorption of Ca^{2+}-APAM complexes on Mt surface had a non-monotonic dependence on Ca^{2+} concentration because the concentration regulated both the charge of the Ca^{2+}-APAM complexes and the cumulative charge near Mt surfaces, determining the long-range electrostatic interaction between them.

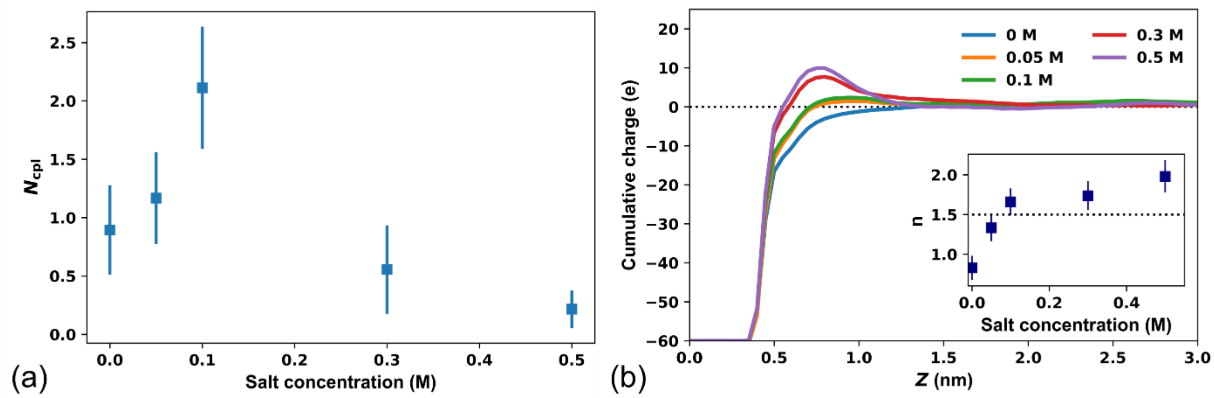

Figure 4.5. (a) Number of Ca^{2+}-APAM complexes adsorbed on Mt surfaces in systems Ca-0, 0.05, 0.1, 0.3 and 0.5. (b) Cumulative charges of Mt, APAM and ions in systems Ca-0, 0.05, 0.1, 0.3 and 0.5, as a function of *Z* coordinate. Average number (n) of Ca^{2+} coordinated to each APAM molecule is shown as inset. In (a) and inset of (b), error bar represents the standard deviation of data, which were collected from the last 20 ns of the simulation.

4.3.4. APAM adsorption through H-bonding facilitated by Ca^{2+} coordination

While the Ca^{2+} and CO of adsorbed Ca^{2+}-APAM complexes were located, on average, at a distance of 0.35-0.42 nm from Mt (see Figure 4.4a), the minimum distance between adsorbed APAM molecules and Mt was within 0.23 nm (see Appendix C, Section C2.4). This shorter distance suggests that other atom groups were forming closer contact with Mt. Analysis of the APAM atoms within 0.23 nm of Mt showed that all of them were hydrogens in the amino groups, which formed direct H-bonding with the surface oxygen of Mt. Hence, while the coordination of Ca^{2+} with APAM and the formation of Ca^{2+}-APAM complexes facilitated the long-range electrostatic attraction and the approach of the complexes to Mt, the short-range H-bonding stabilized the adsorption on the surface. The advantage of this synergy was that there was no competition of active sites on APAM between Ca^{2+} coordination and H-bonding. As illustrated in Figure 4.4b, H-bonds were formed through the amino groups in the amides of APAM, with H atoms pointing towards the oxygens of Mt, while Ca^{2+}-APAM complexes were formed through the carbonyl oxygens in the amides.

To quantify the synergetic effect above, the number of adsorbed APAM molecule is shown in Figure 4.6 as a function of time. Also shown are the percentage of CO in the adsorbed APAM that contributed to the formation of adsorbed Ca^{2+}-APAM complexes, as well as the percentage of amino hydrogens in the adsorbed APAM that contributed to H-bonding with Mt (more calculation details in Appendix C, section C2.6). These three quantities changed with time in synchronous manner and were highly correlated, confirming the synergy between Ca^{2+} coordination and H-bonding in APAM adsorption.

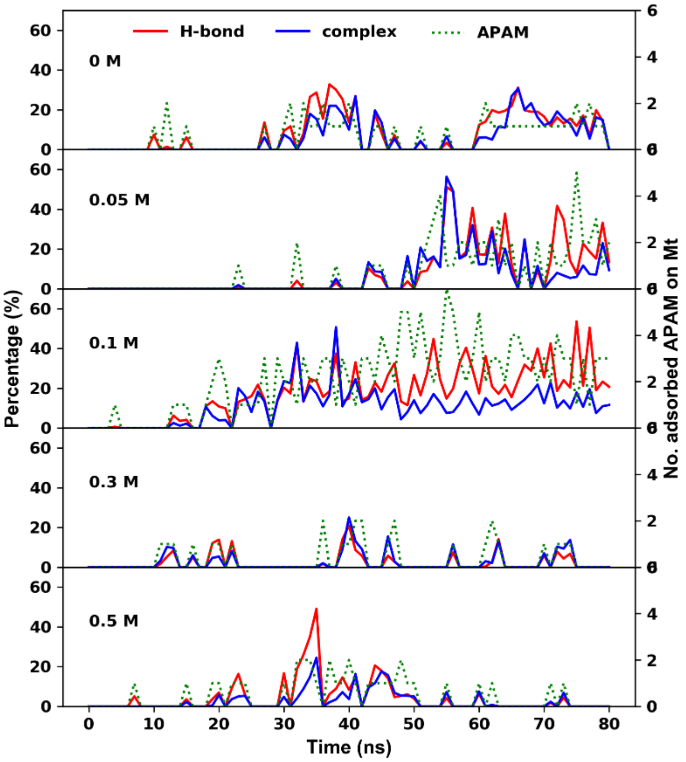

Figure 4.6. Percentage of CO in adsorbed APAM that contributed to the formation of adsorbed Ca^{2+}-APAM complexes (blue solid curve, left axis), percentage of amino hydrogen in adsorbed APAM that contributed to H-bonding with Mt (red solid curve, left axis), and number of adsorbed APAM molecules on Mt (green dashed line, right axis), in systems Ca-0, 0.05, 0.1, 0.3, and 0.5 respectively. Each point is an average of 100 sample points within the previous 1 ns.

In Figure 4.6, the number of adsorbed APAM molecules in all systems was less than 12, the total number of APAM in the simulation box. This result indicates that a fraction of the APAM molecules stayed in the bulk solution without being adsorbed on Mt. Analysis of these unadsorbed APAM revealed that Ca^{2+}-APAM complexes still formed (see Appendix C, Section C1.5 for details), affecting the cumulative charge around APAM. In addition, for the adsorbed APAM, the contribution from the Ca^{2+}-APAM complexes within could be significant. For example, when 0.05 M $CaCl_2$ was added, as high as 56% (at 56 ns) of the CO in the adsorbed APAM molecules was adsorbed on Mt in the form of complexes, stabilizing the polymer adsorption. It is worth mentioning that APAM could adsorb on Mt either as monomers or in the form of clusters. H-bonding as well as Ca^{2+} coordination between different APAM molecules both contributed to the clustering. Detailed illustration of APAM-APAM interaction can be found in Appendix C, section C1.8.

4.3.5. Discussion

Several mechanisms have been proposed in the literature for polymer adsorption mediated by divalent ions. Some argued that the charges of the solid and polymers were suppressed by the ions due to the screening effect [13], or even reversed due to ion correlation [18,19]. Some proposed that counterions became adsorbed on the polymers and/or solid through coordination and water displacing, and that the solid and polymers were bridged in the configurations of polymer-cation-solid [17] or polymer-water-cation-solid [14].

As revealed by the atomistic results in this work, when divalent ions were present, APAM tended to bind to Ca^{2+} by displacing 1-2 water in the first coordination shell of Ca^{2+}, forming Ca^{2+}-APAM complexes. The displacement of water was supported by the experimental study of Ait-

Akbour et al. [17] in which water loss was reported upon the adsorption of anionic PCP on Mt interlayer. In addition, our results showed when the Ca^{2+}-APAM complex was attracted to the Mt surface, Ca^{2+} ions were located slightly further from Mt than the carbonyl oxygens of APAM, instead of forming a bridging structure in the form of APAM-Ca^{2+}-Mt or APAM-water-Ca^{2+}-Mt. Meanwhile, direct H-bonds were formed between the amino groups of APAM and surface oxygens of Mt, and there was a strong positive correlation between the degree of coordination, the number of H-bonds and the amount of APAM adsorption.

This work presented several new discoveries that differed from previous reports. Braganca et al. [16] attributed Ca^{2+}-enhanced anionic styrene-acrylic adsorption on Mt to “ion bridging” where Ca^{2+} ions were suggested to be located between Mt and styrene-acrylic. Deng et al. [14] proposed that the adsorption of APAM on smectite could be promoted through water bridges, where H-bonds were formed between APAM and water in the solvation shell of Ca^{2+}. Such bridging structures, in the form of APAM-Ca^{2+}-Mt or APAM-water-Ca^{2+}-Mt, were not observed in our simulations. Peng et al. [9] reported that Ca^{2+} could suppress H-bonding between APAM and kaolinite due to the competition of active sites, while our results showed the promotion of H-bonding by Ca^{2+}. In fact, our results demonstrated a new adsorption mechanism where different active sites on the APAM interact with different entities to cooperatively enhance the adsorption. The carbonyl oxygens were coordinated to Ca^{2+} while the nearby amino groups were H-bonded to Mt (see Figure 4.4b). This arrangement was able to simultaneously promote Ca^{2+}-APAM interaction and APAM-Mt interaction. The cooperative interactions enabled by the different active sites of APAM also removed the requirement of an explicit “bridge” (Ca^{2+} or water) for the adsorption, as the amino groups were brought sufficiently close to Mt to establish the short-range stabilizing H-bonds.

Compared with divalent ions (Ca^{2+}), monovalent ions (Na^+) had two disadvantages in promoting APAM adsorption on Mt. The first is the less screening of the electrostatic repulsion between APAM and Mt. More importantly, Na^+ lacked the ability to form Na^+-APAM complexes through coordination (Table C2). The long-range electrostatic interaction driving the Ca^{2+}-APAM complexes towards the solid was therefore missing, making it difficult to establish stable short-ranged interactions such as H-bonding.

Because the long-range electrostatic interaction regulated the initial approach of the polymers towards the solid, the effect of divalent ions on adsorption was concentration dependent. Our work showed a non-monotonic trend between the number of adsorbed Ca^{2+}-APAM complexes and the salt concentration, which provides explanations for several conflicting reports on the effect of ion concentration[9,15]. Increasing the dosage of multi-valent salts may promote or impede the polymer adsorption, depending on both the charge of the Ca^{2+}-APAM complexes and cumulative charge near the solid surface, the latter may be reversed as a result of ion correlation.

Several limitations exist in this work. Ions distribution as well as polymer adsorption vary with surface properties of the solid [47,53–55]. In this work, basal surface of Mt was selected to represent the solid for polymer adsorption. However, other types of surfaces exist in practical applications which might lead to different adsorption behaviors. For example, Bourg et al. [56] showed that when atom substitution on the basal surface of mica (sharing similar structure to Mt) was on the tetrahedral sheet instead of the octahedral sheet in this work, the counterions were adsorbed by forming inner surface complexes and an inner Helmholtz plane (IHP) could be identified. Besides, hydroxyl groups also exist on many solid surfaces, such as basal/edge surface of kaolinite and edge surface of Mt, which can promote the formation of H-bonds.

Lastly, as in any MD simulations using classical force fields, the force field parameters can have some influence on intermolecular interactions. For instance, Moucka et al. [57] demonstrated that physical properties such as density and chemical potential of $CaCl_2$ could be well modeled by classical force field (transferable $CaCl_2$ force field for Ca^{2+}, Dang-Smith force field for Cl^- and SPC/E water model) at ambient conditions when the salt concentration was less than 1 mol kg^{-1}, while the prediction was poor at elevated temperature and pressure and high concentrations. Here in this work, we used CLAYFF for Mt, SPC model for water, and GROMOS force field for APAM and ions. There were extensive evidences [58–60] for the good compatibility of the three force fields, including our own validation [29]. Our simulations were performed under ambient conditions and the highest salt concentration used was 0.47 mol kg^{-1}, which is well within the regime where faithful modeling of aqueous $CaCl_2$ solution is expected. Nevertheless, as an exercise, we tested a different force field namely OPLSAA [61] for the APAM molecule and ions. Results from the additional simulation (Appendix C, section C1.7) showed that the preferential coordination of Ca^{2+} with CO, as compared with COO^-, still held but the preference was less prominent. This sensitivity to force field is not surprising since classical force fields require the atomic charges to be constant while charge transfer may play a role in ion-polymer coordination. Additional DFT calculations (Appendix C, section C1.7) did not show clear evidence that one force field (GROMOS or OPLSAA) was superior to the other, and extensively testing other force fields is out of the scope of this work. The adsorption mechanism reported in this work did hold for both force fields that we tested, including the lack of Ca^{2+} bridges and synergy with H-bonding, but future studies may have a more in-depth look at the force field dependence.

4.4. Conclusions

The adsorption of anionic APAM on Mt in saline solutions was investigated by all-atoms MD simulations. Divalent ions (Ca^{2+}) showed a much better enhancement of the polymer adsorption than monovalent ions (Na^{+}). Besides the better charge screening ability, Ca^{2+} was coordinated to the carbonyl oxygens of APAM, resulting in the formation of Ca^{2+}-APAM complexes. The Ca^{2+}-APAM complexes were subsequently captured into the EDL of Mt, but without the need of Ca^{2+} bridges. While the long-range electrostatic attraction drove the approach of Ca^{2+}-APAM complexes to Mt, short-range H-bonding formed directly between APAM and Mt provided an important stabilizing mechanism for the adsorption. A strong positive correlation was found between the degree of coordination, the number of H-bonds and the amount of APAM adsorption. A delicate balance was discovered when varying the concentration of $CaCl_2$. The best adsorption performance required an optimal concentration that did not under-neutralize or over-neutralize the charges of Mt or APAM. This work is a unique contribution to the fundamental understanding of polymer adsorption promoted by multi-valent ions. To our knowledge, it is the first atomistic-level study that examined the interplay of charge screening, ion-ion correlation, cation coordination and hydrogen bonding for the adsorption of anionic polymer on like-charged solid surface. The results demonstrated a new mechanism of synergetic adsorption and explained the long-standing debate on the effect of salinity. New insights gained through this work highlighted the value of using molecular simulations to study polymer adsorption at a resolution much finer than that in experiments. Besides contributing to fundamental understanding, the present work also shed light onto applications in soil remediation, pharmaceutical formulation, wastes consolidation, cosmetics design, hydrogel fabrication, and many others. Future work involving different surfaces can allow us to further address the effect of surface properties on polymer adsorption.

References

[1] S. Llamas, E. Guzmán, N. Baghdadli, F. Ortega, C. Cazeneuve, R.G. Rubio, G.S. Luengo, Adsorption of poly(diallyldimethylammonium chloride)—sodium methyl-cocoyl-taurate complexes onto solid surfaces, Colloids Surfaces A Physicochem. Eng. Asp. 505 (2016) 150–157. doi:10.1016/j.colsurfa.2016.03.003.

[2] J. Ji, H. Xiong, Z. Zhu, L. Li, Y. Huang, X. Yu, Fabrication of Polypyrrole/Chitosan Nanocomposite Aerogel Monolith for Removal of Cr(VI), J. Polym. Environ. 26 (2018) 1979–1985. doi:10.1007/s10924-017-1095-1.

[3] A. Kausar, M. Iqbal, A. Javed, K. Aftab, Z. i. H. Nazli, H.N. Bhatti, S. Nouren, Dyes adsorption using clay and modified clay: A review, J. Mol. Liq. 256 (2018) 395–407. doi:10.1016/j.molliq.2018.02.034.

[4] Y. Zvulunov, Z. Ben-Barak-Zelas, A. Fishman, A. Radian, A self-regenerating clay-polymer-bacteria composite for formaldehyde removal from water, Chem. Eng. J. 374 (2019) 1275–1285. doi:10.1016/j.cej.2019.06.017.

[5] H. Lu, Y. Wang, L. Li, Y. Kotsuchibashi, R. Narain, H. Zeng, Temperature- and pH-Responsive Benzoboroxole-Based Polymers for Flocculation and Enhanced Dewatering of Fine Particle Suspensions, ACS Appl. Mater. Interfaces. 7 (2015) 27176–27187. doi:10.1021/acsami.5b09874.

[6] S.L. Law, J.B. Kayes, Adsorption of non-ionic water-soluble cellulose polymers at the solid-water interface and their effect on suspension stability, Int. J. Pharm. 15 (1983) 251–

260. doi:10.1016/0378-5173(83)90159-X.

[7] H. Xiao, Z. Liu, N. Wiseman, Synergetic effect of cationic polymer microparticles and anionic polymer on fine clay flocculation, J. Colloid Interface Sci. 216 (1999) 409–417. doi:10.1006/jcis.1999.6342.

[8] O. Molatlhegi, L. Alagha, Adsorption characteristics of chitosan grafted copolymer on kaolin, Appl. Clay Sci. 150 (2017) 342–353. doi:10.1016/j.clay.2017.09.032.

[9] F.F. Peng, P. Di, Effect of multivalent salts-calcium and aluminum on the flocculation of kaolin suspension with anionic polyacrylamide, J. Colloid Interface Sci. 164 (1994) 229–237. doi:10.1006/jcis.1994.1161.

[10] J. Long, H. Li, Z. Xu, J.H. Masliyah, Role of colloidal interactions in oil sand tailings treatment, AIChE J. 52 (2006) 371–383. doi:10.1002/aic.10603.

[11] B.K.G. Theng, Formation and Properties of Clay-Polymer Complexes, Vol. 4, Elsevier, 2012. doi:10.1016/B978-0-444-53354-8.00014-1.

[12] H. Kohay, I.I. Bilkis, Y.G. Mishael, Effect of polycation charge density on polymer conformation at the clay surface and consequently on pharmaceutical binding, J. Colloid Interface Sci. 552 (2019) 517–527. doi:10.1016/j.jcis.2019.05.079.

[13] Y. Ji, Q. Lu, Q. Liu, H. Zeng, Effect of solution salinity on settling of mineral tailings by polymer flocculants, Colloids Surfaces A Physicochem. Eng. Asp. 430 (2013) 29–38. doi:10.1016/j.colsurfa.2013.04.006.

[14] Y. Deng, J.B. Dixon, G.N. White, R.H. Loeppert, A.S.R. Juo, Bonding between polyacrylamide and smectite, Colloids Surfaces A Physicochem. Eng. Asp. 281 (2006) 82–91. doi:10.1016/j.colsurfa.2006.02.030.

[15] K. Vermöhlen, H. Lewandowski, H.D. Narres, M.J. Schwuger, Adsorption of

polyelectrolytes onto oxides - The influence of ionic strength, molar mass, and Ca2+ ions, Colloids Surfaces A Physicochem. Eng. Asp. 163 (2000) 45–53. doi:10.1016/S0927-7757(99)00429-X.

[16] F.D.C. Bragança, L.F. Valadares, C.A.P. De Leite, F. Galembeck, Counterion effect on the morphological and mechanical properties of polymer-clay nanocomposites prepared in an aqueous medium, Chem. Mater. 19 (2007) 3334–3342. doi:10.1021/cm070467+.

[17] R. Ait-Akbour, P. Boustingorry, F. Leroux, F. Leising, C. Taviot-Guého, Adsorption of PolyCarboxylate Poly(ethylene glycol) (PCP) esters on Montmorillonite (Mmt): Effect of exchangeable cations (Na^+, Mg^{2+} and Ca^{2+}) and PCP molecular structure, J. Colloid Interface Sci. 437 (2015) 227–234. doi:10.1016/j.jcis.2014.09.027.

[18] A.P. Dos Santos, M. Girotto, Y. Levin, Simulations of Polyelectrolyte Adsorption to a Dielectric Like-Charged Surface, J. Phys. Chem. B. 120 (2016) 10387–10393. doi:10.1021/acs.jpcb.6b06002.

[19] L. Wang, H. Liang, J. Wu, Electrostatic origins of polyelectrolyte adsorption: Theory and Monte Carlo simulations, J. Chem. Phys. 133 (2010). doi:10.1063/1.3463426.

[20] J. Long, Z. Xu, J.H. Masliyah, Adhesion of single polyelectrolyte molecules on silica, mica, and bitumen surfaces, Langmuir. 22 (2006) 1652–1659. doi:10.1021/la052757f.

[21] Q. Lu, B. Yan, L. Xie, J. Huang, Y. Liu, H. Zeng, A two-step flocculation process on oil sands tailings treatment using oppositely charged polymer flocculants, Sci. Total Environ. 565 (2016) 369–375. doi:10.1016/j.scitotenv.2016.04.192.

[22] G. Fraenkel, C. Franconi, Protonation of Amides, J. Am. Chem. Soc. 82 (1960) 4478–4483. doi:10.1021/ja01502a010.

[23] G.A.A. Saracino, R. Improta, V. Barone, Absolute pKa determination for carboxylic acids

using density functional theory and the polarizable continuum model, Chem. Phys. Lett. 373 (2003) 411–415. doi:10.1016/S0009-2614(03)00607-9.

[24] E.W. Allen, Process water treatment in Canada's oil sands industry: I. Target pollutants and treatment objectives, J. Environ. Eng. Sci. 7 (2008) 123–138. doi:10.1139/S07-038.

[25] R.D. Silva, T.D.C. Chaparro, I.S. Monteiro, P.Y. Dugas, F. D'Agosto, M. Lansalot, A. Martins Dos Santos, E. Bourgeat-Lami, Tailoring the Morphology of Polymer/Montmorillonite Hybrid Latexes by Surfactant-Free Emulsion Polymerization Mediated by Amphipathic MacroRAFT Agents, Macromolecules. 52 (2019) 4979–4988. doi:10.1021/acs.macromol.9b00741.

[26] H. Kaddour, S. Gerislioglu, P. Dalai, T. Miyoshi, C. Wesdemiotis, N. Sahai, Nonenzymatic RNA Oligomerization at the Mineral-Water Interface: An Insight into the Adsorption-Polymerization Relationship, J. Phys. Chem. C. 122 (2018) 29386–29397. doi:10.1021/acs.jpcc.8b10288.

[27] B. Zhang, W. Shi, S. Yu, Y. Zhu, R. Zhang, J.H. Tay, Adsorption of anion polyacrylamide from aqueous solution by polytetrafluoroethylene (PTFE) membrane as an adsorbent: Kinetic and isotherm studies, J. Colloid Interface Sci. 544 (2019) 303–311. doi:10.1016/j.jcis.2019.03.008.

[28] A. Viani, A.F. Gualtieri, G. Artioli, The nature of disorder in montmorillonite by simulation of X-ray powder patterns, Am. Mineral. 87 (2002) 966–975.

[29] W. Sun, H. Zeng, T. Tang, Synergetic adsorption of polymers on montmorillonite: Insights from molecular dynamics simulations, Appl. Clay Sci. 193 (2020) 105654. doi:10.1016/j.clay.2020.105654.

[30] A.W. Schüttelkopf, D.M.F. Van Aalten, PRODRG: A tool for high-throughput

crystallography of protein-ligand complexes, Acta Crystallogr. Sect. D Biol. Crystallogr. 60 (2004) 1355–1363. doi:10.1107/S0907444904011679.

[31] C. Oostenbrink, A. Villa, A.E. Mark, W.F. Van Gunsteren, A biomolecular force field based on the free enthalpy of hydration and solvation: The GROMOS force-field parameter sets 53A5 and 53A6, J. Comput. Chem. 25 (2004) 1656–1676. doi:10.1002/jcc.20090.

[32] D.J. Frisch, M. J., Trucks, G. W., Schlegel, H. B., Scuseria, G. E., Robb, M. A., Cheeseman, J. R., Scalmani, G., Barone, V., Petersson, G. A., Nakatsuji, H., Li, X., Caricato, M., Marenich, A. V., Bloino, J., Janesko, B. G., Gomperts, R., Mennucci, B., Hratch, Gaussian 16 Revision B. 01., Wallingford CT. (2016).

[33] C.M. Breneman, K.B. Wiberg, Determining atom-centered monopoles from molecular electrostatic potentials – the need for high sampling density in formamide conformational-analysis, J. Comp. Chem. 11 (1990) 361–73. doi:10.1002/jcc.540110311.

[34] R.T. Cygan, J.J. Liang, A.G. Kalinichev, Molecular models of hydroxide, oxyhydroxide, and clay phases and the development of a general force field, J. Phys. Chem. B. 108 (2004) 1255–1266. doi:10.1021/jp0363287.

[35] M. Pouvreau, J.A. Greathouse, R.T. Cygan, A.G. Kalinichev, Structure of Hydrated Gibbsite and Brucite Edge Surfaces: DFT Results and Further Development of the ClayFF Classical Force Field with Metal-O-H Angle Bending Terms, J. Phys. Chem. C. 121 (2017) 14757–14771. doi:10.1021/acs.jpcc.7b05362.

[36] E. Abraham, M. J., Murtola, T., Schulz, R., Páll, S., Smith, J. C., Hess, B., Lindahl, M.J. Abraham, T. Murtola, R. Schulz, S. Páll, J.C. Smith, B. Hess, E. Lindah, Gromacs: High performance molecular simulations through multi-level parallelism from laptops to supercomputers, SoftwareX. 1–2 (2015) 19–25. doi:10.1016/j.softx.2015.06.001.

[37] S. Pronk, S. Páll, R. Schulz, P. Larsson, P. Bjelkmar, R. Apostolov, M.R. Shirts, J.C. Smith, P.M. Kasson, D. Van Der Spoel, B. Hess, E. Lindahl, GROMACS 4.5: a high-throughput and highly parallel open source molecular simulation toolkit, Bioinformatics. 29 (2013) 845–854. doi:10.1093/bioinformatics/btt055.

[38] H.J.C.J.C. Berendsen, D. van der Spoel, R. van Drunen, GROMACS: A message-passing parallel molecular dynamics implementation, Comput. Phys. Commun. 91 (1995) 43–56. doi:10.1016/0010-4655(95)00042-E.

[39] S. Nosé, A molecular dynamics method for simulations in the canonical ensemble, Mol. Phys. 52 (1984) 255–268. doi:10.1080/00268978400101201.

[40] W.G. Hoover, Canonical dynamics: Equilibrium phase-space distributions, Phys. Rev. A. 31 (1985) 1695–1697. doi:10.1103/PhysRevA.31.1695.

[41] M. Parrinello, A. Rahman, Polymorphic transitions in single crystals: A new molecular dynamics method, J. Appl. Phys. 52 (1981) 7182–7190. doi:10.1063/1.328693.

[42] R.. Hockney, S.. Goel, J.. Eastwood, Quiet high-resolution computer models of a plasma, J. Comput. Phys. 14 (1974) 148–158. doi:10.1016/0021-9991(74)90010-2.

[43] B. Hess, H. Bekker, H.J.C. Berendsen, J.G.E.M. Fraaije, LINCS: A linear constraint solver for molecular simulations, J. Comp. Chem. 18 (1997) 1463–1472.

[44] T. Darden, D. York, L. Pedersen, Particle mesh Ewald: An N·log(N) method for Ewald sums in large systems, J. Chem. Phys. 98 (1993) 10089–10092.

[45] O. Stern, Zur theorie der elektrolytischen doppelschicht, Zeitschrift Für Elektrochemie Und Angew. Phys. Chemie. 30 (1924) 508–516.

[46] J.N. Israelachvili, Intermolecular and Surface Forces, third ed., Elsevier Inc., 2011. doi:10.1016/C2011-0-05119-0.

[47] I.C. Bourg, S.S. Lee, P. Fenter, C. Tournassat, Stern Layer Structure and Energetics at Mica-Water Interfaces, J. Phys. Chem. C. 121 (2017) 9402–9412. doi:10.1021/acs.jpcc.7b01828.

[48] A.K. Katz, J.P. Glusker, S.A. Beebe, C.W. Bock, Calcium ion coordination: A comparison with that of beryllium, magnesium, and zinc, J. Am. Chem. Soc. 118 (1996) 5752–5763. doi:10.1021/ja953943i.

[49] M.P. Aliste, J.L. MacCallum, D.P. Tieleman, Molecular dynamics simulations of pentapeptides at interfaces: Salt bridge and cation-π interactions, Biochemistry. 42 (2003) 8976–8987. doi:10.1021/bi027001j.

[50] R. Kjellander, S. Marčelja, Inhomogeneous Coulomb fluids with image interactions between planar surfaces. III. Distribution functions, J. Chem. Phys. 88 (1988) 7138–7146. doi:10.1063/1.454364.

[51] R. Kjellander, Ion-Ion Correlations Effective Charges in Electrolyte and Macroion Systems, Berichte Der Bunsengesellschaft/Physical Chem. Chem. Phys. 100 (1996) 894–904.

[52] R. Jellander, S. Marčelja, J.P. Quirk, Attractive double-layer interactions between calcium clay particles, J. Colloid Interface Sci. 126 (1988) 194–211. doi:10.1016/0021-9797(88)90113-0.

[53] T. Undabeytia, S. Nir, G. Rytwo, C. Serban, E. Morillo, C. Maqueda, Modeling adsorption - Desorption processes of CU on edge and planar sites of montmorillonite, Environ. Sci. Technol. 36 (2002) 2677–2683. doi:10.1021/es011154x.

[54] L.N. Lammers, I.C. Bourg, M. Okumura, K. Kolluri, G. Sposito, M. Machida, Molecular dynamics simulations of cesium adsorption on illite nanoparticles, J. Colloid Interface Sci. 490 (2017) 608–620. doi:10.1016/j.jcis.2016.11.084.

[55] T.R. Zeitler, J.A. Greathouse, R.T. Cygan, J.T. Fredrich, G.R. Jerauld, Molecular Dynamics

Simulation of Resin Adsorption at Kaolinite Edge Sites: Effect of Surface Deprotonation on Interfacial Structure, J. Phys. Chem. C. 121 (2017) 22787–22796. doi:10.1021/acs.jpcc.7b06688.

[56] I.C. Bourg, G. Sposito, Molecular dynamics simulations of the electrical double layer on smectite surfaces contacting concentrated mixed electrolyte (NaCl-$CaCl_2$) solutions, J. Colloid Interface Sci. 360 (2011) 701–715. doi:10.1016/j.jcis.2011.04.063.

[57] F. Moučka, J. Kolafa, M. Lísal, W.R. Smith, Chemical potentials of alkaline earth metal halide aqueous electrolytes and solubility of their hydrates by molecular simulation: Application to CaCl2, antarcticite, and sinjarite, J. Chem. Phys. 148 (2018). doi:10.1063/1.5024212.

[58] Y. Chen, S. Xue, Q. Xia, H. Li, Q. Liu, B.S. Li, B.Z. Tang, Surface Effect on the Self-Assembly of Nanofibers Revealed by in Situ AFM Imaging and Molecular Simulation, J. Phys. Chem. C. 123 (2019) 9292–9297. doi:10.1021/acs.jpcc.9b02205.

[59] E. Galicia-Andrés, D. Petrov, M.H. Gerzabek, C. Oostenbrink, D. Tunega, Polarization Effects in Simulations of Kaolinite-Water Interfaces, Langmuir. 35 (2019) 15086–15099. doi:10.1021/acs.langmuir.9b02945.

[60] A. Gladytz, T. John, T. Gladytz, R. Hassert, M. Pagel, H.J. Risselada, S. Naumov, A.G. Beck-Sickinger, B. Abel, Peptides@mica: From affinity to adhesion mechanism, Phys. Chem. Chem. Phys. 18 (2016) 23516–23527. doi:10.1039/c6cp03325c.

[61] W.L. Jorgensen, J. Tirado-rives, The OPLS Potential Functions for Proteins. Energy Minimizations for Crystals of Cyclic Peptides and Crambin, J. Am. Chem. Soc. 110 (1988). doi:10.1021/ja00214a001.

Chapter 5. Molecular Dynamics Simulation of Model Asphaltenes between Surfaces with Different Polarity

5.1. Introduction

Polyaromatic compounds consisting of fused aromatic rings and side chains usually process remarkable surface-active properties, arising from the distinctive physical and chemical properties of the fused rings and the side chains. The interfacial behaviors of polyaromatic compounds at solid-liquid interfaces are of great interests in many research fields such as supramolecular assembly [1], waste removal [2], and fabrication of organic electronic devices [3]. Asphaltenes are polyaromatic compounds that originate from crude oil, defined by their solubility: insoluble in alkanes and soluble in toluene [4]. The molecular structures of asphaltene are complex, but generally demonstrated to contain polycyclic aromatic hydrocarbons (PAHs) and aliphatic chains [5–8]. The deposition of asphaltene on solid-liquid interfaces was widely reported in the petroleum industry, causing severe problems such as reducing the reservoir permeability [9] and clogging the production devices [10], thus highlighting the importance of studying their interfacial behaviors.

The adsorption of asphaltene and asphaltene-like polyaromatic compounds on solid-liquid interfaces has been shown in many previous works to be principally regulated by the property of the solid surface. Dudášová et al. [11] measured the adsorption amount of asphaltene on different inorganic surfaces (Kaolin, $CaCO_3$, TiO_2, SiO_2, etc.) from a mixture of heptane and toluene (50:50, vol%). The asphaltenes were extracted from different sources, and the solid surface was shown to be the dominant factor for adsorption regardless of the source. The amount of adsorption decreased with surface polarity while having no obvious correlation with surface wettability. Using quartz crystal microbalance with dissipation (QCM-D) and atomic force microscopy (AFM), Liu et al. [12] measured the amount and strength of adsorption of a neutral model asphaltene, N-(1-Hexylheptyl)-N'-(5-carboxylicpentyl) perylene-3,4,9,10-tetracarboxylic bisimide (C5Pe), from ethanol onto different synthesized solid surfaces. Sensors coated with silica were used as hydrophilic surfaces, which were immersed into octade-cyltrichlorosilane solution to obtain hydrophobic surfaces. The experimental results showed that the adsorption was preferred on the hydrophilic surface as compared to the hydrophobic one. Molecular dynamics (MD) simulation was also performed in which the hydrophilic and hydrophobic surfaces were modeled by adding hydroxyl groups and alkyl groups, respectively, to a quartz surface. The MD simulation showed that in ethanol the adsorption on hydrophilic surface was driven by the hydrogen bonding between the polar groups of C5Pe and the hydroxyl groups of the surface. In comparison, the adsorption on the hydrophobic surface was driven by van der Waals interaction. Similar finding was also reported by Pernyeszi et al. [13], whose observation from X-ray diffraction (XRD) and Fourier transform infrared spectroscopy (FTIR) spectroscopy showed that in organic solvents (toluene and toluene/heptane mixtures), asphaltenes preferred to adsorb on kaolinite (Kaol, with hydroxyl groups on the surface), and the adsorption decreased in the order of illite (no hydroxyl surface groups but negatively charged) and montmorillonite (no hydroxyl surface groups and slightly negatively charged).

Besides the solid surface, solvent also demonstrated the ability to mediate the adsorption of asphaltene and similar compounds. The MD results of Liu et al. [12] showed that in ethanol the adsorption of C5Pe molecules was stronger on a hydrophilic surface (quartz terminated by hydroxyls) than on a hydrophobic surface (quartz terminated by alkanes), while the scenario was opposite in water. Bantignies et al. [14] compared the asphaltene adsorption on Kaol in toluene and in toluene-water mixture using XRD and FTIR spectroscopy. The change in spectra bands showed that the addition of water clearly affected adsorption on the alumina surface of Kaol (containing hydroxyl surface groups), while adsorption on the siloxane surface was insensitive to water. Via MD simulation and AFM imaging, Xiong et al. [15] studied the adsorption of neutral C5Pe onto silica (with hydroxyl groups on the surface) from two types of organic solvents (heptane and toluene). The results showed a stronger adsorption from heptane than from toluene. Additionally, in heptane the C5Pe molecules formed a long strip-shaped aggregate on the silica surface while in toluene most of them remained in the bulk solution. The adsorption was mainly driven by the van der Waals interaction, which was much stronger in heptane than in toluene.

The conformation of molecules at the solid-liquid interface is vital to the study of asphaltene adsorption, such as predicting the adsorbed amount [11,16], calculating the adsorption isotherm [11], and identifying the wettability change of the solid surface [16,17]. Simulations by Liu et al. [12] showed that a single C5Pe molecule tended to lie flat on the interface between water and a hydrophilic or hydrophobic surface, as well as at the interface between ethanol and a hydrophobic surface. However, the molecule preferred to be tilted on the interface between ethanol and a hydrophilic solid. Xiong et al. [18] showed that aggregates of model asphaltenes (C5Pe and its derivatives) adsorbed at the silica-heptane interface in a single-layer structure where the molecules were perpendicular or slant to the solid. The adsorption was stabilized by π-π or T-stacking between the asphaltene molecules and the hydrogen bonding between the asphaltenes and silica. On the other hand, MD simulation of Lan et al. [19] demonstrated multi-layer adsorption of a different model asphaltene (VO-79, with alkanes composing the side chain) on silica from organic solvents (toluene, heptane, and mixtures of both with different ratios). In the multi-layer structure, adsorbed VO-79 molecules were either parallel or slant to the silica surface, while VO-

79 adsorbed as monomers were only parallel. Monolayer and multilayer adsorptions of asphaltene have both been supported by experimental evidences [11,16,20].

From the previous works, the adsorption behaviors of asphaltenes depend on the nature of the solid-liquid interfaces, and different conformations were reported for similar surfaces. Quantification of the strength of adsorption has been scarce, especially at the molecular level. Such quantification, if performed for different interfaces, would greatly benefit the understanding of the free energy landscapes in the adsorption process. Moreover, neutral asphaltene with carboxylic terminal was adopted in most of the previous work, while deprotonated asphaltene is ubiquitous throughout the petroleum exploration and development stages, regulated by the environmental pH [21,22]. For example, saline water with pH of 8-9 was usually employed to recover the bitumen from oil sand ores, during which the carboxylic groups could become deprotonated [23,24]. Previous works have shown that the adsorption conformation was sensitive to the asphaltene type, and ample evidences exist for the importance of acidic functionalities of asphaltenes to their interfacial behaviors [25,26]. The adsorption of deprotonated asphaltene monomers and aggregates on solid surfaces needs more investigation.

In addition, while the previous works studied asphaltene adsorption in the presence of a single type of solid surface, in reality asphaltenes often encounter mixed types of surfaces simultaneously [27,28]. For example, in the flotation process bitumen could be exposed to surfaces with distinct wettability[27,29]. In the enhanced oil recovery process, aqueous solutions containing alkaline or surfactants were commonly injected into the reservoir, which could alter the wettability of the solid surfaces [28,30], causing asphaltenes to precipitate between different surfaces. Precipitation of asphaltenes in the thin films between these differently wetted solid surfaces made the surface alteration problematic, deteriorating the oil recovery efficiency [24]. Last but not least, in the complex fluid media during oil transportation, or in the oil sands tailings ponds for solid-water separation, asphaltenes were found to participate in hetero-coagulation of clay particles [31]. Different clay surfaces may mutually influence their ability to adsorb asphaltenes, leading to complex yet interesting adsorption behaviors.

In this work, the adsorption of a deprotonated model asphaltene at different solid-liquid interfaces was investigated by MD simulations and potential of mean forces (PMF) calculations. MD simulation has been validated by extensive experimental work as a powerful tool in predicting asphaltene's interfacial behaviors, and is especially advantageous in probing the molecular conformation and energetics [15,32]. Kaol is a typical clay mineral present in oil production; it has been well demonstrated that the alumina surface of Kaol is hydrophilic while the siloxane surface is hydrophobic [33–35], making Kaol a superior candidate to study the effect of surface properties on asphaltene adsorption. Both water and model oil (toluene and heptane) were used as the solvent to mimic the environment in which asphaltene deposition occurs. This systematic study allowed us to gain both qualitative and quantitative insights into how the interplay between solid types, solvent property, and aggregation contributes to the adsorption of asphaltenes on solid-liquid interfaces.

5.2. Simulation Methods

5.2.1. Models & Systems

The deprotonated C5Pe was employed as the adsorbate, which consisted of a hydrophilic head and a hydrophobic tail [7], as shown in Figure 5.1a. C5Pe has remarkable surface activity and has been widely used as a model for asphaltene [17,36,37]. The acidic carboxylic group in the hydrophilic head was deprotonated, resulting in a charge of -1. The adsorbent was represented by

Kaol (see Figure 5.1b for the unit cell of Kaol), a natural clay mineral composed of one octahedral alumina sheet and one tetrahedral siloxane sheet [38].

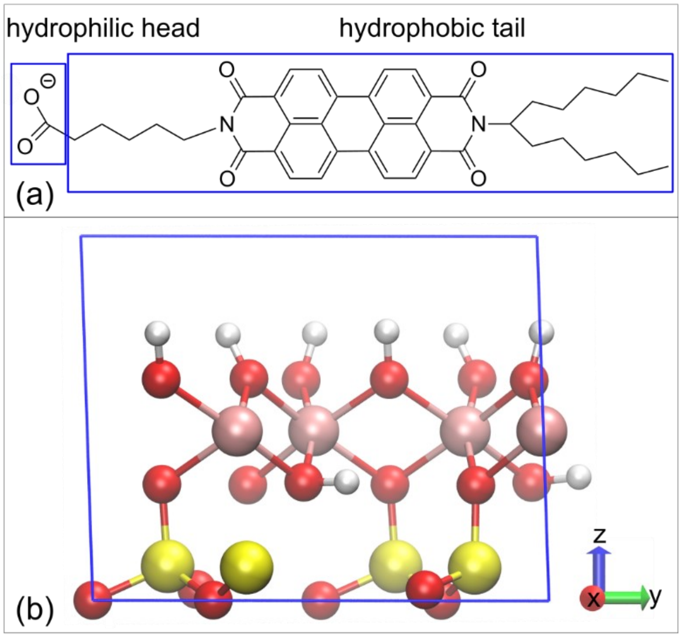

Figure 5.1. (a) Molecular structure of the deprotonated C5Pe and (b) unit cell of Kaol. Color scheme for atoms in Kaol: Si (yellow), Al (pink), O (red), and H (white).

Two groups of simulations were performed, as shown in Table 5.1. In the first group, the motion of a single C5Pe molecule was studied between two alumina surfaces (one Kaol plate at the bottom and one flipped Kaol plate at the top of the simulation box, see Figure 5.2a), between two siloxane surfaces (one flipped Kaol plate at the bottom and one Kaol plate at the top, see Figure 5.2b), and between one alumina and one siloxane surfaces (one Kaol plate at the bottom of the simulation box, implying an identical plate at the top due to the application of periodic boundary condition (PBC), see Figure 5.2c). The systems, each of size 4.12×4.47×5.00 nm^3, were solvated by water, toluene, and heptane, respectively, and were named based on the solid and solvent types. For example, system Al-Al-Wat corresponds to the system where the C5Pe was between two alumina surfaces and in water. In addition to these 9 simulations where the C5Pe was free to move, for systems Al-Si-Wat, Al-Si-Tol and Al-Si-Hep, umbrella sampling (US) [39] simulations were performed to calculate the PMF of the C5Pe molecule as it was pulled away from one surface towards the other.

In the second group of simulations, twelve deprotonated C5Pe molecules were added into the three solvents, each sandwiched between one alumina and one siloxane surfaces, to analyze the adsorption of C5Pe aggregates. The C5Pe molecules were initially added into the systems (size $8.25\times8.94\times8.00$ nm^3) in the form of $2 \times 3 \times 2$ array in the middle of the boxes. In all the simulated systems, the negative charges of C5Pe molecules were neutralized by Ca^{2+} and Cl^- ions. Divalent cations have been shown to suppress the electric double layer around charged molecules, thus promoting the adsorption [40].

Table 5.1. Simulated Systems

system name	solid surfaces	solvent	number of C5Pe	Number of ions
Al-Al-Wat	alumina-alumina	water	1	1 Ca^{2+}, 1 Cl^{-}
Si-Si-Wat	siloxane-siloxane	water	1	1 Ca^{2+}, 1 Cl^{-}
Al-Si-Wat	alumina-siloxane	water	1	1 Ca^{2+}, 1 Cl^{-}
Al-Al-Tol	alumina-alumina	toluene	1	1 Ca^{2+}, 1 Cl^{-}
Si-Si-Tol	siloxane-siloxane	toluene	1	1 Ca^{2+}, 1 Cl^{-}
Al-Si-Tol	alumina-siloxane	toluene	1	1 Ca^{2+}, 1 Cl^{-}
Al-Al-Hep	alumina-alumina	heptane	1	1 Ca^{2+}, 1 Cl^{-}
Si-Si-Hep	siloxane-siloxane	heptane	1	1 Ca^{2+}, 1 Cl^{-}
Al-Si-Hep	alumina-siloxane	heptane	1	1 Ca^{2+}, 1 Cl^{-}
Wat-12	alumina-siloxane	water	12	6 Ca^{2+}
Tol-12	alumina-siloxane	toluene	12	6 Ca^{2+}
Hep-12	alumina-siloxane	heptane	12	6 Ca^{2+}

5.2.2. Simulation details

The MD simulations were carried out with the GROMACS 2019 open source package [41–43]. The geometry of the deprotonated C5Pe was first optimized by density functional theory (DFT) at B3LYP/6-31+G (d) level in Gaussian 16 [44]. The topology for the deprotonated C5Pe was converted from the optimized coordinate files using Automated Topology Builder (ATB) [45]. The force field parameters in the topology were from the GROMOS 96 54A7 force field parameter set [46] except for the partial atomic charges, which were produced using the CHelpG method [47] after the DFT optimization. The topology for Kaol was developed and validated in our previous work [48], where the CLAYFF force field [49,50] was adopted with all partial atomic charges unaltered.

Each system containing a single C5Pe molecule was first minimized by the steepest descent method to limit the maximum force to 1000.0 kJ/(mol·nm). The minimization was followed by simulated annealing where the solid plates was frozen, and the temperature of other molecules was slowly increased from 300 K to 800 K and then decreased back to 300 K. Production MD simulation was then performed in NP_zT semi-isotropic ensemble (pressure coupling only in the *z*-direction, which is the direction perpendicular to the solid surfaces) for 10 ns. During the NP_zT simulations, position restraints were applied to the heavy (non-hydrogen) atoms of the lower plate, while the upper plate could move in the *z*-direction working as a piston. The only exception was the system between two siloxane surfaces in water (see Figure 5.2b), which was simulated in NVT ensemble with position restraints applied on both plates. Due to the application of PBC, when two siloxane surfaces were facing the solvent, the two alumina surfaces in neighbour cells were closely stacked. In water, the strong attraction between the two alumina (hydrophilic) surfaces could lead to structural distortion in the system, and as such special care was taken by using the NVT ensemble. Evidence was presented in the Appendix D (section D1) that the simulation results were not affected by the choice of ensembles.

For the PMF calculation using US, the reaction coordinate was chosen to be the distance (d_{COM}) from the center of mass (COM) of C5Pe to the surface of the bottom plate, which was defined by the average *z* coordinates of the surface oxygens. The C5Pe molecule was first pulled in the *z*-direction from the alumina surface to the siloxane surface, at a speed of 1 nm/ns. A total of 50-100 configurations with different d_{COM} were taken from the pulling trajectories and for each configuration, harmonic biasing potential was applied on the COM of C5Pe for 10 ns of US. During the US, $NP_{xy}T$ simulation was performed so that the z dimension of the simulated box was unvaried, ensuring consistent measurement of d_{COM}. Finally, the PMF as a function of d_{COM} was calculated by the weighted histogram analysis method [51].

The systems containing 12 C5Pe molecules were simulated following the same procedure as the systems containing a single C5Pe molecule, except that the production run was conducted for 80 ns. For all simulations, Nose-Hoover thermostat [52,53] and Parrinello–Rahman barostat [54] were employed to control the temperature and pressure at 300 K and 1 bar respectively. Cut-off distance for van der Waals and short-range electrostatic interactions was 1nm, and particle mesh Ewald method [55] was used to calculate long-range electrostatic interactions.

5.3. Results and Discussion

5.3.1. Adsorption of C5Pe monomer

The final configurations of the deprotonated C5Pe molecule when placed in water between two alumina surfaces, between two siloxane surfaces, and between one alumina and one siloxane surfaces are shown in Figures 5.2a-c, respectively. Statistics from the last 5 ns of the simulations, for the distance d_{COM} from the surface of the bottom plate is shown in Figure 5.2j, and statistics for the angle θ between the PAH plane (defined by three carbon atoms of the PAH) of C5Pe and the solid surfaces (xy plane) is shown in Figure 5.2k. In the last 5 ns, d_{COM} in system Al-Al-Wat (Figure 5.2a) fluctuated around ~0.8 nm. The angle θ had an average of ~35° but the standard deviation was high, suggesting that the C5Pe molecule was loosely adsorbed near the bottom alumina surface. When the C5Pe molecule was between two siloxane surfaces in system Si-Si-Wat (Figure 5.2b), d_{COM} converged to ~0.33 nm and the angle θ was ~10°. Compared with system

Al-Al-Wat, the C5Pe molecule displayed a more stable adsorption on the siloxane surface, with a closer distance and flatter configuration. In system Al-Si-wat, the C5Pe molecule adsorbed on the alumina surface, which was in contrast to the systems containing identical surfaces where the adsorption appeared stronger in Si-Si-Wat than in Al-Al-Wat. d_{COM} between C5Pe and the alumina surface fluctuated heavily between 0.9 and 1.3 nm, suggesting that the C5Pe molecule was not as stably adsorbed on the alumina surface as in system Al-Al-Wat. In addition, there was no preferred angle between the PAH plane and the alumina surface. Thus, the adsorption of C5Pe was affected by the presence of dissimilar surfaces.

In toluene, as shown in Figures 5.2d-f, the C5Pe molecule became adsorbed in all three settings of solid surfaces. In systems Al-Al-Tol and Al-Si-Tol (Figures 5.2d and f) where C5Pe adsorbed on the alumina surface, d_{COM} between C5Pe and the bottom plate (alumina surface facing upwards) shown in Figure 5.2l converged to 0.38 nm. The angles θ was around 10º in both systems, suggesting a flat configuration. In system Si-Si-Tol, d_{COM} fluctuated around 0.41 nm and the angle θ was ~30º with the siloxane surface. In heptane, the C5Pe molecule became adsorbed in the two systems with symmetrical surface setting (Figures 5.2g and h), with d_{COM} converging to 0.3-0.5 nm and $\theta < 30$º. However, when C5Pe was placed between two dissimilar surfaces, its adsorbed configuration was different in heptane compared with in toluene. Contrasted with the preferred adsorption on the alumina surface in toluene, in heptane the C5Pe molecule favoured the siloxane surface. The angle between C5Pe and the siloxane surface was ~80º, suggesting a nearly perpendicular configuration in system Al-Si-Hep.

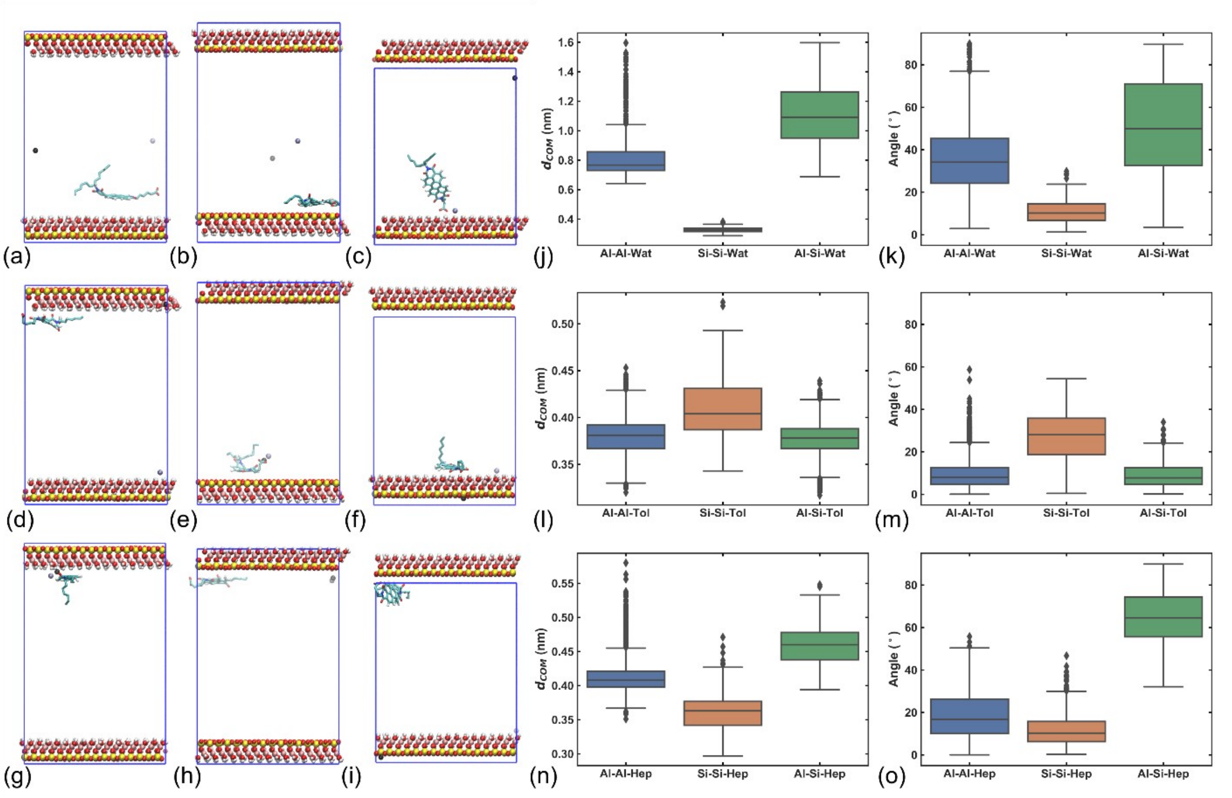

Figure 5.2. Final configurations of systems (a) Al-Al-Wat, (b) Si-Si-Wat, (c) Al-Si-Wat, (d) Al-Al-Tol, (e) Si-Si-Tol (f) Al-Si-Tol, (g) Al-Al-Hep, (h) Si-Si-Hep, and (i) Al-Si-Hep. Statistics for the distance d_{COM} between COM of C5Pe and the surface of the bottom plate, as well as the angle between PAH plane of C5Pe and the solid surfaces, in systems solvated by water (j, k), toluene (l, m), and heptane (n, o). Data from the last 5 ns of the simulations were used to generate the box-and-whisker plots in (j)-(o), where the box was created from the first quartile to the third quartile and the horizontal line inside the box denotes the median. From the upper/lower quartiles (boundary of the box), whiskers were drawn to the largest/smallest datapoint (the farthest datapoint) that fell within 1.5 times the box length. Other datapoints not included within the whiskers were plotted as dots.

5.3.2. Mechanisms of monomer adsorption

The effects of solvent on the adsorption of C5Pe could be better understood by PMF calculations. Since systems Al-Si-Wat, Al-Si-Tol, and Al-Si-Hep contained all types of solid-liquid interfaces investigated, the PMF was calculated in these three systems and shown in Figure 5.3. In water (Figure 5.3a), the first minimum at $d_{\mathrm{COM}} \approx 0.5$ nm corresponded to the configuration where C5Pe laid flat on the alumina surface with its carboxylic terminal forming hydrogen bonds (H-bonds) with the Al-OH groups. The second minimum at $d_{\mathrm{COM}} \approx 1.5$ nm had a lower PMF than the first minimum ($\Delta G_1 = -6.86$ kJ/mol), suggesting a more stable adsorption. In this minimum, C5Pe was tilted to the alumina surface while maintaining the H-bonds. After the second minimum, the PMF kept an increasing trend with d_{COM}, implying the resistance of C5Pe to solvation in water. When C5Pe was sufficiently close to the siloxane surface, another minimum appeared at $d_{\mathrm{COM}} \approx 3.4$ nm, with almost the same PMF value as the second minimum ($\Delta G_2 = 0.09$ kJ/mol). This minimum corresponded to another favorable adsorption configuration: C5Pe perpendicularly adsorbed on the siloxane surface with the hydrophilic head extending to the solvent (water) and the hydrophobic tails lying flat on the surface. The most energetically favorable configuration was suggested by the lowest minimum along the reaction coordinate, which occurred at $d_{\mathrm{COM}} \approx 3.9$ nm where C5Pe adsorbed on the siloxane surface with its PAH plane perpendicular to the surface.

The free energy changes (ΔG) when the C5Pe molecule was moved from the middle of the bulk solution (marked by star in Figure 5.3a) to the most energetically favorable position near each surface (the second and the fourth energy minima in Figure 5.3a) were calculated in Figure 5.3d, as well as the change of the enthalpy (ΔH) and the entropic contribution ($T\Delta S$). ΔG was obtained from the PMF, ΔH calculated from $\Delta H = \Delta U + p\Delta V$ (U, p and V respectively the total internal energy, pressure, and volume of the system), and $T\Delta S$ determined from $T\Delta S = \Delta H - \Delta G$. To become adsorbed, the C5Pe molecule needed to replace the water molecules in the hydrated layer near the solid surfaces. When adsorbed at the alumina-water interface, ΔG (-5.6 kJ/mol) was mainly from ΔH (-5.0 kJ/mol), suggesting that the adsorption was driven by enthalpy. The strong attraction of the carboxylate group of C5Pe to the polar alumina surface facilitated water replacement on the surface so that C5Pe could be adsorbed. On the other hand, compared with water, the hydrophobic part of C5Pe had a weaker attraction to the alumina, and thus the adsorption was in a tilted configuration leaving the hydrophobic part unadsorbed. Contrastingly, at the siloxane-water interface, ΔG (-8.4 kJ/mol) resulted from simultaneous increase of enthalpy (ΔH = 53.9 kJ/mol) and entropy ($T\Delta S$ = 62.3 kJ/mol). In this case, the adsorption was entropy driven. As C5Pe adsorbed on the siloxane surface, a fraction of water molecules previously confined near the surface and around C5Pe were released into the bulk, and the entropy of water release was the main force driving this most stable adsorption.

Free energy analyses in Figure 5.3 can provide some insights into the observations made in Figure 5.2. Figure 5.3d suggests that C5Pe adsorption was mainly driven by enthalpy in system Al-Al-Wat, while by entropy in system Si-Si-Wat. ΔG had a larger magnitude for adsorption on siloxane and as such the adsorption on alumina (Figures 5.2a, j, and k) was not as stable as the adsorption on siloxane (Figures 5.2b, j, and k). In system Al-Si-Wat, when the C5Pe was between two dissimilar surfaces, a competition existed between the two surfaces and theoretically C5Pe could adsorb at either interface. In Figure 5.2c, C5Pe was observed to adsorb on the alumina surface because it was initially placed near the middle of the simulation box where $d_{\mathrm{COM}} \approx 2.3$ nm. Based on the PMF in Figure 5.3a, it was easier for the C5Pe molecule to move from $d_{\mathrm{COM}} \approx 2.3$ nm towards the minimum at $d_{\mathrm{COM}} \approx 1.5$ nm (near alumina surface) while two energy barriers would need to be overcome to reach the PMF minimum at $d_{\mathrm{COM}} \approx 3.9$ nm (near siloxane surface).

The PMF in toluene also displayed two minima near each surface ($d_{\mathrm{COM}} \approx 0.4$ nm, 1.6 nm, 3.9 nm, and 4.3 nm), corresponding to two types of configurations, flat and tilted, as shown by the snapshots in Figure 5.3b. The changes of free energy, enthalpy, and entropic terms when C5Pe was moved from the bulk solution to the first ($d_{\mathrm{COM}} \approx 0.4$ nm, lowest minimum near alumina) and the fourth minimum ($d_{\mathrm{COM}} \approx 4.3$ nm, lowest minimum near siloxane) were calculated in Figure

5.3d. $T\Delta S$ was negative for both interfaces, implying that entropy played against the adsorption of C5Pe in toluene. The movement of C5Pe from the bulk to the surface, followed by adsorption in a flat form, would cause a decrease in the configurational entropy, which might surpass the entropy increase caused by solvent release. The entropy decreased more at the alumina surface than at the siloxane surface because of the flatter configuration of C5Pe. The negative ΔH values in Figure 5.3d confirmed that the adsorption of C5Pe in toluene was enthalpy driven. ΔH as well as ΔG were more negative at the alumina-toluene interface. As a result, the adsorption in systems Al-Al-Tol was more stable (less fluctuated d_{COM} and θ in Figures 5.2l and m) than that in system Si-Si-Tol (Figures 5.2d and e). Similarly, between two dissimilar surfaces in toluene, the C5Pe molecule preferred the alumina surface (Figure 5.2f).

In heptane, similar to the case in toluene, the PMF curve had two minima near each surface ($d_{\mathrm{COM}} \approx 0.4$ nm, 1.5 nm, 3.6 nm, and 4.1 nm) resulting from different C5Pe configurations. One notable distinction from toluene is that in heptane C5Pe underwent an orientation reversal as it departed from the alumina surface and approached the siloxane surface (Figure 5.3c). The reversal arose from the fact that the aliphatic side chains of C5Pe always preferred to stay solvated in heptane which had similar aliphatic feature. Two additional minima were found as a consequence of the orientation reversal: at $d_{\mathrm{COM}} \approx 2.1$ nm and $d_{\mathrm{COM}} \approx 2.8$ nm respectively. The adsorption of C5Pe was also driven by enthalpy and hindered by entropy ($\Delta H < 0$ and $T\Delta S < 0$ in Figure 5.3d). The two solid-heptane interfaces had similar ΔG. As a result, C5Pe displayed similar adsorption (close values of d_{COM} and θ in Figures 5.2n and o) in system Si-Si-Hep and Al-Al-Hep and should have similar tendency toward the two surfaces in system Al-Si-Hep. Given that the C5Pe molecule in system Al-Si-Hep was initially placed at $d_{\mathrm{COM}} \approx 2.5$ nm (near the PMF peak in Figure 5.3c), the final adsorption on the siloxane surface seen in Figure 5.2i could be due to the random velocities assigned at the beginning of the simulation, combined with the slightly sharper decline of the PMF towards the siloxane surface in Figure 5.3c.

The above results have shown that the mechanisms driving monomer adsorption of C5Pe at solid-water interfaces are distinct in water as compared to organic solvents. Entropy played a critical role in promoting adsorption of C5Pe from water onto hydrophobic siloxane surface, while enthalpy dominated the adsorption on other solid-liquid interfaces. In water, although the adsorption on the hydrophobic (siloxane) surface was more stable when the C5Pe molecule was placed between two identical surfaces, it adsorbed on the hydrophilic (alumina) surface when placed between the two dissimilar surfaces, due to the change of mechanism driving the adsorption. In the organic solvents, the driving mechanism for C5Pe adsorption remained consistent (i.e., enthalpy) whether the two solid surfaces were of the same or different types, and thus the adsorption favored the surface that yielded larger enthalpy change.

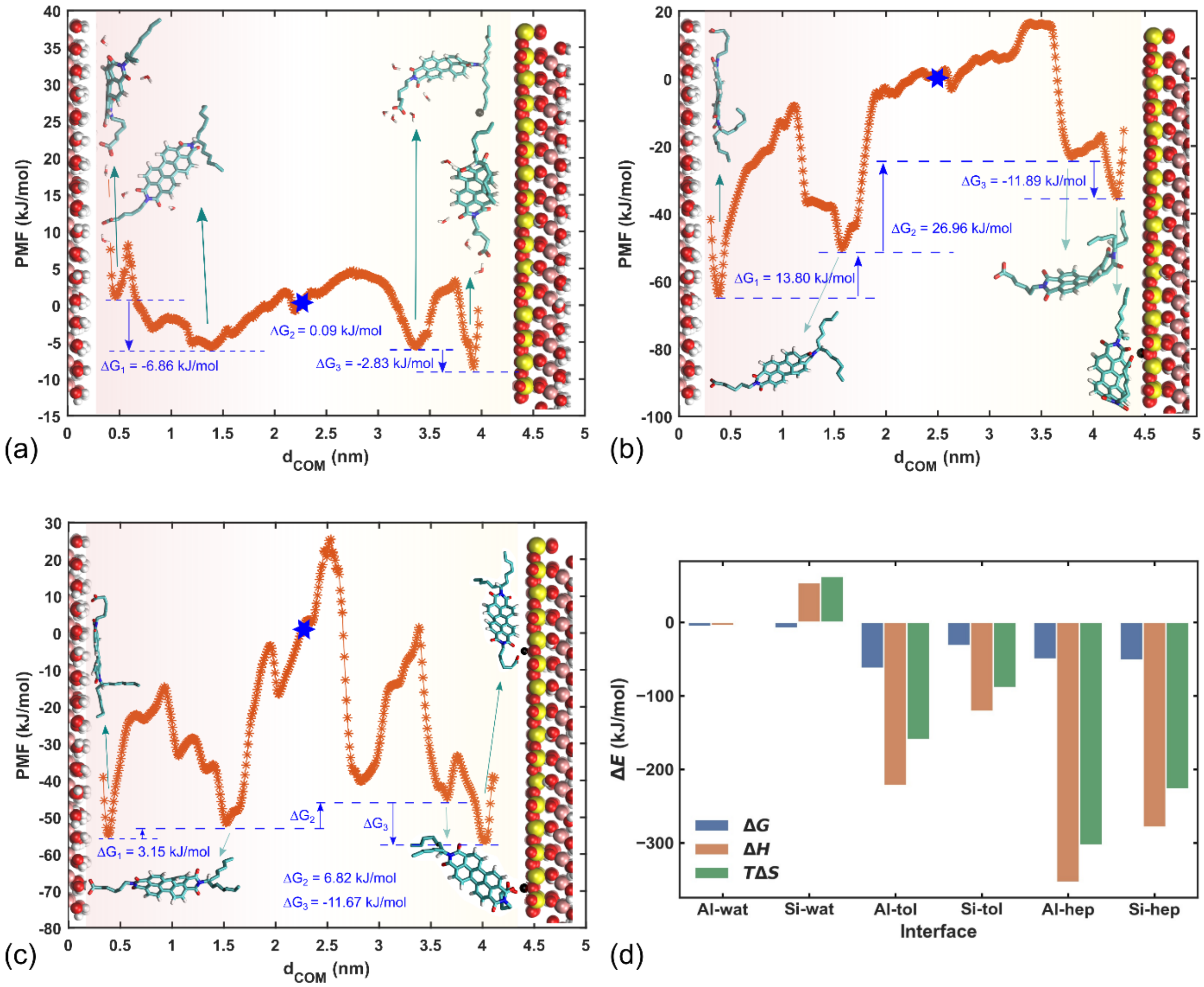

Figure 5.3. PMF along d_{COM} when the C5Pe was between the alumina and siloxane surfaces of Kaol in water (a), toluene (b), and heptane (c). The change of Gibbs free energy (ΔG), enthalpy (ΔH), and entropic term ($T\Delta S$) when C5Pe was moved from the bulk (marked by the star symbol) to the solid-water interfaces (Al-wat and Si-wat), solid-toluene interfaces (Al-tol and Si-tol), and solid-heptane interfaces (Al-hep and Si-hep) (d).

5.3.3. Adsorption of C5Pe aggregates

One notable feature of C5Pe is the self-association where multiple molecules form aggregates through π-π stacking of the PAH planes [7]. To explore the difference in adsorption of C5Pe aggregates as compared to a single molecule, systems composed of 12 deprotonated C5Pe molecules were simulated between one alumina and one siloxane surfaces using PBC. The density profile of C5Pe vs. the distance to the alumina surface was plotted in Figures 5.4a, c, and e, with the final configurations shown as insets. In water (Figure 5.4a), the density displayed one layer that peaked at ~1 nm from the alumina surface (pointed by the arrow) and decayed to zero after 2.5 nm; 2.5 nm therefore represented the thickness of the adsorbed C5Pe aggregate in water. Within the layer, the C5Pe molecules aggregated together as showed in the inset of Figure 5.4a. The evolution of aggregate size with simulation time is shown in Figure 5.4b (see Appendix D, Section D2 for the calculation details), quantified by the number of C5Pe molecules in each aggregate. The number of aggregates is indicated by the color bar on the right of Figure 5.4b. The aggregation in water was stable, evidenced by the steady aggregate size: two aggregates of six C5Pe molecules at the beginning (0-35 ns) and one aggregate of twelve molecules in the final stage (35-80 ns).

The density profile of C5Pe in toluene (Figure 5.4c) reached local peaks at 0.25 nm, 0.7 nm and 2.3 nm, respectively, and decayed to zero after 4 nm from the alumina surface, indicating a three-layered adsorption with a total thickness of 4 nm. The three-layered configuration is illustrated by the snapshot in Figure 5.4c, containing nine C5Pe molecules (last time frame in Figure 5.4d). In toluene, the aggregates were overall in smaller sizes and less stable than in water: through the 80 ns simulation the aggregate size fluctuated significantly, from monomer to undecamer.

In heptane, the density profile displayed two peaks at 0.25 nm and 0.7 nm respectively, near the alumina surface, and decreased to zero at 1.3 nm, suggesting a two-layered adsorption with a total thickness of 1.3 nm. In addition, there were two peaks in the density profile near the siloxane surface, at 6.9 nm and 7.1 nm, suggesting a two-layered adsorption with a thickness of ~0.5 nm. Compared with the toluene and water systems, the aggregate size was smaller in the system solvated by heptane (Figure 5.4f). One pentamer was formed and adsorbed in the 50-75 ns time window, which was the largest aggregate that ever existed in the heptane system. Dimer, trimer, and tetramer were all found throughout the simulation. Meanwhile, the number of molecules that adsorbed in the form of monomers increased, as the maximum number of monomers increased to three in the heptane system.

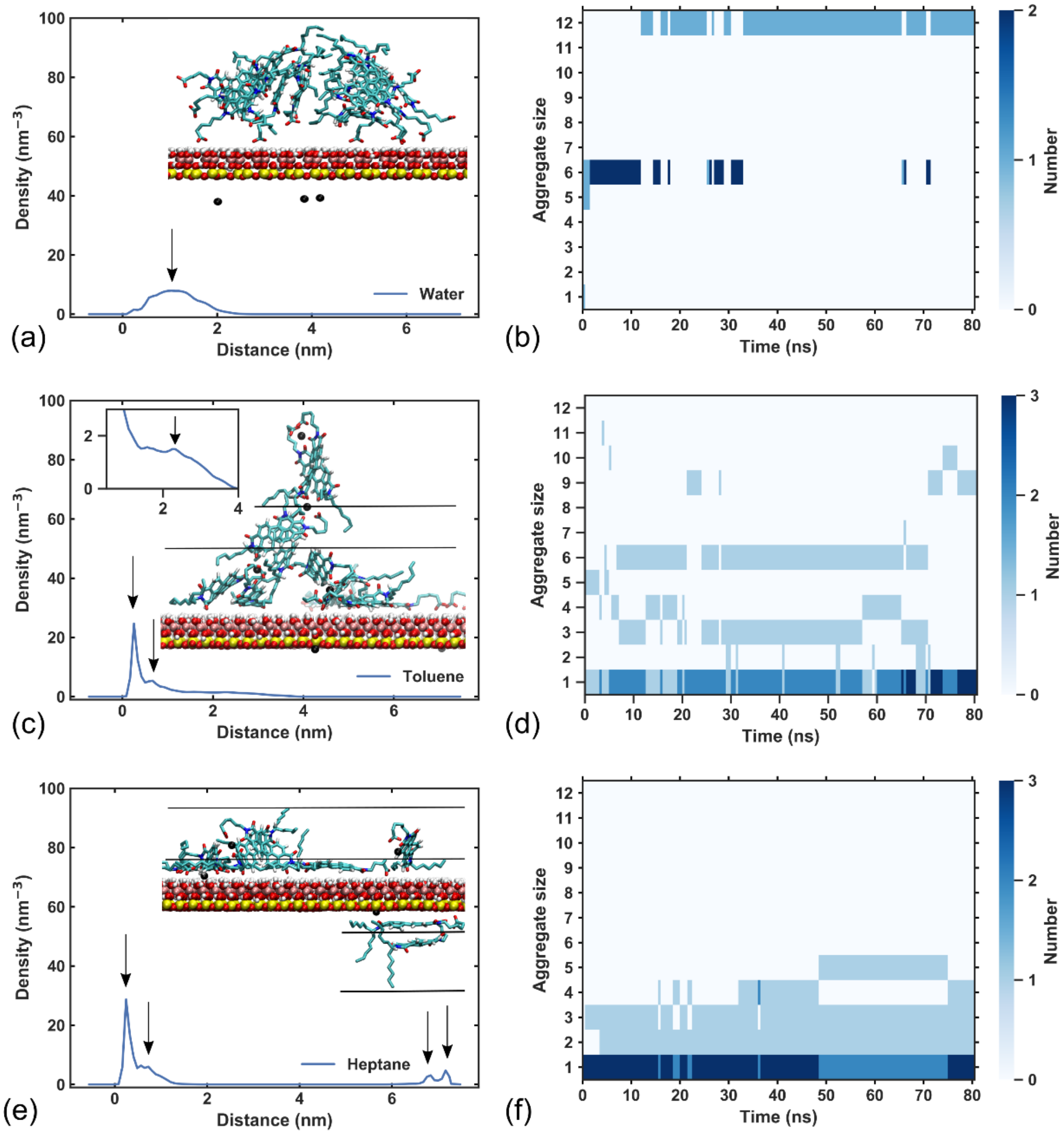

Figure 5.4. Density profile of C5Pe as a function of the distance from the alumina surface in systems solvated by water (a), toluene (c), and heptane (e), sampled from the last 20 ns of the simulations. Size of the adsorbed aggregate on both Kaol surfaces, in systems solvated by water (b), toluene (d), and heptane

(f). In b, d, f, the color bar indicates the number of aggregates corresponding to a certain size. The size of an aggregate was quantified by the number of C5Pe molecules in it. Ca^{2+} ions are shown as black spheres.

5.3.4. Mechanisms of aggregate adsorption

As discussed in section 3.2, the adsorption of C5Pe monomer was entropy-driven on siloxane surface in water, and enthalpy-driven in other systems. As shown in section 3.3, adsorptions of C5Pe aggregates were found on surfaces that were enthalpically favored. In addition, in toluene the preferred adsorption on the alumina surface, as compared to siloxane, was consistent with the lower ΔG value for monomer adsorption. In heptane, ΔG value for monomer adsorption was comparable on the two surfaces, and in alignment with this, aggregate adsorption was found on both surfaces. Besides the interaction with the surface, the interaction between C5Pe molecules also regulated the adsorption of aggregates.

5.3.4.1. Ca^{2+} coordination

Ca^{2+} ions in the solution can provide local charge neutralization and establish bridges between C5Pe and the surfaces through the formation of coordination bonds. The numbers of coordination bonds formed with the Ca^{2+} ions (denoted as N_{coord}) in the systems containing twelve C5Pe molecules and six Ca^{2+} ions are shown in Figure 5.5 (see Appendix D, Section D2 for the calculation details). In the system solvated by water, all the six Ca^{2+} ions were only coordinated to water oxygens (Figure 5.5a), despite the presence of a carboxylic group in C5Pe which intuitively could have higher electrostatic attraction to Ca^{2+}. The number of N_{coord} formed with water oxygens was 4-6, consistent with the structure of hydrated Ca^{2+} reported in the literature [56]. The absence of Ca^{2+} coordination with the carboxylic group of C5Pe might result from the stronger attraction the carboxylic group had with the surface hydroxyl groups (see section 3.4.2 for H-bonds calculation). After the C5Pe aggregate adsorbed on the alumina surface, the Kaol plate exhibited a net negative charge. As a result, the hydrated (coordinated) Ca^{2+} ions stayed in the stern layer of the anionic Kaol plate surface (see Appendix D, section D1 for more details), as shown in Figure 5.4a. The Ca^{2+} thus did not help the aggregation or the adsorption of C5Pe in water.

In toluene, the Ca^{2+} ions were coordinated to both the Kaol surface and the C5Pe molecules (Figure 5.5b), which was in contrast with the coordination scenario in water. The surface coordinated to two Ca^{2+} (Ca_4 and Ca_6) through the bridging oxygens in the siloxane layer or the hydroxyl oxygens in the alumina layer, with N_{coord} = 6-7 per Ca^{2+} ion. Meanwhile, four Ca^{2+} ions (Ca_1, Ca_2, Ca_3, and Ca_5) were coordinated to the C5Pe molecules, each forming 6-7 coordinate bonds through the oxygen atoms on the carboxylic groups and the PAH plane. Multiple C5Pe molecules were bridged together when simultaneously coordinating to one Ca^{2+}. In fact, the three layers of C5Pe near the alumina surface in toluene were bridged together through the Ca^{2+} bridges, as evidenced by the correlation between the density profiles of Ca^{2+} and C5Pe (Appendix D, Section D1). While Ca^{2+} participated in aggregating C5Pe molecules, it is interesting to note that no Ca^{2+} bridges were found between C5Pe and the alumina surface, i.e., Ca^{2+} did not contribute to the direct adsorption of C5Pe. Here a C5Pe molecule was considered to be directly adsorbed when its minimum distance from the solid surface was within 0.25 nm (see Appendix D, Section D2 for the justification). Instead, Ca^{2+} promoted C5Pe adsorption by connecting the molecules together into a loosely packed multi-layer structure which in turn adhered to the surface through H-bonding.

In heptane, the Ca^{2+} ions were coordinated to C5Pe (Ca_3, Ca_5, and Ca_6), Kaol (Ca_1 and Ca_4), as well as C5Pe and Kaol simultaneously (Ca_1, Ca_2, Ca_4, and Ca_5) at different stages (see Appendix D, Section D1 for the real-time dynamic data). The coordination of C5Pe or Kaol to Ca^{2+} was similar to that in toluene, with 6-7 coordinate bonds per Ca^{2+}. Compared to the case in toluene, the Ca^{2+} ions in heptane played the additional role of bridging C5Pe and the surface together and stabilizing the directly adsorbed molecules (Appendix D, Section D1 for evidence from the density profiles).

5.3.4.2. H-bonds between C5Pe and Kaol

H-bonding played an important role in the direct adsorption of C5Pe molecules. The average number of H-bonds (N_{hbond}) formed by each directly adsorbed C5Pe molecule with the alumina surface was calculated and shown in Figure 5.5d. The maximum number of H-bonds a C5Pe molecule could form with the alumina surface was eight (via all available N and O atoms) which corresponded to a completely flat adsorption (Figure 5.2f). Among the three solvents, N_{hbond} was the least in water, which was attributed to the titled configuration of C5Pe aggregates (Figure 5.4a) that limited the opportunities of N and O atoms in the PAH plane to form H-bonds. In contrast, the nearly flat configuration in toluene and heptane (Figure 5.4c and e) benefited the H-bonding between the available groups on C5Pe and the hydroxyl groups on the alumina surface. N_{hbond} in heptane was less than that in toluene, which came from two sources. First, when adsorbed, the average angle between the PAH plane of C5Pe and the surface was slightly higher in heptane than in toluene (Figure 5.6a). This implies the more likelihood of having a tilted configuration in heptane which hindered the H-bonding. Secondly, the ability of forming H-bonds was affected by the Ca^{2+} coordination. As discussed in section 3.4.1, in heptane the Ca^{2+} ions could bridge the C5Pe and Kaol by forming coordinate bonds with both. When forming coordinate bonds with Ca^{2+}, the surface oxygens (-OH) and the oxygens of C5Pe could no longer participate in H-bonding. As a result, the H-bonds per directly adsorbed C5Pe was less in heptane than in toluene.

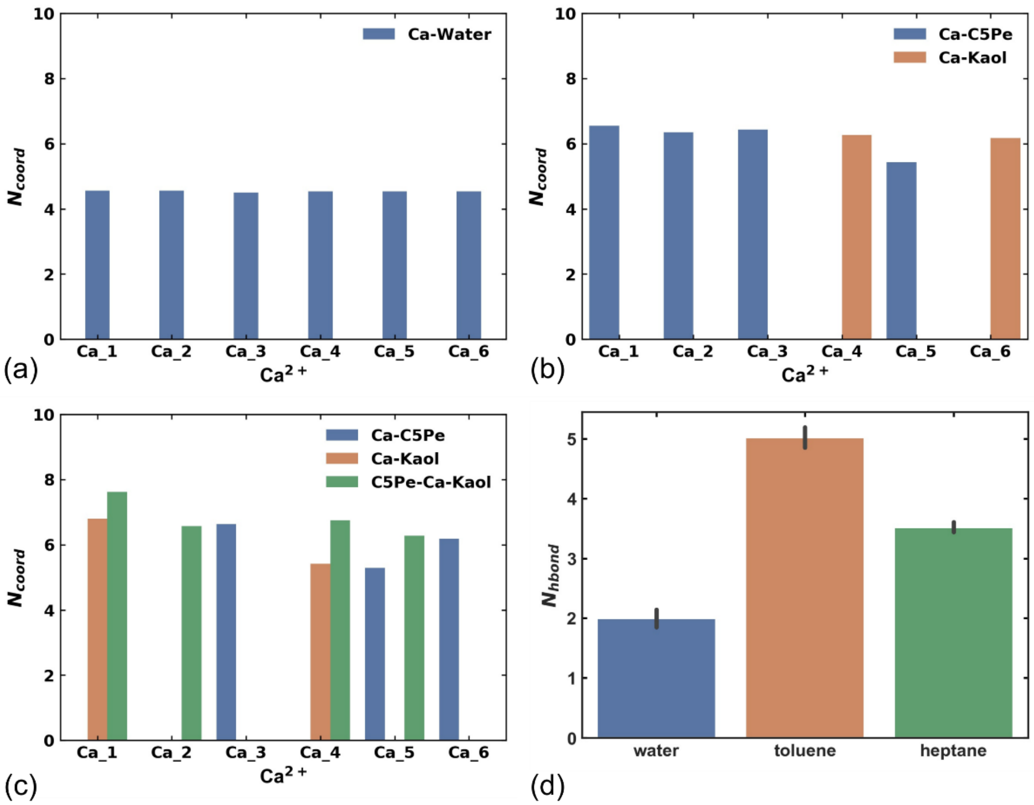

Figure 5.5. Average number of coordinate bonds formed with each Ca^{2+} ion when coordinated to water (Ca-Water), C5Pe (Ca-C5Pe), Kaol (Ca-Kaol), as well as C5Pe and Kaol simultaneously (C5Pe-Ca-Kaol). The data was sampled from the last 20 ns of simulated time in systems solvated by water (a), toluene (b), and heptane (c). Average number of H-bonds with the Kaol surfaces per directly adsorbed C5Pe molecule (d). The data was taken from the last 20 ns of simulation and the standard deviation was shown by the error bar.

5.3.4.3. Interplay between adsorption and aggregation

In water, the C5Pe molecules aggregated together despite the -1 charge each carried. The polar solvent partly screened the coulombic repulsion between the hydrophilic heads, enabling local attractions between the hydrophobic PAHs through π-π stacking, resulting in the formation of a bulky aggregates. Meanwhile, contrast to the reluctant attachment of the hydrophobic part to the alumina surface, the hydrophilic head tended to form H-bonds with the solid surface via the carboxyl groups of C5Pe and the hydroxyl groups on the surface, driving the direct adsorption of some C5Pe molecules in the aggregate (Figure 5.4a). Consistent with C5Pe monomer (Figure 5.2c), the adsorption was near the alumina surface with a similar titled configuration (see Figures 6a and 2k for the statistics on angle). The angle between all C5Pe molecules and the surface (Figure 5.6b) was in the same range as the directly adsorbed C5Pe molecules (Figure 5.6a), suggesting that the indirectly adsorbed molecules were stabilized near the surface via the π-π stacking that was parallel with the directly adsorbed ones.

In toluene, the angle θ of directly adsorbed C5Pe in an aggregate (Figure 5.6a) was similar to that of the adsorbed monomer (Figure 5.2m), with most of them remaining flat ($\theta \approx 20^{\circ}$) and forming the first adsorption layer on the alumina surface. On the contrary, θ of all C5Pe molecules (Figure 5.6b) fell into a much larger range. This was caused by indirectly adsorbed molecules which were kept in the thick aggregate (Figure 5.4c) by Ca^{2+} coordination and π-π interaction while exposing themselves to toluene. Compared with the parallel stacking in water (similar angle distribution in Figures 6a and b), the undermined stacking (different angle distributions in Figures 6a and b) between C5Pe molecules was caused by the competition from π-π interaction between toluene and PAH planes of C5Pe. Consequently, the multi-layered adsorption was less stable (Figure 5.4d).

In heptane, the directly adsorbed C5Pe in an aggregate showed similar configurations with the monomers, and the C5Pe molecules were attracted by both the alumina and the siloxane surfaces. Since heptane is a poor solvent for C5Pe, the molecules tended to quickly minimize the contact area with the solvent and maximize the contact with the solid surface (through both the hydrophobic and the hydrophilic parts as explained in section 3.2) in order to maintain a stable state. As a result, the probability for C5Pe to interact with each other in the solvent was limited and the number of adsorbed monomers increased. This led to a compact adsorption structure

(Figure 5.4e) two to four times thinner than those in water and toluene. The thin adsorption structure still contained two layers of C5Pe molecules more or less parallel to each other (comparing relevant angles in Figures 6a and b), stabilized by the π-π stacking and Ca^{2+} coordination.

To conclude, in all three systems, the direct adsorption of C5Pe (monomers or the first layer in an aggregate) was driven by the enthalpic attraction of the surface, facilitated by H-bonding and in the case of having heptane as the solvent, Ca^{2+} coordination. Meanwhile, the aggregation among C5Pe molecules induced indirect adsorptions and multi-layer adsorbed structures. π-π stacking is a main driving force for aggregation, while Ca^{2+} coordination also assisted in aggregation in organic solvents.

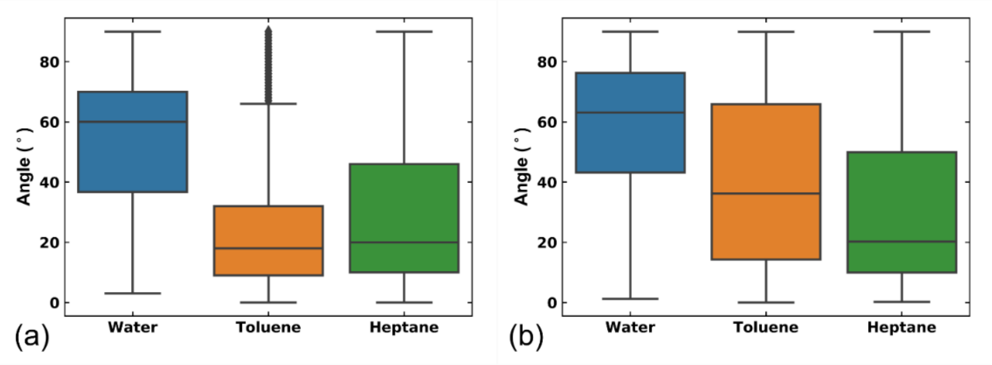

Figure 5.6. Angle between the solid surface and PAH planes of directly adsorbed C5Pe molecules (a), as well as between the surface and all the C5Pe molecules (b). The data was sampled from the last 20 ns of the simulated time.

5.3.5. Discussion

As demonstrated in previous sections, in water the adsorption on the hydrophilic alumina surface was mainly through the H-bonding between the surface and the hydrophilic carboxylate head of C5Pe, while the hydrophobic tail was repelled. Meanwhile, the water molecules competed with the hydrophilic head for adsorption. As a result, the adsorption was weak and in a titled configuration. In contrast, the adsorption on the hydrophobic siloxane surface was driven by the entropy of water release, and thus the adsorption was stable and in a flat configuration where water-solid contact was minimized. It can thus be proposed that for other amphiphilic polymers, the adsorption at different solid-water interfaces could be tuned by adjusting the hydrophilicity of the polymer. The simultaneous presence of two dissimilar surfaces in water would have a large effect on the adsorption of amphiphilic molecules, mediated by the attractions from both surfaces.

In organic solvents, the C5Pe interacted with the surface mainly through van der Waals force (via the PAH plane, with both types of surfaces), H-bonding (via the carboxylate group and the heteroatoms, with the alumina surface only), and ion coordination (if multivalent ions such as Ca^{2+} were presented). The preferred adsorption on the alumina surface (monomer and aggregate in toluene, aggregate in heptane) was supported by the experiments of Dudášová et al. [11]. The distinct solvency of toluene and heptane resulted in different multi-layered adsorption, suggesting that the thickness of adsorbed aggregates could be modulated by the toluene/heptane ratio. Besides the solvent, the configuration of aggregates could also be regulated by adjusting the terminals of C5Pe, for example, when the C5Pe was neutral in toluene, the aggregation would be promoted [18] and the multi-layer configuration connected by Ca^{2+} might be weakened.

5.4. Conclusion

In this work, the behaviors of deprotonated C5Pe between two solid surfaces with different polarity was studied by MD simulation. In water, both C5Pe monomers and aggregates preferred to adsorb on the alumina surface. However, in the control systems where a C5Pe molecule was placed between two identical surfaces, it displayed a much weaker adsorption between two alumina surfaces than between two siloxane surfaces. Potential of mean force (PMF) calculations demonstrated the interplay between enthalpy-driven adsorption on the alumina surface and entropy-driven adsorption on the siloxane surface. In the adsorbed C5Pe aggregates, the hydrophobic parts of the molecules stacked in a parallel manner and aligned perpendicularly to the alumina surface, while the hydrophilic parts formed hydrogen bonds with the surface. In toluene, the C5Pe monomers and aggregates also displayed a preferred adsorption on the alumina surface, driven by van der Waals and coulomb interactions, and hydrogen bonding. A multi-layer adsorption of C5Pe aggregates was observed, which resulted from coordination bonds established through the Ca^{2+} ions in the solvent. In heptane, adsorptions were found on both surfaces, and PMF calculations showed similar strength of binding to alumina and siloxane surfaces. The adsorbed aggregates were compact, with intermolecular π-π stackings that were parallel to the surfaces. This work shed light on the behaviors of asphaltenes in the simultaneous presence of different clay surfaces, and how such behaviors may be influenced by the nature of the solvent.

References

[1] F. Riobé, R. Szűcs, C. Lescop, R. Réau, L. Nyulászi, P.-A. Bouit, M. Hissler, Coordination Complexes of P-Containing Polycyclic Aromatic Hydrocarbons: Optical Properties and Solid-State Supramolecular Assembly, Organometallics. 36 (2017) 2502–2511. doi:10.1021/acs.organomet.6b00715.

[2] W. Li, N. Zhu, Y. Shen, H. Yuan, Towards efficient elimination of polycyclic aromatic hydrocarbons (PAHs) from waste activated sludge by ozonation, Environ. Res. 195 (2021) 110783. doi:10.1016/j.envres.2021.110783.

[3] H.-S. Lin, S. Okawa, Y. Ma, S. Yotsumoto, C. Lee, S. Tan, S. Manzhos, M. Yoshizawa, S. Chiashi, H. Mo Lee, T. Tanaka, H. Kataura, I. Jeon, Y. Matsuo, S. Maruyama, Polyaromatic

Nanotweezers on Semiconducting Carbon Nanotubes for the Growth and Interfacing of Lead Halide Perovskite Crystal Grains in Solar Cells, Chem. Mater. 32 (2020) 5125–5133. doi:10.1021/acs.chemmater.0c01011.

[4] J. G. Speight, S. E. Moschopedis, On the Molecular Nature of Petroleum Asphaltenes, 2009. doi:10.1021/ba-1981-0195.ch001.

[5] O. C. Mullins, H. Sabbah, J. Eyssautier, A. E. Pomerantz, L. Barré, A. Ballard Andrews, Y. Ruiz-Morales, F. Mostowfi, R. McFarlane, L. Goual, R. Lepkowicz, T. Cooper, J. Orbulescu, R. M. Leblanc, J. Edwards, R. N. Zare, Advances in Asphaltene Science and the Yen–Mullins Model, Energy & Fuels. 26 (2012) 3986–4003. doi:10.1021/ef300185p.

[6] O.C. Mullins, The modified yen model, in: Energy and Fuels, 2010: pp. 2179–2207. doi:10.1021/ef900975e.

[7] J. Sjöblom, S. Simon, Z. Xu, Model molecules mimicking asphaltenes, Adv. Colloid Interface Sci. 218 (2015) 1–16. doi:10.1016/j.cis.2015.01.002.

[8] A. Ballard Andrews, A. McClelland, O. Korkeila, A. Demidov, A. Krummel, O. C. Mullins, Z. Chen, Molecular Orientation of Asphaltenes and PAH Model Compounds in Langmuir−Blodgett Films Using Sum Frequency Generation Spectroscopy, Langmuir. 27 (2011) 6049–6058. doi:10.1021/la200466b.

[9] Z. Shen, J.J. Sheng, Experimental and numerical study of permeability reduction caused by asphaltene precipitation and deposition during CO_2 huff and puff injection in Eagle Ford shale, Fuel. 211 (2018) 432–445. doi:10.1016/j.fuel.2017.09.047.

[10] S.M. Hashmi, M. Loewenberg, A. Firoozabadi, Colloidal asphaltene deposition in laminar pipe flow: Flow rate and parametric effects. Phys. Fluids. 27 (2015) 83302. doi:10.1063/1.4927221.

[11] D. Dudášová, S. Simon, P. V. Hemmingsen, J. Sjöblom, Study of asphaltenes adsorption onto different minerals and clays. Part 1. Experimental adsorption with UV depletion detection, Colloids Surfaces A Physicochem. Eng. Asp. 317 (2008) 1–9. doi:10.1016/j.colsurfa.2007.09.023.

[12] F. Liu, H. Yang, J. Wang, Y. Qian, J. Wu, S. Li, Q. Liu, S. Yang, S. Xu, X. Zhang, Z. Zhao, J. Wang, Molecular interaction between asphaltene and quartz with different surface wettability: A combined study of experimental measurement and theoretical calculation, Fuel. 258 (2019) 115937. doi:10.1016/j.fuel.2019.115937.

[13] T. Pernyeszi, Á. Patzkó, O. Berkesi, I. Dékány, Asphaltene adsorption on clays and crude oil reservoir rocks, Colloids Surfaces A Physicochem. Eng. Asp. 137 (1998) 373–384. doi:10.1016/S0927-7757(98)00214-3.

[14] J.L. Bantignies, C. Cartier Dit Moulin, H. Dexpert, Asphaltene adsorption on kaolinite characterized by infrared and X-ray absorption spectroscopies, J. Pet. Sci. Eng. 20 (1998) 233–237. doi:10.1016/S0920-4105(98)00025-4.

[15] Y. Xiong, T. Cao, Q. Chen, Z. Li, Y. Yang, S. Xu, S. Yuan, J. Sjöblom, Z. Xu, Adsorption of a Polyaromatic Compound on Silica Surfaces from Organic Solvents Studied by Molecular Dynamics Simulation and AFM Imaging, J. Phys. Chem. C. 121 (2017) 5020–5028. doi:10.1021/acs.jpcc.6b11763.

[16] S.T. Dubey, M.H. Waxman, Asphaltene adsorption and desorption from mineral surfaces, SPE Reserv. Eng. (Society Pet. Eng. 6 (1991) 389–395. doi:10.2118/18462-PA.

[17] D. Pradilla, S. Subramanian, S. Simon, J. Sjöblom, I. Beurroies, R. Denoyel, Microcalorimetry Study of the Adsorption of Asphaltenes and Asphaltene Model Compounds at the Liquid-Solid Surface, Langmuir. 32 (2016) 7294–7305.

doi:10.1021/acs.langmuir.6b00816.

[18] Y. Xiong, Z. Li, T. Cao, S. Xu, S. Yuan, J. Sjöblom, Z. Xu, Synergistic Adsorption of Polyaromatic Compounds on Silica Surfaces Studied by Molecular Dynamics Simulation, J. Phys. Chem. C. 122 (2018) 4290–4299. doi:10.1021/acs.jpcc.7b10907.

[19] T. Lan, H. Zeng, T. Tang, Understanding Adsorption of Violanthrone-79 as a Model Asphaltene Compound on Quartz Surface Using Molecular Dynamics Simulations, J. Phys. Chem. C. 122 (2018) 28787–28796. doi:10.1021/acs.jpcc.8b09712.

[20] J.F. Lee, M.M. Mortland, S.A. Boyd, C.T. Chiou, Shape-selective adsorption of aromatic molecules from water by tetramethylammonium-smectite, J. Chem. Soc. Faraday Trans. 1 Phys. Chem. Condens. Phases. 85 (1989) 2953–2962. doi:10.1039/F19898502953.

[21] F. Gao, Z. Xu, G. Liu, S. Yuan, Molecular dynamics simulation: The behavior of asphaltene in crude oil and at the oil/water interface, Energy and Fuels. 28 (2014) 7368–7376. doi:10.1021/ef5020428.

[22] J. Long, Z. Xu, J.H. Masliyah, Adhesion of single polyelectrolyte molecules on silica, mica, and bitumen surfaces, Langmuir. 22 (2006) 1652–1659. doi:10.1021/la052757f.

[23] T. Chen, F. Lin, B. Primkulov, L. He, Z. Xu, Impact of salinity on warm water-based mineable oil sands processing, Can. J. Chem. Eng. 95 (2017) 281–289. doi:10.1002/cjce.22637.

[24] G. Yang, T. Chen, J. Zhao, D. Yu, F. Liu, D. Wang, M. Fan, W. Chen, J. Zhang, H. Yang, J. Wang, Desorption Mechanism of Asphaltenes in the Presence of Electrolyte and the Extended Derjaguin-Landau-Verwey-Overbeek Theory, Energy and Fuels. 29 (2015) 4272–4280. doi:10.1021/acs.energyfuels.5b00866.

[25] T. Kuznicki, J.H. Masliyah, S. Bhattacharjee, Molecular dynamics study of model

molecules resembling asphaltene-like structures in aqueous organic solvent systems, Energy and Fuels. 22 (2008) 2379–2389. doi:10.1021/ef800057n.

[26] T. Kuznicki, J. H. Masliyah, S. Bhattacharjee, Aggregation and Partitioning of Model Asphaltenes at Toluene−Water Interfaces: Molecular Dynamics Simulations, Energy & Fuels. 23 (2009) 5027–5035. doi:10.1021/ef9004576.

[27] S. Veeramasuneni, M.R. Yalamanchili, J.D. Miller, Interactions between dissimilar surfaces in high ionic strength solutions as determined by atomic force microscopy, Colloids Surfaces A Physicochem. Eng. Asp. 131 (1998) 77–87. doi:10.1016/S0927-7757(96)03929-5.

[28] Q. Lin, T. Akai, M.J. Blunt, B. Bijeljic, H. Iwama, K. Takabayashi, Y. Onaka, H. Yonebayashi, Pore-scale imaging of asphaltene-induced pore clogging in carbonate rocks, Fuel. 283 (2021) 118871. doi:10.1016/j.fuel.2020.118871.

[29] J. Masliyah, Z.J. Zhou, Z. Xu, J. Czarnecki, H. Hamza, Understanding Water-Based Bitumen Extraction from Athabasca Oil Sands, Can. J. Chem. Eng. 82 (2004) 628–654.

[30] L. Zhang, L. Xie, X. Cui, J. Chen, H. Zeng, Intermolecular and surface forces at solid/oil/water/gas interfaces in petroleum production, J. Colloid Interface Sci. 537 (2019) 505–519. doi:10.1016/j.jcis.2018.11.052.

[31] A. Pourmohammadbagher, J.M. Shaw, Probing Contaminant Transport to and from Clay Surfaces in Organic Solvents and Water Using Solution Calorimetry, Environ. Sci. Technol. 49 (2015) 10841–10849. doi:10.1021/acs.est.5b02416.

[32] C. Jian, M.R. Poopari, Q. Liu, N. Zerpa, H. Zeng, T. Tang, Reduction of Water/Oil Interfacial Tension by Model Asphaltenes: The Governing Role of Surface Concentration, J. Phys. Chem. B. 120 (2016) 5646–5654. doi:10.1021/acs.jpcb.6b03691.

[33] R. Šolc, M.H. Gerzabek, H. Lischka, D. Tunega, Wettability of kaolinite (001) surfaces - Molecular dynamic study, Geoderma. 169 (2011) 47–54. doi:10.1016/j.geoderma.2011.02.004.

[34] D. Tunega, M.H. Gerzabek, H. Lischka, Ab Initio Molecular Dynamics Study of a Monomolecular Water Layer on Octahedral and Tetrahedral Kaolinite Surfaces, J. Phys. Chem. B. 108 (2004) 5930–5936. doi:10.1021/jp037121g.

[35] E.R. Johnson, A. Otero-De-La-Roza, Adsorption of organic molecules on kaolinite from the exchange-hole dipole moment dispersion model, in: J. Chem. Theory Comput., 2012: pp. 5124–5131. doi:10.1021/ct3006375.

[36] D. Ji, G. Liu, X. Zhang, C. Zhang, S. Yuan, Adsorption of C5Pe molecules on silica surfaces with different hydrophobicity studied by molecular dynamics simulation, Appl. Surf. Sci. 495 (2019) 143624. doi:10.1016/j.apsusc.2019.143624.

[37] Z. Niu, X. Ma, R. Manica, T. Yue, Molecular Destabilization Mechanism of Asphaltene Model Compound C5Pe Interfacial Film by EO-PO Copolymer: Experiments and MD Simulation, J. Phys. Chem. C. 123 (2019) 10501–10508. doi:10.1021/acs.jpcc.9b02248.

[38] D.L. Bish, Rietveld refinement of the kaolinite structure at 1.5 K, Clays Clay Miner. 41 (1993) 738–744. doi:10.1346/CCMN.1993.0410613.

[39] G.M.Torrie, J.P.Valleau, Nonphysical sampling distributions in Monte Carlo free-energy estimation: Umbrella sampling, J. Comput. Phys. 23 (1977) 187–199.

[40] W. Sun, H. Zeng, T. Tang, Enhanced Adsorption of Anionic Polymer on Montmorillonite by Divalent Cations and the Effect of Salinity, J. Phys. Chem. A. 125 (2021) 1025–1035. doi:10.1021/acs.jpca.0c08797.

[41] E. Abraham, M. J., Murtola, T., Schulz, R., Páll, S., Smith, J. C., Hess, B., Lindahl,

GROMACS: High performance molecular simulations through multi-level parallelism from laptops to supercomputers, SoftwareX. 1–2 (2015) 19–25.

[42] S. Pronk, S. Páll, R. Schulz, P. Larsson, P. Bjelkmar, R. Apostolov, M.R. Shirts, J.C. Smith, P.M. Kasson, D. Van Der Spoel, B. Hess, E. Lindahl, GROMACS 4.5: a high-throughput and highly parallel open source molecular simulation toolkit, Bioinformatics. 29 (2013) 845–854. doi:10.1093/bioinformatics/btt055.

[43] H.J.C. Berendsen, D. van der Spoel, R. van Drunen, A Message-Passing Parallel Molecular Dynamics Implementation, Phys. Commun. 91 (1995) 43−56.

[44] D.J. Frisch, M. J., Trucks, G. W., Schlegel, H. B., Scuseria, G. E., Robb, M. A., Cheeseman, J. R., Scalmani, G., Barone, V., Petersson, G. A., Nakatsuji, H., Li, X., Caricato, M., Marenich, A. V., Bloino, J., Janesko, B. G., Gomperts, R., Mennucci, B., Hratch, Gaussian 16 Revision B. 01., Wallingford CT. (2016).

[45] A.K. Malde, L. Zuo, M. Breeze, M. Stroet, D. Poger, P.C. Nair, C. Oostenbrink, A.E. Mark, An Automated force field Topology Builder (ATB) and repository: Version 1.0, J. Chem. Theory Comput. 7 (2011) 4026–4037. doi:10.1021/ct200196m.

[46] N. Schmid, A.P. Eichenberger, A. Choutko, S. Riniker, M. Winger, A.E. Mark, W.F. Van Gunsteren, Definition and testing of the GROMOS force-field versions 54A7 and 54B7, (2011) 843–856. doi:10.1007/s00249-011-0700-9.

[47] C.M. Breneman, K.B. Wiberg, Determining atom-centered monopoles from molecular electrostatic potentials – the need for high sampling density in formamide conformational-analysis, J. Comp. Chem. 11 (1990) 361–73. doi:10.1002/jcc.540110311.

[48] W. Sun, H. Zeng, T. Tang, Synergetic adsorption of polymers on montmorillonite: Insights from molecular dynamics simulations, Appl. Clay Sci. 193 (2020) 105654.

doi:10.1016/j.clay.2020.105654.

[49] R.T. Cygan, J.J. Liang, A.G. Kalinichev, Molecular models of hydroxide, oxyhydroxide, and clay phases and the development of a general force field, J. Phys. Chem. B. 108 (2004) 1255–1266. doi:10.1021/jp0363287.

[50] M. Pouvreau, J.A. Greathouse, R.T. Cygan, A.G. Kalinichev, Structure of Hydrated Gibbsite and Brucite Edge Surfaces: DFT Results and Further Development of the ClayFF Classical Force Field with Metal-O-H Angle Bending Terms, J. Phys. Chem. C. 121 (2017) 14757–14771. doi:10.1021/acs.jpcc.7b05362.

[51] Kumar, S., Rosenberg, J. M., Bouzida, D., Swendsen, R. H., Kollman, P. A., 1992. The Weighted Histogram Analysis Method for Free-Energy Calculations on Biomolecules. I. The Method. Journal of computational chemistry, 13(8), 1011-1021.

[52] S. Nosé, A molecular dynamics method for simulations in the canonical ensemble, Mol. Phys. 52 (1984) 255–268. doi:10.1080/00268978400101201.

[53] W.G. Hoover, Canonical dynamics: Equilibrium phase-space distributions, Phys. Rev. A. 31 (1985) 1695–1697. doi:10.1103/PhysRevA.31.1695.

[54] M. Parrinello, A. Rahman, Polymorphic transitions in single crystals: A new molecular dynamics method, J. Appl. Phys. 52 (1981) 7182–7190. doi:10.1063/1.328693.

[55] Darden, T.; York, D.; Pedersen, L. Particle Mesh Ewald: An N·log(N) Method for Ewald Sums in Large Systems. *J. Chem. Phys.* **1993**, *98* (12), 10089–10092. https://doi.org/10.1063/1.464397.

[56] A.K. Katz, J.P. Glusker, S.A. Beebe, C.W. Bock, Calcium ion coordination: A comparison with that of beryllium, magnesium, and zinc, J. Am. Chem. Soc. 118 (1996) 5752–5763. doi:10.1021/ja953943i.

Chapter 6. Interplay between Polycyclic Aromatic Hydrocarbons and Polymers in Their Adsorption on Clay-Water Interfaces

6.1. Introduction

Adsorption of polycyclic aromatic hydrocarbons (PAHs) on clay-water interfaces is present in many problems concerning natural environments and engineering applications, resulting in contamination of soil and sediment [1,2], air pollution [3], fouling of pipes [4], and mature fine tailings [5]. PAHs are planar aromatic molecules formed by fused aromatic rings and aliphatic peripherals, usually derived from fossil fuel products [1–5]. Polymers with hydrophilic or amphiphilic properties have been commonly employed to modulate the PAH adsorption on clay-water interfaces [3,6,7]. Clay minerals such as montmorillonite (Mt) and kaolinite (Kaol) have high affinity to PAHs and many polymers additives [8,9], which demands a thorough understanding on the interplay between the adsorption of PAHs and polymers.

The presence of one adsorbate (PAHs or polymers) could impede the adsorption of the other due to the competition for the finite binding site on the clay surface. Maravilha et al. [10], via ultraviolet-visible spectrometry, observed a decreased asphaltene (the heaviest component of crude oil, consisting of PAH components) adsorption on Kaol with increased concentration of polycardanol (PCN). The scanning electron microscopy (SEM) image of PCN/asphaltene/Kaol system showed that PCN covered a large Kaol surface area, which was similar to the image when only asphaltenes were present. It was proposed that the phenolic group of PCN competed with asphaltene for the adsorption on Kaol through hydrogen bonds (H-bonds), and the pendent hydrocarbon chains of PCN also hindered the asphaltene-Kaol interaction, resulting in the decreased asphaltene adsorption. Similar were also reported for the removal of PAHs from soil [9,11].

The adsorption of PAHs and polymers could be also altered by the repulsive/attractive forces between the two types of adsorbates. Li et al. [12] measured the adhesion forces between bitumen (main constituents being asphaltenes) and clay surfaces (taken from oil sands tailings slurry) in water when hydrolyzed polyacrylamide (HPAM) was added. Zeta potential measured was -20 mV for clay particles and -60 mV for bitumen. Long-range attractive force existed in the absence of HPAM, while the attraction displayed a non-monotonic change (decreased first and then became increased) with the dosage of HPAM. It was proposed that in the absence of HPAM, bitumen and clay particles tended to aggregate together. HPAM preferred to adsorb on clay particles than bitumen due to the smaller electrostatic repulsion at appropriate dosage, modifying the clay surface, and thus the attraction between bitumen and clay particles decreased. However, when HPAM dosage further increased, HPAM bound to both bitumen and clay surface, and the attraction between bitumen and clay increased again. Similar finding was reported by Long et al. [13] where the adhesion forces of HPAM, measured by atomic force microscope (AFM), decreased in the order of mica, silica, and bitumen, in both deionized water and commercial process water. It was proposed that HPAM would preferentially adsorb on the clay surfaces than on the bitumen surfaces. On the other hand, Qin et al. [2] measured a substantial increase in adsorption of PAHs (phenanthrene and pyrene) on montmorillonite by adding DNA. X-ray spectroscopy (XPS), Fourier transform infrared spectroscopy (FTIR) and computational orbital analyses demonstrated that the PAHs first bound with DNA via van der Waals and π-π interactions, and the PHA-DNA complexes became adsorbed through the complexation between DNA phosphates and the exchangeable cations (Na^+, Ca^{2+}, or Fe^{3+}) on the Mt surface.

The mutual influence of PAHs and polymers was also frequently attributed to the modification of surface wettability. Fused aromatic rings in PAHs are hydrophobic, thus having higher affinity to surfaces with higher hydrophobicity [14]. Ei-Nahhal et al. [15] measured the adsorption of phenanthrene on different organoclay complexes using the high-pressure liquid chromatography (HPLC) technique. Little adsorption of phenanthrene was observed on bare montmorillonite surface, whereas the adsorbed amounts dramatically increased when the surface changed from hydrophilic (modified by tetramethylammonium (TMA), phenyltrimethylammonium (PTMA), tetraheptylammonium (THA)) to hydrophobic (modified by hexadecyltrimethylammonium (HDTMA), benzyltrimethylammonium (BTMA), tetraphenylphosphonium (TPP)). The mediation of PAH adsorption by polymers through the modification of surface wettability have also been reported in other works [16,17].

In summary, the interplay between PAHs and polymer reagents in their adsorptions on clay-water interfaces is complex and the properties of clay surfaces are of great importance since the available sites for binding, surface charge, and wettability are all related to the surface functional groups. For clay minerals, two types of surfaces are commonly encountered: basal surface and edge surface. The basal surface consists of oxygen and silicon atoms and could carry permanent surface charges. The edge surface contains hydroxyl groups, and the surface charge is regulated by the ionization under certain pH conditions. When carrying similar charges, the basal surface is usually more hydrophobic than the edge surface. Given the many distinct properties of the two types of clay surfaces and their sensitivity to the change of environments, it is of interest to produce molecular pictures of the adsorption of PAHs and polymers on the basal and edge surfaces. Such “visualization” can not only benefit the study of adsorption mechanisms, but also provide interpretations to experimental observations.

In this work, molecular dynamics (MD) simulation was employed to study the interplay between the adsorptions of PAHs and polymers on clay-water interfaces. Basal surface of Mt and edge surface of Kaol were modeled, as two types of classical clay surfaces with distinct surface groups. Deprotonated N-(1-Hexylheptyl)-N'-(5-carboxylicpentyl) perylene-3,4,9,10-tetracarboxylic bisimide (C5Pe) and deprotonated polyacrylamide (APAM) were studied as adsorbates, to represent the common PAH and polymers found in soil, sediments, wastewater, and etc. [1–5,13] The edge surface, C5Pe, and PAM were all deprotonated to represent a slightly alkaline pH condition, which was commonly found in many contaminated soil and industrial process water [18,19]. A series of systems involving different numbers of C5Pe and APAM were simulated to investigate the dependence of adsorption on the applied dosage, as the surface can be gradually modified with the increase of adsorbates [12,13].

6.2. Simulation Methods

6.2.1. Molecular models

Two types of clay surfaces were modeled. The first was the basal surface of Mt with no hydroxyl groups. Mt is an aluminosilicate referred as a TOT clay mineral: two opposing tetrahedrally coordinated Si atoms sandwiching one octahedrally coordinated Al atoms [20–23]. As shown in Figure 6.1a, a supercell was built by closely stacking the unit cells in a 16 × 8 × 1 array. The *z* dimension of the supercell was then expanded to accommodate the addition of adsorbates in proximity to the surface, resulting in a simulation cell with the size of 8.29 × 7.18 × 8 nm^3. Within the supercell, sixteen Al atoms were isomorphically substituted by Mg, resulting a negative layer charge of -16. The permanent layer charge was neutralized by Ca^{2+}, a common exchangeable ion found in clay minerals [20–23].

Edge surface of Kaol was built as another type of clay surface. The unit cell of Kaol crystal consisted of one tetrahedral silica sheet linked to one octahedral alumina sheet through oxygen atoms [24], and thus Kaol was also referred to as TO layer. The (110) edge surface model of Kaol were built from the unit cell by cleaving the 1×5×1 supercell along the $[1\bar{1}0]$ direction. For the convenience of analysis later, the *y* and *z* axes of the cleaved supercell were swapped so that the clay-water interface was perpendicular to the *z* direction, resulting in a supercell with the size of $0.52 \times 0.71 \times 4.49$ nm^3. On the edge surface, one H atom was added to the non-bridging O and one -OH group was added to the three-coordinated Si so that each surface consisted of SiOH and $Al(OH)(OH_2)$ terminals (upper left of Figure 6.1b). Then the generated supercell was expanded to a 16 × 10 × 1 supercell (bottom of Figure 6.1b), to make the surface area close to that of the basal surface model. The two edge surfaces on the two sides of each TO layer were identical (bottom of Figure 6.1b). The final simulation cell was in $8.29 \times 7.13 \times 12$ nm^3 after expansion in *z* dimension. To mimic the saline environment with pH ~ 8-9, eight nonadjacent unit cells were deprotonated based on the experimental results [25] and density function theory (DFT) calculation [26], yielding the same charge as the basal surface model. Specifically, near the eight deprotonated cells, the H_2O that were associated with Al were deprotonated into OH groups, resulting into $Al(OH)_2$ groups [27] (upper right of Figure 6.1b). Each deprotonated cell carried a charge of -2, and the total charge of the Kaol edge surface model was -16.

The deprotonated C5Pe was built as the model PAH, consisting of fused rings and aliphatic side chains (Figure 6.1c). The carboxylic group was deprotonated so that each C5Pe carried a charge of -1. The deprotonated carboxylic group was hydrophilic while the remaining large part of C5Pe (marked by the rectangle in Figure 6.1c) was hydrophobic. The deprotonated polymer

APAM was added together with C5Pe (Figure 6.1d). All the carboxylates of APAM were deprotonated represent the alkaline pH condition, resulting in a charge of -3.

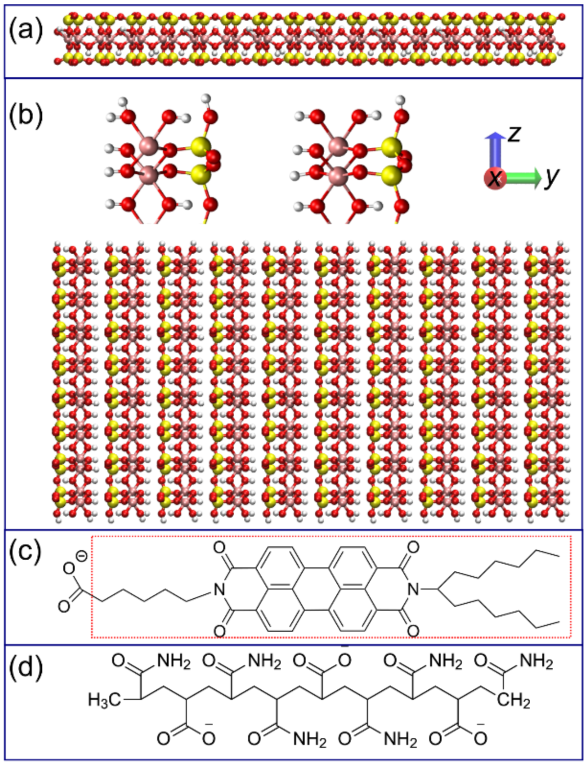

Figure 6.1. Molecular structure of the basal surface of Mt (a), edge surface of Kaol (b), C5Pe (c), and APAM (d). The clays are represented by balls in pink (aluminum), yellow (silicon), red (oxygens), and white (hydrogen).

6.2.2. Systems simulated

The simulated systems are listed in Table 6.1. The adsorption of C5Pe alone on the two types of clay surface were investigated in systems Mt-0 and Kaol-0, respectively. A total of twelve C5Pe molecules were introduced above the clay surface in a 2 × 3 × 2 array, followed by the solvation with water and Ca^{2+} to neutralize the negative charges. To study the effects of APAM on C5Pe adsorption, a certain amount of APAM were simultaneously added with C5Pe, yielding the systems Mt-12, Mt-24, Kaol-12, and Kaol-24 where the numbers indicate the number of added

APAM molecules. To reveal the effects of C5Pe on the adsorption of APAM, systems Mt-C0 and Kaol-C0 were supplemented as comparison sets, where only 12 APAM molecules were present. Systems containing APAM and a high dosage of C5Pe were not simulated based on the results from the current systems.

Table 6.1. Simulated systems

system name	No. C5Pe	No. APAM	No. Ca2+
Mt-0	12	0	14
Mt-12	12	12	32
Mt-24	12	24	50
Kaol-0	12	0	14
Kaol-12	12	12	32
Kaol-24	12	24	50
Mt-C0	0	12	26
Kaol-C0	0	12	26

6.2.3. Simulation details

The force field parameters for Mt and Kaol were adopted from the CLAYFF force field [27–29] with all partial charges unmodified. These clay models have been validated in our previous works [30,31]. The molecular topologies for C5Pe and APAM were generated by submitting the coordinate information to Automated Topology Builder (ATB) [32], which were compatible with the GROMOS 96 54A7 force field parameter set [33]. The atomic charges in the topologies were replaced with the ones assigned by the CHelpG method [34] after the structure optimization by DFT simulation in Gaussian 16 [35]. Water the solvent was represented by the SPC water model [36].

GROMACS 2020 open source package [37–39] was used to carry out all the MD simulations. Periodic boundary conditions were applied in all directions so that the aqueous solution was effectively between two symmetrical solid surfaces. Each system was first energetically optimized by the steepest descent method under the maximum force limit of 1000 kJ/(mol·nm), followed by NVT equilibrations for 1 ns with the clay atoms frozen. Finally, production runs in isotropic NPT ensemble were performed, with position restraints in *z* direction applied on the silicon atoms of the solids (with a force constant of 1000 kJ/mol·nm^2). For all simulations, Nose-Hoover thermostat [40,41] and Parrinello–Rahman barostat [42] were applied to maintain the temperature and pressure at 300 K and 1 bar, respectively. Leap-frog algorithm [43] was used to integrate the equation of motions. PME method was applied to calculate the long-range electrostatic interactions.

6.3. Results and Discussion

6.3.1. Adsorption of C5Pe on basal surface mediated by APAM

The density profiles of C5Pe and final configurations in systems containing basal Mt surface are shown in Figure 6.2, plotted against the *Z* coordinate, which measured the vertical distance from the upper surface plane of Mt defined using the surface oxygens. Increase in *Z* represented departure from the basal surface at the bottom of the simulation box towards its periodic image above. In system Mt-0 where no APAM was present, C5Pe displayed two distinct peaks near the top of the basal surface ($Z = 0.3$ nm, 0.75 nm, marked by 1 and 2 in Figure 6.2a), which corresponded to the adsorption consisting of two layers of molecules (Figure 6.2b, see justification of adsorption in Appendix E, section E1). The first peak ($Z = 0.3$ nm) represented the C5Pe adsorption in a parallel configuration, and the second peak resulted from the molecules that were parallel to the molecules in the first layer. Besides the parallelly adsorbed molecules, some C5Pe also adsorbed in a titled configuration, as shown in Figure 6.2b. The single layer at Z = 6.5-7.2 nm (peak at *Z* = 7 nm) indicated a single-layered adsorption at the bottom of the basal surface (Figure 6.2b). In this system, all the C5Pe molecules became adsorbed and there were no C5Pe in the bulk, as implied from the density value of zero for *Z* = 2-7 nm. The C5Pe could adsorb on either surface since the top and bottom surfaces were identical and the C5Pe were initially placed in the middle of the simulated cell.

In system Mt-12 where twelve APAM molecules were added simultaneously with C5Pe, the C5Pe density displayed three layers peaked at *Z* = 0.3 nm, 0.75 nm, and 1.15 nm (Figure 6.2c), respectively, which resulted from the parallel stacking of C5Pe in three layers on the top surface, as shown in Figure 6.2d. All the C5Pe became adsorbed, as the density became zero after *Z* = 1.8 nm. Compared with system Mt-0, the adsorption amount was not affected by the low dosage of APAM. When the number of APAM further increased in system Mt-24, certain amount of C5Pe stayed in the bulk, as indicated by the non-zero density value in the range of *Z* = 2-7 nm (Figure 6.2e). The adsorbed C5Pe molecules displayed monolayer configurations (Figure 6.2f), supported by the two isolated peaks at *Z* = 3 nm and 7 nm.

Comparison among systems Mt-0, 12, and 24 suggested that C5Pe themselves tended to adsorb on the Mt surfaces and a low dosage of APAM was not able to influence the adsorption, whereas a high dosage of APAM would impede the C5Pe adsorption when added simultaneously. To further investigate the hinderance of APAMC5Pe adsorption brought by APAM, an extra system (hereafter referred to as system Mt-p24) was simulated where 12 C5Pe molecules were pre-adsorbed on the Mt surface (based on the final configuration of Mt-0). In system Mt-p24, C5Pe displayed similar adsorption as that in system Mt-0 and Mt-12: all C5Pe molecules became adsorbed. The adsorbed C5Pe on the top surface consisted of three layers of molecules peaked at $Z = 0.3$ nm, 0.75 nm, and 1.2 nm, respectively, and there was a single layer adsorbed on the bottom surfaces with the peak at 7 nm (Figure 6.2g). Thus, in contrast with system Mt-24, the amount of C5Pe adsorption was not affected when a high dosage of APAM was added after the pre-formation of a C5Pe layer.

In all systems, each APAM carried a charge of -3, each C5Pe carried a charge of -1, and the charge on the top and bottom of the basal surface was -8 each. The C5Pe aggregated together despite the negative charge, and the largest aggregate contained at least 8 molecules in all the Mt systems (see Appendix E, Section E2 for the information on real-time aggregation of C5Pe). For example, in the last 20 ns of system Mt-12, all the C5Pe molecules formed an aggregate with a total charge of -12, while APAM did not display significant clustering (the largest cluster contained 5 molecules and lasted less than 1 ns, see Appendix E, Section E2 for information on real-time clustering of APAM). Intuitively, the electrostatic repulsion between the C5Pe aggregates and the surface would be larger than that between APAM and the surface. However, the adsorption of APAM (see Appendix E, Section E1 for the justification of adsorption) was in a less stable manner, compared with C5Pe (Appendix E, Section E2). Additional evidence for the weaker adsorption of APAM can be seen from the density profiles in Figures 6.2c, e, and f. Thus, electrostatic interaction did not play a significant role in the adsorption of C5Pe, instead, the adsorption was driven by the hydrophobic interaction between the surface and the hydrophobic part of C5Pe. The presence of APAM had limited interference on the hydrophobic interaction between C5Pe and the surface when the dosage ratio of APAM and C5Pe was low. When the dosage of APAM was sufficiently high (in system Mt-24), the C5Pe aggregate became coated by APAM in the bulk, as shown in Figure 6.2f, and the APAM coating reduced the hydrophobicity of C5Pe aggregates. Meanwhile, the electrostatic repulsion from the surface prevented the approach of the APAM coated C5Pe aggregates. As a result, C5Pe stayed in the bulk together with APAM (as told from the density profiles of C5Pe and APAM in Figure 6.2e). However, if C5Pe was pre-adsorbed on the surface, such as in system Mt-p24, APAM was not able to form the coating on C5Pe to repel them away, which verified the dominant role of hydrophobic interaction in the adsorption of C5Pe.

To summarize, the adsorption of C5Pe on the basal clay surface was mainly driven by hydrophobic interaction and was only suppressed by a high dosage of APAM added before a stable adsorption layer of C5Pe was formed on the surface. The suppression was enabled by the complexation of C5Pe and APAM in bulk water which APAM altered the wettability of C5Pe aggregates.

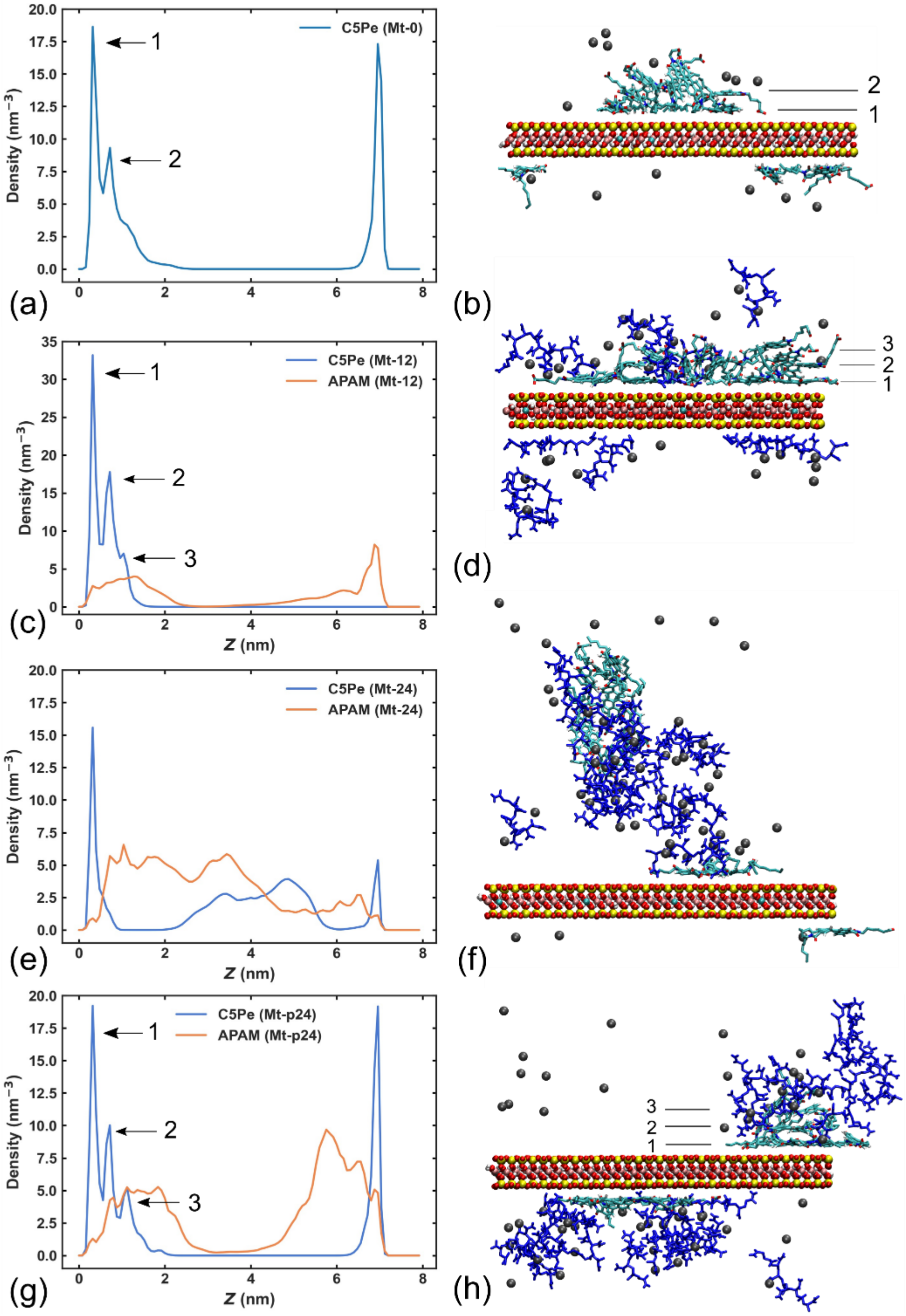

Figure 6.2. Density profiles of C5Pe and APAM along the *Z* coordinate, as well as the final snapshots in system Mt-0 (a, b), Mt-12 (c, d), Mt-24 (e, f), and Mt-p24 (g, h). Data for densities were averaged over the last 20 ns of the simulations. In (b), (d), (f) and (h), C5Pe is represented by sticks, APAM in blue licorice, and Mt represented by balls. Carbon is in cyan and the color scheme for the rest atoms are the same as in Figure 6.1. Water is removed for clarity.

6.3.2. C5Pe stacking on basal surface mediated by APAM

In all systems involving the basal surface, C5Pe aggregated together through π-π stacking regardless of the state of adsorption. To probe the aggregation, radial distribution function (RDF) between the center of geometry (COG) of C5Pe is plotted in Figure 6.3a. The peaks before 0.55 nm corresponded to the parallel stacking between PAHs of C5Pe (see Appendix E, Section E1 for the justification). The location of the first peak in system Mt-0 (0.25 nm) pointed to π-π stacking in a face-to-face orientation, as shown by the snapshot highlighted from the peak location in Figure 6.3a where the PAHs of C5Pe had a large overlap with each other. In system Mt-12, the location of the first peak slightly shifted to 0.3 nm, suggesting that the stacking was in a more offset arrangement, compared with that in system Mt-0. The peak location further shifted to 0.35 nm in system Mt-24.

The distributions for the angle between C5Pe and the basal surface are shown in Figure 6.3b. In system Mt-0, the most prominent peak in the angle distribution was at 10°, suggesting flat configuration was preferred. The prominent peak at 30° in system Mt-12 indicated that the adsorbed C5Pe favored a more titled configuration. In system Mt-24, the aggregate (consisting of 8 molecules) was in the bulk solution and lacked preferred angles. For system Mt-p24, both the RDF and angle distribution were similar to their counterparts in system Mt-0, confirming the lack of influence from APAM on pre-adsorbed C5Pe.

The titled configuration of C5Pe in system Mt-12 was affected by APAM. When added simultaneously with C5Pe, APAM adsorbed on C5Pe through H-bonds before the adsorption and aggregation fully developed (see Appendix E, Section E2 for the calculation of H-bonds and real-time aggregate size). The adsorption of APAM reduced the hydrophobicity of C5Pe, hindering their hydrophobic interaction with the surface and suppressing flat adsorption. In system Mt-24 where the dosage of APAM further increased, the hydrophobic interaction with the surface was further weakened, significantly impeding the adsorption of C5Pe. From the RDFs and angle distributions, a positive correlation can be observed between the extent of PAH overlapping among the π-π stacked molecules and the parallel orientation of the C5Pe PAH relative to the basal surface. Hydrophobic interaction between C5Pe and the surfaces not only drove adsorption, but also promoted face-to-face stacking between the adsorbed C5Pe molecules.

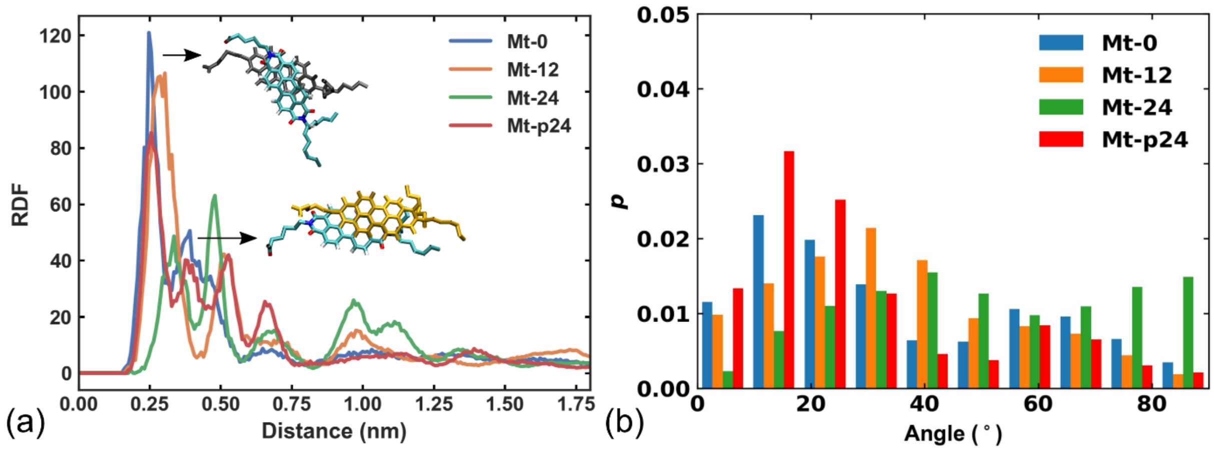

Figure 6.3. (a) RDFs between COG of C5Pe, the representative snapshots are for the first and second peak of RDFs in system Mt-0. (b) Probability distribution (*p*) for the angle between C5Pe molecules and the basal surface. Data was extracted from the last 20 ns of simulations.

6.3.3. Adsorption and aggregation of C5Pe near edge surface

While C5Pe showed fairly good adsorption on the basal surface of Mt, no adsorption was found on the edge surface of Kaol, despite the fact that Kaol carried the same amounts of negative charge as Mt. As shown in Figure 6.4a, the density of C5Pe had a single peak at $Z = 5.5$ nm in system Kaol-0, manifesting that C5Pe did not adsorb on the edge surface when being solely present in the system. The one distinct peak corresponded to the formation of an aggregate in bulk water, as shown in Figure 6.4b. When 12 APAM molecules were simultaneously added in system Kaol-12, similar to system Kaol-0, C5Pe formed a bulky aggregate and showed no adsorption. The overlapping peaks of C5Pe and APAM at $Z = 4.5$-7 nm (Figure 6.4c) was caused by the adsorption of APAM on the C5Pe aggregate, as illustrated in Figure 6.4d. In system Kaol-24, when a high dosage of APAM was added simultaneously, the density of C5Pe peaked at $Z = 2.5$ nm. Though there was still no adsorption, C5Pe stayed closer to the edge surface in system Kaol-24 (Figure 6.4f) than in system Kaol-0 and Kaol-12. Meanwhile, APAM showed some adsorption on the surface, as indicated by the non-zero density immediately after $Z = 0$ nm (Figure 6.4e).

The Kaol edge surface contained not only the neutral Si-OH groups, but also the charged Al-OH group resulting from the deprotonation of Al-OH_2 (Figure 6.1b). On the other hand, the basal Mt surface did not contain any hydroxyl groups and the permanent charges were in the central octahedra. As a result, the hydrophobicity of the basal Mt surface was larger than that of the edge Kaol surface, leading to the contrasting amounts of C5Pe adsorption. The adsorption of C5Pe on the hydrophilic edge surface was mainly regulated by the long-range electrostatic interaction. In system Kaol-0, the C5Pe aggregate showed no adsorption due to the strong electrostatic repulsion between the negatively charged C5Pe and the surface. In system Kaol-12, the addition of polyanions (APAM) could suppress the electric double layer repulsion but was not sufficient to support the approach of C5Pe to the surface. When a high dosage of APAM was added in system Kaol-24, the further suppressed electrostatic repulsion enabled the adsorption of the APAM coated C5Pe aggregate, and the adsorption of APAM was through H-bonding and Ca^{2+} coordination (see Appendix E, Section E2 for more information).

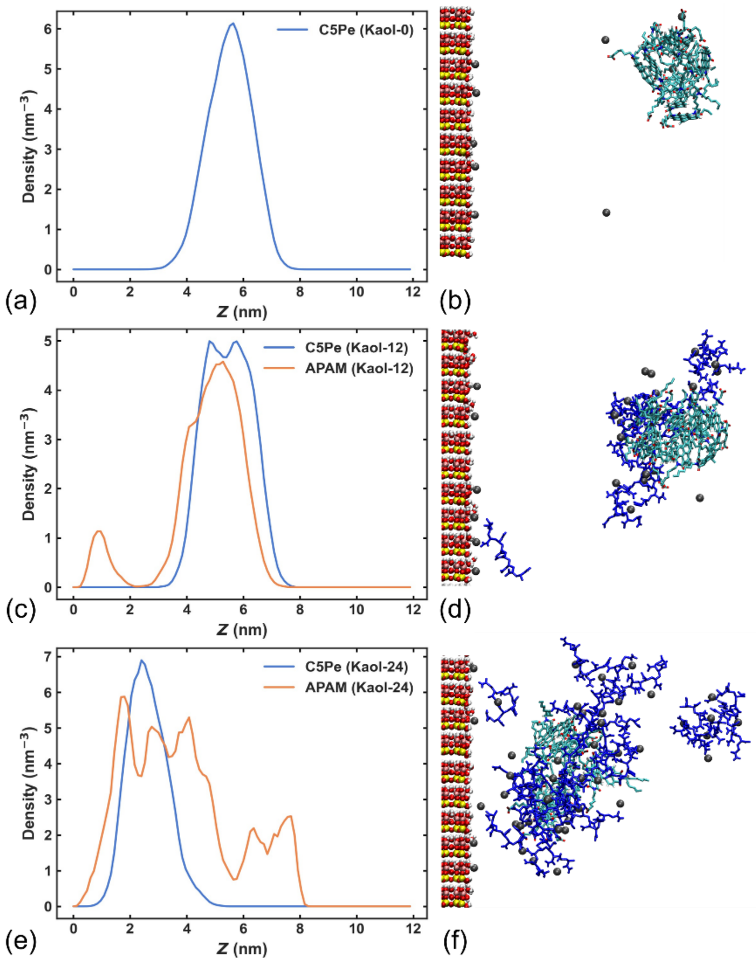

Figure 6.4. Density profiles of C5Pe and APAM along the *Z* coordinate, as well as the final snapshots in system Kaol-0 (a, b), Kaol-12 (c, d), and Kaol-24 (e, f). Data for densities were averaged over the last 20 ns of the simulations. In (b), (d), and (f), C5Pe, APAM, and Kaol are represented in the same scheme with Figure 6.2. Water is removed for clarity.

In water, the unadsorbed C5Pe molecules tended to aggregate together to minimize their contact with water, while the hydrophilic carboxylic groups were exposed to water, as shown in Figure 6.4a, d, and f. The RDFs between COG of the aggregated C5pe molecules in the Kaol systems are plotted in Figure 6.5a. The location of first peak was at 0.28 nm in system Kaol-0, 0.3 nm in system Kaol-12, and 0.36 nm in system Kaol-24. The increase in peak location suggested shifts between π-π stacked PAH cores with reduced overlap. Meanwhile, the amounts of APAM adsorbed on the C5Pe aggregate increased with APAM dosage, as told by the increase of H-bonds between APAM and C5Pe in systems Kaol-12 and Kaol-24 (Figure 6.6a). It can thus be deduced that for unadsorbed C5Pe aggregate, increasing the APAM dosage promoted APAM adsorption on the aggregate which interfered with π-π stacking among the C5Pe molecules.

The shape of the C5Pe aggregate was also altered by APAM. The geometry of the C5Pe aggregate was characterized by its principal radii of gyration, using the method developed by Jian et al. [44]. Briefly, if the three principal radii of gyration were denoted by R_x, R_y and R_z , two gyradius ratios r_1 and r_2 were defined as: $r_1 = \frac{medium\ of\ \{R_x,R_y,R_z\}}{minimum\ of\ \{R_x,R_y,R_z\}}$, $r_2 = \frac{maximum\ of\ \{R_x,R_y,R_z\}}{minimum\ of\ \{R_x,R_y,R_z\}}$. A dimension map defined by the (r_1, r_2) pairs of the C5Pe aggregate was generated in Figure 6.5b. All the points were bounded between $r_2 = r_1$ and $r_2 = \sqrt{1 + r_1^2}$, and the geometry transited from 3D structures (near $r_2 = r_1$) to 2D planar structures (near $r_2 = \sqrt{1 + r_1^2}$) between the two lines [44]. For the aggregate in Kaol-0, the pairs of gyradius ratios concentrated in the lower left region of the dimension map, near the line of $r_2 = r_1$. This corresponded to a geometry having approximately equal R_x, R_y, and R_z, resembling a sphere-like structure, as shown by the inset in the left bottom of Figure 6.6b. In system Kaol-12, the distribution of data points moved slightly to the center, with increase in both r_1 and r_2, corresponding to a cylindrical structure with length comparable to the diameter. As shown by the middle inset, the cylinder-like structure mainly consisted of two sets of parallelly stacked C5Pe (in green and red), and the two sets were bridged together by C5Pe molecules (in blue and yellow) that were slant to both sets. The (r_1, r_2) pairs kept moving upwards in system Kaol-24, representing a cylindrical structure with a larger length to diameter ratio. As shown by the inset in the upper right corner, two sub-aggregates that consisted of parallel stacked molecules (orange and green) were connected by one intermediate molecule (in red), developing into a long cylinder-like structure.

In summary, near the Kaol edge surface C5Pe tended to aggregate together through π-π stacking without adsorption. In absence of APAM, the C5Pe aggregate was sphere-like so that the contact area with water was minimized. When APAM was adsorbed on the C5Pe aggregate, the π-π stacking among C5Pe molecules was loosened and the sphere-like structure was undermined, as the aggregate conformed to accommodate the interaction with APAM. Increasing the APAM dosage further promoted the structure transformation.

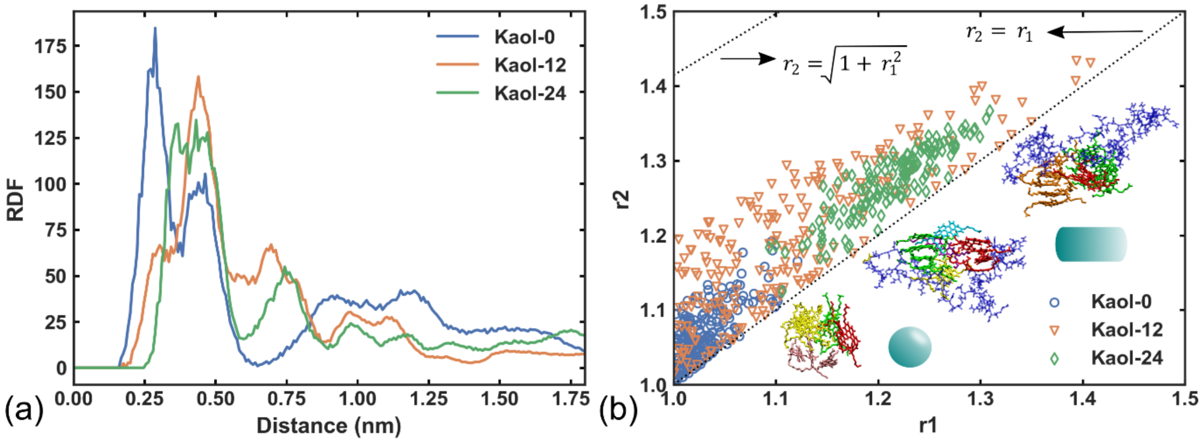

Figure 6.5. (a) RDFs between COG of C5Pe (b) Dimensional map of C5Pe aggregate. For each C5Pe aggregate, the parallelly stacked molecules are in the same color. All data were generated from the last 20 ns of simulations.

6.3.4. Effects of C5Pe on the adsorption and clustering of APAM

While APAM altered the tendency of C5Pe adsorption, the adsorption of APAM on solid surfaces was also affected by C5Pe. Two additional systems Mt-C0 and Kaol-C0, each containing 12 molecules, were run to study the adsorption of APAM without the mediation of C5Pe and compared with system Mt-12. The amount of direct adsorption (see Appendix E, Section E1 for more details) in system Mt-C0 was smaller than in system Mt-12, as indicated by the decreased number of H-bonds between APAM and the Mt surface (Figure 6.6a). Meanwhile, more APAM molecules were forming cluster in system Mt-C0, indicated by the increased maximum cluster size and the decreased cluster number (Figure 6.6b). The presence of adsorbed C5Pe undermined APAM clustering near the surface, as the APAM molecules were attracted by both the surface and C5Pe due to local short-range interactions. As a result, direct APAM adsorption was enhanced by the suppression of clustering.

Near the edge surface, in contrast with the basal surface, direct APAM adsorption decreased when C5Pe was introduced in the system, as told by the decreased H-bonds number between APAM and the surface in system Kaol-12 compared with system Kaol-C0. The H-bonds between APAM and C5Pe was much larger than that between APAM and the surface, suggesting the preference of APAM adsorption on C5Pe. The addition of C5Pe impeded the adsorption of APAM on the clay surface by attracting APAM away. The degree of clustering was similar in the two systems.

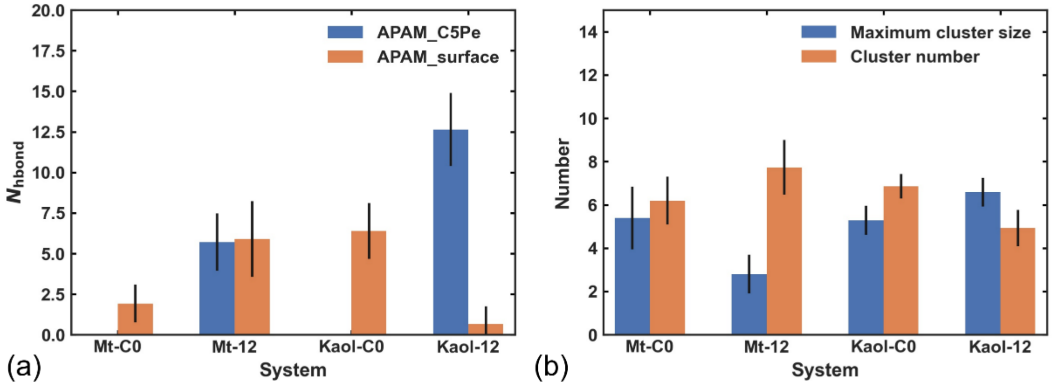

Figure 6.6. (a) Average number of H-bonds (N_{hbond}) formed between APAM and C5Pe, as well as between APAM and the surface. (b) Number of APAM cluster and size of the largest cluster (quantified by number of molecules in the cluster). All data were averaged over the last 20 ns of simulations.

6.3.5. Discussion

As shown in the previous sections, the adsorption of C5Pe on clay surface was mainly driven by hydrophobic interaction, accompanied by long-range electrostatic interaction and H-bonding with the surface. For surfaces with high hydrophobicity, C5Pe displayed a predominant adsorption in the form of single molecules or aggregates, and a low dosage of APAM was not able to alter the adsorption. Even with a high dosage, APAM could only retain the free C5Pe aggregate in the bulk while having limited effects on the adsorbed ones. In the simulated Mt systems, the C5Pe aggregates carried at least the same amounts of negative charges as the surface. The electrostatic repulsion between the C5Pe aggregate and APAM was presumably stronger than the one between the surface and APAM. However, the C5Pe aggregate was not repelled away by APAM as predicted by Li et al. [12]. On the contrary, APAM adsorbed on C5Pe through H-bonding which demonstrated that there was no noticeable competition between APAM and C5Pe for binding with the surface. The adsorption of APAM on C5Pe increased with APAM dosage and eventually exceeded the adsorption of APAM on the surface. The preferred adsorption of APAM on C5Pe might result from the heteroatoms of C5Pe, such as N and O, which had higher tendency to form H-bonds with APAM, compared with the oxygens/hydroxyls on the surface. The adsorption of APAM on C5Pe had negative effects on the π-π stacking in the C5Pe aggregate as well as reduced the contact of C5Pe with the surface.

On the edge surface with higher hydrophilicity, the adsorption of C5Pe was dominated by long-range electrostatic interaction and H-bonding. The addition of APAM not only suppressed the electrostatic repulsion between C5Pe and the surface, but also bridged the C5Pe aggregate to the surface via adsorption to both of them. It could be deduced that if C5Pe was pre-adsorbed on hydrophilic surfaces with lower charge density than the adopted Kaol model in this work, adding

APAM might replace them on the surface while still retain them near the surface as bridges, since APAM displayed a stronger tendency for binding with the surface than C5Pe.

Thus, in systems concerned about the hetero aggregation of clay particles in presence of PAHs, such as tailings with asphaltene, for the clay particles coated by asphaltene, APAM at appropriate dosages could still display fair adsorption on both the hydrophobic and the hydrophilic surfaces. Multiple clay particles could be connected when adsorbed on a long polymer chain simultaneously. Meanwhile, the adsorption of APAM could alter the surface properties of the free asphaltene, reducing the attraction between asphaltene and hydrophobic surfaces.

6.4. Conclusion

In this work, interplay between model asphaltene and polymer flocculant in their adsorption on solid surfaces was studied by all-atom MD simulations. To maintain the consistency with experimental reports with respect to the surface potential, deprotonated asphaltene, APAM, and negatively charged solid surfaces were simulated. For the basal surfaces Mt, asphaltene displayed a predominant adsorption in the form of single molecules or aggregates, and a low dosage of APAM was not able to alter the adsorption. Even with a high dosage, APAM could only retain the free asphaltene aggregate in the bulk while having limited effects on the adsorbed ones. Near the edge surface of Kaol, asphaltene did not approach the surface due to the strong coulombic repulsion, forming sphere-like aggregate in the bulk to minimize the contact with water. APAM preferred to adsorb on the aggregated asphaltene. Increasing the dosage of APAM can better suppress the coulombic repulsion, enabling the adsorption of APAM and that of asphaltene bridged by APAM. In both cases, the adsorption of APAM tended to loosen the structure of asphaltene aggregate, regardless of the adsorption state of asphaltene.

References

[1] S.I. Meramo-Hurtado, K.A. Moreno-Sader, ángel D. González-Delgado, Design, Simulation, and Environmental Assessment of an Adsorption-Based Treatment Process for the Removal of Polycyclic Aromatic Hydrocarbons (PAHs) from Seawater and Sediments in North Colombia, ACS Omega. 5 (2020) 12126–12135. doi:10.1021/acsomega.0c00394.

[2] C. Qin, W. Zhang, B. Yang, X. Chen, K. Xia, Y. Gao, DNA Facilitates the Sorption of Polycyclic Aromatic Hydrocarbons on Montmorillonites, Environ. Sci. Technol. 52 (2018) 2694–2703. doi:10.1021/acs.est.7b05174.

[3] A.O. Adeola, P.B.C. Forbes, Advances in water treatment technologies for removal of polycyclic aromatic hydrocarbons: Existing concepts, emerging trends, and future prospects, Water Environ. Res. 93 (2021) 343–359. doi:10.1002/wer.1420.

[4] Y. Higaki, K. Hatae, T. Ishikawa, T. Takanohashi, J.I. Hayashi, A. Takahara, Adsorption and desorption behavior of asphaltene on polymer-brush-immobilized surfaces, ACS Appl. Mater. Interfaces. 6 (2014) 20385–20389. doi:10.1021/am505904b.

[5] A. Pourmohammadbagher, J.M. Shaw, Probing Contaminant Transport to and from Clay Surfaces in Organic Solvents and Water Using Solution Calorimetry, Environ. Sci. Technol. 49 (2015) 10841–10849. doi:10.1021/acs.est.5b02416.

[6] R. Mukhopadhyay, D. Bhaduri, B. Sarkar, R. Rusmin, D. Hou, R. Khanam, S. Sarkar, J. Kumar Biswas, M. Vithanage, A. Bhatnagar, Y.S. Ok, Clay–polymer nanocomposites: Progress and challenges for use in sustainable water treatment, J. Hazard. Mater. 383 (2020) 121125. doi:10.1016/j.jhazmat.2019.121125.

[7] J. Ng, I. Osborn, D. Harbottle, Q. Liu, J.H. Masliyah, Z. Xu, Stimuli-Responsive Hybrid Polymer for Enhanced Solid-Liquid Separation of Industrial Effluents, Environ. Sci.

Technol. 53 (2019) 6436–6443. doi:10.1021/acs.est.8b07074.

[8] X. Zhu, D. Chen, G. Wu, Insights into asphaltene aggregation in the Na-montmorillonite interlayer, Chemosphere. 160 (2016) 62–70. doi:10.1016/j.chemosphere.2016.06.041.

[9] S. Humel, S.N. Schmidt, M. Sumetzberger-Hasinger, P. Mayer, A.P. Loibner, Enhanced Accessibility of Polycyclic Aromatic Hydrocarbons (PAHs) and Heterocyclic PAHs in Industrially Contaminated Soil after Passive Dosing of a Competitive Sorbate, Environ. Sci. Technol. 51 (2017) 8017–8026. doi:10.1021/acs.est.7b01198.

[10] T.S.L. Maravilha, A. Middea, L.S. Spinelli, E.F. Lucas, Reduction of asphaltenes adsorbed on kaolinite by polymers based on cardanol, Brazilian J. Chem. Eng. 38 (2021) 155–163. doi:10.1007/s43153-020-00082-2.

[11] J.C. White, J.J. Pignatello, Influence of bisolute competition on the desorption kinetics of polycyclic aromatic hydrocarbons in soil, Environ. Sci. Technol. 33 (1999) 4292–4298. doi:10.1021/es990537g.

[12] H. Li, J. Long, Z. Xu, J.H. Masliyah, Synergetic role of polymer flocculant in low-temperature bitumen extraction and tailings treatment, Energy and Fuels. 19 (2005) 936–943. doi:10.1021/ef049744e.

[13] J. Long, Z. Xu, J.H. Masliyah, Adhesion of single polyelectrolyte molecules on silica, mica, and bitumen surfaces, Langmuir. 22 (2006) 1652–1659. doi:10.1021/la052757f.

[14] J. Lemić, M. Tomašević-Čanović, M. Adamović, D. Kovačević, S. Milićević, Competitive adsorption of polycyclic aromatic hydrocarbons on organo-zeolites, Microporous Mesoporous Mater. 105 (2007) 317–323. doi:10.1016/j.micromeso.2007.04.014.

[15] Y.Z. El-Nahhal, J.M. Safi, Adsorption of phenanthrene on organoclays from distilled and saline water, J. Colloid Interface Sci. 269 (2004) 265–273. doi:10.1016/S0021-

9797(03)00607-6.

[16] T.P.A. Shabeer, A. Saha, V.T. Gajbhiye, S. Gupta, K.M. Manjaiah, E. Varghese, Removal of Poly Aromatic Hydrocarbons (PAHs) from Water: Effect of Nano and Modified Nano-clays as a Flocculation Aid and Adsorbent in Coagulation-flocculation Process, Polycycl. Aromat. Compd. 34 (2014) 452–467. doi:10.1080/10406638.2014.895949.

[17] W. Zou, L. Gong, J. Huang, Z. Zhang, C. Sun, H. Zeng, Adsorption of hydrophobically modified polyacrylamide P(AM-NaAA-C16DMAAC) on model coal and clay surfaces and the effect on selective flocculation of fine coal, Miner. Eng. 142 (2019) 105887. doi:10.1016/j.mineng.2019.105887.

[18] G. Fraenkel, C. Franconi, Protonation of Amides, J. Am. Chem. Soc. 82 (1960) 4478–4483. doi:10.1021/ja01502a010.

[19] G.A.A. Saracino, R. Improta, V. Barone, Absolute pKa determination for carboxylic acids using density functional theory and the polarizable continuum model, Chem. Phys. Lett. 373 (2003) 411–415. doi:10.1016/S0009-2614(03)00607-9.

[20] R.D. Silva, T.D.C. Chaparro, I.S. Monteiro, P.Y. Dugas, F. D'Agosto, M. Lansalot, A. Martins Dos Santos, E. Bourgeat-Lami, Tailoring the Morphology of Polymer/Montmorillonite Hybrid Latexes by Surfactant-Free Emulsion Polymerization Mediated by Amphipathic MacroRAFT Agents, Macromolecules. 52 (2019) 4979–4988. doi:10.1021/acs.macromol.9b00741.

[21] H. Kaddour, S. Gerislioglu, P. Dalai, T. Miyoshi, C. Wesdemiotis, N. Sahai, Nonenzymatic RNA Oligomerization at the Mineral-Water Interface: An Insight into the Adsorption-Polymerization Relationship, J. Phys. Chem. C. 122 (2018) 29386–29397. doi:10.1021/acs.jpcc.8b10288.

[22] H. Kohay, I.I. Bilkis, Y.G. Mishael, Effect of polycation charge density on polymer conformation at the clay surface and consequently on pharmaceutical binding, J. Colloid Interface Sci. 552 (2019) 517–527. doi:10.1016/j.jcis.2019.05.079.

[23] B. Zhang, W. Shi, S. Yu, Y. Zhu, R. Zhang, J.H. Tay, Adsorption of anion polyacrylamide from aqueous solution by polytetrafluoroethylene (PTFE) membrane as an adsorbent: Kinetic and isotherm studies, J. Colloid Interface Sci. 544 (2019) 303–311. doi:10.1016/j.jcis.2019.03.008.

[24] D.L. Bish, Rietveld refinement of the kaolinite structure at 1.5 K, Clays Clay Miner. 41 (1993) 738–744. doi:10.1346/CCMN.1993.0410613.

[25] P. V. Brady, R.T. Cygan, K.L. Nagy, Molecular controls on kaolinite surface charge, J. Colloid Interface Sci. 183 (1996) 356–364. doi:10.1006/jcis.1996.0557.

[26] X. Liu, X. Lu, M. Sprik, J. Cheng, E.J. Meijer, R. Wang, Acidity of edge surface sites of montmorillonite and kaolinite, Geochim. Cosmochim. Acta. 117 (2013) 180–190. doi:10.1016/j.gca.2013.04.008.

[27] T.R. Zeitler, J.A. Greathouse, R.T. Cygan, J.T. Fredrich, G.R. Jerauld, Molecular Dynamics Simulation of Resin Adsorption at Kaolinite Edge Sites: Effect of Surface Deprotonation on Interfacial Structure, J. Phys. Chem. C. 121 (2017) 22787–22796. doi:10.1021/acs.jpcc.7b06688.

[28] R.T. Cygan, J.J. Liang, A.G. Kalinichev, Molecular models of hydroxide, oxyhydroxide, and clay phases and the development of a general force field, J. Phys. Chem. B. 108 (2004) 1255–1266. doi:10.1021/jp0363287.

[29] M. Pouvreau, J.A. Greathouse, R.T. Cygan, A.G. Kalinichev, Structure of Hydrated Kaolinite Edge Surfaces: DFT Results and Further Development of the ClayFF Classical

Force Field with Metal-O-H Angle Bending Terms, J. Phys. Chem. C. 123 (2019) 11628–11638. doi:10.1021/acs.jpcc.9b00514.

[30] W. Sun, H. Zeng, T. Tang, Synergetic adsorption of polymers on montmorillonite: Insights from molecular dynamics simulations, Appl. Clay Sci. 193 (2020) 105654. doi:10.1016/j.clay.2020.105654.

[31] W. Sun, H. Zeng, T. Tang, Enhanced Adsorption of Anionic Polymer on Montmorillonite by Divalent Cations and the Effect of Salinity, J. Phys. Chem. A. 125 (2021) 1025–1035. doi:10.1021/acs.jpca.0c08797.

[32] A.K. Malde, L. Zuo, M. Breeze, M. Stroet, D. Poger, P.C. Nair, C. Oostenbrink, A.E. Mark, An Automated force field Topology Builder (ATB) and repository: Version 1.0, J. Chem. Theory Comput. 7 (2011) 4026–4037. doi:10.1021/ct200196m.

[33] C. Oostenbrink, A. Villa, A.E. Mark, W.F. Van Gunsteren, A biomolecular force field based on the free enthalpy of hydration and solvation: The GROMOS force-field parameter sets 53A5 and 53A6, J. Comput. Chem. 25 (2004) 1656–1676. doi:10.1002/jcc.20090.

[34] C.M. Breneman, K.B. Wiberg, Determining atom-centered monopoles from molecular electrostatic potentials – the need for high sampling density in formamide conformational-analysis, J. Comp. Chem. 11 (1990) 361–73. doi:10.1002/jcc.540110311.

[35] D.J. Frisch, M. J., Trucks, G. W., Schlegel, H. B., Scuseria, G. E., Robb, M. A., Cheeseman, J. R., Scalmani, G., Barone, V., Petersson, G. A., Nakatsuji, H., Li, X., Caricato, M., Marenich, A. V., Bloino, J., Janesko, B. G., Gomperts, R., Mennucci, B., Hratch, Gaussian 16 Revision B. 01., Wallingford CT. (2016).

[36] P. Mark, L. Nilsson, Structure and Dynamics of the TIP3P, SPC, and SPC/E Water Models at 298 K, J. Phys. Chem. A. 105 (2001) 9954–9960. doi:10.1021/jp003020w.

[37] E. Abraham, M. J., Murtola, T., Schulz, R., Páll, S., Smith, J. C., Hess, B., Lindahl, GROMACS: High performance molecular simulations through multi-level parallelism from laptops to supercomputers, SoftwareX. 1–2 (2015) 19–25.

[38] S. Pronk, S. Páll, R. Schulz, P. Larsson, P. Bjelkmar, R. Apostolov, M.R. Shirts, J.C. Smith, P.M. Kasson, D. Van Der Spoel, B. Hess, E. Lindahl, GROMACS 4.5: a high-throughput and highly parallel open source molecular simulation toolkit, Bioinformatics. 29 (2013) 845–854. doi:10.1093/bioinformatics/btt055.

[39] H.J.C. Berendsen, D. van der Spoel, R. van Drunen, A Message-Passing Parallel Molecular Dynamics Implementation, Phys. Commun. 91 (1995) 43−56.

[40] S. Nosé, A molecular dynamics method for simulations in the canonical ensemble, Mol. Phys. 52 (1984) 255–268. doi:10.1080/00268978400101201.

[41] W.G. Hoover, Canonical dynamics: Equilibrium phase-space distributions, Phys. Rev. A. 31 (1985) 1695–1697. doi:10.1103/PhysRevA.31.1695.

[42] M. Parrinello, A. Rahman, Polymorphic transitions in single crystals: A new molecular dynamics method, J. Appl. Phys. 52 (1981) 7182–7190. doi:10.1063/1.328693.

[43] R.. Hockney, S.. Goel, J.. Eastwood, Quiet high-resolution computer models of a plasma, J. Comput. Phys. 14 (1974) 148–158. doi:10.1016/0021-9991(74)90010-2.

[44] C. Jian, T. Tang, S. Bhattacharjee, A dimension map for molecular aggregates, J. Mol. Graph. Model. 58 (2015) 10–15. doi:10.1016/j.jmgm.2015.02.003.

7.2 Future perspectives

The functional groups of both solid surfaces and polymer flocculants respond to solution pH by changing their protonation states, as reviewed in Chapter 2. The change of surface potential, available binding groups and adsorbed ions due to change in pH would influence the clay-polymer interactions. MD simulations could identify the dominating factors through direct observations on how the clay surface, polymers, and their interactions responded to the change of pH, overcoming the limitation of lab-scale resolution.

Varying the polymer dosage would give rise to different adsorption behaviors, whether it is for a single type of polymers or the synergy between different types of polymers. The aggregation of polymers, as well as the interaction of polymers with other types of solutes, the solvents, and the solid surfaces are all related to polymer dosages. Dependence of the strength of these interactions on polymer dosages could provide clues for how to improve flocculation performances. With MD simulations, the multiple types of interactions could be explicitly probed, proving mechanistic insights into the effects of dosage.

Other simulation techniques can be also employed. It is recognized that the size of clay minerals and polymer flocculants are usually much larger than the molecular model studied, and hence the flocculation of solids can only be indirectly deducted from the results of all-atom MD simulations. Coarse-grained MD allows the simulation of particles in larger length and time scales, and more direct observation of solid flocculation may be achieved. On the other hand, calculation from quantum mechanics level such as density functional theory (DFT) or mixed quantum-classical MD simulations (e.g., ab initio MD) could be adopted to accurately capture the reactions on the solid surfaces. It is of interest to integrate methods at different scales to provide a complete picture of physical and chemical phenomena that occur in MFT flocculation.

7.1 Overall conclusion

All-atom molecular dynamics simulations were performed in this dissertation to investigate the clay-polymer interactions in the treatment of MFT, as well as the effects of solution chemistry. In Chapter 3, the adsorption of cationic (chitosan), neutral polyacrylamide (PAM), and anionic polyacrylamide (APAM) polymers on the negatively charged basal surface of montmorillonite (Mt) was firstly simulated. The adsorption of chitosan was fast and stable, driven by electrostatic attraction; PAM displayed weak adsorption driven by hydrogen bonding, mainly in an aggregated form; and APAM showed no adsorption due the strong electrostatic repulsion. The adsorption of PAM and APAM could be significantly enhanced when added with chitosan, despite of being added simultaneously or subsequently. Chitosan not only served as bridges between PAM/APAM and Mt, but also promoted direct adsorption of PAM on Mt. The findings were in good agreement with the flocculation experiments, supporting the complementarity of the two approaches.

The effects of an important factor of the solution chemistry, the exchangeable ions, on the clay-polymer interactions were studied in Chapter 4. Interactions between anionic polymer (APAM) and anionic solid surface (basal Mt) were investigated since their interaction were usually substantially influenced by the ions. In saline solutions, divalent ions (Ca^{2+}) showed a much better enhancement of the polymer adsorption than monovalent ions (Na^{+}). Besides the better charge screening ability, the coordination of APAM to Ca^{2+} also contribute to the promoted adsorption. APAM coordinated to Ca^{2+} through the displacement of water oxygens by the carbonyl oxygens of APAM in the first coordination shell of Ca^{2+}. Ca^{2+}-APAM complexes formed resulted from the coordination, and the complexes were subsequently captured into the EDL of Mt, but without the need of Ca^{2+} bridges. The coordination also helped stabilize the APAM adsorption by promoting the H-bonding between APAM and Mt, as supported by the strong positive correlation between the degree of coordination, the number of H-bonds and the amount of APAM adsorption. However, the coordination could over-neutralize the charges of Mt or APAM, giving rise to coulomb repulsion between them when the salinity was sufficiently high. Thus, the best adsorption performance required an optimal salt concentration that did not under-neutralize or over-neutralize the charges of Mt or APAM.

The influence of asphaltene residue in MFT was not negligible. The presence of asphaltene could modify the solid surface, altering the solid-solid interaction. Due to the amphiphilic nature of asphaltene, its interaction with solids was tightly related to the solid type. The adsorption of a model asphaltene when exposed to different types of solid surfaces was investigated in Chapter 5. The two solid surfaces were hydrophilic alumina and hydrophobic siloxane surfaces of kaolinite (Kaol), two representative surfaces with different polarity in MFT. To obtain a systematic understanding on the adsorption mechanisms, besides water, systems were also solvated in toluene and heptane, respectively. In water, both asphaltene monomers and aggregates preferred to adsorb on the alumina surface. Interestingly, in the control systems where an asphaltene molecule was placed between two identical surfaces, it displayed a much weaker adsorption between two alumina surfaces than between two siloxane surfaces. The profile of potential of mean force demonstrated enthalpy driven adsorption on the alumina surface and entropy driven adsorption on the siloxane surface. Asphaltene molecules in the adsorbed aggregate stacked in a parallel manner, which were aligned perpendicularly to the alumina surface, with hydrogen bonds formed through the hydrophilic parts of asphaltene. In toluene, the adsorption on alumina surface was still preferred. The asphaltene aggregates showed a multi-layer configuration, resulting from the coordination bonds established through the Ca^{2+} ions. In heptane, the affinity of both surfaces to asphaltene was comparable, as such asphaltene adsorbed on both surfaces. Compact aggregate was formed resulting from the intermolecular π-π stackings that were parallel to the surfaces.

In Chapter 6, the interplay between model asphaltene and polymer flocculant in their adsorption on solid surfaces was studied. To maintain the consistency with experimental reports with respect to the surface potential, deprotonated asphaltene, APAM, and negatively charged solid surfaces were simulated. The basal surface of Mt and edge surface of Kaol were employed, as two representative charged surfaces with different wettability in MFT. Different dosages of APAM were solvated in bulk water together with asphaltene. For surfaces with high hydrophobicity (basal surface of Mt), asphaltene displayed a predominant adsorption in the form of single molecules or aggregates, and a low dosage of APAM was not able to alter the adsorption. Even with a high dosage, APAM could only retain the free asphaltene aggregate in the bulk while having limited effects on the adsorbed ones. In the vicinity of the edge surface, asphaltene did not approach the surface due to the strong coulombic repulsion, forming sphere-like aggregate in the bulk to minimize the contact with water. APAM preferred to adsorb on the aggregated asphaltene. Increasing the dosage of APAM can better suppress the coulombic repulsion, enabling the adsorption of APAM and that of asphaltene bridged by APAM. The adsorption of APAM tended to loosen the structure of asphaltene aggregate, regardless of the adsorption state of asphaltene.

The mechanistic insights gained through this dissertation highlighted the value of using molecular simulations to study clay-polymer interactions at a resolution much finer than that in experiments. Besides contributing to fundamental understanding in the treatment of MFT, the work also shed light onto applications including soil remediation, wastes consolidation, fabrication of nanocomposite and many others.

Bibliography

Abraham, M. J., Murtola, T., Schulz, R., Páll, S., Smith, J. C., Hess, B., Lindahl, E., 2015. GROMACS: High performance molecular simulations through multi-level parallelism from laptops to supercomputers. SoftwareX 1–2, 19–25.

Abraham, M. J., Murtola, T., Schulz, R., Páll, S., Smith, J. C., Hess, B., Lindahl, E., Abraham, M.J., Murtola, T., Schulz, R., Páll, S., Smith, J.C., Hess, B., Lindah, E., 2015. Gromacs: High performance molecular simulations through multi-level parallelism from laptops to supercomputers. SoftwareX 1–2, 19–25.

Adeola, A.O., Forbes, P.B.C., 2021. Advances in water treatment technologies for removal of polycyclic aromatic hydrocarbons: Existing concepts, emerging trends, and future prospects. Water Environ. Res. 93, 343–359.

Ait-Akbour, R., Boustingorry, P., Leroux, F., Leising, F., Taviot-Guého, C., 2015. Adsorption of PolyCarboxylate Poly(ethylene glycol) (PCP) esters on Montmorillonite (Mmt): Effect of exchangeable cations (Na^+, Mg^{2+} and Ca^{2+}) and PCP molecular structure. J. Colloid Interface Sci. 437, 227–234.

Alamgir, A., Harbottle, D., Masliyah, J., Xu, Z., 2012. Al-PAM assisted filtration system for abatement of mature fine tailings. Chem. Eng. Sci. 80, 91–99.

Alberta Government, 2017a. Alberta Oil Sands Industry Quarterly Update: Winter 2017 1–16.

Alberta Government, 2017b. Coal and Mineral Development in Alberta 2017 Year in Review.

Alberta Government, 2015. Lower Athabasca Region: Tailings Management Framework for the Mineable Athabasca Oil Sands.

Aliste, M.P., MacCallum, J.L., Tieleman, D.P., 2003. Molecular dynamics simulations of pentapeptides at interfaces: Salt bridge and cation-π interactions. Biochemistry 42, 8976–8987.

Allen, E.W., 2008. Process water treatment in Canada's oil sands industry: I. Target pollutants and treatment objectives. J. Environ. Eng. Sci. 7, 123–138.

Altaf, F., Batool, R., Gill, R., Rehman, Z.U., Majeed, H., Ahmad, A., Shafiq, M., Dastan, D., Abbas, G., Jacob, K., 2021. Synthesis and electrochemical investigations of ABPBI grafted montmorillonite based polymer electrolyte membranes for PEMFC applications. Renew. Energy 164, 709–728.

Andedward, R.G.P., Lewis, L.Y.N., 1980. The Practical Salinity Scale 1978 : Fitting the Data.

Asakura, S., Oosawa, F., 1958. Interaction between particles suspended in solutions of macromolecules. J. Polym. Sci. 33, 183–192.

Asakura, S., Oosawa, F., 1954. On interaction between two bodies immersed in a solution of macromolecules. J. Chem. Phys. 22, 1255–1256.

Azevedo Rios Silva, F., Araújo Sales, M.J., Ghoul, M., Chebil, L., Duarte Ramos Matos, G., Maia, E.R., 2018. Molecular dynamics simulations of montmorillonite reinforcing amylose plasticized by Brazilian Cerrado oils: Polymer-clay nanocomposite. MRS Commun. 8, 266–274.

Bagai, S., Sun, C., Tang, T., 2012. Potential of Mean Force of Polyethylenimine-Mediated DNA Attraction.

Bakhshi, N.N., Gillies, R.G., Khare, P., 1975. Treatment of Tar Sands Tailings with Fly Ash. Environ. Sci. Technol.

Ballard Andrews, A., McClelland, A., Korkeila, O., Demidov, A., Krummel, A., C. Mullins, O., Chen, Z., 2011. Molecular Orientation of Asphaltenes and PAH Model Compounds in Langmuir−Blodgett Films Using Sum Frequency Generation Spectroscopy. Langmuir 27, 6049–6058.

Bantignies, J.L., Cartier Dit Moulin, C., Dexpert, H., 1998. Asphaltene adsorption on kaolinite characterized by infrared and X-ray absorption spectroscopies. J. Pet. Sci. Eng. 20, 233–237.

Barnhisel, R.I., Bertsch, P.M., 1989. Minerals in Soil Environments, SSSA Book Series. Soil Science Society of America, Madison, WI, USA.

Berendsen, H.J.C., van der Spoel, D., van Drunen, R., 1995. A Message-Passing Parallel Molecular Dynamics Implementation. Phys. Commun 91, 43−56.

Berendsen, H.J.C.J.C., van der Spoel, D., van Drunen, R., 1995. GROMACS: A message-passing parallel molecular dynamics implementation. Comput. Phys. Commun. 91, 43–56.

Bergaya, F., Theng, B.K.G., Lagaly, G., 2006. Handbook of Clay Science, Developments in Clay Science. Elsevier Ltd, Amsterdam.

Besra, L., Sengupta, D.K., Roy, S.K., Ay, P., 2002. Polymer adsorption: Its correlation with flocculation and dewatering of kaolin suspension in the presence and absence of surfactants. Int. J. Miner. Process. 66, 183–202.

Bish, D.L., 1993. Rietveld refinement of the kaolinite structure at 1.5 K. Clays Clay Miner. 41, 738–744.

Bolland, M.D.A., Posner, A.M., Quirk, J.P., 1976. Surface charge on kaolinites in aqueous suspension. Soil Res. 14, 197–216.

Bourg, I.C., Lee, S.S., Fenter, P., Tournassat, C., 2017. Stern Layer Structure and Energetics at Mica-Water Interfaces. J. Phys. Chem. C 121, 9402–9412.

Bourg, I.C., Sposito, G., 2011. Molecular dynamics simulations of the electrical double layer on smectite surfaces contacting concentrated mixed electrolyte (NaCl-$CaCl_2$) solutions. J. Colloid Interface Sci. 360, 701–715.

Bourg, I.C., Sposito, G., Bourg, A.C.M., 2007. Modeling the acid-base surface chemistry of montmorillonite. J. Colloid Interface Sci. 312, 297–310.

Brady, P. V., Cygan, R.T., Nagy, K.L., 1996. Molecular controls on kaolinite surface charge. J. Colloid Interface Sci. 183, 356–364.

Bragança, F.D.C., Valadares, L.F., De Leite, C.A.P., Galembeck, F., 2007. Counterion effect on the morphological and mechanical properties of polymer-clay nanocomposites prepared in an aqueous medium. Chem. Mater. 19, 3334–3342.

Breneman, C.M., Wiberg, K.B., 1990. Determining atom-centered monopoles from molecular electrostatic potentials – the need for high sampling density in formamide conformational-analysis,. J. Comp. Chem. 11, 361–73.

Brown, G., Brindley, G.W., 1980. Crystal structures of clay minerals and their Xray identification. J. Mineral. Soc. 305-356.

C. Mullins, O., Sabbah, H., Eyssautier, J., E. Pomerantz, A., Barré, L., Ballard Andrews, A., Ruiz-Morales, Y., Mostowfi, F., McFarlane, R., Goual, L., Lepkowicz, R., Cooper, T., Orbulescu, J., M. Leblanc, R., Edwards, J., N. Zare, R., 2012. Advances in Asphaltene Science and the Yen–Mullins Model. Energy & Fuels 26, 3986–4003.

Chalaturnyk, R.J., Scott, J.D., Özüm, B., 2002. Management of oil sands tailings. Pet. Sci. Technol. 20, 1025–1046.

Chen, J., Min, F., Liu, L., Cai, C., 2020. Systematic exploration of the interactions between Fe-doped kaolinite and coal based on DFT calculations. Fuel 266, 117082.

Chen, T., Lin, F., Primkulov, B., He, L., Xu, Z., 2017. Impact of salinity on warm water-based mineable oil sands processing. Can. J. Chem. Eng. 95, 281–289.

Chen, Y., Xue, S., Xia, Q., Li, H., Liu, Q., Li, B.S., Tang, B.Z., 2019. Surface Effect on the Self-Assembly of Nanofibers Revealed by in Situ AFM Imaging and Molecular Simulation. J. Phys. Chem. C 123, 9292–9297.

Cheng, H., Zhang, S., Liu, Q., Li, X., Frost, R.L., 2015. The molecular structure of kaolinite-potassium acetate intercalation complexes: A combined experimental and molecular dynamic simulation study. Appl. Clay Sci. 116–117, 273–280.

Cygan, R.T., Greathouse, J.A., Heinz, H., Kalinichev, A.G., 2009. Molecular models and simulations of layered materials. J. Mater. Chem. 19, 2470.

Cygan, R.T., Liang, J.J., Kalinichev, A.G., 2004. Molecular models of hydroxide, oxyhydroxide, and clay phases and the development of a general force field. J. Phys. Chem. B 108, 1255–1266.

Darden, T., York, D., Pedersen, L., 1993. Particle mesh Ewald: An N·log(N) method for Ewald sums in large systems. J. Chem. Phys 98, 10089–10092.

Deng, Y., Dixon, J.B., White, G.N., Loeppert, R.H., Juo, A.S.R., 2006. Bonding between polyacrylamide and smectite. Colloids Surfaces A Physicochem. Eng. Asp. 281, 82–91.

Don Scott, J., Dusseault, M.B., David Carrier, W., 1985. Behaviour of the clay/bitumen/water sludge system from oil sands extraction plants. Appl. Clay Sci. 1, 207–218.

Dos Santos, A.P., Girotto, M., Levin, Y., 2016. Simulations of Polyelectrolyte Adsorption to a Dielectric Like-Charged Surface. J. Phys. Chem. B 120, 10387–10393.

Downs, R.T., Hall-Wallace, M., 2003. The American Mineralogist crystal structure database. Am. Mineral. 88, 247–250.

Dubey, S.T., Waxman, M.H., 1991. Asphaltene adsorption and desorption from mineral surfaces.

SPE Reserv. Eng. Society Pet. Eng. 6, 389–395.

Dudášová, D., Simon, S., Hemmingsen, P. V., Sjöblom, J., 2008. Study of asphaltenes adsorption onto different minerals and clays. Part 1. Experimental adsorption with UV depletion detection. Colloids Surfaces A Physicochem. Eng. Asp. 317, 1–9.

El-Nahhal, Y.Z., Safi, J.M., 2004. Adsorption of phenanthrene on organoclays from distilled and saline water. J. Colloid Interface Sci. 269, 265–273.

Farkish, A., Fall, M., 2013. Rapid dewatering of oil sand mature fine tailings using super absorbent polymer (SAP). Miner. Eng. 50–51, 38–47.

Fernandes, D., Conway, W., Wang, X., Burns, R., Lawrance, G., Maeder, M., Puxty, G., 2012. Protonation constants and thermodynamic properties of amines for post combustion capture of CO_2. J. Chem. Thermodyn. 51, 97–102.

Fraenkel, G., Franconi, C., 1960a. Protonation of Amides. J. Am. Chem. Soc. 82, 4478–4483.

Fraenkel, G., Franconi, C., 1960b. Protonation of Amides. J. Am. Chem. Soc. 82, 4478–4483.

Frisch, M. J., Trucks, G. W., Schlegel, H. B., Scuseria, G. E., Robb, M. A., Cheeseman, J. R., Scalmani, G., Barone, V., Petersson, G. A., Nakatsuji, H., Li, X., Caricato, M., Marenich, A. V., Bloino, J., Janesko, B. G., Gomperts, R., Mennucci, B., Hratch, D.J., 2016. Gaussian 16 Revision B. 01. Wallingford CT.

G. Speight, J., E. Moschopedis, S., 2009. On the Molecular Nature of Petroleum Asphaltenes, Advances in Chemistry.

G.M.Torrie, J.P.Valleau, 1977. Nonphysical sampling distributions in Monte Carlo free-energy estimation: Umbrella sampling. J. Comput. Phys. 23, 187–199.

Galicia-Andrés, E., Petrov, D., Gerzabek, M.H., Oostenbrink, C., Tunega, D., 2019. Polarization Effects in Simulations of Kaolinite-Water Interfaces. Langmuir 35, 15086–15099.

Gao, F., Xu, Z., Liu, G., Yuan, S., 2014. Molecular dynamics simulation: The behavior of asphaltene in crude oil and at the oil/water interface. Energy and Fuels 28, 7368–7376.

Gladytz, A., John, T., Gladytz, T., Hassert, R., Pagel, M., Risselada, H.J., Naumov, S., Beck-Sickinger, A.G., Abel, B., 2016. Peptides@mica: From affinity to adhesion mechanism. Phys. Chem. Chem. Phys. 18, 23516–23527.

Gorakhki, M.H., Bareither, C.A., 2015. Salinity effects on sedimentation behavior of kaolin, bentonite, and soda ash mine tailings. Appl. Clay Sci. 114, 593–602.

Govedarica, A., Molina Bacca, E.J., Trifkovic, M., 2020. Structural investigation of tailings flocculation and consolidation via quantitative 3D dual fluorescence/reflectance confocal microscopy. J. Colloid Interface Sci. 571, 194–204.

Graber, E.R., Mingelgrin, U., 1994. Clay Swelling and Regular Solution Theory. Environ. Sci. Technol. 28, 2360–2365.

Grant, H., Mctigue, P., Ward, D., 2010. The basicities of aliphatic amides. Aust. J. Chem. 36, 2211.

Grewer, D.M., Young, R.F., Whittal, R.M., Fedorak, P.M., 2010. Naphthenic acids and other acid-extractables in water samples from Alberta: What is being measured? Sci. Total Environ. 408, 5997–6010.

Gu, G., Zhou, Z., Xu, Z., Masliyah, J.H., 2003. Role of fine kaolinite clay in toluene-diluted bitumen / water emulsion 215, 141–153.

Gumfekar, S.P., Rooney, T.R., Hutchinson, R.A., Soares, J.B.P., 2017. Dewatering Oil Sands Tailings with Degradable Polymer Flocculants. ACS Appl. Mater. Interfaces 9, 36290–36300.

Hao, Y., Yuan, L., Li, P., Zhao, W., Li, D., Lu, D., 2018. Molecular Simulations of Methane Adsorption Behavior in Illite Nanopores Considering Basal and Edge Surfaces. Energy and Fuels 32.

Hasan, A., Fatehi, P., 2018. Separation and Purification Technology Cationic kraft lignin-acrylamide as a fl occulant for clay suspensions : 1 . Molecular weight effect 207, 213–221.

Hashmi, S.M., Loewenberg, M., Firoozabadi, A., 2015. Colloidal asphaltene deposition in laminar pipe flow: Flow rate and parametric effects. Phys. Fluids 27, 83302.

Hedström, M., Karnland, O., 2012. Donnan equilibrium in Na-montmorillonite from a molecular dynamics perspective. Geochim. Cosmochim. Acta 77, 266–274.

Hess, B., Bekker, H., Berendsen, H.J.C., Fraaije, J.G.E.M., 1997. LINCS: A linear constraint solver for molecular simulations. J. Comp. Chem 18, 1463–1472.

Higaki, Y., Hatae, K., Ishikawa, T., Takanohashi, T., Hayashi, J.I., Takahara, A., 2014. Adsorption and desorption behavior of asphaltene on polymer-brush-immobilized surfaces. ACS Appl. Mater. Interfaces 6, 20385–20389.

Hockney, R.., Goel, S.., Eastwood, J.., 1974. Quiet high-resolution computer models of a plasma. J. Comput. Phys. 14, 148–158.

Hogg, R., 2000. Flocculation and dewatering. Int. J. Miner. Process. 58, 223–236.

Hoover, W.G., 1985. Canonical dynamics: Equilibrium phase-space distributions. Phys. Rev. A 31, 1695–1697.

Hsiao, Y.-W., Hedström, M., 2017. Swelling Pressure in Systems with Na-Montmorillonite and Neutral Surfaces: A Molecular Dynamics Study. J. Phys. Chem. C 121, 26414–26423.

Huang, H., Zhang, H., Han, D., 2021. Ferrocene addition for suppression of hydrogen sulfide formation during thermal recovery of oil sand bitumen. Energy 230, 120744.

Humel, S., Schmidt, S.N., Sumetzberger-Hasinger, M., Mayer, P., Loibner, A.P., 2017. Enhanced Accessibility of Polycyclic Aromatic Hydrocarbons (PAHs) and Heterocyclic PAHs in Industrially Contaminated Soil after Passive Dosing of a Competitive Sorbate. Environ. Sci.

Technol. 51, 8017–8026.

Israelachvili, J.N., 2011. Intermolecular and Surface Forces, third ed. ed, Intermolecular and Surface Forces. Elsevier Inc.

Jada, A., Debih, H., Khodja, M., 2006. Montmorillonite surface properties modifications by asphaltenes adsorption. J. Pet. Sci. Eng. 52, 305–316.

James, Robert O., G.A.P., 1982. Characterization of aqueous colloids by their electrical double-layer and intrinsic surface chemical properties., Surface and colloid science. Springer US, Boston, MA.

Jellander, R., Marčelja, S., Quirk, J.P., 1988. Attractive double-layer interactions between calcium clay particles. J. Colloid Interface Sci. 126, 194–211.

Ji, D., Liu, G., Zhang, X., Zhang, C., Yuan, S., 2019. Adsorption of C5Pe molecules on silica surfaces with different hydrophobicity studied by molecular dynamics simulation. Appl. Surf. Sci. 495, 143624.

Ji, J., Xiong, H., Zhu, Z., Li, L., Huang, Y., Yu, X., 2018. Fabrication of Polypyrrole/Chitosan Nanocomposite Aerogel Monolith for Removal of Cr(VI). J. Polym. Environ. 26, 1979–1985.

Ji, Y., Lu, Q., Liu, Q., Zeng, H., 2013. Effect of solution salinity on settling of mineral tailings by polymer flocculants. Colloids Surfaces A Physicochem. Eng. Asp. 430, 29–38.

Jian, C., Poopari, M.R., Liu, Q., Zerpa, N., Zeng, H., Tang, T., 2016. Reduction of Water/Oil Interfacial Tension by Model Asphaltenes: The Governing Role of Surface Concentration. J. Phys. Chem. B 120, 5646–5654.

Jian, C., Tang, T., Bhattacharjee, S., 2015. A dimension map for molecular aggregates. J. Mol. Graph. Model. 58, 10–15.

Kästner, J., 2011. Umbrella sampling. Wiley Interdisciplinary Reviews: Computational Molecular

Science, 1(6), pp.932-942.

Johnson, E.R., Otero-De-La-Roza, A., 2012. Adsorption of organic molecules on kaolinite from the exchange-hole dipole moment dispersion model, in: Journal of Chemical Theory and Computation. pp. 5124–5131.

Jorgensen, W.L., Maxwell, D.S., Tirado-Rives, J., 1996. Development and testing of the OPLS all-atom force field on conformational energetics and properties of organic liquids. J. Am. Chem. Soc. 118, 11225–11236.

Jorgensen, W.L., Tirado-rives, J., 1988. The OPLS Potential Functions for Proteins. Energy Minimizations for Crystals of Cyclic Peptides and Crambin. J. Am. Chem. Soc. 110.

Kaarmukhilnilavan, R.S., Selvam, A., Wong, J.W.C., Murugesan, K., 2020. Ca^{2+} dependent flocculation efficiency of avian egg protein revealed unique surface specific interaction with kaolin particles: A new perception in bioflocculant research. Colloids Surfaces A Physicochem. Eng. Asp. 603, 125177.

Kaddour, H., Gerislioglu, S., Dalai, P., Miyoshi, T., Wesdemiotis, C., Sahai, N., 2018. Nonenzymatic RNA Oligomerization at the Mineral-Water Interface: An Insight into the Adsorption-Polymerization Relationship. J. Phys. Chem. C 122, 29386–29397.

Kaminsky, H.A.W., Etsell, T.H., Ivey, D.G., Omotoso, O., 2009. Distribution of clay minerals in the process streams produced by the extraction of bitumen from athabasca oil sands. Can. J. Chem. Eng. 87, 85–93.

Kaminsky, H.A.W., Etsell, T.H., Ivey, D.G., Omotoso, O.E., 2014. Characterization of clay minerals in froth, middlings and tailings streams produced by hot water extraction of Athabasca oil sands 1–29.

Kang, X., Xia, Z., Chen, R., Sun, H., Yang, W., 2019. Effects of inorganic ions, organic polymers, and fly ashes on the sedimentation characteristics of kaolinite suspensions. Appl. Clay Sci. 181, 105220.

Kaniki, A.T., Tumba, K., 2019. Management of mineral processing tailings and metallurgical slags of the Congolese copperbelt: Environmental stakes and perspectives. J. Clean. Prod. 210, 1406–1413.

Karplus, M., Petsko, G.A., 1990. Molecular dynamics simulations in biology. Nature, 347(6294), 631-639.

Katz, A.K., Glusker, J.P., Beebe, S.A., Bock, C.W., 1996. Calcium ion coordination: A comparison with that of beryllium, magnesium, and zinc. J. Am. Chem. Soc. 118, 5752–5763.

Kausar, A., Iqbal, M., Javed, A., Aftab, K., Nazli, Z. i. H., Bhatti, H.N., Nouren, S., 2018. Dyes adsorption using clay and modified clay: A review. J. Mol. Liq. 256, 395–407.

Kim, S., Chen, J., Cheng, T., Gindulyte, A., He, J., He, S., Li, Q., Shoemaker, B.A., Thiessen, P.A., Yu, B., Zaslavsky, L., Zhang, J., Bolton, E.E., 2019. PubChem 2019 update: Improved access to chemical data. Nucleic Acids Res. 47, D1102–D1109.

Kjellander, R., 1996. Ion-Ion Correlations Effective Charges in Electrolyte and Macroion Systems. Berichte der Bunsengesellschaft/Physical Chem. Chem. Phys. 100, 894–904.

Kjellander, R., Marčelja, S., 1988. Inhomogeneous Coulomb fluids with image interactions between planar surfaces. III. Distribution functions. J. Chem. Phys. 88, 7138–7146.

Klein, C., Harbottle, D., Alagha, L., Xu, Z., 2013. Impact of fugitive bitumen on polymer-based flocculation of mature fine tailings. Can. J. Chem. Eng. 91, 1427–1432.

Kohay, H., Bilkis, I.I., Mishael, Y.G., 2019. Effect of polycation charge density on polymer conformation at the clay surface and consequently on pharmaceutical binding. J. Colloid Interface Sci. 552, 517–527.

Kong, X., Brooks, C.L., 1996. λ-dynamics: A new approach to free energy calculations. J. Chem. Phys. 105, 2414–2423.

Kumar, S., Rosenberg, J. M., Bouzida, D., Swendsen, R. H., Kollman, P. A., 1992. The Weighted Histogram Analysis Method for Free-Energy Calculations on Biomolecules. I. The Method. Journal of computational chemistry, 13(8), 1011-1021.

Kuznicki, T., H. Masliyah, J., Bhattacharjee, S., 2009. Aggregation and Partitioning of Model Asphaltenes at Toluene−Water Interfaces: Molecular Dynamics Simulations. Energy & Fuels 23, 5027–5035.

Kuznicki, T., Masliyah, J.H., Bhattacharjee, S., 2008. Molecular dynamics study of model molecules resembling asphaltene-like structures in aqueous organic solvent systems. Energy and Fuels 22, 2379–2389.

Lammers, L.N., Bourg, I.C., Okumura, M., Kolluri, K., Sposito, G., Machida, M., 2017. Molecular dynamics simulations of cesium adsorption on illite nanoparticles. J. Colloid Interface Sci. 490, 608–620.

Lan, T., Zeng, H., Tang, T., 2018. Understanding Adsorption of Violanthrone-79 as a Model Asphaltene Compound on Quartz Surface Using Molecular Dynamics Simulations. J. Phys. Chem. C 122, 28787–28796.

Landman, K.A., White, L.R., 1994. Solid/liquid separation of flocculated suspensions. Adv. Colloid Interface Sci. 51, 175–246.

Law, S.L., Kayes, J.B., 1983. Adsorption of non-ionic water-soluble cellulose polymers at the solid-water interface and their effect on suspension stability. Int. J. Pharm. 15, 251–260.

Lee, J.F., Mortland, M.M., Boyd, S.A., Chiou, C.T., 1989. Shape-selective adsorption of aromatic molecules from water by tetramethylammonium-smectite. J. Chem. Soc. Faraday Trans. 1

Phys. Chem. Condens. Phases 85, 2953–2962.

Lemić, J., Tomašević-Čanović, M., Adamović, M., Kovačević, D., Milićević, S., 2007. Competitive adsorption of polycyclic aromatic hydrocarbons on organo-zeolites. Microporous Mesoporous Mater. 105, 317–323.

Li, H., Long, J., Xu, Z., Masliyah, J.H., 2005. Synergetic role of polymer flocculant in low-temperature bitumen extraction and tailings treatment. Energy and Fuels 19, 936–943.

Li, P., Khan, M.A., Xia, M., Lei, W., Zhu, S., Wang, F., 2019. Efficient preparation and molecular dynamic (MD) simulations of Gemini surfactant modified layered montmorillonite to potentially remove emerging organic contaminants from wastewater. Ceram. Int. 45, 10782–10791.

Li, W., Zhu, N., Shen, Y., Yuan, H., 2021. Towards efficient elimination of polycyclic aromatic hydrocarbons (PAHs) from waste activated sludge by ozonation. Environ. Res. 195, 110783.

Lin, H.-S., Okawa, S., Ma, Y., Yotsumoto, S., Lee, C., Tan, S., Manzhos, S., Yoshizawa, M., Chiashi, S., Mo Lee, H., Tanaka, T., Kataura, H., Jeon, I., Matsuo, Y., Maruyama, S., 2020. Polyaromatic Nanotweezers on Semiconducting Carbon Nanotubes for the Growth and Interfacing of Lead Halide Perovskite Crystal Grains in Solar Cells. Chem. Mater. 32, 5125–5133.

Lin, Q., Akai, T., Blunt, M.J., Bijeljic, B., Iwama, H., Takabayashi, K., Onaka, Y., Yonebayashi, H., 2021. Pore-scale imaging of asphaltene-induced pore clogging in carbonate rocks. Fuel 283, 118871.

Liu, F., Yang, H., Wang, Jingyao, Qian, Y., Wu, J., Li, S., Liu, Q., Yang, S., Xu, S., Zhang, X., Zhao, Z., Wang, Jinben, 2019. Molecular interaction between asphaltene and quartz with different surface wettability: A combined study of experimental measurement and theoretical calculation. Fuel 258, 115937.

Liu, J., Zhou, Z., Xu, Z., Masliyah, J., 2002. Bitumen-clay interactions in aqueous media studied by zeta potential distribution measurement. J. Colloid Interface Sci. 252, 409–418.

Liu, X., Lu, X., Sprik, M., Cheng, J., Meijer, E.J., Wang, R., 2013. Acidity of edge surface sites of montmorillonite and kaolinite. Geochim. Cosmochim. Acta 117, 180–190.

Liu, Y., Lv, C., Ding, J., Qian, P., Zhang, X., Yu, Y., Ye, S., Chen, Y., 2016. The use of the organic-inorganic hybrid polymer Al(OH)3-polyacrylamide to flocculate particles in the cyanide tailing suspensions. Miner. Eng. 89, 108–117.

Llamas, S., Guzmán, E., Baghdadli, N., Ortega, F., Cazeneuve, C., Rubio, R.G., Luengo, G.S., 2016. Adsorption of poly(diallyldimethylammonium chloride)—sodium methyl-cocoyl-taurate complexes onto solid surfaces. Colloids Surfaces A Physicochem. Eng. Asp. 505, 150–157.

Long, J, Li, H., Xu, Z., Masliyah, J.H., 2006. Role of colloidal interactions in oil sand tailings treatment. AIChE J. 52, 371–383.

Long, Jun, Xu, Z., Masliyah, J.H., 2006. Adhesion of single polyelectrolyte molecules on silica, mica, and bitumen surfaces. Langmuir 22, 1652–1659.

Lu, H., Wang, Y., Li, L., Kotsuchibashi, Y., Narain, R., Zeng, H., 2015. Temperature- and pH-Responsive Benzoboroxole-Based Polymers for Flocculation and Enhanced Dewatering of Fine Particle Suspensions. ACS Appl. Mater. Interfaces 7, 27176–27187.

Lu, H., Xiang, L., Cui, X., Liu, J., Wang, Y., Narain, R., Zeng, H., 2016. Molecular Weight Dependence of Synthetic Glycopolymers on Flocculation and Dewatering of Fine Particles. Langmuir 32, 11615–11622.

Lu, Q., Yan, B., Xie, L., Huang, J., Liu, Y., Zeng, H., 2016. A two-step flocculation process on oil sands tailings treatment using oppositely charged polymer flocculants. Sci. Total Environ. 565, 369–375.

MacEwan, D.M.C., 1948. Adsorption by montmorillonite, and its relation to surface adsorption. Nature 439–440.

Majid, A., Sparks, B.D., Ripmeester, J.A., 1991. Characterization of solvent-insoluble organic matter isolated from Alberta oil sands. Fuel 70, 78–83.

Malde, A.K., Zuo, L., Breeze, M., Stroet, M., Poger, D., Nair, P.C., Oostenbrink, C., Mark, A.E., 2011. An Automated force field Topology Builder (ATB) and repository: Version 1.0. J. Chem. Theory Comput. 7, 4026–4037.

Maravilha, T.S.L., Middea, A., Spinelli, L.S., Lucas, E.F., 2021. Reduction of asphaltenes adsorbed on kaolinite by polymers based on cardanol. Brazilian J. Chem. Eng. 38, 155–163.

Mark, P., Nilsson, L., 2001. Structure and Dynamics of the TIP3P, SPC, and SPC/E Water Models at 298 K. J. Phys. Chem. A 105, 9954–9960.

Marlow, B.J., Sresty, G.C., Hughes, R.D., Mahajan, O.P., 1987. Colloidal stabilization of clays by asphaltenes in hydrocarbon media. Colloids and Surfaces 24, 283–297.

Masliyah, J., Zhou, Z.J., Xu, Z., Czarnecki, J., Hamza, H., 2004. Understanding Water-Based Bitumen Extraction from Athabasca Oil Sands. Can. J. Chem. Eng. 82, 628–654.

McAnally, W. H., A. J. Mehta., 2000. Collisional aggregation of fine estuarial sediment." Proceedings in Marine Science. Vol. 3. Elsevier, 19-39.

Meramo-Hurtado, S.I., Moreno-Sader, K.A., González-Delgado, ángel D., 2020. Design, Simulation, and Environmental Assessment of an Adsorption-Based Treatment Process for the Removal of Polycyclic Aromatic Hydrocarbons (PAHs) from Seawater and Sediments in North Colombia. ACS Omega 5, 12126–12135.

Moja, T.N., Bunekar, N., Mishra, S.B., Tsai, T.Y., Hwang, S.S., Mishra, A.K. 2020. Melt processing of polypropylene-grafted-maleic anhydride/chitosan polymer blend functionalized with montmorillonite for the removal of lead ions from aqueous solutions. Scientific reports. 10(1), 1-14.

Miyamoto, S., Kollman, P.A., 1992. Settle: An analytical version of the SHAKE and RATTLE algorithm for rigid water models. J. Comput. Chem. 13, 952–962.

Molatlhegi, O., Alagha, L., 2017. Adsorption characteristics of chitosan grafted copolymer on kaolin. Appl. Clay Sci. 150, 342–353.

Moreno, L., Neretnieks, I., 2006. Long-term environmental impact of tailings deposits. Hydrometallurgy 83, 176–183.

Moučka, F., Kolafa, J., Lísal, M., Smith, W.R., 2018. Chemical potentials of alkaline earth metal halide aqueous electrolytes and solubility of their hydrates by molecular simulation: Application to $CaCl_2$, antarcticite, and sinjarite. J. Chem. Phys. 148.

Mukhopadhyay, R., Bhaduri, D., Sarkar, B., Rusmin, R., Hou, D., Khanam, R., Sarkar, S., Kumar Biswas, J., Vithanage, M., Bhatnagar, A., Ok, Y.S., 2020. Clay–polymer nanocomposites: Progress and challenges for use in sustainable water treatment. J. Hazard. Mater. 383, 121125.

Mullins, O.C., 2010. The modified yen model, in: Energy and Fuels. pp. 2179–2207.

Nasim, T., Pal, A., Bandyopadhyay, A., 2018. Flocculation of aqueous kaolin suspension using a biodegradable flocculant system of poly (vinyl alcohol)-Acacia nilotica gum blends. Appl. Clay Sci. 152, 83–92.

Nasser, M.S., James, A.E., 2007. Numerical simulation of the continuous thickening of flocculated kaolinite suspensions. Int. J. Miner. Process. 84, 144–156.

Natural Resources Defense Council, 2017. Alberta’s tailings ponds 1–8.

Ng, J., Osborn, I., Harbottle, D., Liu, Q., Masliyah, J.H., Xu, Z., 2019. Stimuli-Responsive Hybrid Polymer for Enhanced Solid-Liquid Separation of Industrial Effluents. Environ. Sci. Technol. 53, 6436–6443.

Ngnie, G., Baitan, D., Dedzo, G.K., Detellier, C., 2018. Sedimentation of fine particles of kaolinite and polymer-coated kaolinite in cyclohexane: Implications for fines removal from extracted bitumen in non-aqueous processes. Fuel 234, 218–224.

Nittala, A.K., Gumfekar, S.P., Soares, J.B.P., 2019. Multifunctional CO 2 -switchable polymers for the flocculation of oil sands tailings. J. Appl. Polym. Sci. 136, 1–9.

Niu, Z., Ma, X., Manica, R., Yue, T., 2019. Molecular Destabilization Mechanism of Asphaltene Model Compound C5Pe Interfacial Film by EO-PO Copolymer: Experiments and MD Simulation. J. Phys. Chem. C 123, 10501–10508.

Nosé, S., 1984. A molecular dynamics method for simulations in the canonical ensemble. Mol. Phys. 52, 255–268.

Okada, A., Usuki, A., 1995. The chemistry of polymer-clay hybrids. Mater. Sci. Eng. C 3, 109–115.

Oliveira, C.R. de, Werlang, T., 2007. Ergodic hypothesis in classical statistical mechanics. Rev. Bras. Ensino Física 189–201.

Omotoso, O.E., Mikula, R.J., 2004. High surface areas caused by smectitic interstratification of kaolinite and illite in Athabasca oil sands. Appl. Clay Sci. 25, 37–47.

Oostenbrink, C., Villa, A., Mark, A.E., Van Gunsteren, W.F., 2004. A biomolecular force field based on the free enthalpy of hydration and solvation: The GROMOS force-field parameter sets 53A5 and 53A6. J. Comput. Chem. 25, 1656–1676.

Parrinello, M., Rahman, A., 1981. Polymorphic transitions in single crystals: A new molecular dynamics method. J. Appl. Phys. 52, 7182–7190.

Peng, F.F., Di, P., 1994. Effect of multivalent salts-calcium and aluminum on the flocculation of kaolin suspension with anionic polyacrylamide. J. Colloid Interface Sci. 164, 229–237.

Pennetta de Oliveira, L., Gumfekar, S.P., Lopes Motta, F., Soares, J.B.P., 2018. Dewatering of Oil Sands Tailings with Novel Chitosan-Based Flocculants. Energy & Fuels 32(4), 5271-5278.

Pernyeszi, T., Patzkó, Á., Berkesi, O., Dékány, I., 1998. Asphaltene adsorption on clays and crude oil reservoir rocks. Colloids Surfaces A Physicochem. Eng. Asp. 137, 373–384.

Pourmohammadbagher, A., Shaw, J.M., 2016. Probing the Impact of Asphaltene Contamination on Kaolinite and Illite Clay Behaviors in Water and Organic Solvents: A Calorimetric Study. Energy and Fuels 30, 6561–6569.

Pourmohammadbagher, A., Shaw, J.M., 2015. Probing Contaminant Transport to and from Clay Surfaces in Organic Solvents and Water Using Solution Calorimetry. Environ. Sci. Technol. 49, 10841–10849.

Pouvreau, M., Greathouse, J.A., Cygan, R.T., Kalinichev, A.G., 2019. Structure of Hydrated Kaolinite Edge Surfaces: DFT Results and Further Development of the ClayFF Classical Force Field with Metal-O-H Angle Bending Terms. J. Phys. Chem. C 123, 11628–11638.

Pouvreau, M., Greathouse, J.A., Cygan, R.T., Kalinichev, A.G., 2017a. Structure of Hydrated Gibbsite and Brucite Edge Surfaces: DFT Results and Further Development of the ClayFF Classical Force Field with Metal-O-H Angle Bending Terms. J. Phys. Chem. C 121, 14757–14771.

Pouvreau, M., Greathouse, J.A., Cygan, R.T., Kalinichev, A.G., 2017b. Structure of Hydrated Gibbsite and Brucite Edge Surfaces: DFT Results and Further Development of the ClayFF Classical Force Field with Metal-O-H Angle Bending Terms. J. Phys. Chem. C 121, 14757–

14771.

Pradilla, D., Subramanian, S., Simon, S., Sjöblom, J., Beurroies, I., Denoyel, R., 2016. Microcalorimetry Study of the Adsorption of Asphaltenes and Asphaltene Model Compounds at the Liquid-Solid Surface. Langmuir 32, 7294–7305.

Pronk, S., Páll, S., Schulz, R., Larsson, P., Bjelkmar, P., Apostolov, R., Shirts, M.R., Smith, J.C., Kasson, P.M., Van Der Spoel, D., Hess, B., Lindahl, E., 2013. GROMACS 4.5: a high-throughput and highly parallel open source molecular simulation toolkit. Bioinformatics 29, 845–854.

Qin, C., Zhang, W., Yang, B., Chen, X., Xia, K., Gao, Y., 2018. DNA Facilitates the Sorption of Polycyclic Aromatic Hydrocarbons on Montmorillonites. Environ. Sci. Technol. 52, 2694–2703.

Rapaport, D.C., 2004. The art of molecular dynamics simulation. Cambridge university press.

Razmimanesh, F., Amjad-Iranagh, S., Modarress, H., 2015. Molecular dynamics simulation study of chitosan and gemcitabine as a drug delivery system. J. Mol. Model. 21.

Ren, B., Min, F., Liu, L., Chen, J., Liu, C., Lv, K., 2020. Adsorption of different PAM structural units on kaolinite (0 0 1) surface: Density functional theory study. Appl. Surf. Sci. 504.

Riobé, F., Szűcs, R., Lescop, C., Réau, R., Nyulászi, L., Bouit, P.-A., Hissler, M., 2017. Coordination Complexes of P-Containing Polycyclic Aromatic Hydrocarbons: Optical Properties and Solid-State Supramolecular Assembly. Organometallics 36, 2502–2511.

Robert, T., Mercer, S.M., Clark, T.J., Mariampillai, B.E., Champagne, P., Cunningham, M.F., Jessop, P.G., 2012. Nitrogen-containing polymers as potent ionogens for aqueous solutions of switchable ionic strength: application to separation of organic liquids and clay particles from water. Green Chem. 14, 3053.

Ryckaert, J.P., Ciccotti, G., Berendsen, H.J.C., 1977. Numerical integration of the cartesian equations of motion of a system with constraints: molecular dynamics of n-alkanes. J. Comput. Phys. 23, 327–341.

Saada, A., Siffert, B., Papirer, E., 1995. Comparison of the Hydropholicity/Hydrophobicity of Illites and Kaolinites. J. Colloid Interface Sci. 174(1), 185-190.

Saracino, G.A.A., Improta, R., Barone, V., 2003. Absolute pKa determination for carboxylic acids using density functional theory and the polarizable continuum model. Chem. Phys. Lett. 373, 411–415.

Schmid, N., Eichenberger, A.P., Choutko, A., Riniker, S., Winger, M., Mark, A.E., Gunsteren, W.F. Van, 2011. Definition and testing of the GROMOS force-field versions 54A7 and 54B7 843–856.

Schneider, R., Sharma, A.R., Rai, A., 2008. Introduction to Molecular Dynamics. pp. 3–40.

Schofield, R.K., Samson, H.R., 1954. Flocculation of kaolinite due to the attraction of oppositely charged crystal faces. Discuss. Faraday Soc. 18, 135–145.

Schüttelkopf, A.W., Van Aalten, D.M.F., 2004. PRODRG: A tool for high-throughput crystallography of protein-ligand complexes. Acta Crystallogr. Sect. D Biol. Crystallogr. 60, 1355–1363.

Shabeer, T.P.A., Saha, A., Gajbhiye, V.T., Gupta, S., Manjaiah, K.M., Varghese, E., 2014. Removal of Poly Aromatic Hydrocarbons (PAHs) from Water: Effect of Nano and Modified Nano-clays as a Flocculation Aid and Adsorbent in Coagulation-flocculation Process. Polycycl. Aromat. Compd. 34, 452–467.

Shaikh, S.M.R., Nasser, M.S., Magzoub, M., Benamor, A., Hussein, I.A., El-Naas, M.H., Qiblawey, H., 2018. Effect of electrolytes on electrokinetics and flocculation behavior of bentonite-polyacrylamide dispersions. Appl. Clay Sci. 158, 46–54.

Shen, Z., Sheng, J.J., 2018. Experimental and numerical study of permeability reduction caused by asphaltene precipitation and deposition during CO2 huff and puff injection in Eagle Ford shale. Fuel 211, 432–445.

Silva, R.D., Chaparro, T.D.C., Monteiro, I.S., Dugas, P.Y., D'Agosto, F., Lansalot, M., Martins Dos Santos, A., Bourgeat-Lami, E., 2019. Tailoring the Morphology of Polymer/Montmorillonite Hybrid Latexes by Surfactant-Free Emulsion Polymerization Mediated by Amphipathic MacroRAFT Agents. Macromolecules 52, 4979–4988.

Simonnin, P., Marry, V., Noetinger, B., Nieto-Draghi, C., Rotenberg, B., 2018. Mineral- and Ion-Specific Effects at Clay-Water Interfaces: Structure, Diffusion, and Hydrodynamics. J. Phys. Chem. C 122, 18484–18492.

Sivasubramanian, R., Chen, G. hao, Mackey, H.R., 2021. The effectiveness of divalent cation addition for highly saline activated sludge cultures: Influence of monovalent/divalent ratio and specific cations. Chemosphere 274, 129864.

Sjöblom, J., Simon, S., Xu, Z., 2015. Model molecules mimicking asphaltenes. Adv. Colloid Interface Sci. 218, 1–16.

Šolc, R., Gerzabek, M.H., Lischka, H., Tunega, D., 2011. Wettability of kaolinite (001) surfaces - Molecular dynamic study. Geoderma 169, 47–54.

Song, K., Sandí, G., 2001. Characterization of montmorillonite surfaces after modification by organosilane. Clays Clay Miner. 49, 119–125.

Stern, O., 1924. Zur theorie der elektrolytischen doppelschicht. Zeitschrift für Elektrochemie und Angew. Phys. Chemie 30, 508–516.

Stubičan, V., Roy, R., 1961. Isomorphous substitution and infra-red spectra of the layer lattice silicates. Am. Mineral. J. Earth Planet. Mater. 46, 32–51.

Sun, W., Zeng, H., Tang, T., 2021. Enhanced Adsorption of Anionic Polymer on Montmorillonite by Divalent Cations and the Effect of Salinity. J. Phys. Chem. A 125, 1025–1035.

Sun, W., Zeng, H., Tang, T., 2020. Synergetic adsorption of polymers on montmorillonite: Insights from molecular dynamics simulations. Appl. Clay Sci. 193, 105654.

Suter, J.L., Coveney, P. V., Anderson, R.L., Greenwell, H.C., Cliffe, S., 2011. Rule based design of clay-swelling inhibitors. Energy Environ. Sci. 4, 4572–4586.

Sworska, A., Laskowski, J.S., Cymerman, G., 2000. Flocculation of the Syncrude fine tailings Part I. Effect of pH, polymer dosage and Mg^{2+} and Ca^{2+} cations. Int. J. Miner. Process. 60, 143–152.

Price, Matt, 2008. 11 Million Litres a Day: the tar sands' leaking legacy.

Tekin, N., Demirbaş, Ö., Alkan, M., 2005. Adsorption of cationic polyacrylamide onto kaolinite. Microporous Mesoporous Mater. 85, 340–350.

Theng, B.K.G., 2012. Formation and Properties of Clay-Polymer Complexes, Vol. 4. ed, Elsevier Science. Elsevier.

Tolman, R.C., 1979. The principles of statistical mechanics. Courier Corporation.

Tournassat, C., Davis, J.A., Chiaberge, C., Grangeon, S., Bourg, I.C., 2016. Modeling the acid-base properties of montmorillonite edge surfaces. Environ. Sci. Technol. 50, 13436–13445.

Tunega, D., Gerzabek, M.H., Lischka, H., 2004. Ab Initio Molecular Dynamics Study of a Monomolecular Water Layer on Octahedral and Tetrahedral Kaolinite Surfaces. J. Phys. Chem. B 108, 5930–5936.

Undabeytia, T., Nir, S., Rytwo, G., Serban, C., Morillo, E., Maqueda, C., 2002. Modeling adsorption - Desorption processes of CU on edge and planar sites of montmorillonite. Environ.

Sci. Technol. 36, 2677–2683.

Menon, V. B., D. T. Wasan., 1986. Particle—fluid interactions with application to solid-stabilized emulsions part I. The effect of asphaltene adsorption. Colloids and Surfaces 19.1: 89-105.

Vajihinejad, V., Guillermo, R., Soares, J.B.P., 2017. Dewatering Oil Sands Mature Fine Tailings (MFTs) with Poly(acrylamide-co-diallyldimethylammonium chloride): Effect of Average Molecular Weight and Copolymer Composition. Ind. Eng. Chem. Res. 56, 1256–1266.

Vali, H., Bachmann, L., 1988. Ultrastructure and flow behavior of colloidal smectite dispersions. J. Colloid Interface Sci. 126, 278–291.

Van Olphen, H., 1963. Introduction to Clay Colloid Chemistry. Interscience, New York.

van Oss, C.J., 2007. Development and applications of the interfacial tension between water and organic or biological surfaces. Colloids Surfaces B Biointerfaces 54, 2–9.

Vedoy, D.R.L., Soares, J.B.P., 2015. Water-soluble polymers for oil sands tailing treatment: A Review. Can. J. Chem. Eng. 93, 888–904.

Veeramasuneni, S., Yalamanchili, M.R., Miller, J.D., 1998. Interactions between dissimilar surfaces in high ionic strength solutions as determined by atomic force microscopy. Colloids Surfaces A Physicochem. Eng. Asp. 131, 77–87.

Vermöhlen, K., Lewandowski, H., Narres, H.D., Schwuger, M.J., 2000. Adsorption of polyelectrolytes onto oxides - The influence of ionic strength, molar mass, and Ca^{2+} ions. Colloids Surfaces A Physicochem. Eng. Asp. 163, 45–53.

Viani, A., Gualtieri, A.F., Artioli, G., 2002. The nature of disorder in montmorillonite by simulation of X-ray powder patterns. Am. Mineral. 87, 966–975.

Wang, C., Han, C., Lin, Z., Masliyah, J., Liu, Q., Xu, Z., 2016. Role of Preconditioning Cationic Zetag Flocculant in Enhancing Mature Fine Tailings Flocculation. Energy and Fuels 30, 5223–5231.

Wang, C., Harbottle, D., Liu, Q., Xu, Z., 2014. Current state of fine mineral tailings treatment: A critical review on theory and practice. Miner. Eng. 58, 113–131.

Wang, L., Liang, H., Wu, J., 2010. Electrostatic origins of polyelectrolyte adsorption: Theory and Monte Carlo simulations. J. Chem. Phys. 133.

Wang, Q.Z., Chen, X.G., Liu, N., Wang, S.X., Liu, C.S., Meng, X.H., Liu, C.G., 2006. Protonation constants of chitosan with different molecular weight and degree of deacetylation. Carbohydr. Polym. 65, 194–201.

Wang, X.W., Feng, X., Xu, Z., Masliyah, J.H., 2010. Polymer aids for settling and filtration of oil sands tailings. Can. J. Chem. Eng. 88, 403–410.

Wang, Y., Wohlert, J., Bergenstråhle-Wohlert, M., Tu, Y., Ågren, H., 2015. Molecular mechanisms for the adhesion of chitin and chitosan to montmorillonite clay. RSC Adv. 5, 54580–54588.

Watson, A.H., Corser, P.G., Garces Pardo, E.E., Lopez Christian, T.E., Vandekeybus, J., 2010. A comparison of alternative tailings disposal methods—the promises and realities, in: In Proceedings of the First International Seminar on the Reduction of Risk in the Management of Tailings and Mine Waste. Australian Centre for Geomechanics, pp. 499–514.

Wei, Q., Wang, Y., Wang, S., Zhang, Y., Chen, X., 2017. Investigating the properties and interaction mechanism of nano-silica in polyvinyl alcohol/polyacrylamide blends at an atomic level. J. Mech. Behav. Biomed. Mater. 75, 529–537.

White, J.C., Pignatello, J.J., 1999. Influence of bisolute competition on the desorption kinetics of polycyclic aromatic hydrocarbons in soil. Environ. Sci. Technol. 33, 4292–4298.

Whitehouse, U.G., Jeffrey, L.M., Debbrecht, J.D., 2013. Differential Settling Tendencies of Clay

Minerals in Saline Waters. Clays and clay minerals. Pergamon, 2013. 1-79.

Willemsen, J.A.R., Myneni, S.C.B., Bourg, I.C., 2019. Molecular Dynamics Simulations of the Adsorption of Phthalate Esters on Smectite Clay Surfaces. J. Phys. Chem. C 123, 13624–13636.

Xiao, H., Liu, Z., Wiseman, N., 1999. Synergetic effect of cationic polymer microparticles and anionic polymer on fine clay flocculation. J. Colloid Interface Sci. 216, 409–417.

Xiong, Y., Cao, T., Chen, Q., Li, Z., Yang, Y., Xu, S., Yuan, S., Sjöblom, J., Xu, Z., 2017. Adsorption of a Polyaromatic Compound on Silica Surfaces from Organic Solvents Studied by Molecular Dynamics Simulation and AFM Imaging. J. Phys. Chem. C 121, 5020–5028.

Xiong, Y., Li, Z., Cao, T., Xu, S., Yuan, S., Sjöblom, J., Xu, Z., 2018. Synergistic Adsorption of Polyaromatic Compounds on Silica Surfaces Studied by Molecular Dynamics Simulation. J. Phys. Chem. C 122, 4290–4299.

Yang, G., Chen, T., Zhao, J., Yu, D., Liu, F., Wang, D., Fan, M., Chen, W., Zhang, J., Yang, H., Wang, J., 2015. Desorption Mechanism of Asphaltenes in the Presence of Electrolyte and the Extended Derjaguin-Landau-Verwey-Overbeek Theory. Energy and Fuels 29, 4272–4280.

Yang, Z., Shang, Y., Lu, Y., Chen, Y., Huang, X., Chen, A., Jiang, Y., Gu, W., Qian, X., Yang, H., Cheng, R., 2011. Flocculation properties of biodegradable amphoteric chitosan-based flocculants. Chem. Eng. J. 172, 287–295.

Zeitler, T.R., Greathouse, J.A., Cygan, R.T., Fredrich, J.T., Jerauld, G.R., 2017. Molecular Dynamics Simulation of Resin Adsorption at Kaolinite Edge Sites: Effect of Surface Deprotonation on Interfacial Structure. J. Phys. Chem. C 121, 22787–22796.

Zeng, Q.H., Yu, A.B., Lu, G.Q., Standish, R.K., 2003. Molecular Dynamics Simulation of Organic-Inorganic Nanocomposites: Layering Behavior and Interlayer Structure of

Organoclays. Chem. Mater. 15, 4732–4738.

Zhang, B., Shi, W., Yu, S., Zhu, Y., Zhang, R., Tay, J.H., 2019. Adsorption of anion polyacrylamide from aqueous solution by polytetrafluoroethylene (PTFE) membrane as an adsorbent: Kinetic and isotherm studies. J. Colloid Interface Sci. 544, 303–311.

Zhang, D., Thundat, T., Narain, R., 2017. Flocculation and dewatering of mature fine tailings using temperature-responsive cationic polymers. Langmuir 33, 5900–5909.

Zhang, J.F., Zhang, Q.H., Maa, J.P.Y., 2018. Coagulation processes of kaolinite and montmorillonite in calm, saline water. Estuar. Coast. Shelf Sci. 202, 18–29.

Zhang, L., Lu, X., Liu, X., Yang, K., Zhou, H., 2016. Surface Wettability of Basal Surfaces of Clay Minerals: Insights from Molecular Dynamics Simulation. Energy and Fuels 30, 149–160.

Zhang, L., Xie, L., Cui, X., Chen, J., Zeng, H., 2019. Intermolecular and surface forces at solid/oil/water/gas interfaces in petroleum production. J. Colloid Interface Sci. 537, 505–519.

Zhao, H., Bhattacharjee, S., Chow, R., Wallace, D., Masliyah, J.H., Xu, Z., 2008. Probing surface charge potentials of clay basal planes and edges by direct force measurements. Langmuir 24, 12899–12910.

Zhu, R., Liu, Q., Xu, Z., Masliyah, J.H., Khan, A., 2011. Role of dissolving carbon dioxide in densification of oil sands tailings. Energy and Fuels 25, 2049–2057.

Zhu, X., Chen, D., Wu, G., 2016. Insights into asphaltene aggregation in the Na-montmorillonite interlayer. Chemosphere 160, 62–70.

Zhu, Y., Tan, X., Liu, Q., 2017. Dual polymer flocculants for mature fine tailings dewatering. Can. J. Chem. Eng. 95, 3–10.

Zou, W., Gong, L., Huang, J., Zhang, Z., Sun, C., Zeng, H., 2019. Adsorption of hydrophobically modified polyacrylamide P(AM-NaAA-C16DMAAC) on model coal and clay surfaces and the effect on selective flocculation of fine coal. Miner. Eng. 142, 105887.

Zvulunov, Y., Ben-Barak-Zelas, Z., Fishman, A., Radian, A., 2019. A self-regenerating clay-polymer-bacteria composite for formaldehyde removal from water. Chem. Eng. J. 374, 1275–1285.

Appendix A: Supporting Information for Chapter 2

A1. Deduction of WHAM

Recall in Chapter 2.5.2, the unbiased probability distribution P_j^0 of the *j*th window is written as:

$$P_j^0 = \left\langle P_{ij} \frac{Z_i}{Z_0} e^{\frac{U_{b,i}(x_j)}{k_B T}} \right\rangle = \langle \Omega_{ij} \rangle \tag{A1}$$

where Ω_{ij} is defined as:

$$\Omega_{ij} = P_{ij} \frac{Z_i}{Z_0} e^{\frac{U_{b,i}(x_j)}{k_B T}} \tag{A2}$$

The average of Ω_{ij} from all the *s* simulation gives a more realistic unbiased probability distribution P_j^0. To calculate P_j^0 from Ω_{ij} statistically,

$$P_j^0 = \sum_{i=1}^{s} w_i \, \Omega_{ij} \tag{A3}$$

where w_i is the weighting factor for each simulation, and $\sum_{i=1}^{s} w_i = 1$. The variance of P_j^0 could be minimized by determining w_i. Thus,

$$\sigma^2(P_j^0) = \left\langle \left(P_j^0 - \langle P_j^0 \rangle\right)^2 \right\rangle \tag{A4}$$

Plugging Equation A3 into Equation A4,

$$\sigma^2(P_j^0) = \left\langle \left(\sum_{i=1}^{s} w_i \Omega_{ij} - \left\langle \sum_{i=1}^{s} w_i \Omega_{ij} \right\rangle\right)^2 \right\rangle = \left\langle \left(\sum_{i=1}^{s} w_i \left(\Omega_{ij} - \langle \Omega_{ij} \rangle\right)\right)^2 \right\rangle \tag{A5}$$

Supposing $\Omega_{ij} - \langle \Omega_{ij} \rangle = \alpha_{ij}$,

$$\sigma^2(\Omega_{ij}) = \langle {\alpha_{ij}}^2 \rangle \tag{A6}$$

$$\sigma^2(P_j^0) = \left\langle \left(\sum_{i=1}^{s} w_i \alpha_{ij}\right)^2 \right\rangle = \left\langle \sum_{i=1}^{s} {w_i}^2 {\alpha_{ij}}^2 + \sum_{k=1,k\neq l}^{s} w_k w_l \alpha_{kj} \alpha_{lj} \right\rangle = \sum_{i=1}^{s} {w_i}^2 \langle {\alpha_{ij}}^2 \rangle + \sum_{k=1,k\neq l}^{s} w_k w_l \langle \alpha_{kj} \alpha_{lj} \rangle \tag{A7}$$

The *k*th and *l*th simulations are independent, then $\langle \alpha_{kj}\alpha_{lj} \rangle = 0$,

$$\sigma^2\left(P_j^0\right) = \sum_{i=1}^{s} w_i{}^2 \sigma^2\left(\Omega_{ij}\right) \tag{A8}$$

Some variables need to be introduced for the ease of calculation. Define N_i as the total number of counts for the *i*th simulation, and n_{ij} as the number of counts in the *j*th windows of the *i*th simulation.

$$P_{ij} = \frac{n_{ij}}{N_i} \tag{A9}$$

Define $f_i = \frac{Z_0}{Z_i}$ as the normalizing constant, and c_{ij} as the biasing factor.

$$c_{ij} = e^{-\frac{U_{b,i}\left(x_j\right)}{k_B T}} \tag{A10}$$

Substitute into Equation 2.21,

$$P_{ij} = f_i c_{ij} P_j^0 \tag{A11}$$

In addition, $\sum_{j=1}^{m} P_{ij} = 1$, where *m* is the total number of windows. Thus,

$$f_i = \frac{1}{\sum_1^m e^{-\frac{U_{b,i}\left(x_j\right)}{k_B T}} P_j^0}$$

$$\Omega_{ij} = \frac{n_{ij}}{N_i c_{ij} f_i} \tag{A12}$$

Substitute Equation A12 into Equation A8,

$$\sigma^2\left(P_j^0\right) = \sum_{i=1}^{s} \frac{w_i^2}{\left(N_i f_i c_{ij}\right)^2} \sigma^2\left(n_{ij}\right) \tag{A13}$$

Next, σ^2 (n_{ij}) needs to be solved. The probability of finding n_{ij} samples in a window *j* is given by the binominal distribution that $C_N^n = (\overline{p})^n (1-\overline{p})^{N-n}$, $\overline{p}$ is the probability of the window. When *N* is large,$\overline{n} = \sigma^2(n)$.

$$\sigma^2\left(n_{ij}\right) = \langle n_{ij} \rangle = \langle \Omega_{ij} N_i c_{ij} f_i \rangle = N_i f_i c_{ij} P_j^0 \tag{A14}$$

Substitute Equation A14 into A13,

$$\sigma^2\left(P_j^0\right) = \sum_{i=1}^{s} \frac{w_i^2}{N_i f_i c_{ij}} P_j^0 \tag{A15}$$

and it is subjected to $\sum_{i=1}^{s} w_i = 1$.

Mathematical optimization method named *Method of Lagrange Multiplier* needs to be applied, which is a strategy for finding the local maximum and minimum of a function subjecting to equality constraints. Suppose the optimization problem is to maximize the function *f* which is subjected to *g*. Assume both function *f* and *g* have continuous first partial derivatives, and then introduce a new variable *λ*, the Lagrange multiplier, defined as:

$$L(x_1, \dots x_n, \lambda_1, \dots \lambda_M) = f(x_1, \dots x_n) - \sum_{k=1}^{M} \lambda_k g_k(x_1, \dots x_n)$$

If $f(x_0, y_0)$ corresponds to a maximum of $f(x, y)$, then $f(x_0, y_0, \lambda_0)$ is a stationary point for the Lagrange function, indicating a zero first derivative. The method of Lagrange Multiplier is:

$$\nabla_{x_1,\dots x_n,\lambda_1,\dots\lambda_M} L(x_1, \dots x_n, \lambda_1, \dots \lambda_M) = 0$$

$$\Leftrightarrow \begin{array}{c} \nabla f(x) - \sum_{k=1}^{M} \lambda_k g_k(x) = 0 \\ g_1(x) = \cdots = g_M(x) = 0 \end{array}$$

Recall Equation A15, to minimize $\sigma^2(P_j^0)$ with constraint, define

$$L(w_i) = \sum_{i=1}^{s} \frac{w_i^2}{N_i f_i c_{ij}} P_j^0 - \lambda \sum_{i=1}^{s} w_i \tag{A16}$$

where λ is the Lagrange multiplier. Differentiate $L(w_i)$ with respect to $w_i$and set the results to 0:

$$\frac{\partial L}{\partial w_i} = \sum_{i=1}^{s} \frac{2w_i}{N_i f_i c_{ij}} P_j^0 - \lambda = 0 \tag{A17a}$$

i.e.

$$w_i = \frac{N_i f_i c_{ij}}{2P_j^0} \lambda \tag{A17b}$$

Recall the constraint $\sum_{i=1}^{s} w_i = 1$. Substitute Equation A17b into the constraint,

$$\sum_{i=1}^{s} w_i = \frac{\lambda \sum_{i=1}^{s} N_i f_i c_{ij}}{2P_j^0} = 1$$

Therefore,

$$\lambda = \frac{2P_j^0}{\sum_{i=1}^{s} N_i f_i c_{ij}} \tag{A18}$$

Now w_i can be obtained from A17b,

$$w_i = \frac{N_i f_i c_{ij}}{\sum_{i=1}^{s} N_i f_i c_{ij}} \tag{A19}$$

Substitute into Equation A3, $P_j^0 = \sum_{i=1}^{s} w_i \, \Omega_{ij}$,

$$P_j^0 = \frac{\sum_{i=1}^{s} n_{ij}}{\sum_{i=1}^{s} N_i f_i c_{ij}} = \frac{\sum_{i=1}^{s} n_{ij}}{\sum_{i=1}^{s} N_i f_i e^{-\frac{U_{b,i}(x_j)}{k_B T}}} \tag{A20}$$

Recall Equation A11

$$f_i = \frac{1}{\sum_{j=1}^{m} e^{-\frac{U_{b,i}(x_j)}{k_B T}} P_j^0}$$

There are *s* equations for P_j^0 and *m* equations for f_i, which should be solved iteratively until self-consistency is achieved. As explained in section 2.5.1, the free energy difference between the unbiased sate and the biased state can be calculated by:

$$\Delta F_i = -k_B T \, ln \, f^{-1} = -k_B T \, ln \left[\sum_{j=1}^{m} p_j^0 \, e^{-\frac{U_{b,i}(x_j)}{k_B T}} \right] \tag{A21}$$

Equation A20 could thus be written as:

$$P_j^0 = \frac{\sum_{i=1}^{s} n_{ij}}{\sum_{i=1}^{s} N_i e^{-\frac{U_{b,i}(x_j)}{k_B T}} e^{-\frac{\Delta F_i}{k_B T}}} \tag{A22}$$

Appendix B: Supporting Information for Chapter 3

B1. Validation of force fields for clay minerals and organic molecules

Parameters for 18 atoms in CLAYFF were added to the GROMOS96 53A6 force field, including metal, hydrogen, and oxygen that are connected to hydrogen and metal atoms. Since the potentials describing van der Waals interaction are of different forms in the two force fields, adjustments were made to ensure self-consistency of the force field parameters. A series of MD simulations were performed to validate the combination of the two force fields. Design of the simulated systems was based on available experimental data or quantum mechanical calculations, which were used for comparison with the simulation results here. As such, simulations were performed for both kaolinite (Kaol) and montmorillonite (Mt), although only Mt was simulated as the clay mineral model in the main texts. In the simulations reported below, the molecular topologies for clay mineral crystals were defined by CLAYFF, and those for organic molecules were acquired from ATB sever [1] defining by GROMOS96 53A6.

B1.1. Modeling of clay mineral structure

Two structures of Kaol, one optimized from CLAYFF alone, and the other optimized from the combined force filed, were first compared to examine if the changes made on CLAYFF to accommodate the GROMOS96 53A6 force field undermines its validity in representing crystal structure of clay minerals. The radial distribution function (RDF) between two silicon atoms is given in Figure B1, which shows that the structure was not affected by the changes. The locations of second, fourth, and fifth peaks corresponded to parameters of a Kaol unit cell, consistent with values (0.515 nm, 0.736 nm, and 0.896 nm respectively) reported in experiments [2].

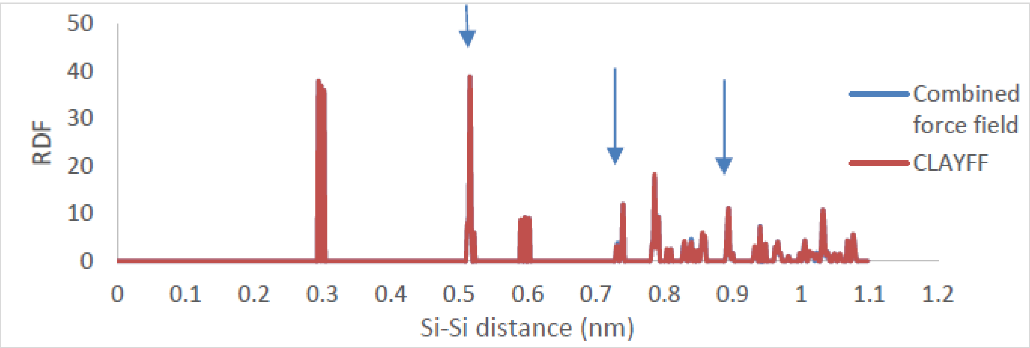

Figure B1. Radial distribution function between two silicon atoms of KAOL.

B1.2. Modeling of clay mineral/water interface

A Kaol/water system was simulated to check if the clay mineral-water interface can be modeled properly. The [001] alumina surface of Kaol crystal was cleaved and a 5×3×1 supercell was developed. The vertical direction of the crystal cell was expanded to 3 nm and solvated with single point charge (SPC) water molecules. The temperature was maintained at 300K and pressure was kept at 1 bar. The crystal structure of Kaol was found to be maintained, with the same peak locations in the Si-Si RDF as seen in Figure B1. The density of water oxygen as a function of the distance from the alumina surface (Figure 3.2) agreed with existing work [3,4]. The first and most pronounced peak in the density profile, located at about 0.12 nm, represented the formation of hydrogen bonds between water and alumina surface. There is also a distinctive peak at 2.16 nm, which corresponded to the hydrogen bonding between water and siloxane surface because of the periodic boundary condition along the vertical direction.

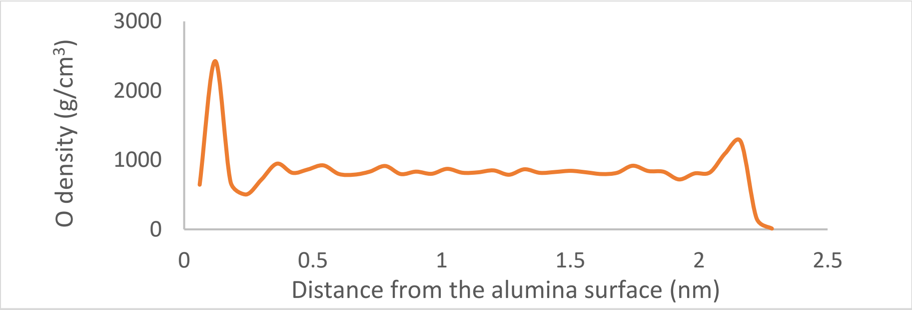

Figure B2. Oxygen density profile, averaged over the last 3 ns of 3.7 ns simulation.

B1.3. Modeling of small molecule adsorption on clay mineral surface

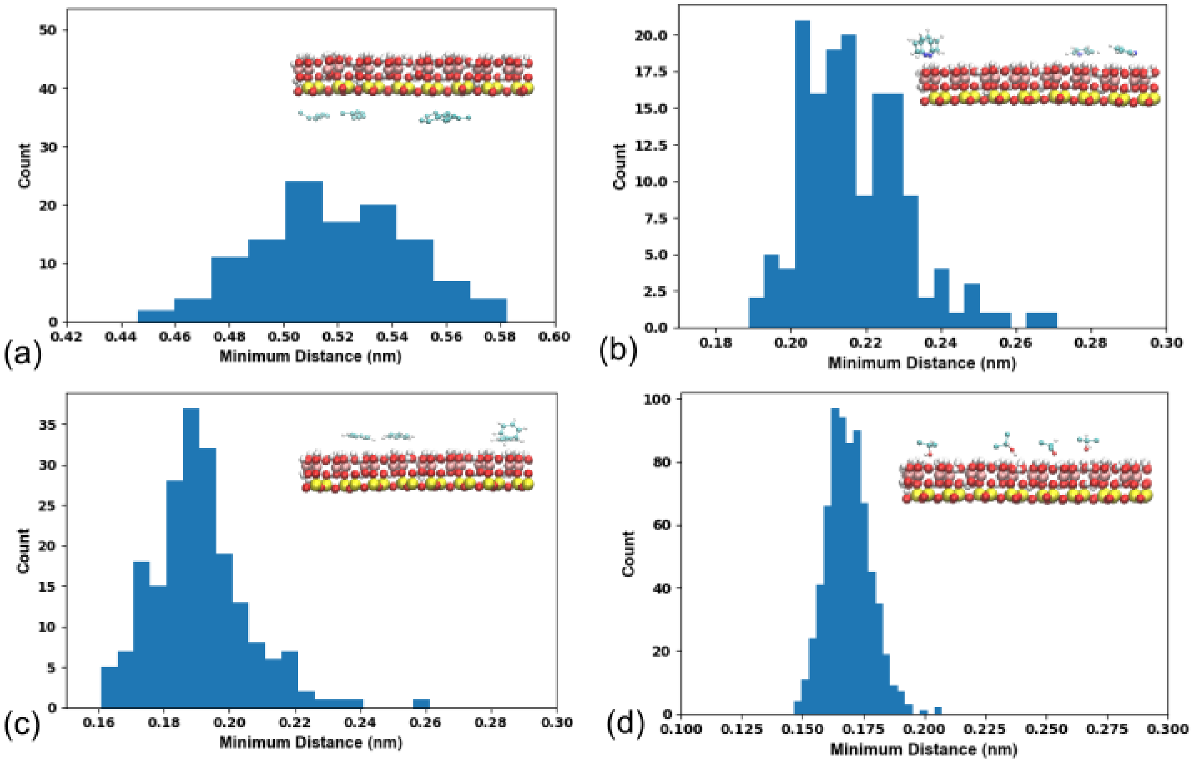

Figure B3. Histograms for the minimum distance between C (in heptane) and H (in Kaol) (a), between C (in benzene) and H (in Kaol) (b), between N (in pyridine) and H (in Kaol) (c), and between O (in isopropanol) and O (in Kaol) (d). Data averaged over the last 2 ns; each subfigure contains the snapshot of the adsorption at *t*=5 ns; H (white), O (red), Si (yellow), Al (pink).

MD simulations were performed on the adsorption of heptane, benzene, pyridine and isopropanol on Kaol. The [001] alumina surface of Kaol crystal was cleaved and a 4 × 4 × 1 supercell was developed. The vertical direction of the crystal cell was expanded to 2.5 nm for benzene adsorption, and 3.5 nm for heptane, pyridine and isopropanol adsorption. In each case, 4 organic molecules were randomly placed above the alumina surface, and MD simulations were conducted in NVT ensemble at 300K. Snapshots of the adsorption as well as representative histograms are shown in Figure 3.3. Consider the results for pyridine adsorption (Figure 3C) as an example, the dominant mode of adsorption was where pyridine was perpendicular to the alumina surface, while parallel adsorption was also possible. In the last 2 ns, the minimum distance between the N atoms in pyridine and the H atoms in Kaol was normally distributed with a peak location at 1.91 nm. These results were consistent with the DFT calculation by Johnson et al. [5]. Similar agreement with this DFT work was also found in the adsorption of heptane, pyridine and isopropanol.

Finally, the adsorption of methane hydrate on Mt surface was simulated. The [001] siloxane surface of Mt crystal was cleaved and a 2×2×1 supercell was developed. Nine methane molecules were arranged above the Mt surface to form a 3×3×1 array. The cell was expanded to 2.7 nm in the vertical direction and solvated with SPC water. 6 water molecules were replaced by Na^+ to neutralize the negative charge of Mt crystal caused by the random substitution of aluminum by magnesium. RDF between carbon atoms of methane is shown in Figure 4a, and RDFs between Na^+ and oxygen of water, as well as between Na^+ and oxygen of Mt are shown in Figure 4b, averaged over the last 2.5 ns of the 3.5 ns simulation. The results agreed well with the work of Cygan et al. [6], shown in Figures B4c and d, respectively. Similar comparisons were made for RDFs between carbon in methane and oxygen in water (Figures B4e and g), as well as oxygen atoms in water (Figures B4f and h). The results demonstrated that the methane hydrates were formed, the Mt was stable, and the interaction between methane hydrates and Mt was well modeled.

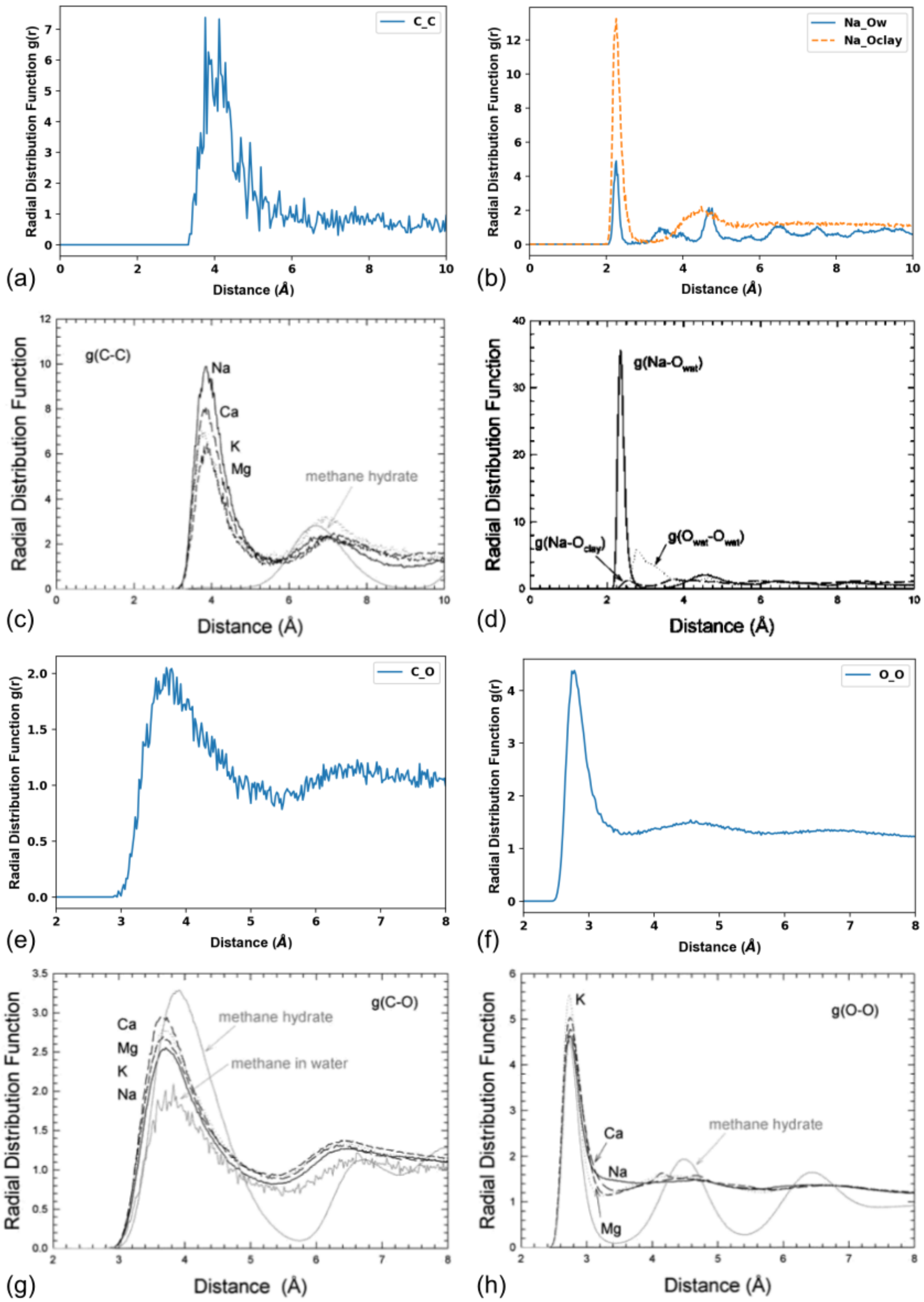

Figure B4. (a) RDF between carbon atoms of methane; (b) RDFs between Na^+ and oxygen in water, as well as between Na^+ and oxygen in Mt; (c) RDF between carbons of methane in the work of [6]; (d) RDF between Na^+ and oxygen in water, as well as between Na^+ and oxygen in Mt in the work of [6]; (e) RDF between carbon in methane and oxygen in water; (f) RDF between oxygen atoms in water; (g) RDF between carbon in methane and oxygen in water in the work of [6]; (h) RDF between oxygen atoms in water in the work of [6]. Figure B4c,d,g,and h were reprinted with permission from [6]. Copyright 2004 American Chemical Society.

B2. Partial charge calculation

A trimer chitosan, 5-mer PAM, and 9-mer MF were geometrically optimized using density functional theory (DFT) calculations at the B3LYP/6-31+G (d) level. The CHelpG [7] algorithm was used to generate charges that fitted to the electrostatic potential.

A 10-mer chitosan was obtained by expanding the trimer chitosan, keeping the units at the two ends and repeating the middle unit for 8 times. However, this process generated a 10-mer chitosan with a net charge of +10.112 instead of +10, since the net charge of the middle unit was +1.016. An equal adjustment of the charges was made on all the heavy atoms in the units between the two ends, so that the net charge of the 10-mer chitosan was exactly equal to +10. The adjustment on each atom was very small (-0.00128) and not expected to introduce any errors in the simulations. Similar approach was taken to expand the 5-mer PAM to a 10-mer PAM. As shown in Figure B5, units 1, 2, 4, and 5 were kept while unit 3 was repeated 6 times. The 9-mer MF obtained from the DFT optimization and its charges were directly adopted in the MD simulations.

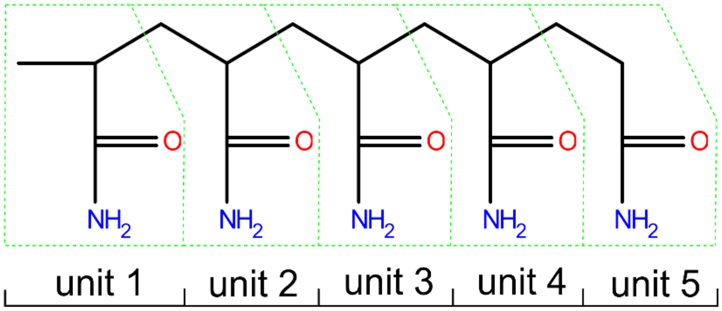

Figure B5. Schematics of a 5-mer PAM model.

B3. Additional results for the simulated systems

B3.1. System Mt-H_2O

The density profile of Na^+ and the oxygen atoms of water are shown in Figure B6 as a function of z-coordinate, which was defined perpendicular to the surface of Mt with its zero locates at bottom of the simulation cell. Location of Mt was between *Z* = 4.68-5.08 nm. Sodium ions diffuse to the negative surface of Mt and form the stern layer. Meanwhile, water showed peaks in the vicinity of the surface of Mt, consistent with its hydrophilic property.

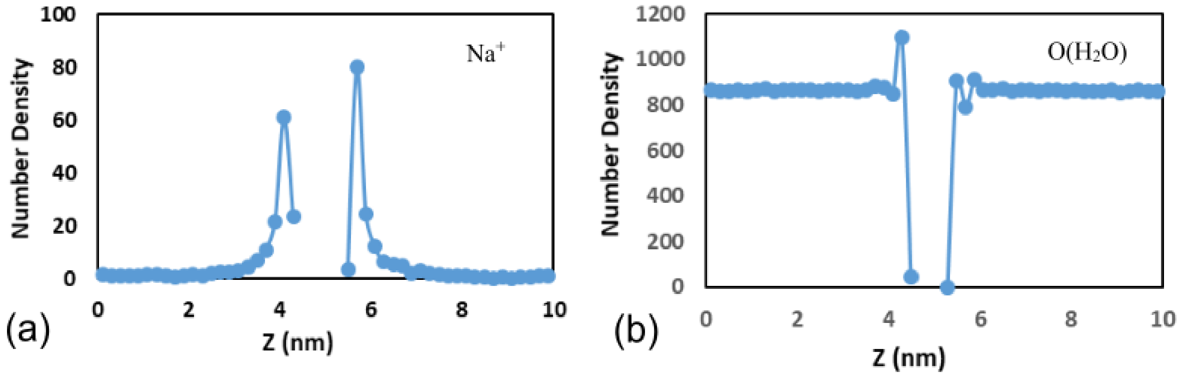

Figure B6. Density profile of Na^+ (a) and Oxygen of H_2O (b) along the *Z* axis in system Mt-H_2O in the last 0.5 ns.

B3.2. System Mt-CT

The vertical distance (*D*), as a function of time, between the center of geometry (COG) of Mt and COG of all chitosan molecules are shown in Figure B7. Each curve converged to a stable value, which showed the attainment of equilibrium.

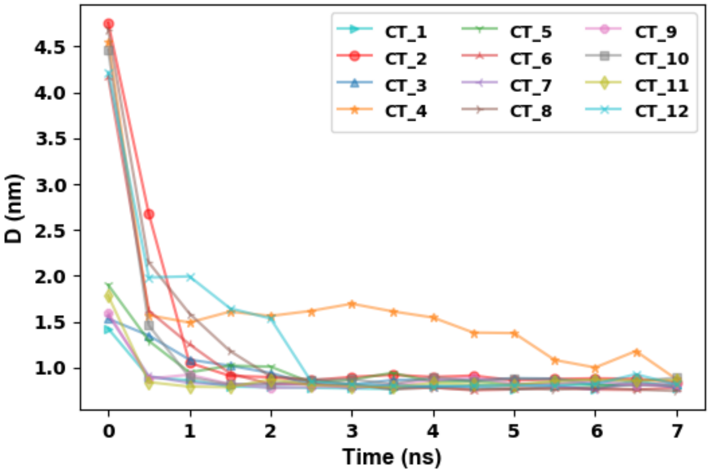

Figure B7. Vertical distance (*D*) between COG of Mt and COG of all chitosan molecules in system Mt-CT, plotted against simulation time.

The top view of the chitosan adsorption on Mt (system Mt-CT, *t* = 7 ns) is shown in Figure B8. Because of the electrostatic repulsion between chitosan molecules, the adsorption occurred separately instead of being in an aggregated form. In addition, a correlation was observed between the adsorption sites and the locations of the isomorphic substitutions.

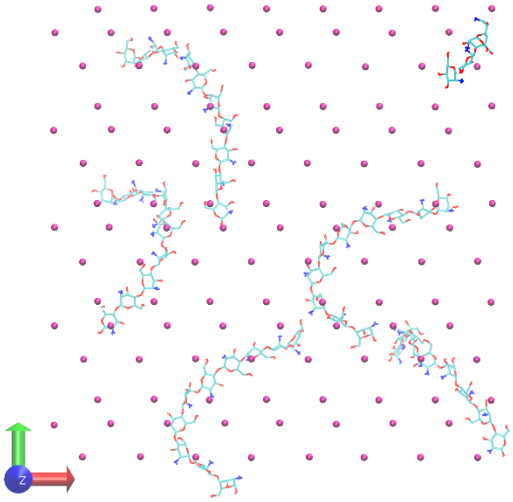

Figure B8. Adsorbed chitosan molecules in system Mt-CT at t = 7 ns. Only the Mg atoms of Mt are shown.

B3.3. System Mt-PAM

The vertical distances between COG of Mt and COG of all the PAM molecules are shown in Figure B9. Due to the unstable and highly dynamic nature of PAM adsorption *D* for all the PAM molecules fluctuated between 0.5 and 5 nm, and there was no trend of convergence during the MD run of 110 ns. However, the average root mean square deviation (RMSD) of the PAM molecules were within 1Å (Figure B10), indicating that the structures of PAM molecules were equilibrated.

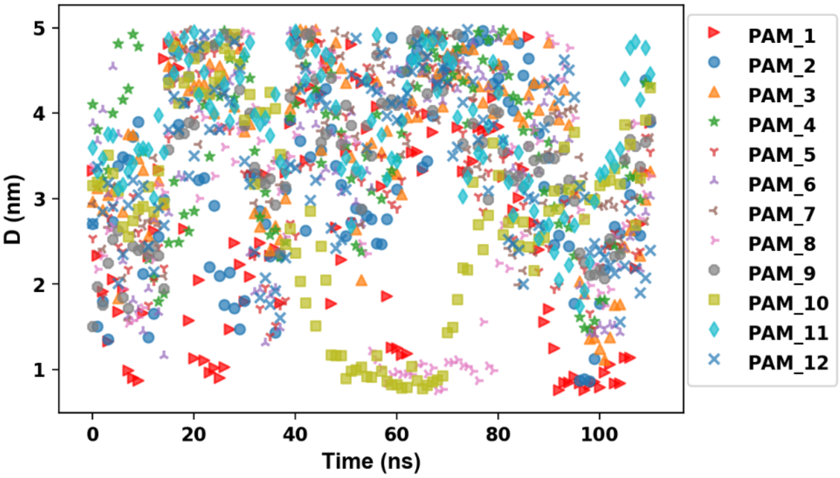

Figure B9. Vertical distances (*D*) between COG of Mt and COG of all PAM molecules in system Mt-PAM, plotted against simulation time.

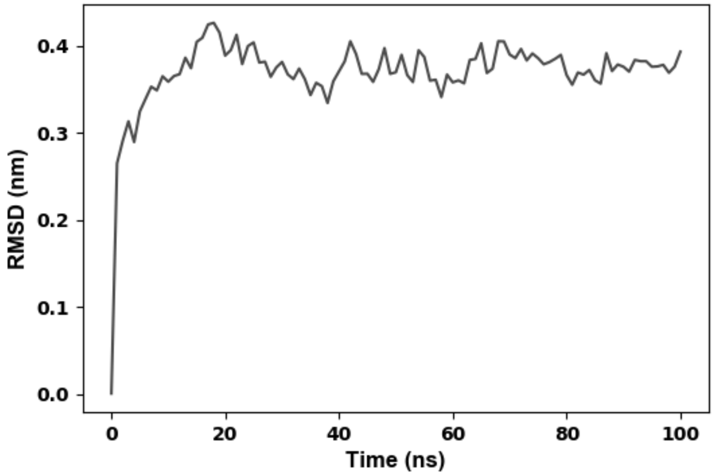

Figure B10. Average root mean square deviation of PAM molecules during the simulation.

B3.4 System Mt-MF

The vertical distance between the COG of Mt and COG of MF molecules in system Mt-MF are shown in Figure B11. The data were quite random and always beyond 1 nm, indicating the lack of adsorption for the MF molecules.

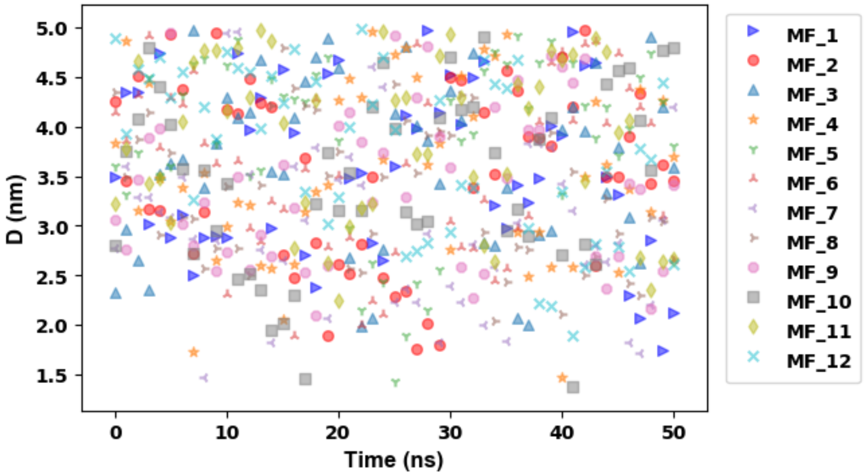

Figure B11. Vertical distances (*D*) between COG of Mt and COG of all MF molecules in system Mt-MF, plotted against simulation time.

B3.5 Systems Mt-(CT-PAM), (Mt-CT)-PAM & (Mt-PAM)-CT

The vertical distance (*D*) between COG of Mt and all polymer molecules in system Mt-(CT-PAM), system (Mt-CT)-PAM, and system (Mt-PAM)-CT are shown in Figure B12. As shown in Figures B12a, c, and e, regardless of the adding sequence, eventually chitosan formed the monolayer next to Mt with *D* less than 1 nm. PAM molecules shown in Figures B12b, d, and f either directly adsorbed, adsorbed via chitosan bridge, or remained dispersed in water.

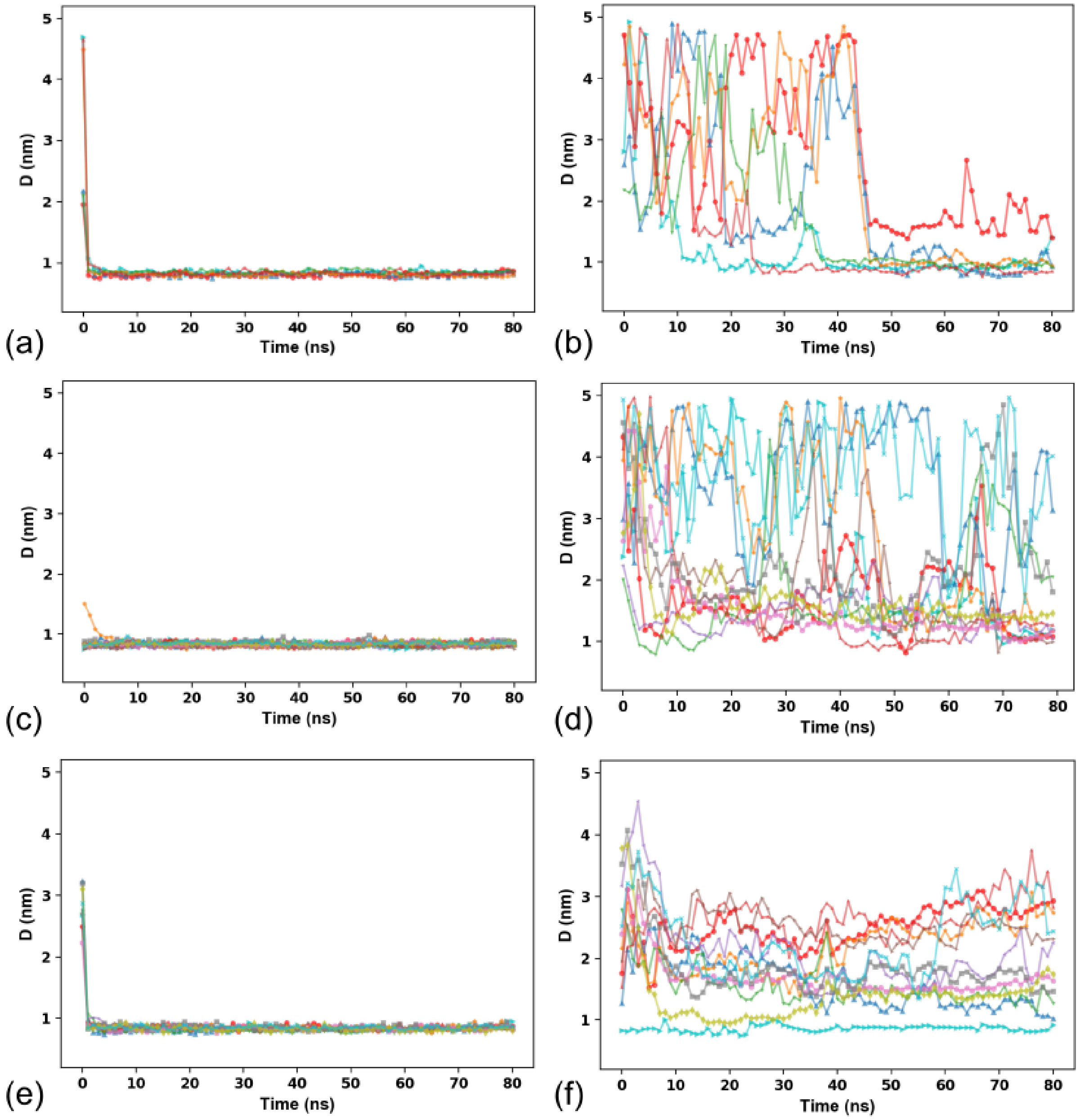

Figure B12. Vertical distances (*D*) between COG of Mt and COG of all chitosan molecules in system Mt-(CT-PAM)(a), system (Mt-CT)-PAM(c), and system (Mt-PAM)-CT(e); as well as all PAM molecules in system Mt-(CT-PAM)(b), system (Mt-CT)-PAM(d), and system (Mt-PAM)-CT(f).

B3.6 Systems Mt-(CT-MF) & (Mt-CT)-MF

The vertical distance (*D*) between COG of Mt and all polymer molecules in system Mt-(CT-MF), and system (Mt-CT)-MF are shown in Figure B13. In equilibrium stage of all systems, *D* of chitosan molecules converged to less than 1 nm, while the curves for of MF molecules converged to ~1.5 nm. Regardless of the adding sequence, MF always adsorbed on Mt via the bridging monolayer of chitosan.

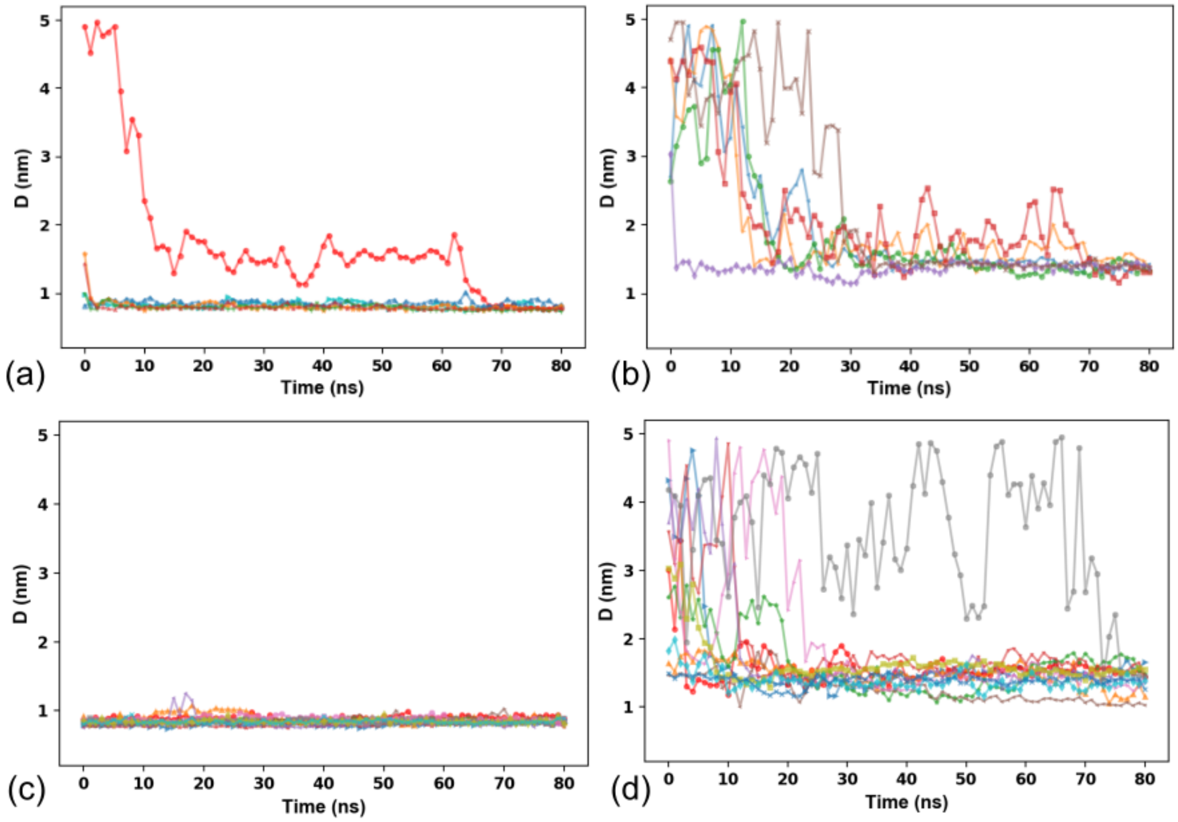

Figure B13. Vertical distances (*D*) between COG of Mt and COG of all chitosan molecules in system Mt-(CT-MF)(a), system (Mt-CT)-MF(c); as well as all MF molecules in system Mt-(CT-MF)(b), system (Mt-CT)-MF(d).

B4. Calculation of hydrogen bonds

Hydrogen bonds (H-bonds) were calculated by GROMACS command *gmx hbond*, based on cut-offs for the angle and distance. The cut-off angle for all H-bonds was set as 30°. The cut-off distance was defined by the hydrogen-acceptor distance based on the RDFs. RDF is a probability distribution of atoms as a function of distance from a reference particle. H-bonds between PAMs are formed via the amides. The cut-off distance was determined by the H(PAM)-N(PAM) and H(PAM)-O(PAM) distance based on the location of first peak (namely, 0.19 nm) in Figure B14a. Cut-off for H-bonds between PAM and Mt was determined by H(PAM)-O(Mt) distance based on the location of first peak in Figure B14b (namely, 0.21 nm), as the H-bonds are formed between the amides of PAM and bridging oxygen of Mt. Similarly, cut-off for H-bonds between PAM and chitosan was determined by the first prominent peak in Figure B14c at 0.19 nm. They are formed via amides of PAM and hydroxyl group of chitosan.

Clustering (aggregation) of PAM was identified by GROMACS command *gmx_clutsize*, with the cut-off set as 0.19 nm, the distance used for defining H-bonds. For a given PAM molecule, its minimum distances with the rest of the PAM molecules were calculated. If at least one of those distances was smaller than 0.19 nm, this PAM molecule was considered to be in the aggregated state.

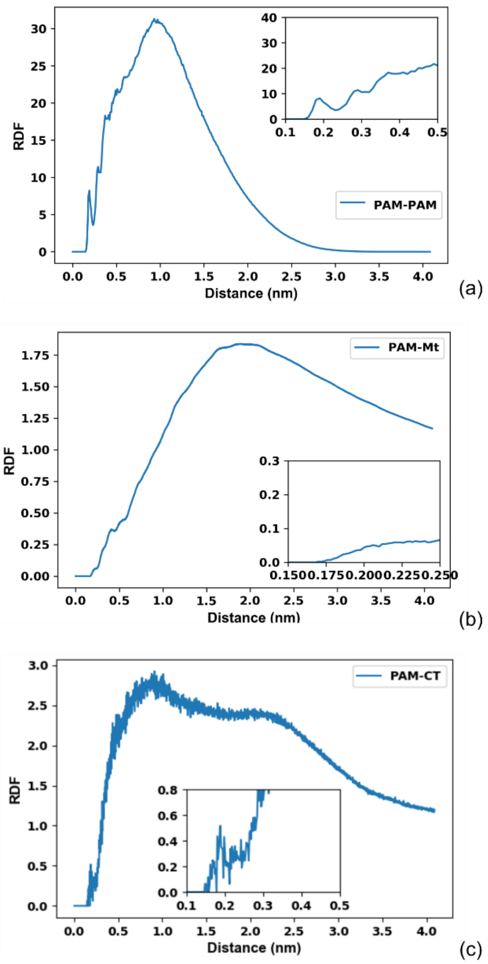

Figure B14. RDF between (a) all atoms of PAM in system Mt-PAM, (b) all atoms of PAM and all atoms of Mt in system Mt-(CT-PAM), (c) all atoms of PAM and all atoms of chitosan in system Mt-(CT-PAM).

Table B1 N_0 values for H-bonds normalization

System	Maximum number of H-bond donor/acceptor pairs, N_0		
	PAM-PAM[a]	PAM-Mt[b]	PAM-chitosan[c]
Mt-PAM	120	240	-
Mt-(CT-PAM)	60	120	240

a. N_0 between PAM molecules was calculated by multiplying the maximum H-bonds donors (20 -NH donors) per PAM molecule and half of the total number of PAM molecules together. b. N_0 between PAM and Mt was calculated by multiplying the maximum H-bonds donors (20 -NH donors) per PAM molecule and the total number of PAM molecules together. c. N_0 between PAM and chitosan was calculated by multiplying the maximum H-bonds active sites (20 -NH donors, 10 -NH acceptors, and 10 =O acceptors) per PAM molecule and the total number of PAM molecules together.

References

[1] A.K. Malde, L. Zuo, M. Breeze, M. Stroet, D. Poger, P.C. Nair, C. Oostenbrink, A.E. Mark, An Automated force field Topology Builder (ATB) and repository: Version 1.0, J. Chem. Theory Comput. 7 (2011) 4026–4037. doi:10.1021/ct200196m.

[2] D.L. Bish, Rietveld refinement of the kaolinite structure at 1.5 K, Clays Clay Miner. 41 (1993) 738–744. doi:10.1346/CCMN.1993.0410613.

[3] R.T. Cygan, J.J. Liang, A.G. Kalinichev, Molecular models of hydroxide, oxyhydroxide, and clay phases and the development of a general force field, J. Phys. Chem. B. 108 (2004) 1255–1266. doi:10.1021/jp0363287.

[4] H. Heinz, H. Koerner, K.L. Anderson, R.A. Vaia, B.L. Farmer, Force field for mica-type silicates and dynamics of octadecylammonium chains grafted to montmorillonite, Chem. Mater. 17 (2005) 5658–5669. doi:10.1021/cm0509328.

[5] E.R. Johnson, A. Otero-De-La-Roza, Adsorption of organic molecules on kaolinite from the exchange-hole dipole moment dispersion model, in: J. Chem. Theory Comput., 2012: pp. 5124–5131. doi:10.1021/ct3006375.

[6] R.T. Cygan, S. Guggenheim, A.F. Van Koster Groos, Molecular models for the intercalation of methane hydrate complexes in montmorillonite clay, J. Phys. Chem. B. 108 (2004) 15141–15149. doi:10.1021/jp037900x.

[7] C.M. Breneman, K.B. Wiberg, Determining atom-centered monopoles from molecular electrostatic potentials – the need for high sampling density in formamide conformational-analysis, J. Comp. Chem. 11 (1990) 361–73. doi:10.1002/jcc.540110311.

Appendix C: Supporting Information for Chapter 4

C1. Additional data

C1.1. Atom types and partial charges for APAM

The types and partial charges of all the atoms in the topology of APAM are shown in Table C1. The atom types were compatible with GROMO96 53A6 force field. Partial charges were calculated by density functional theory (DFT) calculation at B3LYP/6-31+G (d) level in Gaussian 16 [1]. Each atom was numbered consistently as shown in Figure C1.

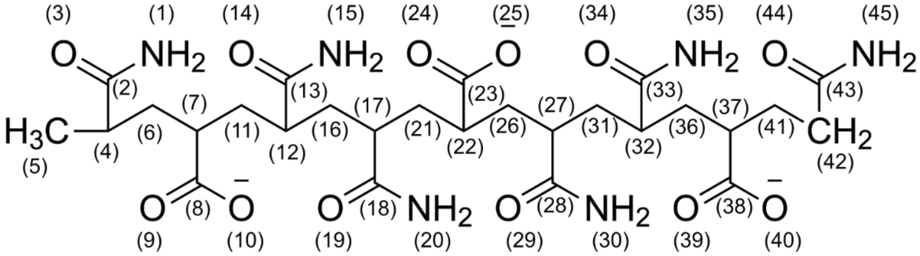

Figure C1. Molecular structure of APAM.

Table C1. Atom types and partial charges in APAM

Atom type	charge	Atom type	charge	Atom type	charge	Atom type	charge	Atom type	charge
(1) NT	-1.050668	(11) CH2	0.095395	(20) H	0.533952	(30) H	0.357904	(39) OM	-0.876707
(1) H	0.444432	(12) CH1	-0.118151	(20) H	0.386179	(30) H	0.374818	(40) OM	-0.782307
(1) H	0.397871	(13) C	0.975345	(21) CH2	-0.016018	(31) CH2	-0.048176	(41) CH2	0.104715
(2) C	0.886637	(14) O	-0.714108	(22) CH1	0.02076	(32) CH1	-0.08984	(42) CH2	-0.203243
(3) O	-0.712595	(15) N	-1.088947	(23) C	0.927076	(33) C	0.95589	(43) C	0.915147
(4) CH1	0.053116	(15) H	0.524616	(24) OM	-0.892324	(34) O	-0.702307	(44) O	-0.696045
(5) CH3	-0.128071	(15) H	0.375259	(25) OM	-0.814103	(35) NT	-0.980154	(45) NT	-1.008152
(6) CH2	0.076696	(16) CH2	0.026319	(26) CH2	-0.091521	(35) H	0.47318	(45) H	0.402702
(7) CH1	-0.29954	(17) CH1	-0.109613	(27) CH1	-0.002378	(35) H	0.324087	(45) H	0.389095
(8) C	0.995807	(18) C	0.905917	(28) C	0.951354	(36) CH2	0.005329		
(9) OM	-0.903841	(19) O	-0.711525	(29) O	-0.715925	(37) CH1	-0.054299		
(10) OM	-0.834983	(20) NT	-1.099945	(30) NT	-0.98408	(38) C	0.849963		

C1.2. Final Configurations

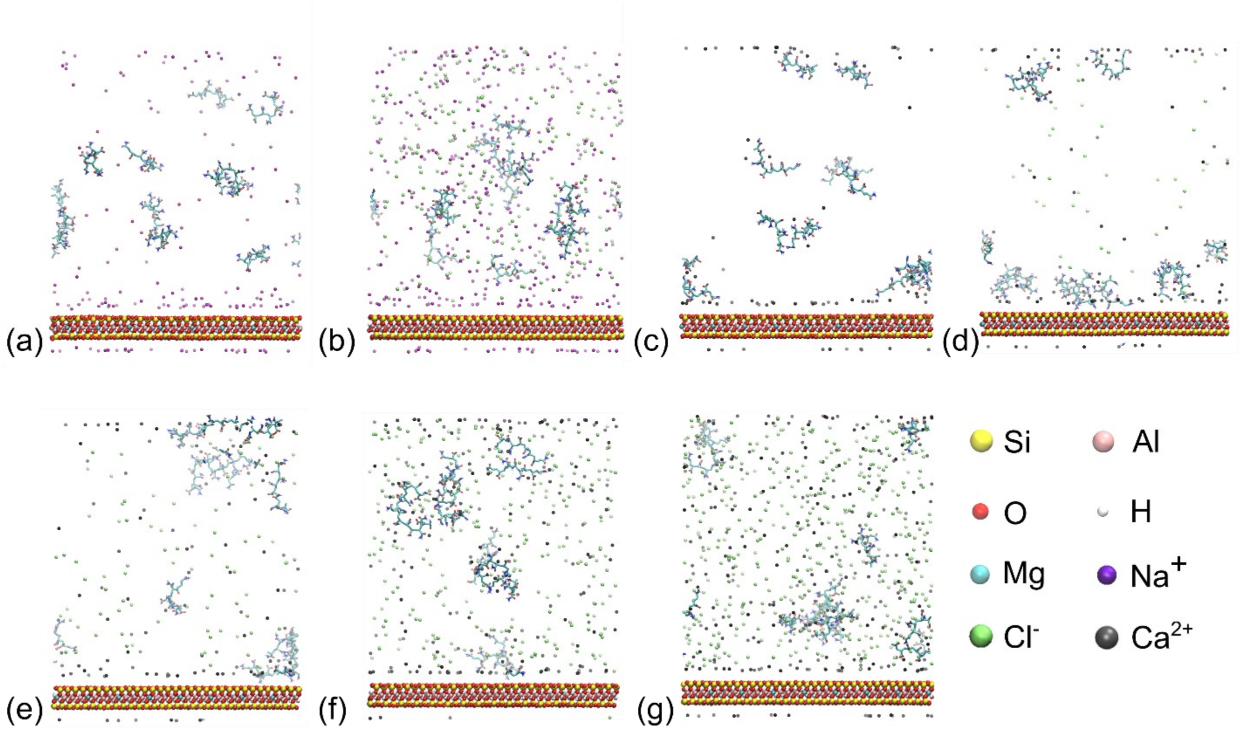

Figure C2. Snapshots of final configurations for system (a) Na-0, (b) Na-0.5, (c) Ca-0, (d) Ca-0.05, (e) Ca-0.1, (f) Ca-0.3, and (g) Ca-0.5. Water molecules are removed for clarity.

C1.3. Density profiles

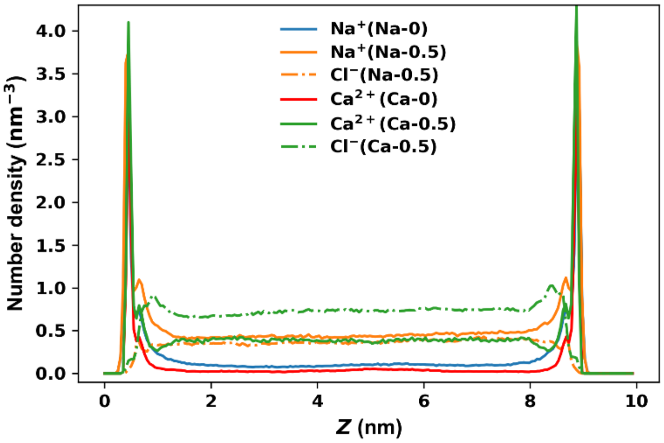

Figure C3. Density profile of counterions and co-ions, averaged over the last 20 ns of the simulations, plotted against the full range of *Z*.

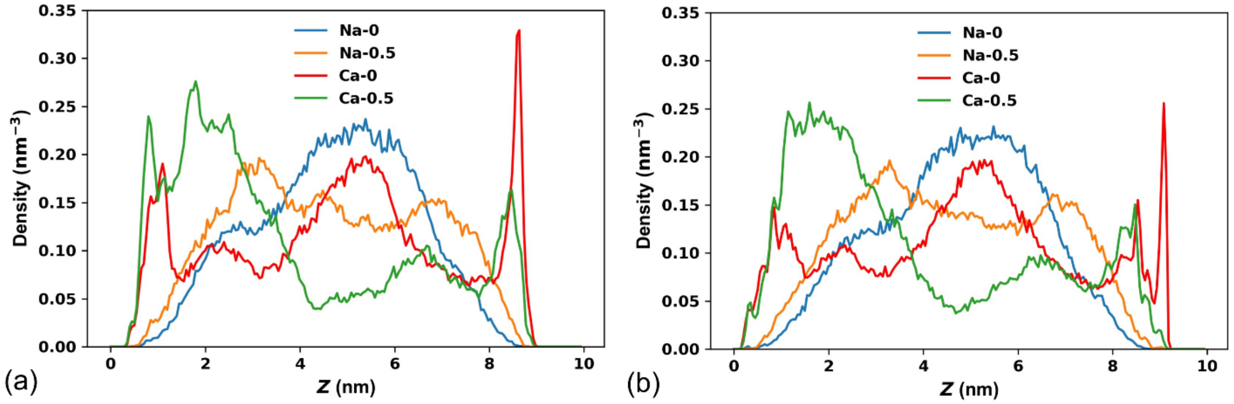

Figure C4. Density profile of COO$^-$ (a) and N (b) atoms of APAM, averaged over the last 20 ns of the simulations, plotted against the full range of *Z*.

C1.4. Cumulative charges

The net charge of the Mt model is -120. Due to periodic boundary condition, the same distributions of ions were observed around plane I of Mt and plane II in the periodic image above (see Figure C3 and Figure 4.2b in the main text). As such, when calculating the cumulative charge distribution, each plane (I and II) was considered to carry a charge of -60. As illustrated in Figure C5, the lower half of the primitive simulation cell contained a total charge of +60 from APAM and all ions; similarly, the upper half contained a total charge of +60. This repeated in any periodic images of the primitive simulation cell. At any *Z* position, the total charge of APAM and ions within *Z* was calculated by integrating their density profiles, and the value was added to -60 to determine the cumulative charge around one Mt surface. The results over the entire simulation box are shown in Figures C6 and C7.

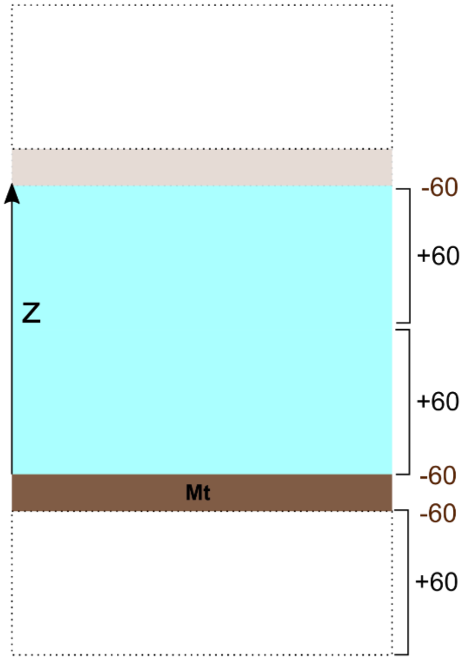

Figure C5. Illustration of charges on Mt surface and in the two halves of the primitive simulation cell. The periodic image of each half is also included.

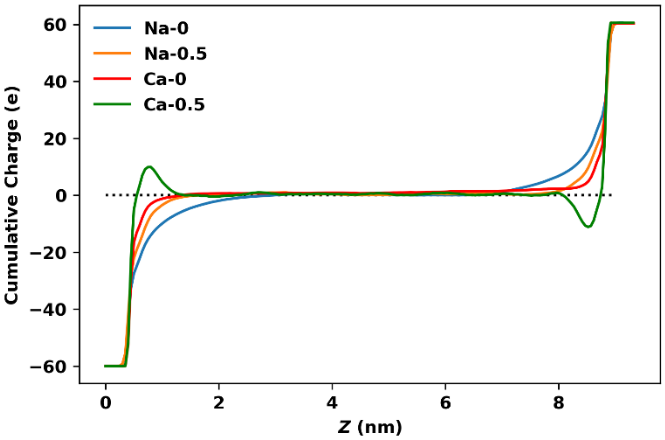

Figure C6. Cumulative charges of Mt, APAM and ions in systems Na-0, Na-0.5, Ca-0, and Ca-0.5, as a function of *Z* coordinate.

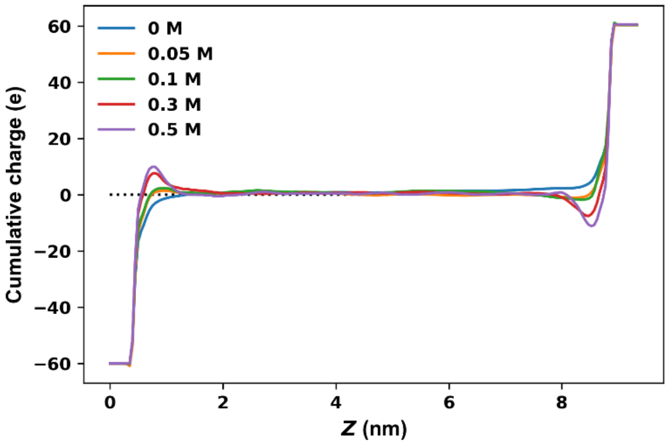

Figure C7. Cumulative charges of Mt, APAM and ions in systems Ca-0, 0.05, 0.1, 0.3, and 0.5, as a function of *Z* coordinate.

C1.5. Three-dimensional map of adsorbed Ca^{2+}-APAM complexes

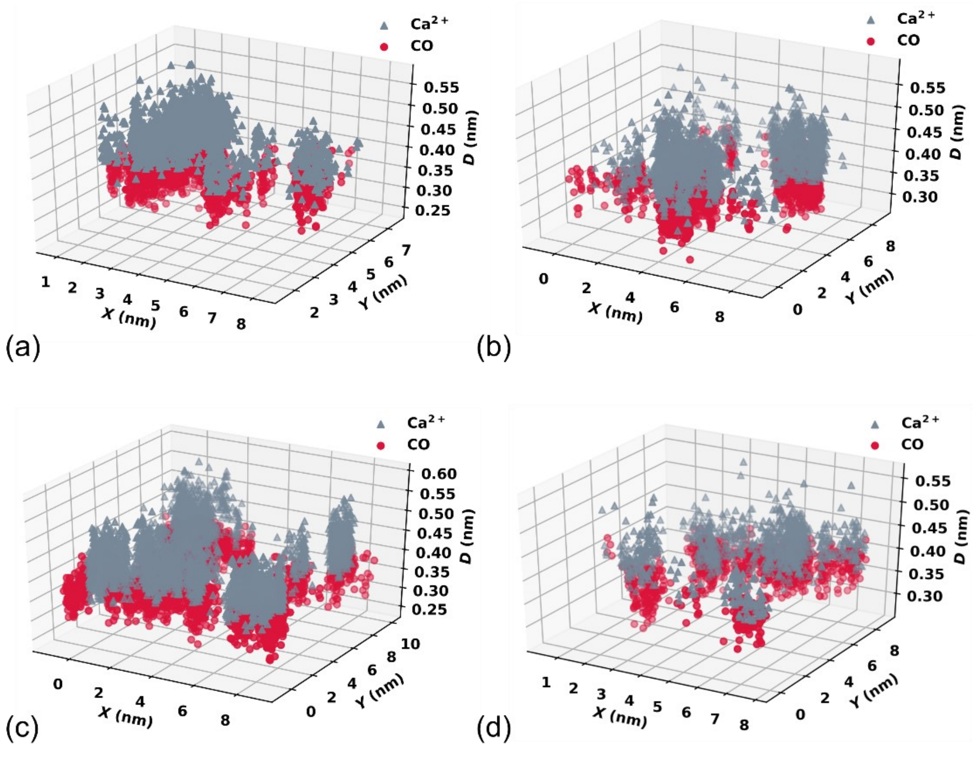

Figure C8. 3-D map of adsorbed APAM carbonyl oxygens (CO) that were simultaneously coordinated to at least one Ca^{2+} ions , based on data from the last 20 ns of the simulation in system (a) Ca-0, (b) Ca-0.05, (c) Ca-0.1, and (d) Ca-0.3. The coordinated Ca^{2+} ions are also shown.

C1.6. Statistics of Ion-APAM complexes

Table C2 shows the number of COO^- and CO from all APAM molecules that are within 0.24 nm of Ca^{2+}, Ca^{2+} that are within 0.24 nm of COO^- and CO from all APAM molecules, as well as the number of adsorbed Ca^{2+}-APAM complexes. The corresponding data in systems Na-0 and Na-0.5 are also included, using coordination bond length of 0.22 nm (the first peak location of Na-CO RDF shown in Figure C9). The data was averaged over the last 20 ns of the simulations. The number of COO^- within 0.24 nm of Ca^{2+} and the number of Ca^{2+} within 0.24 nm of COO^- were close but not necessarily equal, because one Ca^{2+} could be simultaneously within 0.24 nm of two COO^- and vice versa. The same was true for the data between CO and Ca^{2+}, as well as between the oxygens and Na^+. The numbers in Table C2 for COO^- were clearly much smaller than the numbers for CO, confirming that coordination to Ca^{2+} through the carbonyl oxygens was preferred than through carboxylate groups. Finally, the total number of CO coordinated to Ca^{2+} was 10-folder higher than the number of CO in adsorbed Ca^{2+}-APAM complexes, because some unadsorbed APAM still formed Ca^{2+}-APAM complexes.

Table C2. Statistics for the Ion-APAM coordination

salt concentration	O within 0.24/0.22 nm of cations		cations within 0.24/0.22 nm of O		adsorbed Ion-APAM complexes on Mt
	COO^-	CO	COO^-	CO	CO
Ca-0	0.001	14.61	0.001	11.85	0.89
Ca-0.05 M	0.005	25.30	0.005	18.57	1.17
Ca-0.1 M	0.003	32.49	0.003	23.05	2.11
Ca-0.3 M	0.02	33.59	0.02	24.19	0.55
Ca-0.5 M	0.01	35.34	0.005	14.27	0.22
Na-0	0	0.681	0	0.669	0
Na-0.5 M	0	1.915	0	1.878	0

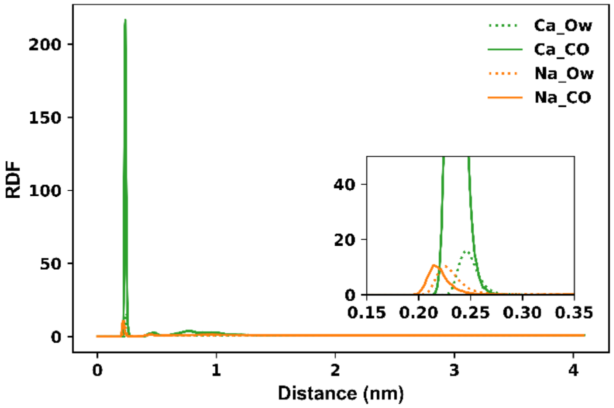

Figure C9. RDFs of carbonyl oxygens of APAM (Ca_CO) and water oxygens (Ca_Ow) around Ca^{2+} in system Ca-0.5, and corresponding data in system Na-0.5. All data sampled from the last 20 ns of the simulations.

C1.7. Additional simulations using OPLSAA force field and density functional theory

An additional system (hereafter referred to as Ca-OPLS) was simulated by using the OPLSAA force field [2], instead of GROMOS 53a6, for the polymer and ions. The partial charges of APAM were still assigned according to Table C1. Six APAM molecules were added above an Mt plate in a system of size 4.14 × 5.38 × 5.00 nm^3. The system was neutralized by 27 Ca^{2+} ions and no extra $CaCl_2$ was added. The simulation was run following the same procedure as described in the main text, for 50 ns.

The RDFs of oxygens around Ca^{2+} are shown in Figure C10 for both systems Ca-OPLS and Ca-0. Between COO^- and CO, the latter exhibited greater coordination with Ca^{2+} regardless of the force field. However, the preference was less prominent with OPLSAA. Other adsorption mechanisms discussed in the main text were also found with the OPLSAA force field. For example, as shown in Figure C11, the location of Ca^{2+} layer was still at ~0.4 nm from the Mt surface. N and CO of APAM became even closer to Mt surface, suggesting the lack of Ca^{2+} bridges. Synergy between long-range electrostatic attraction and short-range H-bonding was also observed as shown in Figure C12.

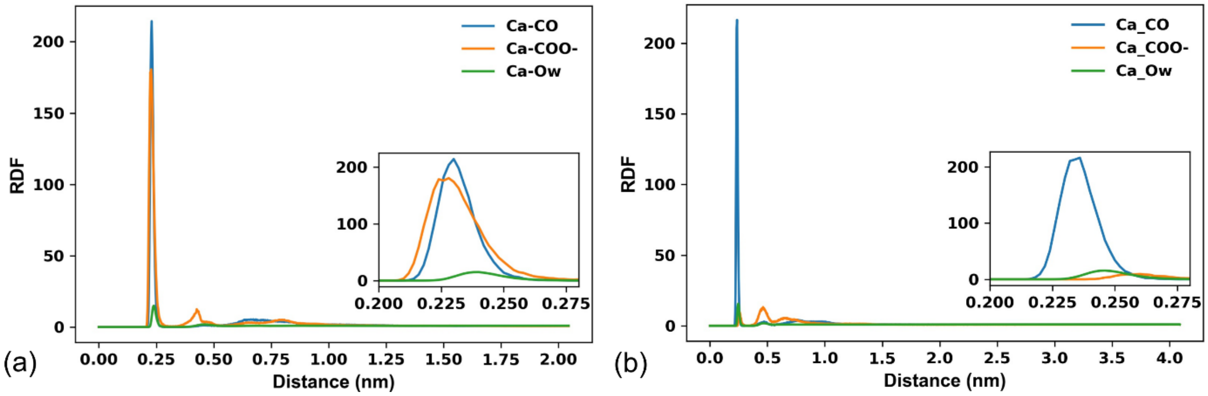

Figure C10. RDFs of carbonyl oxygens (CO), carboxyl oxygens (COO^-), and water oxygens (Ow) around Ca^{2+} in system Ca-OPLS (a) and system Ca-0 (b), sampled from the last 20 ns of the simulations.

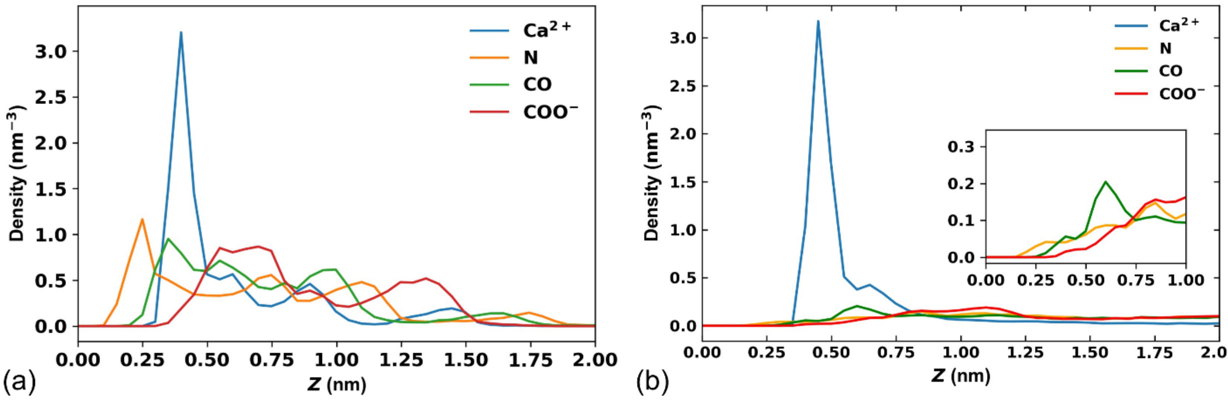

Figure C11. Density profiles of Ca^{2+} and APAM atoms as functions of distance from the Mt surface in system Ca-OPLS (a) and system Ca-0 (b). The data were sampled from the last 20 ns of the simulations.

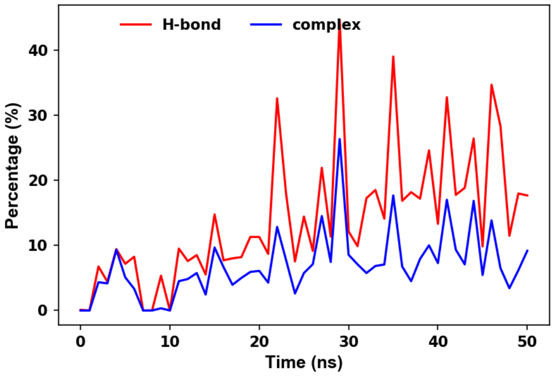

Figure C12. Percentage of CO in the adsorbed APAM molecules that contributed to the formation of adsorbed Ca^{2+}-APAM complexes (blue curve), percentage of amino hydrogen the adsorbed APAM molecules that contributed to H-bonding with Mt (red curve) in system Ca-OPLS. Each point is an average of 100 sample points within the previous 1 ns.

DFT calculations were performed in Gaussian 16[1] to examine the binding of Ca^{2+} to different groups in APAM. An APAM segment with one amide and one carboxylate was simulated. In one of the simulations, a Ca^{2+} ion was placed close to a carbonyl oxygen, and 5 water molecules were dispersed around the cation. Another simulation was designed in the same way except that the Ca^{2+} was placed close to a carboxyl oxygen. Geometrical optimization at B3LYP/6-31+G (d,p) level was performed followed by frequency calculation to make sure the optimized results reached stationary points instead of transitional states. In each case, the model (APAM segment, Ca^{2+} and explicit water molecules) was subjected to a two-step optimization process: first in vacuum and then in implicit aqueous environment. The optimized geometries for the two models are displayed in Figure C13. In Figure C13a, the Ca^{2+} was coordinated to one CO and four water in its first coordination shell. In Figure C13b, the Ca^{2+} was coordinated to one carboxyl oxygen and five water in its first coordination shell. The energy of the configuration shown in Figure C13b was 3.21 kJ/mol lower than that in Figure C13a.

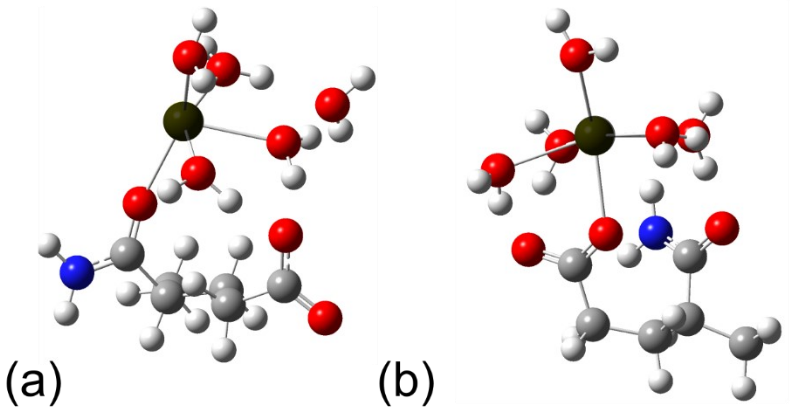

Figure C13. Geometries optimized from DFT calculations. For a two-unit polymer segment in implicit water: (a) Ca^{2+} coordinated to one CO and four explicit water in its first coordination shell, as well as one explicit water in its second coordination shell; (b) Ca^{2+} coordinated to one oxygen of COO$^-$ and five explicit water in its first coordination shell.

The coordination bond length and bond angle in Ca^{2+}-amide and Ca^{2+}-carboxylate complexes are compared in Table C3 for results obtained from GROMOS 53A6, OPLSAA and DFT calculations. For the bond length and angle in the Ca^{2+}-amide complex, bond length in the Ca^{2+}-carboxylate complex, and bond length of Ca^{2+}-Ow, values obtained from GROMOS 53A6 simulation were closer to the DFT results. However, OPLSAA outperformed GROMOS 53A6 in the modeling of coordination bond angle in the Ca^{2+}-carboxylate complex. Therefore, there is no clear evidence that one of the force fields tested is superior to the other.

Table C3. Coordination bond length and angle in Ca^{2+}-amide and Ca^{2+}-carboxylate complexes

	Bond length (Å)			Bond angle (degree)[c]	
	Ca-CO	Ca-COO$^-$	Ca-Ow	Ca-CO-C	Ca-COO$^-$-C
DFT[a]	2.386	n/a	2.476	158.3	n/a
DFT[b]	n/a	2.424	2.506	n/a	126.9
GROMOS	2.38	2.52	2.46	165	n/a
OPLSAA	2.25	2.30	2.38	167	92

a. In the case represented by Figure C13a.

b. In the case represented by Figure C13b.

c. The bond length from MD simulations was determined from the location of the first peak in the RDFs in Figure C10. The bond angle was identified as the location of the most pronounced peak in Figure C14.

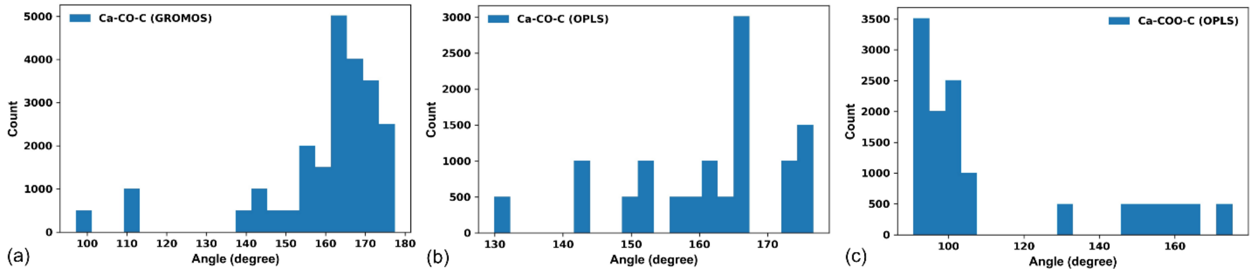

Figure C14. Distribution of coordination bond angles sampled from the last 10 ns from system Ca-0.1 (a) and system Ca-OPLS (b) (c), sampled from the last 20 ns of the simulations

C1.8. APAM-APAM interaction

Figure C15a shows, for system Ca-0.1, the RDF around one APAM molecule of all other APAM molecules. The first peak was at 0.19 nm, indicating the formation of H-bonds. The location of the second peak (around 0.3 nm) was consistent with the peak location of RDF between CO atoms (Figure C15b), suggesting interaction between two APAM molecules via Ca^{2+} coordination.

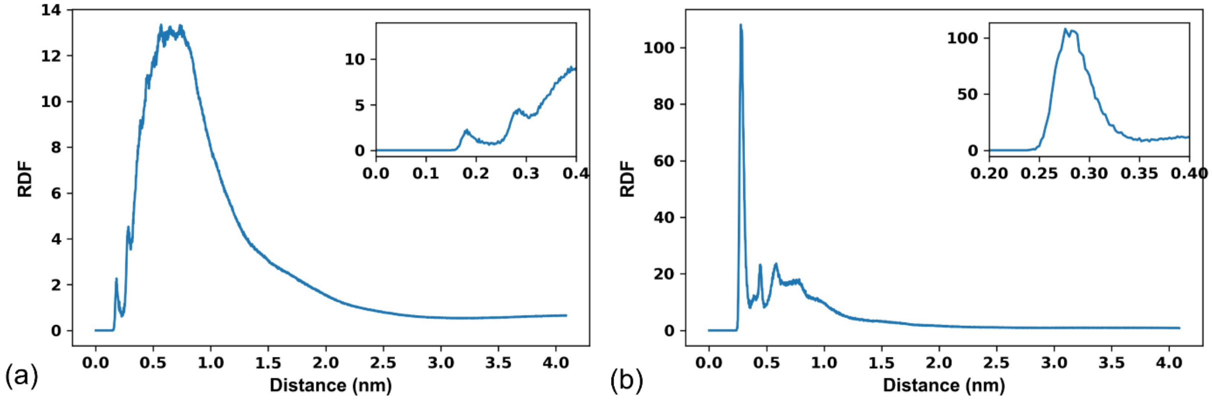

Figure C15. RDF around one APAM molecule of all other APAM molecules (a) and RDF between CO atoms (b) in system Ca-0.1, sampled from the last 20 ns of the simulation.

Figure C16 shows the number of APAM molecules that were directly adsorbed on Mt as monomers and in the form of clusters. An APAM molecule was considered as directly adsorbed in a cluster form when it was within 0.23 nm of Mt and its minimum distance from another APAM was less than 0.19 nm. As illustrated by the figure, APAM could become adsorbed in either form.

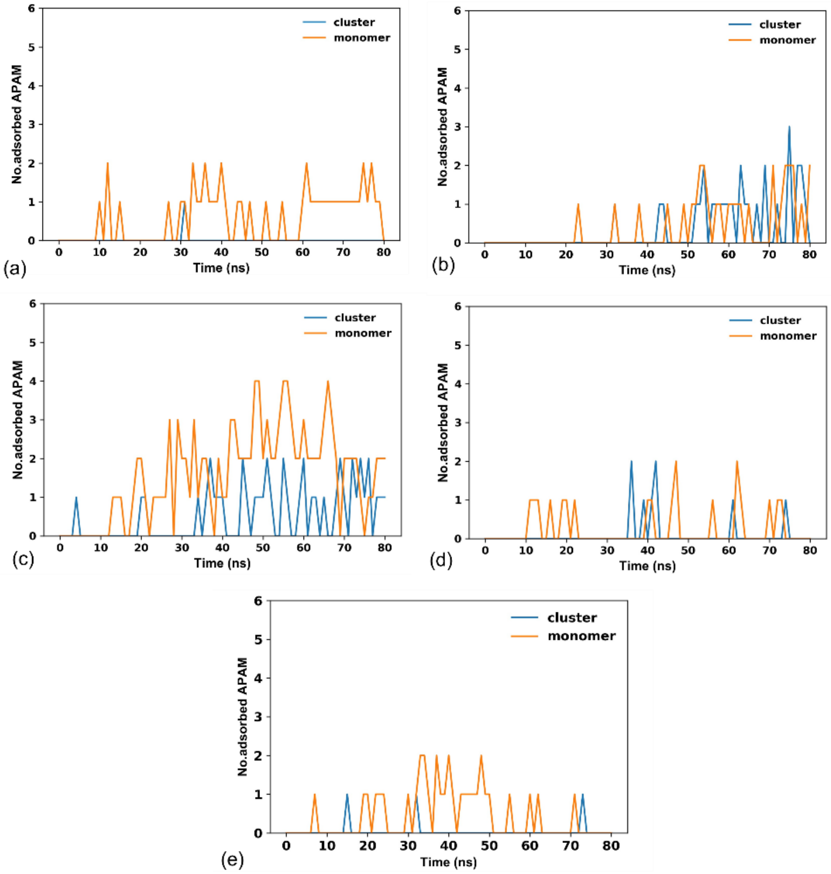

Figure C16. Number of adsorbed APAM molecules on Mt, in systems Ca-0 (a), 0.05 (b), 0.1 (c), 0.3 (d), and 0.5 (e) respectively.

C2. Calculation details

C2.1. Thickness of electric double layer

The outer boundary of the electric double layer (EDL) was considered to be where the number density of cations converged to the bulk value. For each system, the procedure to determine this location was as follows:

1. All data for the number density of cations and anions as functions of *Z* were collected.

2. For systems containing only cations, the 99% confidence interval was calculated based on the data collected from the range of *Z* = 2-3.5 nm. The true mean value of the bulk number density of cations was 99% likely to be within this range.
3. Similarly, for systems containing both cations and anions, the 99% confidence interval for the difference in number density between cations and anions was calculated based on the data collected from the range of *Z* = 2-3.5 nm. The smallest *Z* value at which the number density difference fell into the 99% confidence interval was determined as the outer boundary of the EDL.

Table C4. EDL thickness in the simulated systems

System	Ca-0	Ca-0.05	Ca-0.1	Ca-0.3	Ca-0.5	Na-0	Na-0.5
EDL thickness (nm)	1.90	2.19 [a]	1.25 [b]	1.35	1.35	2.49	1.39

a & b: The calculated thicknesses in systems Ca-0.05 and 0.1 were abnormally large, which may be because of the adsorption of APAM. The presence of adsorbed APAM on Mt may perturb the EDL, and from Figure 4.6 in the main text, the number of adsorbed APAM was the largest in these two systems.

C2.2. Number of ions in the calculation of Debye length

The number of counterions (Na^+/Ca^{2+}) and co-ions (Cl^-) in the calculation of Debye length (Table 4.2 in the main text) are given in Table C5.

Table C5. Number of counterions (Na^+/Ca^{2+}) and co-ions (Cl^-)

System	Counterions	Co-ions
Na-0	156	0
Na-0.5	378	222
Ca-0	78	0
Ca-0.5	302	448

C2.3. Type of atoms within 0.25 nm of Ca^{2+} ions

To identify the types of atoms within 0.25 nm of a specific Ca^{2+} ion, the indices of all atoms within 0.25 nm of the Ca^{2+} ion were collected. The indices were then compared with the molecular structure file that recorded the atom types. A python script was written to automate the comparison step.

C2.4. Definitions for adsorption

System Ca-0.1 was analyzed to determine the critical distances used to define adsorption, because the adsorption is strongest in this system. The histogram of minimum distance between all the APAM CO and all atoms of Mt (including plane I and the periodic image of plane II) over the 80 ns simulation is shown in Figure C17. The large values of the histogram between 0.30 nm and 0.43 nm represented the stable adsorption of CO, and there was a clear gap after 0.43 nm. Therefore, for all systems discussed in the main text, if the minimum distance between an APAM CO and all atoms of Mt was less than 0.43 nm, the CO atom was considered adsorbed on Mt. An adsorbed Ca^{2+}-APAM complex corresponded to an adsorbed APAM CO that was simultaneously coordinated to (i.e., within 0.24 nm of) at least one Ca^{2+} ion.

Similarly, the histogram of minimum distance between all atoms of APAM molecules and all atoms of Mt is shown in Figure C18, sampled from the last 20 ns of simulations for systems Ca-0, 0.05, 0.1, 0.3 and 0.5. The first peak ended at 0.23 nm. Thus, for the Ca^{2+} containing system, an APAM molecule was considered adsorbed if its minimum distance from the Mt surface was less than 0.23 nm.

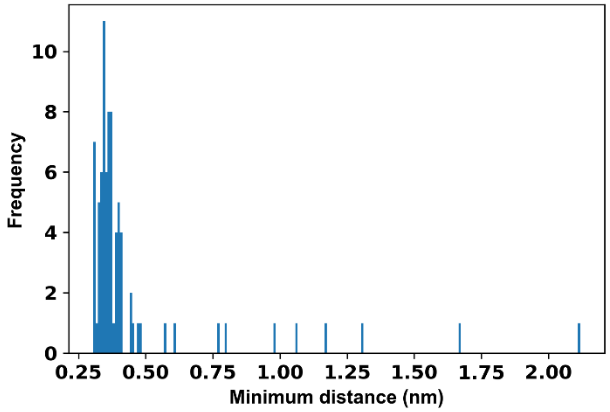

Figure C17. Histogram of minimum distance between all APAM CO (as a group) and all atoms of Mt (as another group), data from the simulation for system Ca-0.1.

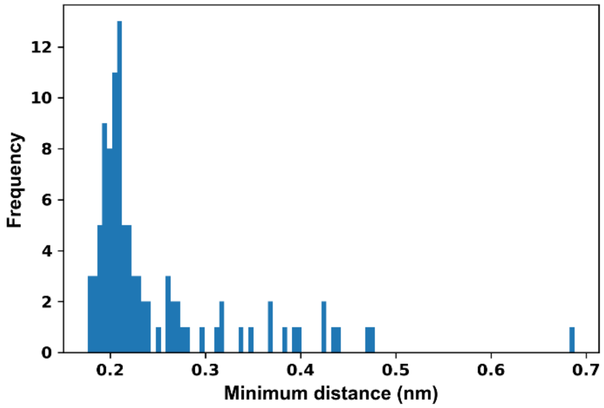

Figure C18. Histogram of minimum distance between all APAM atoms (as a group) and all atoms of Mt (as another group), data from the simulations for systems Ca-0, 0.05, 0.1, 0.3, and 0.5.

C2.5. Average number of Ca^{2+} ions coordinated to each APAM molecule

The total number of Ca^{2+} ions within 0.24 nm (first peak in the Ca_CO RDF in Figure 4.3a) of all APAM CO atoms (both adsorbed and unadsorbed) was calculated for the last 20 ns of each simulation. The number was divided by 12 (number of APAM molecules in each system) to acquire the number of Ca^{2+} ions coordinated to each APAM. The mean and standard deviation, with respect to time, were reported in Figure 4.5b of the main text.

C2.6. Percentage of functional groups contributing to Ca^{2+}-APAM complexation and APAM-Mt hydrogen bonding

The criterion to determine an APAM CO in a Ca^{2+}-APAM complex was described in section 3.2 of the main text. For each simulated system, if an APAM molecule is adsorbed on Mt, the 6 CO atoms in it were examined to see if they formed Ca^{2+}-APAM complexes and if they were simultaneously adsorbed on Mt (criterion specified in section S2.4). The total number of CO from adsorbed APAM molecules that also adsorbed on Mt in the form of Ca^{2+}-APAM complexes was calculated. This number was then normalized with respect to the total numbers of CO in the adsorbed APAM (6 from each), resulting in the percentage of CO in adsorbed APAM molecules that contributed to the formation of adsorbed Ca^{2+}-APAM complexes.

Hydrogen bonds (H-bonds) between APAM and Mt were calculated by GROMACS command *gmx hbond*, in which NH groups on APAM were donors and O on Mt were acceptors. The cut-off angle was set as 30^o and the cut-off distance was 0.35 nm. The total number of H-bonds were then normalized with respect to the total number of NH groups in the adsorbed APAM (12 from each), representing the percentage of NH groups contributing to the H-bonding in adsorbed APAM molecules.

References

[1] D.J. Frisch, M. J., Trucks, G. W., Schlegel, H. B., Scuseria, G. E., Robb, M. A., Cheeseman, J. R., Scalmani, G., Barone, V., Petersson, G. A., Nakatsuji, H., Li, X., Caricato, M., Marenich, A. V., Bloino, J., Janesko, B. G., Gomperts, R., Mennucci, B., Hratch, Gaussian 16 Revision B. 01., Wallingford CT. (2016).

[2] W.L. Jorgensen, J. Tirado-rives, The OPLS Potential Functions for Proteins. Energy

Minimizations for Crystals of Cyclic Peptides and Crambin, J. Am. Chem. Soc. 110 (1988). doi:10.1021/ja00214a001.

Appendix D: Supporting Information for Chapter 5

D1. Additional results

D1.1. Justification of simulating Si-Si-Wat in NVT ensemble

System Si-Si-Wat was simulated in NVT ensemble to avoid structural distortion of the clay plates. Density of water was calculated as an evidence that decoupling of pressure did not have significant effect on the solution property (Figure D1a), compared with systems Al-Al-Wat and Al-Si-Wat simulated in NPT ensemble. Meanwhile, the diffusion coefficient as a dynamic property of water was extracted from the slope of the mean square displacement (MSD) (Figure D1b) according to the Einstein relation [1]. The diffusion coefficients of water in the three systems were $(2.70 \pm 0.30) \times 10^{-5}$ cm^2/s, $(2.79 \pm 0.30) \times 10^{-5}$ cm^2/s, and $(2.72 \pm 0.35) \times 10^{-5}$ cm^2/s, respectively, demonstrating similar motions of the water molecules.

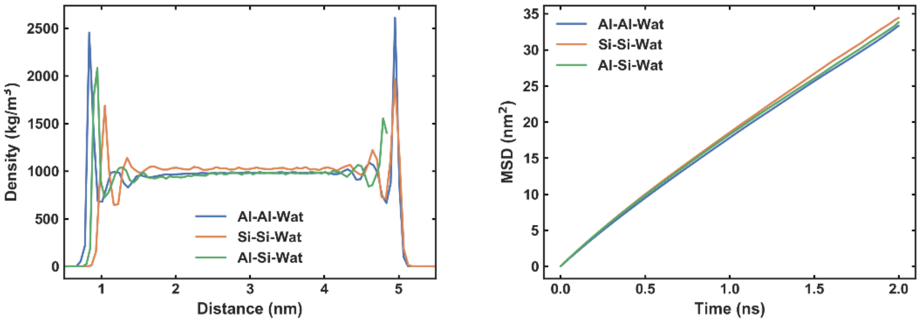

Figure D1. Plots of water density (a) and MSD (b) in system Al-Al-Wat, Si-Si-Wat, and Al-Si-Wat.

D1.2. Ca^{2+} bridges

The coordination of oxygens to Ca^{2+} in systems containing one C5Pe molecule was plotted in Figure D2. In the systems solvated by water (Figures D2a-c), the Ca^{2+} ion was only coordinated to water oxygens. In toluene solvated systems, when C5Pe became adsorbed on the alumina surface (Figures 5.2d and f), Ca^{2+} was coordinated to either C5Pe or the surface, which contrasted with the adsorption on siloxane surface where Ca^{2+} was simultaneously coordinated to both C5Pe and the surface. In heptane, the Ca^{2+} ion was simultaneously coordinated to C5Pe and surface in all cases (Figures D2g-i), bridging them together.

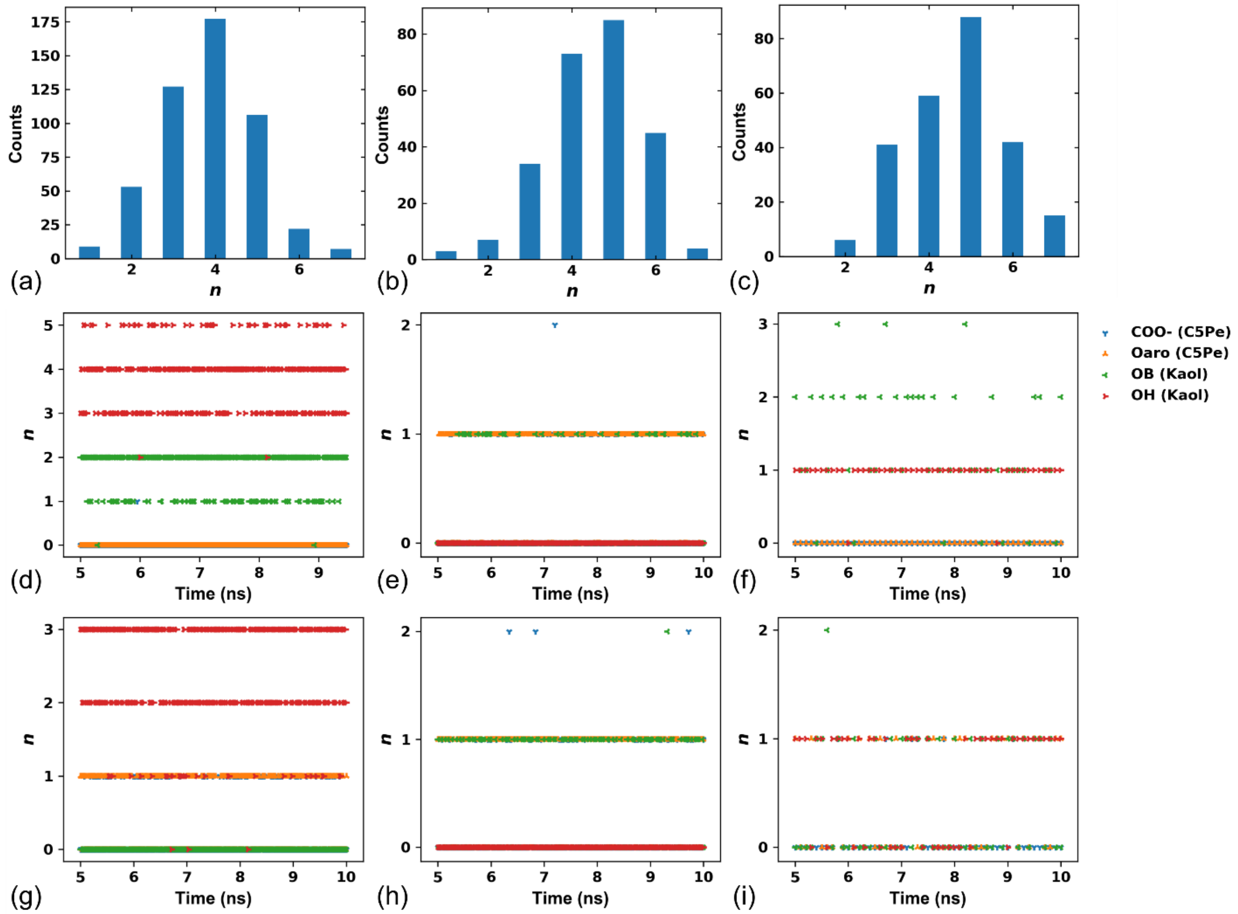

Figure D2. Distribution of the number of water oxygens coordinating to Ca^{2+} in systems (a) Al-Al-Wat, (b) Si-Si-Wat, and (c) Al-Si-Wat. Number of oxygens coordinated to Ca^{2+} in systems (d) Al-Al-Tol, (e) Si-Si-Tol, (f) Al-Si-Tol, (g) Al-Al-Hep, (h) Si-Si-Hep, (i) Al-Si-Hep. In (d)-(i), the oxygens are carboxylic oxygens of C5Pe (COO^-), oxygens of PAH of C5Pe (Oaro), oxygens of the basal surface of Kaol (OB), and hydroxyl oxygens of Kaol (OH). The data in all systems were extracted from the last 5 ns of simulations.

The coordinating oxygens to the six Ca^{2+} in system Tol-12 are shown in Figure D3. Each Ca^{2+} ion coordinated to either C5Pe (the carboxylic oxygens or the aromatic oxygens), or the surface (the bridging oxygens or the hydroxyl oxygens), but not both. The real-time coordination scenario of the six Ca^{2+} in system Hep-12 is shown in Figure D4. Ca_3 and Ca_6 were coordinated to C5Pe only over the last 20 ns, while the other Ca^{2+} ions coordinated to both C5Pe and the surface.

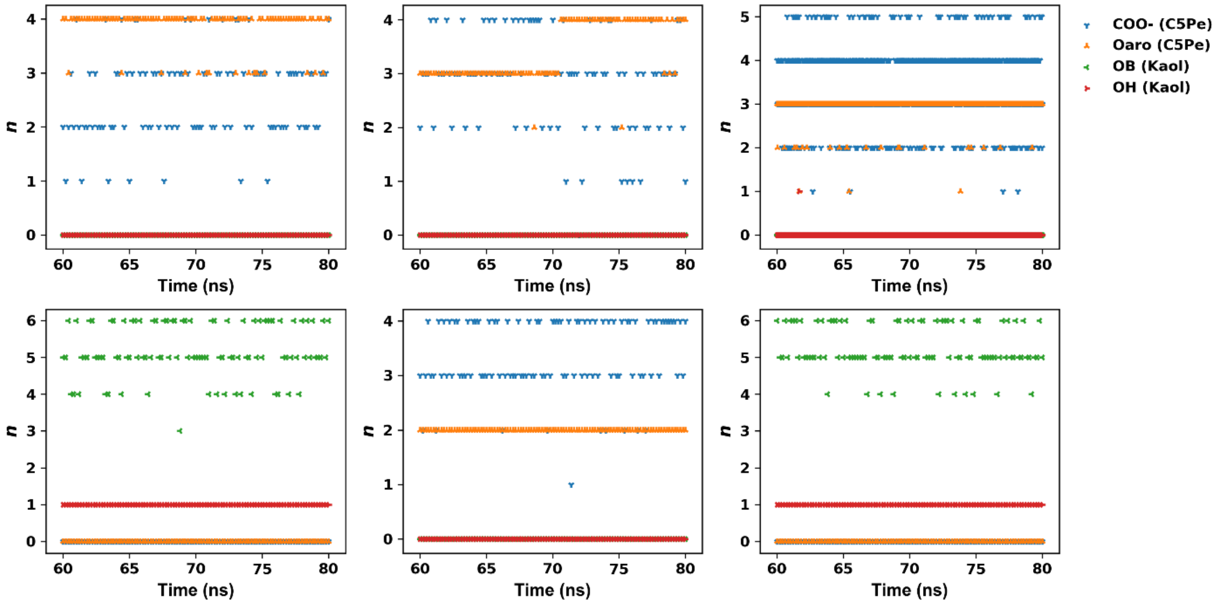

Figure D3. Real-time coordination statistics for the six Ca^{2+} in system Tol-12, the subfigures from the upper left to the bottom right represent the coordination of Ca_1 to Ca_6.

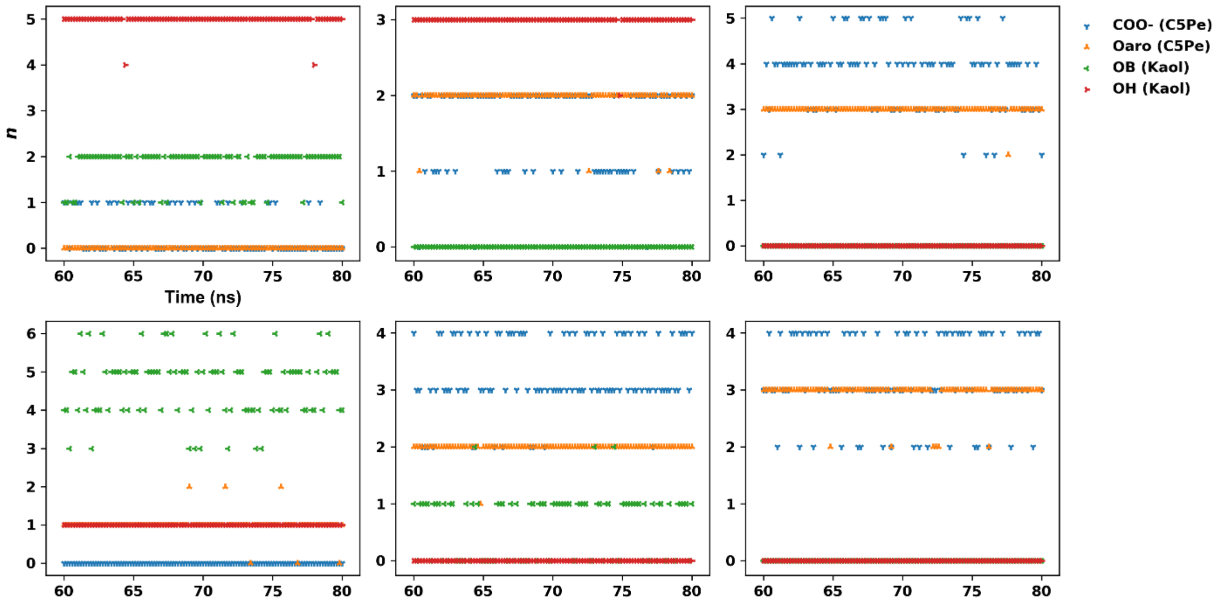

Figure D4. Real-time coordination statistics for the six Ca^{2+} in system Hep-12, the subfigures from the upper left to the bottom right represent the coordination of Ca_1 to Ca_6.

D1.3. Density profile

The density profiles of C5Pe and Ca^{2+} in system containing 12 C5Pe molecules are shown in Figure D5. The alumina surface is located on the left (0 nm on the horizontal axis) and siloxane surface on the right (7.6 nm, 7.8 nm, 8.0 nm respectively on the horizontal axis). Figure D5a shows the Ca^{2+} ions stayed in the stern layer of the siloxane surface while the C5Pe became adsorbed on the alumina surface of Kaol. In system Tol-12, as showed in Figure D5b, the first peak of Ca^{2+} (0.75 nm) was between the peaks of C5Pe (0.5 nm and 0.95 nm), implying the bridging of different C5Pe layers by Ca^{2+}. The peak of Ca^{2+} (7.75 nm) represented the coordination of Ca^{2+} to the oxygens on the siloxane surface. In system Hep-12 (Figure D5c), there was a peak of Ca^{2+} (0.33 nm) before the first peak of C5Pe (0.45 nm), indicating the bridging of C5Pe and the surface by Ca^{2+}.

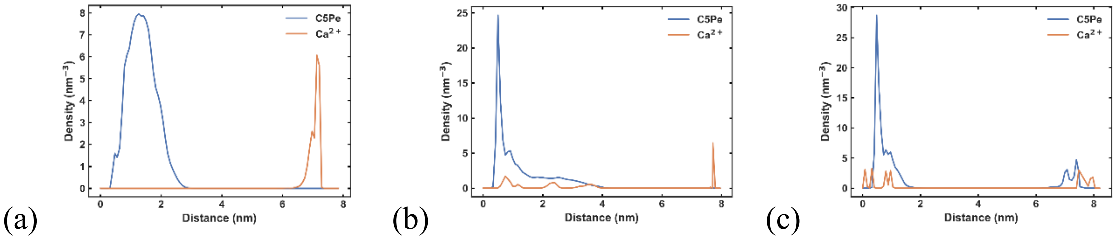

Figure D5. Density profiles of C5Pe and Ca^{2+} in system Wat-12 (a), Tol-12 (b), and Hep-12 (c).

D2. Calculation details

D2.1. Calculation of aggregate size

The size of the aggregates that adsorbed on the surface was calculated based on two cutoff values: one to define the aggregation (cutoff 1) and the other to define the direct adsorption of C5Pe (cutoff 2). Take system Wat-12 as an example, the histogram of the minimum distance between the PAH of one C5Pe and the PAH of the other 11 C5Pe molecules is shown in Figure D6a. The first peak ended at 0.55nm, and this distance was taken as cutoff 1 for C5Pe aggregation. The characterization method and cutoff value for aggregation were consistent with the work of Xiong et al [2]. Similarly, the minimum distances between the C5Pe molecules and the surface were calculated (Figure D6b), and the end of the first peak (0.25 nm) was adopted as cutoff 2. The scenario for systems Tol-12 and Hep-12 were similar with Wat-12.

A C5Pe molecule was defined as directly adsorbed when its minimum distance from the surface fell into cutoff 2. If a C5Pe molecules was within 0.55 nm of a directly adsorbed one, the two molecules were taken as an aggregate that adsorbed on the surface.

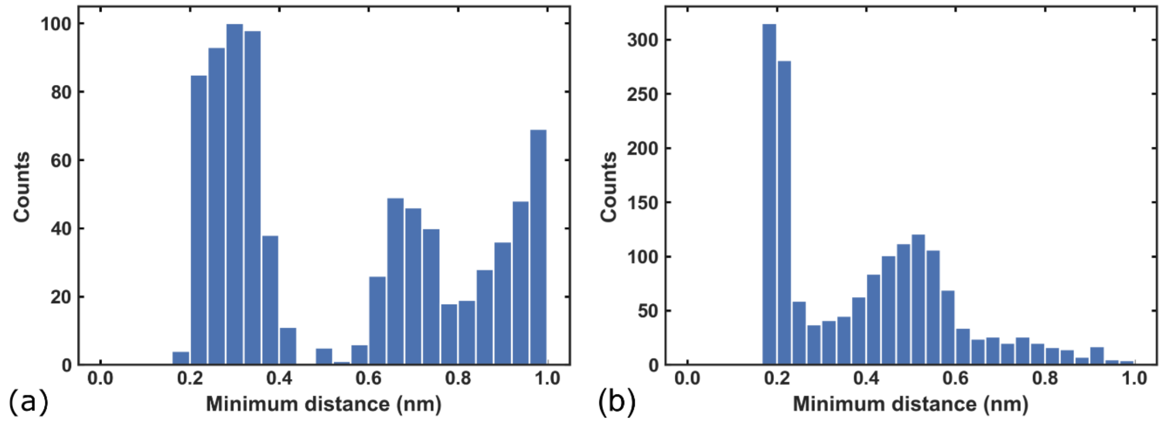

Figure D6. Histograms of minimum distance between PAH of one C5Pe and PAH of the other 11 C5Pe molecules (a), as well as between C5Pe and the surface (b) in system Wat-12. The data was sampled from the last 20 ns of simulation.

D2.2. Calculation of coordination bonds

The coordination bonds were counted when the distance between Ca^{2+} and oxygens were within certain cutoffs. In water, only the water oxygens coordinated to Ca^{2+} since there were no prominent peaks in the RDFs between Ca^{2+} and other oxygens as shown in Figure D7a. The location of the first peak in the RDF of Ca_Ow (0.25 nm) was adopted as the cutoff for the formation of coordination bonds between Ca^{2+} and water. Similarly, the peak location of the RDF of Ca_COO^- (0.26 nm, Figures D7b and c) was used as the cutoff to calculate the coordination bonds in the organic systems.

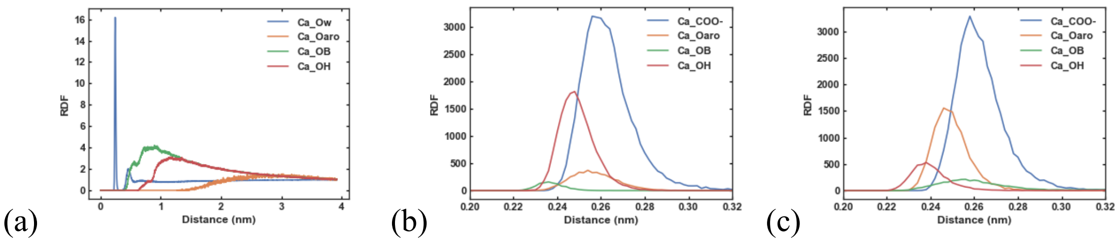

Figure D7. RDF of Ca^{2+} around water oxygens (Ow), carboxylic oxygens (COO^{-}), oxygens of PAHs (Oaro), bridging oxygens of the surface (OB), and hydroxyl oxygens of the surface (OH) in system Wat-12 (a), Tol-12 (b) and Hep-12 (c).

References

[1] Y. Roichman, N. Tessler, Generalized Einstein relation for disordered semiconductors—implications for device performance, Appl. Phys. Lett. 80 (2002) 1948–1950.

[2] Y. Xiong, T. Cao, Q. Chen, Z. Li, Y. Yang, S. Xu, S. Yuan, J. Sjöblom, Z. Xu, Adsorption of a Polyaromatic Compound on Silica Surfaces from Organic Solvents Studied by Molecular Dynamics Simulation and AFM Imaging, J. Phys. Chem. C. 121 (2017) 5020–5028. doi:10.1021/acs.jpcc.6b11763.

Appendix E: Supporting Information for Chapter 6

E1. Calculation details

E1.1. Justification of adsorption of C5Pe and APAM on solid surfaces

The minimum distance between all the C5Pe molecules and the basal surfaces in system Mt-0 is plotted in Figure E1a. The first peak ended at 0.3 nm, and this distance was taken as the cutoff for C5Pe adsorption in all the Mt systems. Similarly, the cutoff was 0.25 nm for direct APAM adsorption on Mt surfaces and Kaol surfaces, as taken from the ends of the first peaks. Within the cutoff, APAM formed H-bonds with the surface.

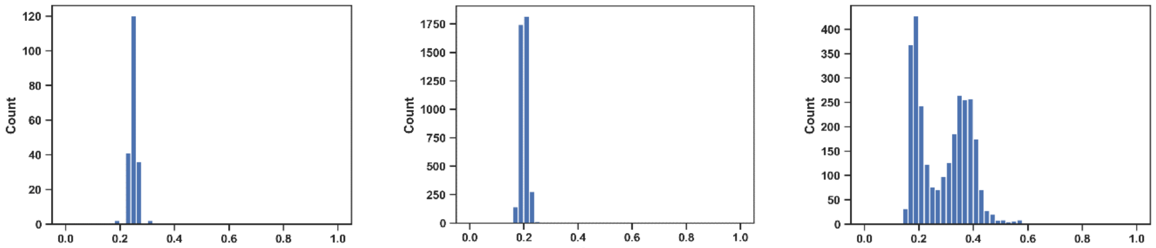

(a) (b) (c)

Figure E1. Distribution of minimum distance between all the C5Pe molecules and Mt basal surfaces in system Mt-0 (a), between all the APAM molecules and Mt basal surfaces in system Mt-12 (b), and between all the APAM molecules and the Kaol edge surfaces in system Kaol-24 (c). All data was averaged over the last 20 ns of simulations.

E1.2. Justification of C5Pe parallel stacking

The justification for parallel stacking between C5Pe molecules was based on the distribution of minimum distances between one and the rest C5Pe molecules. As shown in Figure E2, the first prominent peak ended at 0.55 nm, and this distance was thus taken as the cutoff for C5Pe parallel stacking.

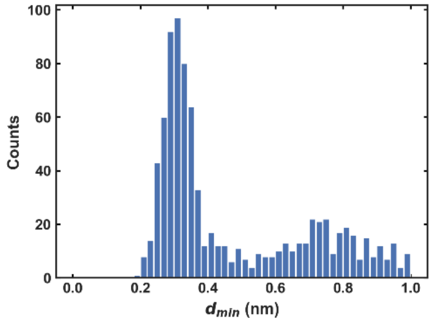

Figure E2. Distribution of minimum distance between one and the rest C5Pe molecules in system Mt-0, averaged over the last 20 ns.

E2. Additional results

E2.1. Size of all the C5Pe aggregates

The sizes of all the C5Pe aggregates in Mt systems are shown in Figure E3. As shown in the figure, the biggest aggregate in all the systems contained at least 8 molecules.

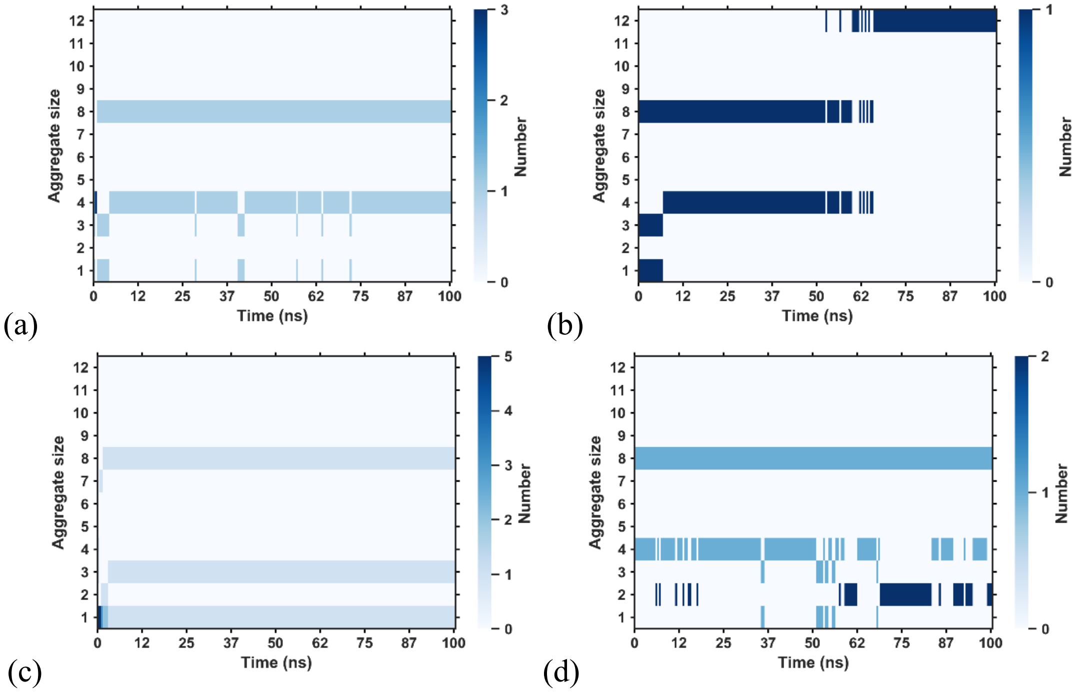

(a) (b) (c) (d)

Figure E3. Size of all the C5Pe aggregates in systems Mt-0 (a), Mt-12 (b), Mt-24 (c), and Mt-p24 (d). The color bar indicates the number of aggregates corresponding to a certain size. The size of an aggregate was quantified by the number of C5Pe molecules it contained.

E2.2. Size of the largest APAM cluster

The maximum cluster size of APAM is shown in Figure E4. The largest cluster in system Mt-12 contained a maximum of 5 molecules in the last 20 ns, which lasted instantaneously.

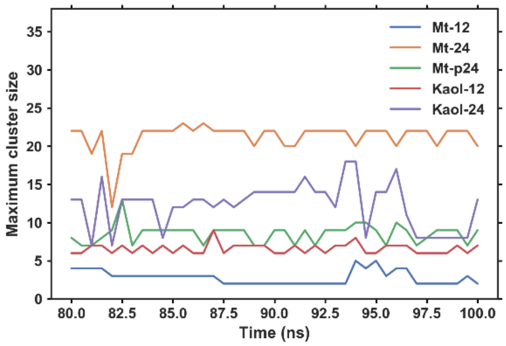

Figure E4. Maximum cluster size of APAM in the last 20 ns of simulations.

E2.3. Size of the adsorbed C5Pe aggregates on the surface

The sizes of all the adsorbed C5Pe aggregates in Mt systems are shown in Figure E5. The adsorption as well as the aggregation of C5Pe on the surfaces were quite stable.

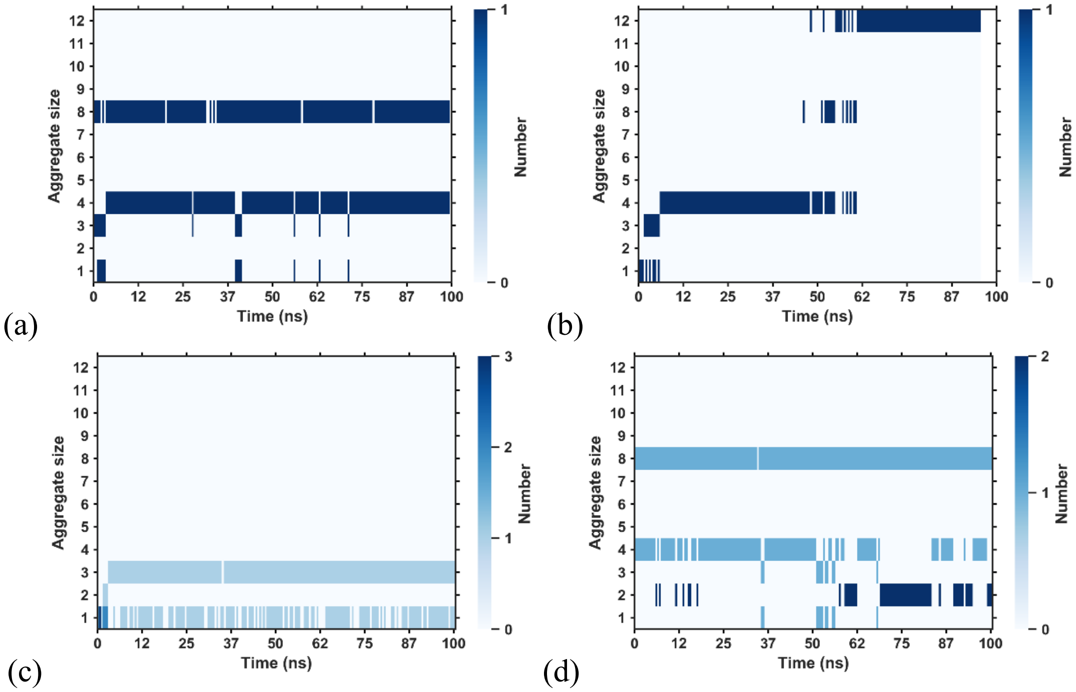

Figure E5. Size of all the adsorbed C5Pe aggregates in systems Mt-0 (a), Mt-12 (b), Mt-24 (c), and Mt-p24 (d). The plotting scheme is the same with Figure E3.

E2.4. Size of the adsorbed APAM clusters on the surface

The sizes of all the adsorbed APAM clusters are shown in Figure E6. As compared with the adsorption of C5Pe in Figure E5, the adsorption of APAM was in a less stable manner.

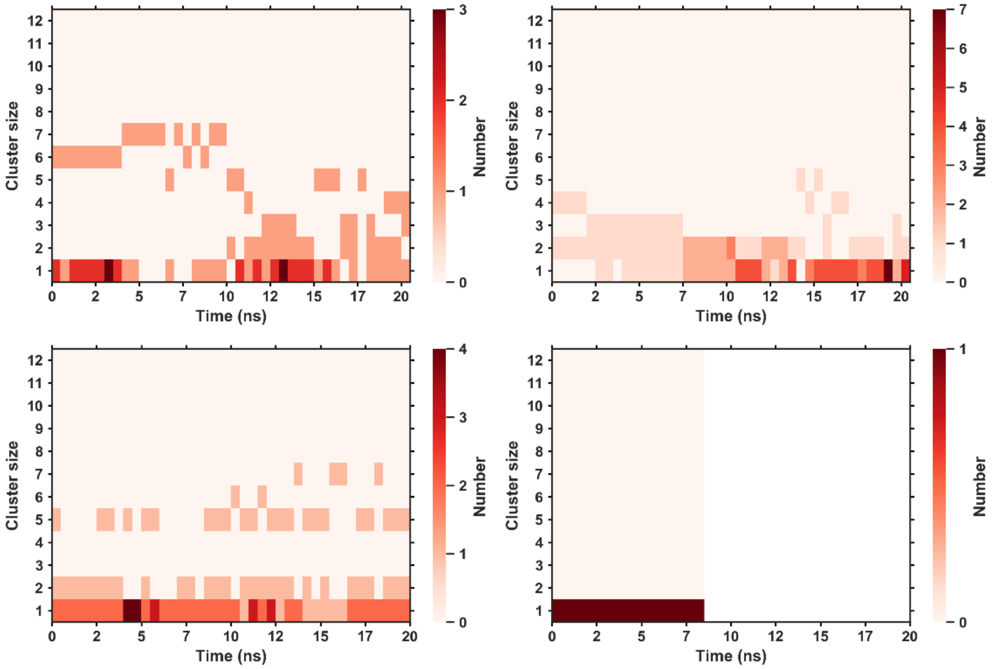

Figure E6. Size of all the adsorbed APAM clusters in systems Mt-C0 (a), Mt-12 (b), Kaol-C0 (c), and Kaol-12 (d). The plotting scheme is the same with Figure E3.

E2.5. H-bonds number between C5Pe and APAM in system Mt-12

The number of H-bonds (N_{hbond}) between C5Pe and APAM in system Mt-12 is shown in Figure E7. As shown in the figure, H-bonds became non-zero within the first 10 ns, indicating the adsorption of APAM on C5Pe, while the aggregation (Figure E3) and adsorption (Figure E5) of C5Pe were still under developing.

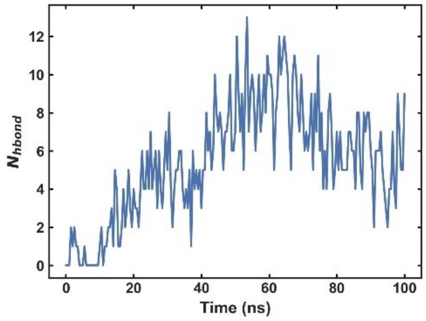

Figure E7. Number of H-bonds (N_{hbond}) between C5Pe and APAM in system Mt-12.

E2.6. Ca^{2+} coordination in the adsorption of APAM

The role of Ca^{2+} coordination was studied in system Kaol-24 as an example for the adsorption of APAM in Kaol systems. The density profiles showed that Ca^{2+} adsorbed at Z = 0.24 nm, before the peak of APAM, which suggested that Ca^{2+} was sandwiched between APAM and the edge surface. Since Ca^{2+} preferred to coordinate to oxygens in water[1], RDFs of multiple types of oxygens around Ca^{2+} are plotted in Figure E8b. Ca^{2+} display preferential coordination to the carbonyl oxygens of APAM and the hydroxyl oxygens of the edge surface. Meanwhile, the coordination of other oxygens except for the bridging oxygens inside the surface was also possible. When coordinated to oxygens from the surface and APAM simultaneously, Ca^{2+} was thus able to bridge them together.

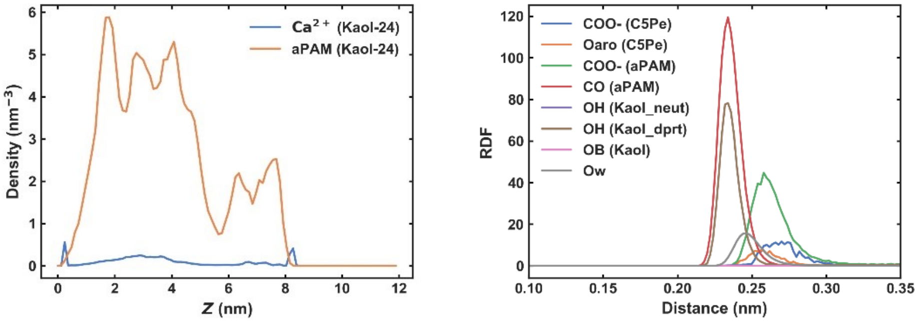

Figure E8. (a) Density profiles of Ca^{2+} and APAM along the *Z* axis above the Kaol surface. (b) RDFs of oxygens from carboxyl of C5Pe, PAH of C5Pe, carboxyl of APAM, carbonyl of APAM, hydroxyls of the neutral cells of Kaol, hydroxyls of the deprotonated cells of Kaol, bridging groups of Kaol, and water, respectively, around Ca^{2+} in system Kaol-24. The value of RDF between carbonyl oxygens of APAM (CO (APAM)) and Ca^{2+} was reduced 5 times for better visualization.

References

[1] W. Sun, H. Zeng, T. Tang, Enhanced Adsorption of Anionic Polymer on Montmorillonite by Divalent Cations and the Effect of Salinity, J. Phys. Chem. A. 125 (2021) 1025–1035. doi:10.1021/acs.jpca.0c08797.